STRUCTURE AND BONDING 131

Series Editor D. M. P. Mingos
Volume Editors X. Lu · Y. Hu

Molecular Thermodynamics of Complex Systems

Springer

131

Structure and Bonding

Series Editor: D. M. P. Mingos

Structure and Bonding

Series Editor: D. M. P. Mingos

Recently Published and Forthcoming Volumes

Molecular Thermodynamics of Complex Systems
Volume Editors: Lu, X., Hu, Y.
Vol. 131, 2009

Contemporary Metal Boron Chemistry I
Volume Editors: Marder, T. B., Lin, Z.
Vol. 130, 2008

Recognition of Anions
Volume Editor: Vilar, R.
Vol. 129, 2008

Liquid Crystalline Functional Assemblies and Their Supramolecular Structures
Volume Editor: Kato, T.
Vol. 128, 2008

Organometallic and Coordination Chemistry of the Actinides
Volume Editor: Albrecht-Schmitt, T. E.
Vol. 127, 2008

Halogen Bonding
Fundamentals and Applications
Volume Editors: Metrangolo, P., Resnati, G.
Vol. 126, 2008

High Energy Density Materials
Volume Editor: Klapötke, T. H.
Vol. 125, 2007

Ferro- and Antiferroelectricity
Volume Editors: Dalal, N. S., Bussmann-Holder, A.
Vol. 124, 2007

Photofunctional Transition Metal Complexes
Volume Editor: V. W. W. Yam
Vol. 123, 2007

Single-Molecule Magnets and Related Phenomena
Volume Editor: Winpenny, R.
Vol. 122, 2006

Non-Covalent Multi-Porphyrin Assemblies
Synthesis and Properties
Volume Editor: Alessio, E.
Vol. 121, 2006

Recent Developments in Mercury Science
Volume Editor: Atwood, David A.
Vol. 120, 2006

Layered Double Hydroxides
Volume Editors: Duan, X., Evans, D. G.
Vol. 119, 2005

Semiconductor Nanocrystals and Silicate Nanoparticles
Volume Editors: Peng, X., Mingos, D. M. P.
Vol. 118, 2005

Magnetic Functions Beyond the Spin-Hamiltonian
Volume Editor: Mingos, D. M. P.
Vol. 117, 2005

Intermolecular Forces and Clusters II
Volume Editor: Wales, D. J.
Vol. 116, 2005

Intermolecular Forces and Clusters I
Volume Editor: Wales, D. J.
Vol. 115, 2005

Superconductivity in Complex Systems
Volume Editors: Müller, K. A., Bussmann-Holder, A.
Vol. 114, 2005

Molecular Thermodynamics of Complex Systems

Volume Editors: Xiaohua Lu · Ying Hu

With contributions by

H. Chen · W. Cheng · X. Feng · L. Han · Y. Hu · Y. Ji · M. Kleiner · S. Li · C. Liu · H. Liu · X. Liu · X. Lu · C. Peng · G. Sadowski · Q. Shao · J. Sun · F. Tumakaka · J.Z. Wu · H. Xu · G. Yue · S. Zhang · Y. Zhang · Q. Zhou

Springer

The series *Structure and Bonding* publishes critical reviews on topics of research concerned with chemical structure and bonding. The scope of the series spans the entire Periodic Table. It focuses attention on new and developing areas of modern structural and theoretical chemistry such as nanostructures, molecular electronics, designed molecular solids, surfaces, metal clusters and supramolecular structures. Physical and spectroscopic techniques used to determine, examine and model structures fall within the purview of Structure and Bonding to the extent that the focus is on the scientific results obtained and not on specialist information concerning the techniques themselves. Issues associated with the development of bonding models and generalizations that illuminate the reactivity pathways and rates of chemical processes are also relevant.
As a rule, contributions are specially commissioned. The editors and publishers will, however, always be pleased to receive suggestions and supplementary information. Papers are accepted for *Structure and Bonding* in English.
In references *Structure and Bonding* is abbreviated *Struct Bond* and is cited as a journal.

Springer WWW home page: springer.com
Visit the Struct Bond content at springerlink.com

ISBN: 978-3-540-69114-3 e-ISBN: 978-3-540-69116-7
DOI: 10.1007/978-3-540-69116-7

Structure and Bonding ISSN 0081-5993

Library of Congress Control Number: 2008937498

Cover design: SPi Publisher Services

Printed on acid-free paper

springer.com

Series Editor

Prof. D. Michael P. Mingos

Principal
St. Edmund Hall
Oxford OX1 4AR, UK
michael.mingos@st-edmund-hall.oxford.ac.uk

Volume Editors

Prof. Dr. Xiaohua Lu

Nanjing University of Science
& Technology
Dept. Chemical Engineering
210009 Nanjing
China, People's Republic
xhlu@njut.edu.cn

Prof. Dr. Ying Hu

East China University of Science
and Technology
Dept. Chemistry
200237 Shanghai
China, People's Republic
yinghu@ecust.edu.cn

Editorial Board

Structure and Bonding
Also Available Electronically

For all customers who have a standing order to Structure and Bonding, we offer the electronic version via SpringerLink free of charge. Please contact your librarian who can receive a password or free access to the full articles by registering at:

springerlink.com

If you do not have a subscription, you can still view the tables of contents of the volumes and the abstract of each article by going to the SpringerLink Homepage, clicking on "Browse by Online Libraries", then "Chemical Sciences", and finally choose Structure and Bonding.

You will find information about the

– Editorial Board
– Aims and Scope
– Instructions for Authors
– Sample Contribution

at springer.com using the search function.

Color figures are published in full color within the electronic version on SpringerLink.

Preface

With the development of science and technology, more and more complex materials such as porous materials, ion liquid, liquid crystals, thin films and colloids etc. are being developed in laboratories. However, it is difficult to prepare these advanced materials and use them on a large scale without some experience. Therefore, molecular thermodynamics, a method that laid emphasis on correlating and interpreting the thermodynamic properties of a variety of fluids in the past, has been recently employed to study the equilibrium properties of complex materials and establish thermodynamic models to analyse the evolution process of their components, microstructures and functions during the preparation process. In this volume, some important progress in this field, from fundamental aspects to practical applications, is reviewed.

In the first chapter of this volume, Prof. Jianzhong Wu presents the application of Density Functional theory (DFT) for the study of the structure and thermodynamic properties of both bulk and inhomogeneous fluids. This chapter presents a tutorial overview of the basic concepts of DFT for classical systems, the mathematical relations linking the microstructure and correlation functions to measurable thermodynamic quantities, and the connections of DFT with conventional liquid-state theories. While for pedagogy the discussion is limited to one-component simple fluids, similar ideas and concepts are directly applicable to mixtures and polymeric systems of practical concern. This chapter also covers a few theoretical approaches to formulate the thermodynamic functional. Some illustrative examples are given on applications of DFT to liquid structure, interfacial properties, and surface and colloidal forces. DFT provides a rigorous mathematic framework to describe the structure and thermodynamic properties of liquids from a molecular perspective.

In the second chapter of this volume, Prof. G. Sadowski describes the state of the art in modeling complex fluids, using analytical equations of state. Many applications demonstrate that these models can successfully be applied to describe and even to predict the phase behavior of a whole variety of substances, ranging from small gas molecules to organic solvents and polymeric systems.

Polymer blends or copolymers have multi-scale complex structures that can be used as templates to prepare various complex materials. In the third chapter of this

volume, Prof. Honglai Liu has developed theoretical methods based on equation of state, which can be used comprehensively to study the multi-scale structure of polymer systems, including phase diagrams, morphologies and their evolution of the micro-phase separation, densities and composition profiles in different domains and molecular configurations in the interfacial region.

Ionic liquids have been extensively evaluated as environmental-friendly or "green" solvents, catalysts and materials for a broad range of multifarious processes. They are becoming one of the important development aspects of the complex system, so chapter IV, written by Prof. Suojiang Zhang et al introduces ionic liquids and relative process design. They discuss the related research work on ionic liquids and process design, including the preparation and physical properties of ionic liquids, the application of molecular simulation in the development of applications and process design of ionic liquids, typical applications of ionic liquids and a brief overview of the toxicity of ionic liquids. The study of ionic liquids is just beginning and it is hoped that this chapter will help in the industrial applications of ionic liquids in the future.

Advanced materials are usually obtained by hydrothermal, microwave, and CVD processes. It is generally difficult to achieve the scale-up of advanced materials due to the lack of fundamental theory. The chemical engineering approach, based on thermodynamics, transfer theory and reaction engineering, has been proved to be effective for the scale-up of the product synthesis. In the final chapter of this volume, Prof. Xiaohua Lu and his co-authors present recent progress in this field and discuss how to use the thermodynamic method, combined with transport principles, molecular simulation and modern characterization, for synthesis and application of advanced materials on a large scale.

September 2008 *Xiaohua Lu, Ying Hu*

Contents

Struct Bond
DOI:10.1007/430_2008_3

Density Functional Theory for Liquid Structure and Thermodynamics

J.Z. Wu

Abstract Density functional theory (DFT) provides a powerful computational tool for study of the structure and thermodynamic properties of both bulk and inhomogeneous fluids. On the one hand, DFT is able to describe the microscopic structure and meso/macroscopic properties on the basis of intermolecular forces; and on the other hand, it connects seamlessly with conventional phenomenological equations for modeling macroscopic phenomena. The DFT-based methods are generic yet versatile they are naturally applicable to systems with multiple length scales that may fail alternative computational methods. This chapter presents a tutorial overview of the basic concepts of DFT for classical systems, the mathematical relations linking the microstructure and correlation functions to measurable thermodynamic quantities, and connections of DFT to conventional liquid-state theories. While for pedagogy the discussion is limited to one-component simple fluids, similar ideas and concepts are applicable to mixtures and polymeric systems of practical concern. This chapter also covers a few theoretical approaches to formulate the thermodynamic functional. Some illustrative examples are given on applications to liquid structure, interfacial properties, and surface and colloidal forces.

Keywords: Inhomogeneous fluids · Interfacial thermodynamics · Liquid-state theory · Statistical mechanics

Contents

J.Z. Wu
Department of Chemical and Environmental Engineering, University of California, Riverside, CA 92521-0425, USA
e-mail: jwu@engr.ucr.edu

Abbreviations

A	Surface area
a	Energy parameter in van der Waals' equation of state
B	MSA parameter
b	Volume parameter in van der Waals' equation of state
$b(r)$	Bridge function
C	Number of carbon atoms per molecule
c	Parameter in van der Waals' square gradient theory
C_F	Semi-empirical parameter introduced by Prigogine
$c(r)$	Direct correlation function
E	Energy/ground-state energy
F	Helmholtz energy
$\vec{F}$	Force
$F[\rho(r)]$	Intrinsic Helmholtz energy functional
$f(\vec{r})$	Local Helmholtz energy
$g(r)$	Radial distribution function
g	Gravitational constant
H	Interfacial thickness/pore width
$h(r)$	Total correlation function

h	Elevation
$\tilde{I}$	Unit tensor
K	Kinetic energy
k_{B}	Boltzmann constant
L_{c}	Capillary length
L_{T}	Thermal length
M_n	Molecular weight
$\vec{M}$	Momentum transfer
m	Molecular mass
N	Number of molecules
n_α	Weighted densities
$\vec{n}$	Normal vector
P	Pressure
$\tilde{P}$	Pressure tensor
$\vec{p}$	Molecular momentum
p_ν	Probability density
Q	Surface charge density
q_i	Ionic charge
R	Radius
r	Center-to-center distance
$\vec{r}$	Position vector
S	Entropy
$\mathbb{S}(\vec{k})$	Static structure factor
$s(\vec{r})$	Local entropy
T	Temperature, K
U	Internal energy
$u(\vec{r})$	Local internal energy
V	Volume
v	Cell volume
W	Reversible work
$W(r)$	Potential of mean force
$w(\vec{r})$	Weight function
$\chi_0^{(\mathrm{A})}$	Local fraction of nonbonded associating site A
$y(r)$	Cavity correlation function
z	Distance
BMCSL	Boublik–Mansoori–Carnahan–Starling–Leland
DFT	Density functional theory
FMSA	First-order mean-spherical approximation
FMT	Fundamental measure theory
HNC	Hypernetted chain
LDA	Local-density approximation
LJ	Lennard-Jones
MC	Monte Carlo
MHNC	Modified hypernetted chain
MSA	Mean-spherical approximation

OZ	Ornstein–Zernike
PB	Poisson–Boltzmann
PDT	Potential distribution theorem
PY	Percus–Yevick
RHNC	Reference hypernetted chain
SAFT	Statistical associating fluid theory
TDDFT	Time-dependent density functional theory
WDA	Weighted-density approximation

Greek letters

β	$1/k_{\mathrm{B}}T$
Γ	Intermolecular potential
γ	Surface tension
$\delta(r)$	Dirac delta function
ε	Interaction energy
ε_{D}	Dielectric constant
ζ	Zeta potential
η	Packing density
$\theta(r)$	Heaviside step function
κ	Inverse screening length
κ_{T}	Isothermal compressibility
Λ	Thermal wavelength
λ	Coupling parameter
μ	Chemical potential
Ξ	Grand partition function
$\rho(\vec{r})$	Density profile
σ	Diameter
$\varphi(\vec{r})$	One-body potential function
$\chi(\vec{r}',\vec{r}'')$	Density–density correlation function
$\psi(z)$	Function used in the square-gradient theory
$\Psi(1,2,\ldots,N)$	Wave function
Ω	Grand potential
ν	Microstate
$v(\vec{r})$	One-body external potential
ς	Inhomogeneous factor

Superscripts

*	Reduced quantities
id	Ideal gas
ex	Excess
ext	External

Subscripts

0	Bulk/reference system
α	Index of weight functions = 0, 1, 2, 3, V1 and V2
A	Intermolecular attraction
ass	Association
c	Critical point
el	Electric
hs	Hard sphere
L	Liquid
LJ	Lennard-Jones
R	Intermolecular repulsion
V	Vapor

1 Introduction

Since the pioneering work by van der Waals [1,2], there has been a continuous interest among physicists, chemists, and engineers alike to develop molecular theories for liquid structure and thermodynamic properties. The significance of a reliable liquid-state theory is evident by simply considering the vast liquids on this planet and their omnipresence in industrial processes. A liquid-state theory is essential for understanding the origin of life and formation of matter, and, from an engineering perspective, for production of chemicals and pharmaceuticals, and for the manufacture of materials.

Unlike a solid, a liquid consists of molecules locally organized according to the statistical laws of thermodynamics. The lack of a long-range order makes direct measurement of a liquid structure difficult even with the most powerful neutron or X-scattering scattering instruments [3]. Significant progress has been made over the past few decades by using molecular simulations and, more recently, by mapping liquid states to colloidal dispersions where the structural and phase transitions appear at magnified time and length scales [4]. In parallel, a number of analytical theories have been developed for interpretation/extrapolation of simulation and experimental data [5]. With a modern computer, prediction of the structure and thermodynamic properties of simple uniform systems is no longer a theoretical challenge. However, understanding the thermodynamic properties of liquid systems with complicated microscopic structures remains very much a theoretical aspiration.

Density-functional theory (DFT) provides a rigorous mathematic framework to describe the structure and thermodynamic properties of liquids from a molecular perspective. While early applications of DFT were limited to inhomogeneous systems of simple fluids [6, 7], DFT is equally useful for more complicated systems, including those containing polymers, polyelectrolytes, and biomacromolecules [8,9]. Different from molecular simulations, DFT accounts for the microscopic details of a many-body system without explicitly dealing with thermal fluctuations;

its computational efficiency is comparable to conventional phenomenological methods. The superior numerical efficiency and concomitant physical clarity enable DFT to bridge multiple length and time scales spanning from molecular events to meso/macroscopic phase transitions.

This chapter provides a tutorial overview of DFT for liquid-state matter. We will discuss the basic principles and their applications to modeling the structure and thermodynamic properties. For pedagogy, the equations and illustrative examples are discussed in the context of simple one-component fluids where the molecules can be represented by structureless spherical particles. As shown in elsewhere [8, 9], similar concepts are applicable to mixtures and polymeric systems of practical concern. We begin with van der Waals' seminal contribution to the variational principle of equilibrium and its applications to the vapor–liquid interface and capillarity. The Hohenberg–Kohn theorem is then introduced to furbish a rigorous mathematical foundation for van der Waals' variational principle of equilibrium. Next, we define various density distribution and correlation functions to quantify liquid structure, and illustrate their interrelations and connections to thermodynamic functionals. We will also illustrate the connections of DFT to conventional liquid-state theories and present exact formalism to predict thermodynamic and interfacial properties in terms of the microscopic structure and correlation functions. Finally, we introduce a few practical methods for formulating the thermodynamic functional in terms of semi-empirical force fields that represent the intermolecular interactions responsible for the thermodynamic nonideality.

2 Variational Principle of Equilibrium

The principle of thermodynamic equilibrium was established by Josiah W. Gibbs in the late nineteenth century. In a seminal paper published in two parts in 1876 and in 1878 [10], Gibbs asserted that in an equilibrium system, the distribution of matter follows the second law of thermodynamics, i.e., within the constraints of equilibrium, matter distributes itself in such a way that the system attains a maximum entropy. In deriving the principle of equilibrium, Gibbs assumed that a heterogeneous system can be represented by coexisting bulk phases of uniform density.

In Gibbs' derivation, the interface between different phases is represented by a two-dimensional mathematical surface. The two-dimensional representation of an interface is well justified if one is concerned with the phase equilibrium of bulk systems. In a macroscopic system containing $N \approx 10^{23}$ molecules, the ratio of the number of molecules at the interface to that in the bulk is on the order of $N^{-1/3}$, which is exceedingly small. However, the situation is quite different if the surface or the interfacial properties are of direct concern. Although in his paper published in 1878 Gibbs acknowledged the inhomogeneity of the molecular density near an interface, a more general thermodynamic treatment of inhomogeneous systems was not attempted until a decade later by Karl Fuchs, and independently by Lord Rayleigh in 1892 and by van der Waals in 1893 [1]. Van der Waals was the first to establish

the variational principle of thermodynamic equilibrium with explicit consideration of the density inhomogeneity near an interface.

Without loss of generality, van der Waals considered the vapor–liquid interface of an argon-like system and postulated that molecules distribute continuously in the heterogeneous region, i.e., the number density of molecules $\rho(\vec{r})$ is a smooth function of position $\vec{r}$ at the interface. In addition, van der Waals assumed that at equilibrium, any extensive thermodynamic function X can be expressed by an integration of a local function $x(\vec{r})$:

$$X = \int \mathrm{d}\vec{r}\rho(\vec{r})x(\vec{r}). \tag{1}$$

For example, the total entropy of the system is given by:

$$S = \int \mathrm{d}\vec{r}\rho(\vec{r})s(\vec{r}), \tag{2}$$

where $s(\vec{r})$ is the entropy per molecule at position $\vec{r}$. Because of the intermolecular interactions and correlation effects, van der Waals emphasized that the local value of a thermodynamic function depends not only on the local density $\rho(\vec{r})$ but also on the densities of molecules at the neighboring space.

On the basis of the second law of thermodynamics, van der Waals asserted that for an isolated system at equilibrium (i.e., constant volume, energy, and number of molecules), the distribution of matter maximizes the total entropy. Using the calculus of variations, van der Waals' statement amounts to that at equilibrium; the density profile $\rho(\vec{r})$ maximizes the total entropy, subject to the constraints of the total number of molecules N and total internal energy U:

$$N = \int \mathrm{d}\vec{r}\rho(\vec{r}), \tag{3}$$

$$U = \int \mathrm{d}\vec{r}\rho(\vec{r})u(\vec{r}), \tag{4}$$

where $u(\vec{r})$ denotes the internal energy per molecule at position $\vec{r}$.

Because there is no general expression for the local entropy $s(\vec{r})$ or for the local internal energy $u(\vec{r})$, a more convenient but equivalent expression for the variational principle of equilibrium is that for a closed system at fixed temperature T and volume V, the distribution of molecules minimizes the Helmholtz energy:

$$F = \int \mathrm{d}\vec{r}\rho(\vec{r})f(\vec{r}). \tag{5}$$

Given a formulation of the local Helmholtz energy $f(\vec{r})$, the equilibrium density profile can be solved following the rules from the calculus of variations:

$$\frac{\delta F}{\delta\rho(\vec{r})} - \mu = 0, \tag{6}$$

where μ is the Lagrangian multiplier arising from the constraint of mass conservation in the closed system. Based on the density profile, one can calculate the Helmholtz energy and other thermodynamic properties of the inhomogeneous system.

Van der Waals' variational principle of equilibrium has been used extensively to describe the interfacial properties and thermodynamics of inhomogeneous fluids [11]. One prominent example is the Cahn–Hilliard theory, which has been successfully used to describe various interfacial phenomena, including the kinetics of phase transitions and wetting [12]. The Cahn–Hilliard theory is based on a Helmholtz energy functional identical to that from the square-gradient approximation originally proposed by van der Waals; it also shares similarity with the Ginzburg–Landau theory in condensed-matter physics [13].

As an extension of Gibbs' principle of equilibrium, van der Waals' variational principle is universally applicable to any thermodynamic systems. In other words, the variational principle of equilibrium is formally exact just like the laws of thermodynamics.

3 Square-Gradient Theory

The square-gradient theory was derived by van der Waals as an illustrative example for application of the variational principle of equilibrium [2]. Although this important work was well-received right after publication, it was essentially lost after the First World War. The theory was reinvented by Landau and Lifshitz in 1935 in their study of the boundary of two magnetic domains [13], and later by Mitsui and Furuichi in 1953 for describing the interface between ferroelectric structures [14], and most notably by Cahn and Hilliard in 1958 in investigating the structure and surface tension of vapor–liquid as well as liquid–liquid interfaces [12]. The later versions of the square-gradient theory remain useful for describing the thermodynamics of inhomogeneous systems, including not only surface tension but also wetting transitions, nucleation, and spinodal decomposition [15–17].

Van der Waals considered the vapor–liquid interface of a one-component fluid at equilibrium. As shown in Fig. 1, far from the interface the molecular density is equal to that of the vapor or liquid in the bulk; but in the interfacial region, the density varies continuously between the two bulk values. Van der Waals assumed that the effect of gravitational force and capillary wave[1] are negligible, and the molecular density changes only in the direction perpendicular to the planar interface. The direction perpendicular to the interface is designated the z-axis and the origin is taken at the place where the molecular density is equal to the average of the two bulk densities.

In the bulk phases ($z = \infty$), the Helmholtz energy is determined by an equation of state. For example, according to the van der Waals theory, the Helmholtz energy

[1] For a simple liquid, the capillary length $L_c = \sqrt{\gamma/\Delta\rho g}$ is on the order of a few millimeters but the thermal length $L_T = \sqrt{k_B T/\gamma}$ is only a few Angstroms. The gravitational force and capillary wave is insignificant if $L_c >> L_T$.

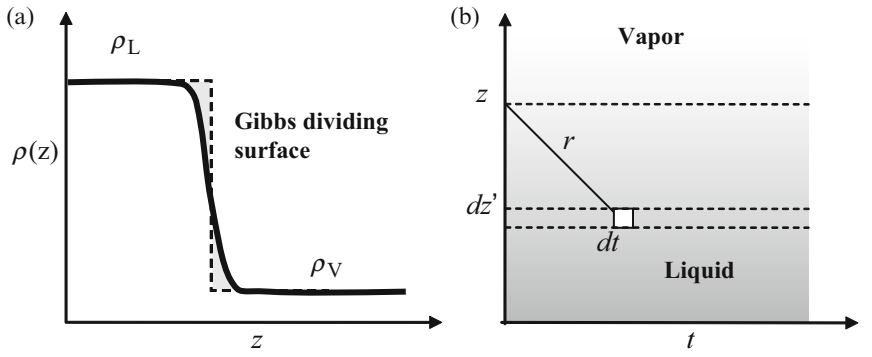

Fig. 1 (**a**) Schematic density profile at a vapor-liquid interface. Along the direction perpendicular to the interface (z), the number density of molecules varies smoothly from the liquid side to the vapor side. The Gibbs dividing surface, shown as the vertical dashed line, defines a mathematical boundary such that the shaded regions have the same area. (**b**) The geometry for a molecule at position z interacting with other molecules at distance $r = \sqrt{z'^2 + t^2}$. Here z' is the vertical distance from z, and t represents the radial coordinate. The infinitesimal volume is $2\pi t\, \mathrm{d}t\, \mathrm{d}z'$

per molecule in a bulk liquid or vapor is given by:

$$\beta f_{\mathrm{L/V}} = \ln\left(\frac{\rho\Lambda^3}{1-b\rho}\right) - 1 - \beta\rho a, \tag{7}$$

where a and b are the van der Waals' parameters, Λ represents the thermal wavelength, and $\beta = 1/k_{\mathrm{B}}T$ with k_{B} being the Boltzmann constant and T the temperature.

To find the Helmholtz energy in the interfacial region, van der Waals assumed that the Helmholtz energy per molecule includes a reference part and an attractive perturbation part, as in the equation of state for bulk systems. The reference part accounts for the kinetic energy and for the excluded-volume effects; this part is assumed to depend only on the local molecular density $\rho(z)$:

$$\beta f_{\mathrm{R}}(z) = \ln\left[\frac{\rho(z)\Lambda^3}{1-b\rho(z)}\right] - 1. \tag{8}$$

Because the intermolecular attraction is longer ranged, the perturbation part of the Helmholtz energy depends not only on the local density but also on the density of molecules in the vicinity.

The nonlocal effect of the intermolecular attraction on the Helmholtz energy can be found by considering the reversible work to move a molecule from the liquid phase ($z = -\infty$) to the interface. In calculating this work, van der Waals considered only the attractive potential between molecules, which is denoted by $\Gamma_{\mathrm{A}}(r)$. Because of the variation of the molecular density in the interface region, the attractive force from the liquid side is not balanced by that from the vapor side, and the net force is given by (see Fig. 1b):

$$\vec{F}(z) = \int_{-\infty}^{\infty} \mathrm{d}z' \int_{0}^{\infty} 2\pi t\, \mathrm{d}t\, \rho(z-z') \frac{\partial \Gamma_{\mathrm{A}}(r)}{\partial r} \frac{z'}{r}, \tag{9}$$

where z' denotes a distance from z, $2\pi t\,\mathrm{d}t\,\mathrm{d}z'$ is an infinitesimal volume at z' with separation $r=\sqrt{z'^2+t^2}$ from a molecule at z, and t is the polar coordinate of the plane at z'. Because $t\,\mathrm{d}t = r\,\mathrm{d}r$ and $\Gamma_{\mathrm{A}}(\infty)=0$, Eq. 9 can be simplified to:

$$\vec{F}(z) = -\int_{-\infty}^{\infty} 2\pi z'\,\mathrm{d}z'\,\rho(z-z')\Gamma_{\mathrm{A}}(|z'|). \tag{10}$$

Now we introduce a function $\psi(z)$ by requiring $\mathrm{d}\psi(z) = 2\pi z\Gamma_{\mathrm{A}}(|z|)\mathrm{d}z$ with the boundary condition $\psi(\infty)=0$[2]. We define $\psi(z)$ as an even function of z and $\psi(-\infty)=0$. Integrate Eq. 10 by parts:

$$\begin{aligned}\vec{F}(z) &= -\,\rho(z-z')\psi(z')\big|_{z'=-\infty}^{z'=\infty} + \int_{-\infty}^{\infty}\psi(z')\rho'(z-z')\mathrm{d}z',\\ &= \int_{-\infty}^{\infty}\psi(z')\rho'(z-z')\mathrm{d}z'.\end{aligned} \tag{11}$$

Because $\psi(\pm\infty)=0$, the first term on the right side of Eq. 11 vanishes.

From the net force, we can calculate the reversible work to move a molecule from the liquid to the interface:

$$W(z) = \int_{-\infty}^{z}\vec{F}(z)\mathrm{d}z. \tag{12}$$

To evaluate the integral, van der Waals used a Taylor expansion for the local density $\rho(z-z')$:

$$\rho(z-z') = \rho(z) - \rho'(z)z' + \frac{\rho'''(z)}{2!}z'2 - \frac{\rho'''(z)}{3!}z'^3 + \cdots. \tag{13}$$

The differentiation of $\rho(z-z')$ with respect to z' is given by:

$$\rho'(z-z') = -\rho'(z) + \rho'''(z)z' - \frac{\rho'''(z)}{2}z'^2 + \cdots. \tag{14}$$

Substitution of Eqs. 11 and 14 into Eq. 12 gives:

$$\begin{aligned}W(z) = &-\int_{-\infty}^{z}\rho'(z)\mathrm{d}z\int_{-\infty}^{\infty}\psi(z')\mathrm{d}z' + \int_{-\infty}^{z}\rho''(z)\mathrm{d}z\int_{-\infty}^{\infty}\psi(z')z'\mathrm{d}z'\\ &-\frac{1}{2}\int_{-\infty}^{z}\rho'''(z)\mathrm{d}z\int_{-\infty}^{\infty}\psi(z')z'^2\mathrm{d}z' + \cdots.\end{aligned} \tag{15}$$

Because $\psi(z)$ is an even function of z, the second term on the right size of Eq. 15 disappears.

After truncation of high-order terms, the final expression for the reversible work can be derived by integration of the density derivatives with the boundary conditions $\rho(-\infty)=\rho_{\mathrm{L}}$ and $\rho''(\pm\infty)=0$:

[2] For van der Waals attraction, $\Gamma_A(z)\sim 1/z^6$ and following the definition $\psi(z)\sim 1/z^4$, which is an even function of z.

$$W(z) = [\rho_{\mathrm{L}} - \rho(z)] \int_{-\infty}^{\infty} \psi(z')\mathrm{d}z' - \frac{\rho''(z)}{2} \int_{-\infty}^{\infty} \psi(z') z'^2 \mathrm{d}z', \tag{16}$$

where the first integral is related to the van der Waals energy parameter ($\because \psi(\pm\infty) = 0$):

$$\int_{-\infty}^{\infty} \psi(z')\mathrm{d}z' = -\int_{-\infty}^{\infty} z'\mathrm{d}\psi(z') = -\int_{-\infty}^{\infty} 2\pi z'^2 \Gamma_{\mathrm{A}}(|z|)\mathrm{d}z' = 2a \tag{17}$$

and the second integral is conventionally expressed as:

$$c \equiv \frac{1}{2}\int_{-\infty}^{\infty} \psi(z) z^2 \mathrm{d}z = -\frac{2\pi}{3}\int_{0}^{\infty} z^4 \Gamma_{\mathrm{A}}(z)\mathrm{d}z. \tag{18}$$

Because the reversible work to move a molecule from the liquid phase to the interface is related to the change in the Helmholtz energy the nonlocal Helmholtz energy due to the unbalanced intermolecular attractions is given by:

$$f_{\mathrm{A}}(z) = -\rho_{\mathrm{L}} a + W(z)/2 = -\rho(z)a - \rho''(z)c/2, \tag{19}$$

where the work term is multiplied by a factor of $1/2$ accounting for the pair interactions.

A combination of Eqs. 8 and 19 gives the final expression of the local Helmholtz energy:

$$\beta f(z) = \ln\left[\frac{\rho(z)\Lambda^3}{1 - b\rho(z)}\right] - 1 - \beta\rho(z)a - \rho''(z)\beta c/2. \tag{20}$$

The first two terms on the right side of Eq. 20 are identical to that for a uniform system; the last term arises from the attractive energy due to the density inhomogeneity. This term disappears for a bulk fluid where the density is everywhere uniform.

The total Helmholtz energy of the vapor–liquid interface is given by integration of the local Helmholtz energy:

$$F/A = \int \mathrm{d}z\rho(z)f(z) = \int \mathrm{d}z\left\{f_0 + c[\rho'(z)]^2/2\right\}, \tag{21}$$

where A stands for the surface area, and f_0 is the Helmholtz energy per unit volume for a bulk fluid:

$$\beta f_0 = \rho(z)\ln\left[\frac{\rho(z)\Lambda^3}{1 - b\rho(z)}\right] - \rho(z) - \beta\rho^2(z)a. \tag{22}$$

In Eq. 21, the second term in the integrand is obtained from integration by parts with the boundary condition $\rho'(z = \pm\infty) = 0$. Because this term is proportional to the square of the density gradient, van der Waals' expression for the Helmholtz energy is known as the square-gradient theory. The gradient expansion is most appropriate when there is only a small change in the density profile.

Van der Waals demonstrated that the variational principle yields conditions of equilibrium fully consistent with those established earlier by Gibbs. According to

the variational principle of equilibrium (Eq. 6), the density profile $\rho(z)$ minimizes the total Helmholtz energy with the constraint of mass conservation:

$$\mu_0[\rho(z)] - c\rho''(z) = \mu, \tag{23}$$

where $\mu_0 = \partial f_0/\partial\rho$, which reduces to the chemical potential for a bulk phase. Far from the interface, the density is uniform, i.e., $\rho(-\infty) = \rho_{\rm L}$ and $\rho(\infty) = \rho_{\rm V}$. The Lagrangian multiplier μ is identical to the chemical potential in the bulk:

$$\mu = \mu_{\rm L} = \mu_{\rm V}. \tag{24}$$

The pressure of the two coexisting phases should also be the same. To see this, we recast Eq. 23 into an integrable form:

$$c\rho''(z) = \mu_0[\rho(z)] - \mu. \tag{25}$$

Let $\omega(\rho) = f_0(\rho) - \rho\mu$; the derivative of $\omega(\rho)$ with respect to ρ is:

$$\frac{\partial\omega}{\partial\rho} = \mu_0[\rho(z)] - \mu. \tag{26}$$

For a bulk system, $\omega(\rho)$ is related to the pressure, i.e., $\omega(\rho_{\rm L}) = -P_{\rm L}$ and $\omega(\rho_{\rm V}) = -P_{\rm V}$. Multiply both sides of Eq. 25 by $\rho'(z)\mathrm{d}z$ and rearrange the terms on the right:

$$c\rho''(z)\rho'(z)\mathrm{d}z = \frac{\partial\omega}{\partial\rho}\rho'(z)\mathrm{d}z. \tag{27}$$

Equation 27 can be simplified to:

$$\frac{c}{2}\mathrm{d}[\rho'(z)]^2 = \mathrm{d}\omega. \tag{28}$$

With the boundary conditions $\rho'(\pm\infty) = 0$ and $\omega_{z=-\infty} = -P_{\rm L}$, integration of Eq. 28 gives:

$$\omega(\rho_{\rm L}) = \omega(\rho_{\rm V}) \tag{29}$$

or equivalently:

$$P_{\rm L} = P_{\rm V}. \tag{30}$$

Because Eqs. 24 and 30 can be derived without explicit use of an equation of state, the variational principle of equilibrium by van der Waals is indeed fully consistent with the conditions of equilibrium established by Gibbs.

The density profile at the vapor–liquid interface can be obtained by integration of Eq. 23. For example, Fig. 2 shows predictions of van der Waals' square-gradient theory for the density profiles of the Lennard-Jones fluid at two reduced temperatures. Far away from the critical temperature ($k_{\rm B}T_{\rm c}/\varepsilon_{\rm LJ} \approx 1.3$), the interfacial thickness is comparable to the size of a molecule. Close to the critical temperature, however, the interfacial thickness H diverges as $H \sim (1 - T/T_{\rm c})^{-0.5}$ which agrees qualitatively with the exact results [7].

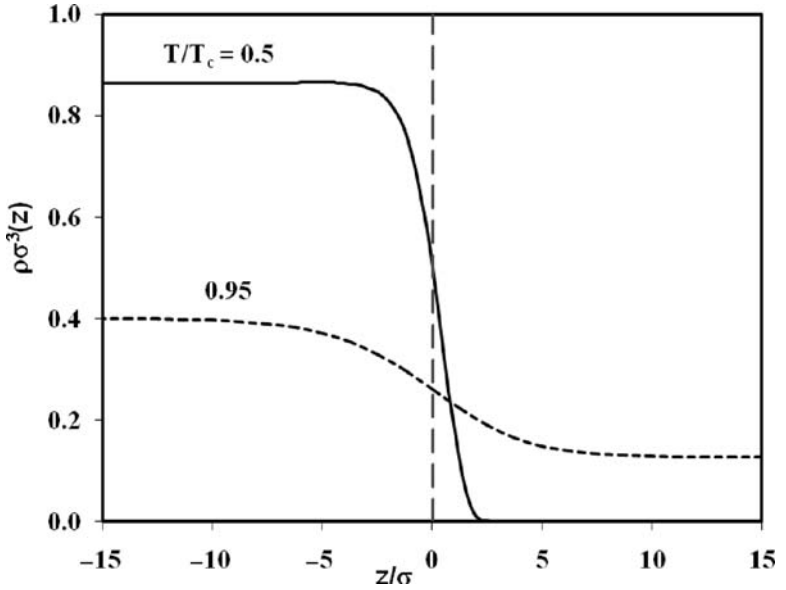

Fig. 2 Variation of molecular density at the interface of a Lennard-Jones fluid predicted by van der Waals' square-gradient theory. The *dashed line* is drawn through the average density of the coexisting phases

Once we have the interfacial density profile, we can calculate the vapor–liquid interfacial tension γ

$$\gamma = \frac{F - F_{\mathrm{L}} - F_{\mathrm{V}}}{A}, \tag{31}$$

where F_{L} and F_{V} are the Helmholtz energies of the bulk liquid and vapor according to the definition of Gibbs dividing surface. Because $f_0(\rho) = \omega(\rho) + \rho\mu$ and $\omega[\rho(z)] = \frac{c}{2}[\rho'(z)]^2 - P$, we can express the local Helmholtz energy in Eq. 21 in terms of the bulk pressure P and the chemical potential μ:

$$F/A = \int \mathrm{d}z \left\{ \rho(z)\mu - P + c[\rho'(z)]^2 \right\} = (N\mu - PV)/A + c \int \mathrm{d}z[\rho'(z)]^2. \tag{32}$$

For the bulk phases, $F_{\mathrm{L}} + F_{\mathrm{V}} = N\mu - PV$; substitution of Eq. 32 into Eq. 31 yields a simple expression for the interfacial tension:

$$\gamma = c \int \mathrm{d}z[\rho'(z)]^2 = c \int \rho'(z)\mathrm{d}\rho(z). \tag{33}$$

Because $\omega[\rho(z)] = \frac{c}{2}[\rho'(z)]^2 - P$, the derivative of the density profile can be expressed as:

$$\rho'(z) = \sqrt{2[\omega(z) + P^{\mathrm{sat}}]/c}. \tag{34}$$

Substituting Eq. 34 into 33 gives:

$$\gamma = \int_{\rho_V}^{\rho_L} \sqrt{2c(\omega + P^{sat})} d\rho. \tag{35}$$

Equation 35 is convenient for practical applications because the surface tension can be calculated directly from an equation of state for the uniform fluids without knowing the density profile.

Van der Waals' square-gradient theory can be directly compared with the results from experiments or from molecular simulations (that become available more than 50 years after the publication of his original work). Figure 3 shows, for example, the surface tension of the Lennard-Jones fluid predicted from the gradient theory, from a nonlocal density functional theory, and from Monte Carlo simulations [19]. Similar to the van der Waals equation of state for bulk systems, the performance of the square-gradient theory is only qualitative. Nevertheless, it captures the essential features of interfacial inhomogeneity and surface tension. A more quantitative representation of the surface tension can be accomplished by using adjustable parameters [20].

Near the critical point of the vapor–liquid equilibrium, the surface tension approaches zero following the scaling relation [7]:

$$\gamma \sim \kappa_T^{-1/2} (\rho_L - \rho_V)^2, \tag{36}$$

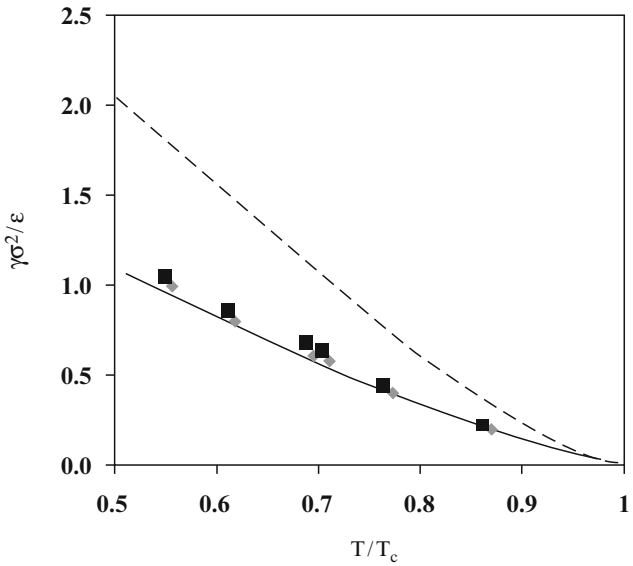

Fig. 3 Surface tension of the Lennard-Jones fluid predicted from van der Waals' square-gradient theory (*dashed line*) and from a nonlocal density functional theory (*solid line*). The *points* are simulation data from [21]. Here σ and ε are the size and energy parameters of the Lennard-Jones potential, and T_c represents the critical temperature

where κ_T represents the isothermal compressibility. Following the exact scaling relations for κ_T and for $(\rho_L - \rho_V)$:

$$\kappa_T \sim (1 - T/T_c)^{-1.2}, \tag{37}$$

$$\rho_L - \rho_V \sim (1 - T/T_c)^{0.34}, \tag{38}$$

we find that the interfacial tension disappears at the critical point following the scaling relation:

$$\gamma \sim (1 - T/T_c)^{1.28}. \tag{39}$$

Even though the mean-field theory gives accurate scaling relation neither for κ_T nor for $(\rho_L - \rho_V)$, the exponent given in Eq. 39 agrees remarkably well with the experimental results for xenon (1.302) and for carbon dioxide (1.253). The good agreement here is probably due to cancellation of errors.

While the discussion above is based on the gas–liquid interface of a one-component fluid, a similar procedure can be applied to more complicated systems at inhomogeneous conditions [19, 22]. For example, van der Waals' square-gradient theory has been extended to polymeric fluids and to mixtures. To compare the theoretical predictions with experimental results, we show one example from Dee and Sauer concerning the surface tensions of linear alkanes and polyethylene [23]. In this work, the Flory–Orwoll–Vrij equation of state, which is a free-volume modification of Flory–Huggins theory, is used to describe the properties of the bulk phases:

$$\frac{P^*V^*}{T^*} = \frac{V^{*1/3}}{V^{*1/3} - 1} - \frac{1}{T^*V^*}, \tag{40}$$

where P_r, T_r and V_r are reduced quantities defined as:

$$P^* = \frac{Pv^*}{\varepsilon} \quad T^* = \frac{c_F k_B T}{\varepsilon} \quad V^* = \frac{v}{v^*}. \tag{41}$$

Parameters ε and v^* stand for, respectively, the potential energy for two nonbonded neighboring segments and for the volume of one polymer segment; v is the cell volume that is related to the experimental polymer density; and c_F is a semi-empirical parameter introduced by Prigogine to take into account the reduction of degrees of freedom due to the chain connectivity[3]. The model parameters appeared in Eq. 41 can be obtained by fitting the volumetric data as a function of the temperature and pressure. To fix the parameter c in van der Waals' square-gradient theory, Dee and Sauer assumed that $c* = c/(\varepsilon v*^{5/3})$ is a constant independent of the polymer molecular weight and temperature.

Figure 4 compares the experimental and predicted surface tensions of normal alkanes and polyethylenes of different molecular weights and temperatures. We see that the square-gradient theory provides a good description of the experimental

[3] For a molecule of n segments, the number of external degrees of freedom is $3nc_F$. For argon, $n = 1$ and $c_F = 1$. For molecules when $n > 1$, $c_F < 1$ because of chain connectivity. For a long paraffin, $c_F \approx 1/3$.

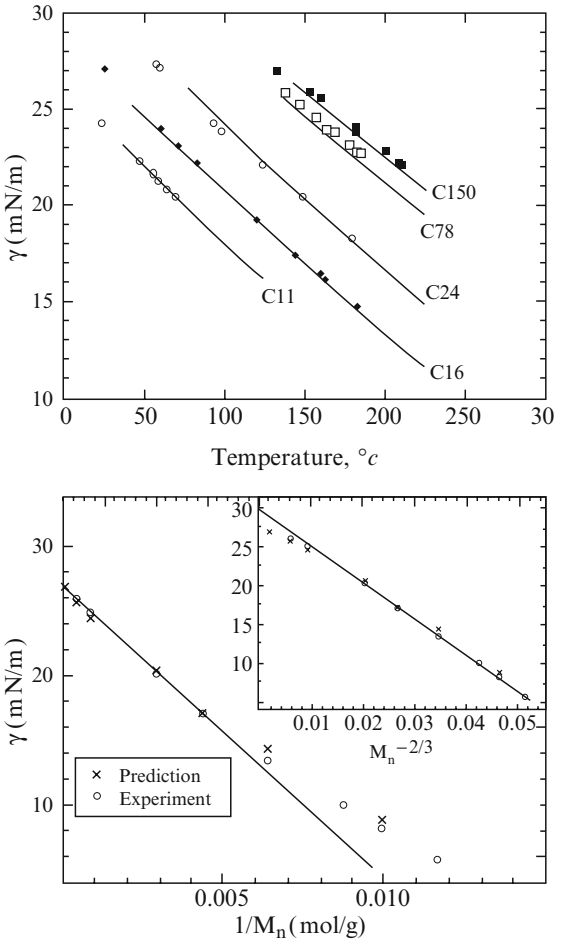

Fig. 4 Surface tensions of linear alkanes (top) and polyethylene (bottom) at 150°C predicted by the square-gradient theory with the Flory–Orwoll–Vrij equation of state for the bulk phases. *Points* are experimental data and *lines* are theoretical predictions. Here M_n is the number-average molecular weight. Parameters in the Flory–Orwoll–Vrij equation of state are obtained from experimental bulk properties [23]

results. A correlation for the surface tension is useful, e.g., for design of low-friction surfaces in disk drives and for adhesion reduction in biomedical devices such as those used in hip or knee replacements. The surface tension also determines the degree to which two immiscible polymers can be dispersed in each other. Because in general it is difficult to measure the surface tension of a polymer melt, a predictive model for the surface tension is valuable for practical application of polymers.

Van der Waals' square-gradient theory is appealing for practical applications because of its simplicity. However, the square-gradient approximation is valid only for systems with a slowly varying density profile, as for example, at the liquid–gas

interface near the critical point. Because the density expansion is truncated after the quadratic terms, the square-gradient theory cannot be applied to inhomogeneous systems with a sharp interface. In addition, the requirement of convergence for the parameter c implies that the square-gradient is not useful for systems with long-range interactions.

4 Density Functional Theory

Van der Waals' variational principle of equilibrium is practically equivalent to what is now known as the density functional theory (DFT) for classical systems. The terminology was originated in quantum mechanics for electronic systems [24]. As early as the 1920s, Thomas [25] and, independently, Fermi [26] noted that the energy of electrons moving in the potential of nuclei can be directly calculated from the electron density instead of the wave function. The electronic density at the ground state corresponds to a minimal total energy. The variational method of Thomas and Fermi provides an alternative to the Schrödinger equation for calculating the electronic energy and properties of atoms and molecules. For systems with many electrons, the computational advantage of the variational method is evident: instead of solving the N-electron wave function $\Psi(1,2,\ldots,N)$ in the Schrödinger equation, which has $4N$ degrees of freedom (three space coordinates and one spin coordinate per electron), the variational method deals only with the electron density $\rho(\vec{r})$, which involves four degrees of freedom.

While the computational simplicity of the variational method is apparent, it was not at all apparent, at least in the early days, that DFT was indeed theoretically as rigorous as the well-established wave mechanics. Although the variational method had been practiced by prominent researchers including P. A. M. Dirac and others in the 1930s, the theoretical foundation was not established until the publication of two landmark papers by Kohn and coworkers in 1964 [27] and in 1965 [28], respectively. In the first paper, Hohenberg and Kohn proved mathematically that the intrinsic part of the ground-state energy is a *unique* functional of the electron density profile $\rho(\vec{r})$, i.e., the ground-state energy E is *uniquely* determined by the corresponding electron density $\rho(\vec{r})$, $E = E[\rho(\vec{r})]$. In the second paper, Kohn and Sham *postulated* that a system of many electrons can be equivalently represented by a noninteracting reference system where each electron moves independently in an effective potential that consists of the attractive energy due to the nuclei, the direct Coulomb repulsion among electrons, and a self-consistent local potential arising from the exchange and correlation effects. The effective one-electron *ansatz* provides a starting point for modern applications of DFT to quantum many-body problems. Today there are numerous versions of DFT, ranging from simplistic local density approximations (LDA) to more sophisticated versions such as B3LYP or B3PW91 [29]. Different versions of DFT differ mostly in the exchange-correlation potential.

The connection of the variational method in statistical mechanics with DFT in quantum chemistry was first recognized by Ebner, Saam, and Stroud, who used a variational method originally developed for liquid ^{4}He, a quantum fluid, to describe the vapor–liquid interfacial tension and the wetting behavior of the Lennard-Jones fluid [30]. Over the past few decades, it has been gradually realized that a number of liquid-state theories in statistical mechanics, including the square-gradient theory of van der Waals, perturbation theories, and integral-equation theories, could be derived in a systematic fashion within the framework of DFT. In two comprehensive reviews published in 1979 [31] and in 1992 [6] respectively, Bob Evans summarized early developments of DFT for classical systems and applications to inhomogeneous fluids and wetting transitions. The basic concepts were also illustrated by J. Rowlinson and B. Widom in a text on molecular theory of capillarity [11]. In a monograph on the statistical mechanics of phases and interfaces, H. T. Davis discussed extensive applications of DFT to interfacial phenomena and thin films [7]. While early developments of DFT for classical systems were primarily focused on simple fluids, much progress has been made in recent years towards more accurate formulation of the Helmholtz energy functionals applicable to complex fluids, including those containing block copolymers, polyelectrolytes, and biomacromolecules [8, 9]. In this section, we introduce the fundamental principles of DFT. For pedagogical reasons, the discussion is limited to an argon-like fluid where the molecules can be represented as structureless spheres.

4.1 Density Profile

A density profile describes the average distribution of molecules in a many-body system. According to classical physics, the location of a spherical particle can be specified by a three-dimensional vector $\vec{r}$. Given a particle i at position $\vec{r}$, the instantaneous density can be represented by a three-dimensional Dirac- δ function:

$$\hat{\rho}_i(\vec{r}) = \delta(\vec{r} - \vec{r}_i). \tag{42}$$

Figure 5 illustrates the definition of a one-dimensional Dirac- δ function: it is zero everywhere but infinite at the location of the particle. The Dirac- δ function is subject to the normalization condition:

$$\int \mathrm{d}\vec{r}\,\delta(\vec{r} - \vec{r}_i) = 1. \tag{43}$$

Equation 43 connotes the very existence of particle i in the space. Intuitively, the Dirac- δ function $\delta(\vec{r} - \vec{r}_i)$ can be understood as a probability density.

For a system containing N identical particles, the instantaneous total density is simply given by a summation of the Dirac- δ functions for all particles:

$$\hat{\rho}(\vec{r}) = \sum_{i=1}^{N} \delta(\vec{r} - \vec{r}_i). \tag{44}$$

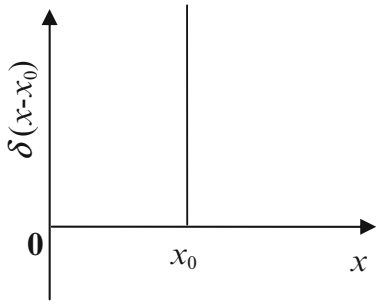

Fig. 5 One-dimensional Dirac-δ function is zero everywhere except at $x = x_0$ where its value is infinitely large

The density profile is defined as an ensemble average of the instantaneous density:

$$\rho(\vec{r}) = <\hat{\rho}(\vec{r})> = \sum_{i=1}^{N} <\delta(\vec{r}-\vec{r}_i)> . \tag{45}$$

Because the Dirac-δ function specifies the probability density of finding a single particle, the density profile $\rho(\vec{r})$ represents the average distribution of all particles in space.

In a uniform system, the molecular number density is everywhere the same, i.e., $\rho(\vec{r}) = N/V$. Nevertheless, near a "tagged" particle the local density $\rho(\vec{r})$ is inhomogeneous. For example, in the close-packed limit, hard spheres are arranged on a face-centered-cubic lattice and the average reduced density is $\rho_{av}\sigma^3 = \sqrt{2}$, where σ stands for the hard-sphere diameter. The local density is infinite at the lattice sites and zero otherwise. Contrary to the conventional notion for the density of a macroscopic matter, at a given position, the local density can be as large as infinity even in a uniform system.

To connect thermodynamic properties to the one-body density $\rho(\vec{r})$, we consider an open system at fixed temperature T and volume V. The grand partition function is given by:

$$\Xi = \sum_N \frac{1}{N!\Lambda^{3N}} \int \mathrm{d}\vec{r}^N \exp\left\{-\beta\left[\Gamma(\vec{r}^N) + \sum_{i=1}^{N} \varphi(\vec{r}_i)\right]\right\}, \tag{46}$$

where Λ is the thermal wavelength, $\Gamma(\vec{r}^N)$ stands for the total interaction potential of N particles at configuration $\vec{r}^N = (\vec{r}_1, \vec{r}_2, \ldots, \vec{r}_N)$, and $\beta = 1/(k_B T)$. The one-body potential $\varphi(\vec{r})$ combines the chemical potential μ and the external potential $v(\vec{r})$:

$$\varphi(\vec{r}) \equiv v(\vec{r}) - \mu. \tag{47}$$

The grand partition function is a function of T and volume V but a functional of the one-body potential $\varphi(\vec{r})$.

According to Eq. 45, the one-body density $\rho(\vec{r})$ is related to the grand partition function:

$$\rho(\vec{r}) = \frac{1}{\Xi}\sum_N \frac{1}{N!\Lambda^{3N}}\int \mathrm{d}\vec{r}^N \sum_{i=1}^N \delta(\vec{r}_i - \vec{r}) \exp\left\{-\beta\left[\Gamma(\vec{r}^N) + \sum_{i=1}^N \varphi(\vec{r}_i)\right]\right\} = -\frac{1}{\beta\Xi}\frac{\delta\Xi}{\delta\varphi(\vec{r})}, \tag{48}$$

where $\delta\,\Xi/\delta\varphi(\vec{r})$ represents a functional derivative. In terms of the grand potential:

$$\beta\Omega = -\ln\Xi \tag{49}$$

the one-body density $\rho(\vec{r})$ can be expressed as:

$$\rho(\vec{r}) = \frac{\delta\Omega}{\delta\varphi(\vec{r})}. \tag{50}$$

Equation 50 indicates that given the grand potential as a functional of the one-body potential $\varphi(\vec{r})$, we can determine the one-body density $\rho(\vec{r})$ from the grand potential by functional differentiation.

In formulation of the thermodynamic functional, we often use a free energy as a functional of the one-body density instead of the one-body potential. Towards that end, we may define the intrinsic Helmholtz energy by using the Legendre transformation[4]:

$$F \equiv \Omega - \int \mathrm{d}\vec{r}\,\varphi(\vec{r})\rho(\vec{r}). \tag{51}$$

Because $\delta\Omega = \rho(\vec{r})\delta\varphi(\vec{r})$, the Legendre transform ensures that the intrinsic Helmholtz energy F is a functional of $\rho(\vec{r})$, i.e., $F = F[\rho(\vec{r})]$. As in classical thermodynamics, the Legendre transform suggests that an open system of fixed temperature T, volume V and one-body potential $\varphi(\vec{r})$ can be *equivalently* defined in terms of the same temperature T and volume V, and an equilibrium one-body density $\rho(\vec{r})$. In other words, the one-body potential $\varphi(\vec{r})$ can be *uniquely* determined by the one-body density $\rho(\vec{r})$. Equations 50 and 51 provide a starting point for the variational principle of equilibrium in statistical mechanics.

4.2 Hohenberg–Kohn Theorem

Van der Waals' variational principle of equilibrium is formally exact except that it misses a subtle point in defining the meaning of thermodynamic functional when the density profile $\rho(\vec{r})$ does not correspond to the equilibrium density. Towards that end, we need to use the Hohenberg–Kohn theorem [27], which was established

[4] A Legendre transform switches independent variables in the fundamental equation of thermodynamics. For example, $F = E - TS$ is a Legendre transform that changes the fundamental equation of thermodynamics from $E = E(S,V,N)$ to $F = F(T,V,N)$. Here the thermodynamic variable is a function.

originally in the quantum mechanics of the ground-state energy of electrons at 0 K. Its generalization to electrons at a finite temperature was given by Mermin [32]. As shown by Evans [31], the generalized Hohenberg–Kohn theorem is equally applicable to classical systems.

The Hohenberg–Kohn theorem asserts that the one-body potential $\varphi(\vec{r})$ can be *uniquely* determined by a density profile $\rho(\vec{r})$ that minimizes the grand-potential functional:

$$\Omega_{\mathrm{v}}[p_\nu] \equiv \sum_\nu p_\nu [K_\nu + \Gamma_\nu + \int \mathrm{d}\vec{r}\hat{\rho}_\nu(\vec{r})\varphi(\vec{r}) + \beta^{-1}\ln p_\nu]. \tag{52}$$

In Eq. 52, K_ν and Γ_ν stand for the kinetic and intermolecular potential energies of the system at microstate ν, respectively; and p_ν represents the probability distribution of an equilibrium system with the one-body density $\rho(\vec{r})$:

$$p_\nu \sim \exp\{-\beta[K_\nu + \Gamma_\nu + \int \mathrm{d}\vec{r}\hat{\rho}_\nu(\vec{r})\varphi(\vec{r})]\}. \tag{53}$$

Because p_ν depends on $\varphi(\vec{r})$ which in turn can be *uniquely* determined by $\rho(\vec{r})$, the grand potential functional Ω_V is a functional of $\rho(\vec{r})$, i.e., $\Omega_V[p_\nu] = \Omega_V[\rho(\vec{r})]$.

If $\rho(\vec{r})$ is the equilibrium density corresponding to the one-body potential $\varphi(\vec{r})$, p_ν is the same as the equilibrium grand-canonical distribution, and $\Omega_V[p_\nu]$ becomes equal to the grand potential Ω. Otherwise, if $\rho'(\vec{r}) \neq \rho(\vec{r})$ is a trial density for the problem of interest, it can *uniquely* define a one-body potential $\varphi'(\vec{r})$ such that the system under $\varphi'(\vec{r})$ would result in the density profile $\rho'(\vec{r})$. In the latter case, the distribution of microstates satisfies:

$$p'_\nu \sim \exp\{-\beta[K_\nu + \Gamma_\nu + \int \mathrm{d}\vec{r}\hat{\rho}_\nu(\vec{r})\varphi'(\vec{r})]. \tag{54}$$

Because the grand potential functional is minimized by the equilibrium density profile $\rho(\vec{r})$, the Hohenberg–Kohn theorem states:

$$\Omega_{\mathrm{V}}[p_\nu] < \Omega_{\mathrm{V}}[p'_\nu]. \tag{55}$$

A central element to prove the Hohenberg–Kohn theorem is the Gibbs inequality

$$-\sum_\nu p_\nu \ln p_\nu \leq -\sum_\nu p_\nu \ln p'_\nu, \tag{56}$$

where p_ν and p'_ν are two sets of probability distributions that are defined on the basis of the same set of microstates $\{\nu\}$. The equal sign holds only when the two distributions are identical, i.e., $p_\nu = p'_\nu$. The Gibbs inequality can be easily derived from the mathematical relation $\ln(x) \leq x - 1$ for $x > 0$, specifically:

$$-\sum_\nu p_\nu \ln p'_\nu/p_\nu \geq \sum_\nu (p_\nu - p'_\nu) = 0. \tag{57}$$

Now suppose that in an open system at fixed temperature and volume, there exist two one-body potentials $\varphi(\vec{r})$ and $\varphi'(\vec{r})$ leading to the same density profile $\rho(\vec{r})$. These one-body potentials result in two sets of microstate distribution functions:

$$p_\nu = \exp\{-\beta[K_\nu + \Gamma_\nu + \int \mathrm{d}\vec{r}\hat{\rho}_\nu(\vec{r})\varphi(\vec{r})]/\Xi, \tag{58}$$

$$p'_\nu = \exp\{-\beta[K_\nu + \Gamma_\nu + \int \mathrm{d}\vec{r}\hat{\rho}_\nu(\vec{r})\varphi'(\vec{r})]/\Xi', \tag{59}$$

where Ξ and Ξ' are the grand partition functions corresponding to $\varphi(\vec{r})$ and $\varphi'(\vec{r})$ respectively.
According to the Gibbs inequality (Eq. 56), we have:

$$\sum_\nu p_\nu[K_\nu + \Gamma_\nu + \int \mathrm{d}\vec{r}\hat{\rho}_\nu(\vec{r})\varphi(\vec{r})] - \Omega \le \sum_\nu p_\nu[K_\nu + \Gamma_\nu + \int \mathrm{d}\vec{r}\hat{\rho}_\nu(\vec{r})\varphi'(\vec{r})] - \Omega', \tag{60}$$

where $\beta\Omega = -\ln\Xi$ and $\beta\Omega' = -\ln\Xi'$. Cancellation of terms in Eq. 60 gives:

$$\Omega' \le \Omega + \int \mathrm{d}\vec{r}[\varphi'(\vec{r}) - \varphi(\vec{r})]\rho(\vec{r}). \tag{61}$$

The same derivation holds when the primed and unprimed quantities are switched:

$$\Omega \le \Omega' + \int \mathrm{d}\vec{r}[\varphi(\vec{r}) - \varphi'(\vec{r})]\rho(\vec{r}). \tag{62}$$

To satisfy inequalities Eqs. 61 and 62 simultaneously, we must have:

$$\varphi(\vec{r}) = \varphi'(\vec{r}). \tag{63}$$

Therefore, for a given density profile $\rho(\vec{r})$, there is an *unique* one-body potential $\varphi(\vec{r})$.

To prove the inequality of Eq. 55, we note that according to Eq. 58:

$$K_\nu + \Gamma_\nu + \int \mathrm{d}\vec{r}\hat{\rho}_\nu(\vec{r})\varphi(\vec{r}) = \Omega - \beta^{-1}\ln[p_\nu]. \tag{64}$$

The grand potential functional corresponding to a trial density $\rho'(\vec{r})$ can be expressed as:

$$\begin{aligned}\Omega_V[p'_\nu] &= \sum_\nu p'_\nu[K_\nu + \Gamma_\nu + \int \mathrm{d}\vec{r}\hat{\rho}_\nu(\vec{r})\varphi(\vec{r}) + \beta^{-1}\ln p'_\nu] \\ &= \Omega + \beta^{-1}\sum_\nu \left[p'_\nu \ln p'_\nu - p'_\nu \ln p_\nu\right].\end{aligned} \tag{65}$$

The Gibbs inequality warrants that the last term on the right-side of Eq. 65 is always positive:

$$\Omega_V[\rho'(\vec{r})] > \Omega = \Omega_V[\rho(\vec{r})]. \tag{66}$$

Therefore, the equilibrium density $\rho(\vec{r})$ corresponds to the minimum value of the variational grand potential functional Ω_V. Following the rules of calculus of variations, the condition of minimum can be expressed as:

$$\frac{\delta\Omega_V[\rho(\vec{r})]}{\delta\rho(\vec{r})} = 0. \tag{67}$$

For a trial density profile $\rho'(\vec{r})$, the grand potential functional Ω_V depends on the one-body potential $\varphi(\vec{r})$ and implicitly on $\varphi'(\vec{r})$ that would yield p'_ν and $\rho'(\vec{r})$ at equilibrium. This awkward situation can be avoided by defining the variational intrinsic Helmholtz energy functional:

$$F_V[\rho(\vec{r})] \equiv \Omega_V[\rho(\vec{r})] - \int d\vec{r}\,\varphi(\vec{r})\rho(\vec{r}) = \sum_\nu p_\nu[K_\nu + \Gamma_\nu + \beta^{-1}\ln p_\nu]. \tag{68}$$

Unlike Ω_V, F_V depends only on the density profile $\rho(\vec{r})$ because for a given system, the distribution of microstates p_ν is uniquely determined by $\rho(\vec{r})$. In other words, $F_V[\rho(\vec{r})]$ is a *unique* functional of $\rho(\vec{r})$, independent of the one-body potential $\varphi(\vec{r})$.

The independence of $F_V[\rho(\vec{r})]$ on $\varphi(\vec{r})$ suggests that $F_V[\rho(\vec{r})]$ is an intrinsic property of the thermodynamic system. If $\rho(\vec{r})$ is the equilibrium density, $F_V[\rho(\vec{r})]$ becomes identical to the intrinsic Helmholtz energy functional $F[\rho(\vec{r})]$, which can be further written as:

$$F[\rho(\vec{r})] = F - \int d\vec{r}\,\nu(\vec{r})\rho(\vec{r}), \tag{69}$$

where F is the Helmholtz energy, and $\nu(\vec{r})$ is the external potential.

In terms of the variational intrinsic Helmholtz energy functional, the variational principle is given by the Euler–Lagrange equation:

$$\frac{\delta F_V[\rho(\vec{r})]}{\delta\rho(\vec{r})} + \nu(\vec{r}) - \mu = 0. \tag{70}$$

Given the chemical potential μ, the external potential $\nu(\vec{r})$, and an expression for the variational intrinsic Helmholtz energy functional $F_V[\rho(\vec{r})]$, we can solve for the equilibrium density $\rho(\vec{r})$ from the Euler–Lagrange equation. The equilibrium density can then be used to determine the grand potential and all thermodynamic properties of interest.

Apparently, the Euler–Lagrange equation is formally equivalent to the variational principle of equilibrium established by van der Waals. While in DFT the thermodynamic functionals are rigorously defined in terms of the equilibrium variables, in the van der Waals' variational principle of equilibrium, the existence of these functionals was introduced a priori and the variational principle was established as a direct consequence of the second law of thermodynamics. Practically, however, the variational principle of equilibrium and DFT lead to the same set of mathematical equations. To simplify the notation in the subsequent sections, we do not distinguish the difference between quantities like the variational intrinsic Helmholtz energy functional and the variational grand potential functional and their thermodynamic counterparts.

5 Density Distribution and Correlation Functions

Application of DFT to realistic systems often involves the density distribution and correlation functions, which contain information about the interrelated or nonrandom distributions of molecules. These functions quantify the statistical nature of a fluid structure and facilitate effectual formulation of the unknown intrinsic Helmholtz energy functional for nonideal thermodynamic systems without explicit consideration of the partition functions.

In principle, the density distribution and correlation functions of a liquid can be measured by using X-ray or neutron scattering methods. From these functions, we can predict the equation of state and any other thermodynamic properties of interest on the basis of the structure–property relationships of statistical mechanics.

5.1 Density Distribution Functions

Density distribution functions can be understood as generalization of the one-body density profile $\rho(\vec{r})$. Recall that the Dirac delta function $\delta(\vec{r}-\vec{r}_i)$ specifies the density of a spherical molecule i at position $\vec{r}$ or the probability density of finding molecule i at $\vec{r}$. For a system of N identical molecules, the one-body distribution function $\rho(\vec{r})$ corresponds for an ensemble average for the summation of $\delta(\vec{r}-\vec{r}_i)$:

$$\rho(\vec{r}) = < \sum_i \delta(\vec{r}-\vec{r}_i) > . \tag{71}$$

In analogy to the one-body density distribution function, a two-body density distribution function is related to the probability of finding two molecules at positions $\vec{r}'$ and $\vec{r}''$:

$$\hat{\rho}_{i,j}(\vec{r}_1,\vec{r}_2) = \delta(\vec{r}_1-\vec{r}_i)\delta(\vec{r}_2-\vec{r}_j), \tag{72}$$

where subscripts i and j denote two labeled molecules, one at position $\vec{r}_1$ and the other at $\vec{r}_2$. If there is only a single pair of labeled molecules in the system, integration of Eq. 72 is equal to one. For a system containing N identical spherical molecules, there are $N(N-1)$ undistinguishable molecular pairs at positions $\vec{r}_1$ and $\vec{r}_2$. The two-body density distribution function represents a summation of the ensemble averages of all possible molecular pairs:

$$\rho^{(2)}(\vec{r}_1,\vec{r}_2) = N(N-1) < \delta(\vec{r}'-\vec{r}_1)\delta(\vec{r}''-\vec{r}_2) > \approx N^2 < \delta(\vec{r}'-\vec{r}_1)\delta(\vec{r}''-\vec{r}_2) > . \tag{73}$$

In an ideal-gas system where molecules do not interact, the two-body density distribution function is reduced to $\rho^{(2)}(\vec{r}_1,\vec{r}_2) = \rho(\vec{r}_1)\rho(\vec{r}_2)$. In that case, we say that the densities are uncorrelated, i.e., the probability of finding a molecule at $\vec{r}_1$ is

independent of that of finding another molecule at $\vec{r}_2$. In a real system, the local densities become uncorrelated only if positions $\vec{r}_1$ and $\vec{r}_2$ are far apart.

The m-body density distribution function is defined as:

$$\rho^{(m)}(\vec{r}_1,\vec{r}_2,\ldots,\vec{r}_m) = N(N-1)\cdots(N-m+1) \tag{74}$$

$$< \delta(\vec{r}' - \vec{r}_1)\delta(\vec{r}'' - \vec{r}_2)\cdots\delta(\vec{r}^{(m)} - \vec{r}_m) > . \tag{75}$$

Similar to the two-body density distribution function, an m-body density correlation function specifies the joint probability density of finding m molecules at positions $\vec{r}_1,\vec{r}_2,\ldots,\vec{r}_m$. Density distribution functions beyond the two-body are rarely used in practical applications. In principle, knowledge of all multibody density distributions provides a complete description of the microscopic structure of a macroscopic system.

5.2 Pair Correlation Function

The pair correlation function is defined as the two-body density distribution function normalized by the corresponding one-body densities:

$$g^{(2)}(\vec{r}_1,\vec{r}_2) \equiv \rho^{(2)}(\vec{r}_1,\vec{r}_2)/[\rho(\vec{r}_1)\rho(\vec{r}_2)]. \tag{76}$$

Equation 76 indicates that given $\rho(\vec{r}_1)$ as the density at position $\vec{r}_1$, the density at another position $\vec{r}_2$ is given by $\rho(\vec{r}_2) = g^{(2)}(\vec{r}_1,\vec{r}_2)\rho(\vec{r}_1)$. In other words, the pair correlation function provides a measure of the degree of density correlations in space. For an ideal-gas system, the densities at different positions are uncorrelated. In a real fluid, the pair correlation function is close to zero if the separation is smaller than the collision diameter and strongly oscillates at small separation; it approaches unity only when the the two positions are far apart.

At fixed temperature T and average density ρ_{av}, the pair correlation function of a uniform fluid depends only on the distance. In this case, $g^{(2)}(\vec{r}_1,\vec{r}_2)$ is also referred to as the radial distribution function[5], designated as $g(r)$, where $r = |\vec{r}_1 - \vec{r}_2|$ represents the center-to-center distance or radial distance. As shown schematically in Fig. 6, the radial distribution function can be understood as the reduced one-body density at radial distance r from a tagged molecule at the origin. Because of the short-range intermolecular repulsion, $g(r)$ is zero at small values of r (i.e., less than the collision diameter). The first peak appears approximately when r is equal to the molecular diameter; it reflects the number density of the immediate neighbors of the tagged molecule relative to the bulk value. In an ideal gas, there is no intermolecular interaction so that $g(r) = 1$ at all conditions. For a real fluid, $g(r)$ approaches one

[5] This notation does not mean that a pair correlation function depends only on separation distance r. Instead, $g(r)$ is a function of the system and depends on temperature, density, and intermolecular interactions.

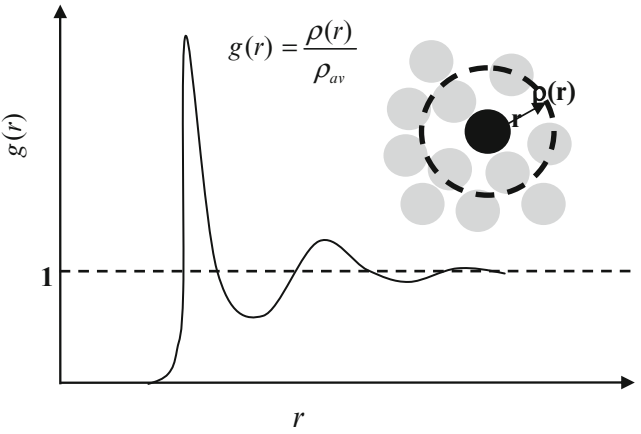

Fig. 6 Radial distribution function of a bulk fluid, $g(r)$, can be defined as the ratio of the local density $\rho(r)$ around a tagged molecule divided by the average density ρ_{av}

beyond only a few molecular diameters if it is far from the critical point. In general, $g(r)$ depends not only on r but also on the temperature and average density of the system.

While a bulk fluid has a uniform density, the local density near a tagged molecule is inhomogeneous due to the intermolecular interactions. By tagging an arbitrarily selected molecule, we can analyze the structure of a uniform fluid in terms of an equivalent inhomogeneous system where the external potential is identical to the pair interaction with the tagged molecule. Such equivalence is known as the Percus trick. With this trick, we can apply DFT to bulk systems and, as discussed later, derive a number of conventional liquid-state theories including the Ornstein–Zernike equation and its closures.

5.3 Density Fluctuations

For an open bulk system, the total number of molecules fluctuates and the fluctuation is directly related to the system stability. Similar concepts are applicable to the density distribution function $\rho(\vec{r})$ in an inhomogeneous system.

The density–density correlation function $\chi(\vec{r}_1, \vec{r}_2)$ specifies the correlated fluctuation of the number densities in space:

$$\chi(\vec{r}_1, \vec{r}_2) \equiv < [\hat{\rho}(\vec{r}_1) - \rho(\vec{r}_1)] \cdot [\hat{\rho}(\vec{r}_2) - \rho(\vec{r}_2)] >, \tag{77}$$

where $\rho(\vec{r})$ is the average number density of molecules at location $\vec{r}$, and $\hat{\rho}(\vec{r})$ represents the instantaneous density.

The density–density correlation function is directly related to the one and two-body density distribution functions. To see such connection, we rewrite Eq. 77 as:

$$\begin{aligned}\chi(\vec{r}_1,\vec{r}_2) =& <\sum_{i\neq j}^{N}\delta(\vec{r}_1-\vec{r}_i)\delta(\vec{r}_2-\vec{r}_j)> + <\sum_{i=j}^{N}\delta(\vec{r}_1-\vec{r}_i)\delta(\vec{r}_2-\vec{r}_j)> -\rho(\vec{r}_1)\rho(\vec{r}_2),\\ &= \rho^{(2)}(\vec{r}_1,\vec{r}_2)+\rho(\vec{r}_1)\delta(\vec{r}_1-\vec{r}_2)-\rho(\vec{r}_1)\rho(\vec{r}_2).\end{aligned} \tag{78}$$

Recall that the density distribution function is equal to the functional derivative of the grand potential Ω with respect to the one-body potential $\varphi(\vec{r})$(Eq. 50):

$$\rho(\vec{r}) = \langle\hat{\rho}(\vec{r})\rangle = \frac{\delta\Omega}{\delta\varphi(\vec{r})}, \tag{79}$$

a second functional derivative of the grand potential with respect to $\varphi(\vec{r})$ gives:

$$\frac{\delta^2\Omega}{\delta\varphi(\vec{r}_1)\delta\varphi(\vec{r}_2)} = \frac{\delta\rho(\vec{r}_1)}{\delta\varphi(\vec{r}_2)} = -\beta[\langle\hat{\rho}(\vec{r}_1)\rho(\vec{r}_2)\rangle - \rho(\vec{r}_1)\rho(\vec{r}_2)] = -\beta\chi(\vec{r}_1,\vec{r}_2). \tag{80}$$

Because the grand potential is minimized at equilibrium, Eq. 80 indicates that the density–density correlation function $\chi(\vec{r}_1,\vec{r}_2)$ is related to thermodynamic stability.

Table 1 compares the average density and its fluctuation in a bulk fluid with those in an inhomogeneous system. The left column shows the number of molecules and its fluctuation in an open uniform fluid; the right column gives the average density profile and its fluctuation over the space in an inhomogeneous fluid. The two set of equations are formally identical, except that the partial differentiations are replaced by the functional derivatives.

The density fluctuation in a bulk fluid can be detected by using small angle X-ray or neutron scattering methods. For a bulk system of uniform density $\rho(\vec{r}) = \rho_{\text{av}}$, the density–density correlation function becomes:

$$\chi(r) = \rho^2 h(r) + \rho\delta(\vec{r}), \tag{81}$$

where $h(r) \equiv g(r) - 1$ is the total correlation function and $r = |\vec{r}_2 - \vec{r}_1|$. The X-ray or neutron experiments measure the scattering intensity as a function of the wave vector $\vec{k}$, which is related to the static structure factor $\mathbb{S}(\vec{k})$. The latter is defined as

Table 1 Average density and fluctuation in uniform and inhomogeneous fluids

Bulk systems	Inhomogeneous systems
$< N >= -(\partial\Omega/\partial\mu)_{V,\beta}$	$\rho(\vec{r}) = \delta\Omega/\delta\varphi(\vec{r})$
$< \delta N^2 >= (\partial < N > /\partial\beta\mu)_{V,\beta}$	$\chi(\vec{r}_1,\vec{r}_2) = -\delta\rho(\vec{r}_1)/\delta\beta\varphi(\vec{r}_2)$
$< \delta N^2 >=< N^2 > - < N >^2$	$\chi(\vec{r}_1,\vec{r}_2) = \rho^{(2)}(\vec{r}_1,\vec{r}_2) - \rho(\vec{r}_1)\rho(\vec{r}_2)$ $+\rho(\vec{r}_1)\delta(\vec{r}_1-\vec{r}_2)$

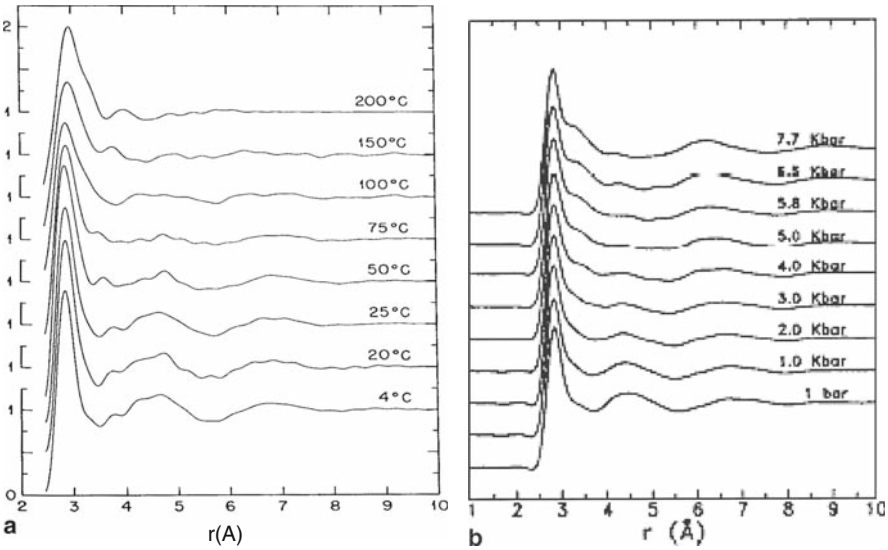

Fig. 7 Radial distribution function of water at different temperatures and pressures measured by X-ray scattering experiments: **(a)** at atmospheric pressure and various temperatures; **(b)** at 20°C and various pressures. From [33, 34]

the Fourier transform[6] of the normalized density–density correlation function:

$$\mathbb{S}(\vec{k}) = \frac{1}{\rho}\int \mathrm{d}\vec{r}\chi(r)\mathrm{e}^{-i\vec{k}\cdot\vec{r}} = \rho h(\vec{k}) + 1. \tag{82}$$

With the static structure factor $\mathbb{S}(\vec{k})$ obtained from experiments, an inverse Fourier transform of Eq. 82 gives the total correlation function $h(r)$ and subsequently the pair correlation function $g(r)$. Figure 7 presents, for example, the radial distribution function of liquid water at different pressures and different temperatures, as determined from X-ray scattering experiments [33, 34]. Because of the hydrogen bonding between water molecules, the structure of liquid water is quite different from that for a simple fluid. The first peak is significantly smaller than that for example, from the pair correlation functions for Ne or Ar at a similar density; the prolonged shoulders in the next immediate neighbors reflect the tetrahedral ordering of the hydrogen-bonded water molecules. The tetrahedral structure disappears gradually with increasing temperature. Interesting, a similar trend is observed with the increase of pressure.

[6] For a function that depends only on the radial distance r, the Fourier transform is defined as $\hat{f}(k) = \int \mathrm{d}\vec{r}\mathrm{e}^{-i\vec{k}\cdot\vec{r}} f(r) = (4\pi/k)\int_0^\infty r\sin(kr)f(r)\mathrm{d}r$.

5.4 Direct Correlation Functions

Direct correlation functions specify the response of the intrinsic Helmholtz energy functional with respect to the density changes. Because there is no intermolecular correlations in an ideal-gas system, the direct correlation functions applies only to the nonideal part of the intrinsic Helmholtz energy functional, i.e., the excess intrinsic Helmholtz energy:

$$F^{\mathrm{ex}}[\rho(\vec{r})] \equiv F[\rho(\vec{r})] - F^{\mathrm{id}}[\rho(\vec{r})], \tag{83}$$

where $F^{\mathrm{id}}[\rho(\vec{r})]$ is the intrinsic Helmholtz energy of an ideal-gas system. Just like an excess variable in classical thermodynamics, the excess intrinsic Helmholtz energy provides a measure of the thermodynamic nonideality, i.e., the quantity in excess to what the system would have at the same T and $\rho(\vec{r})$ if all intermolecular forces were "shut off".

The singlet direct correlation function is defined as:

$$c^{(1)}(\vec{r}) \equiv -\frac{\delta\beta F^{\mathrm{ex}}[\rho(\vec{r})]}{\delta\rho(\vec{r})}. \tag{84}$$

Following the Euler–Lagrange equation (Eq. 70) and the definition of F^{ex}, we obtain:

$$\frac{\delta F^{\mathrm{ex}}[\rho(\vec{r})]}{\delta\rho(\vec{r})} = \mu - v(\vec{r}) - \beta^{-1}\ln[\rho(\vec{r})\Lambda^3]. \tag{85}$$

A combination of Eqs. 84 and 85 indicates that the singlet direct correlation function can be understood as the local excess chemical potential:

$$\beta\mu = \ln[\rho(\vec{r})\Lambda^3] + \beta v(\vec{r}) - c^{(1)}(\vec{r}). \tag{86}$$

Equation 86 suggests that the chemical potential in an inhomogeneous system contains three contributions: an ideal-gas term that accounts for the translational momentum of molecules, an external potential, and $-\beta^{-1}c^{(1)}(\vec{r})$ accounts for the excess chemical potential due to intermolecular interactions.

The singlet direct correlation function can also be interpreted as the distribution of the effective one-body potential due to the intermolecular interactions. To perceive this point, we note that as in a bulk system, the excess chemical potential $\mu^{\mathrm{ex}}(\vec{r})$ represents the reversible work to transfer a molecule from an ideal-gas system of the same density to the real system at position $\vec{r}$. In an inhomogeneous system, this work consists of two parts: one is due to the presence of the external potential, which can be calculated directly from $v(\vec{r})$; the other arises from the intermolecular interactions, which is given by $-\beta^{-1}c^{(1)}(\vec{r})$.

In a bulk fluid, $v(\vec{r}) = 0$, and the number density is everywhere uniform. In that case, the singlet direct correlation function $c^{(1)}(\vec{r})$ is position-independent. According to Eq. 85, the chemical potential becomes:

$$\beta\mu = \ln[\rho\Lambda^3] - c^{(1)}, \tag{87}$$

i.e., $c^{(1)}$ is nothing but the conventional reduced excess chemical potential $-\beta\mu^{\text{ex}}$.

The second- and higher-order direct correlation functions are defined by consecutive functional derivatives of the singlet direction correlation function:

$$c^{(2)}(\vec{r}_1,\vec{r}_2) \equiv \frac{\delta c^{(1)}(\vec{r}_1)}{\delta\rho(\vec{r}_2)}, \tag{88}$$

$$c^{(m)}(\vec{r}_1,\vec{r}_2\cdots\vec{r}_m) \equiv \frac{\delta c^{(m-1)}(\vec{r}_1,\vec{r}_2\cdots\vec{r}_{m-1})}{\delta\rho(\vec{r}_m)}. \tag{89}$$

Because the singlet direct correlation function is the functional derivative of the excess intrinsic Helmholtz energy with respect to the density distribution, the *m*th-order direct correlation function, $c^{(m)}(\vec{r}_1,\vec{r}_2\cdots\vec{r}_m)$, corresponds to the *m*th-order functional derivative of the excess intrinsic Helmholtz energy with respect to the density distribution.

The physical significance of the second-order direct correlation function can be illustrated by considering the change in the one-body potential at position $\vec{r}_1$ in response to a change in the molecular density at $\vec{r}_2$. To the first-order approximation, the potential change can be represented by the pair interaction potential $\Gamma(\vec{r}_1,\vec{r}_2)$:

$$c^{(2)}(\vec{r}_1,\vec{r}_2) \approx -\beta\Gamma(\vec{r}_1,\vec{r}_2). \tag{90}$$

Equation 90 is known as the mean-spherical approximation (MSA), which is exact in the limit of low density or when the separation between $\vec{r}_1$ and $\vec{r}_2$ is infinite. In general, the second-order direct correlation function at small separation is much more complicated than the pair potential. Figure 8 shows a schematic comparison of the direct correlation function and the pair potential for a uniform fluid.

The direct correlation functions of a bulk fluid are often used as an input for formulation of the excess intrinsic Helmholtz energy in weighted-density approximations (WDA). Besides, it can be used for the functional expansion of F^{ex} with respect to that of a reference system with $\rho_0(\vec{r})$:

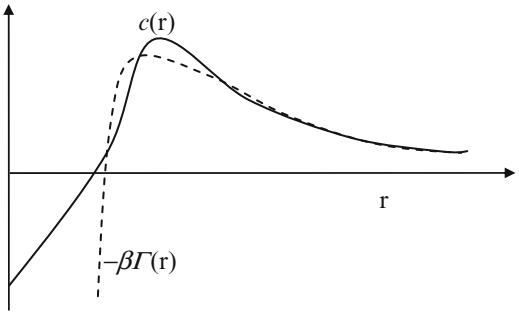

Fig. 8 A schematic representation of the direct correlation function for a uniform fluid. At large distance, $c(r)$ becomes identical to the negative of the reduced pair interaction potential

$$\beta F^{\mathrm{ex}}[\rho(\vec{r})] = \beta F^{\mathrm{ex}}[\rho_0(\vec{r})] - \int \mathrm{d}\vec{r} c_0^{(1)}(\vec{r})\Delta\rho(\vec{r}) - \frac{1}{2!} \times \iint \mathrm{d}\vec{r}_1 \mathrm{d}\vec{r}_2 c_0^{(2)}(\vec{r}_1,\vec{r}_2)\Delta\rho(\vec{r}_1)\Delta\rho(\vec{r}_2) + \cdots, \quad (91)$$

where subscript 0 denotes the reference system, $\Delta\rho(\vec{r}) = \rho(\vec{r}) - \rho_0(\vec{r})$; the coefficients $c_0^{(1)}$ and $c_0^{(2)}$ are the first and second direct correlation functions of the reference system (e.g., a bulk fluid). On the basis of the direct correlation functions, we can, in principle, calculate the intrinsic Helmholtz energy and, subsequently, the density distribution functions and thermodynamic properties. As we shall discuss later, there are alternative approaches to calculation of thermodynamic properties from the direct correlation functions. For example, the direct correlation functions can also be used as an input to calculate the equation of state of a thermodynamic system.

The density distribution and correlation functions provide a quantitative representation of the fluid structure and statistics. They also facilitate effective application of liquid-state theories including DFT to realistic systems. As discussed later, these functions are interrelated by integral equations. By using the distribution and correlation functions, we can predict all relevant thermodynamic properties, including those for inhomogeneous systems.

6 Integral Equation Theories

In statistical mechanics, the microstructure of a thermodynamic system is described by the density distribution and correlation functions. These functions facilitate connections of the microscopic structure and intermolecular interactions to macroscopic thermodynamic properties. While in principle the correlation functions can be determined by experiments or by molecular simulations, interpretation of the experimental and simulation data requires an analytical method. By relating the density and correlation functions, the integral equation theories represent an efficient means to predict the microscopic structure of thermodynamic systems.

6.1 Ornstein–Zernike Equation

The Ornstein–Zernike (OZ) equation links the density–density correlation function $\chi(\vec{r}_1,\vec{r}_2)$ to the second-order direct correlation function $c^{(2)}(\vec{r}_1,\vec{r}_2)$. The former depends on variation of the density distribution with respect to a change in the one-body potential and the latter, vice versa, describes the response of the effective one-body potential with respect to the density change. Because the density–density correlation function can be defined in terms of the density distribution functions $\rho^{(2)}(\vec{r}_1,\vec{r}_2)$ and $\rho(\vec{r})$ (78), the OZ equation is commonly expressed as an integral

equation linking the total correlation function $h(\vec{r}_1,\vec{r}_2)$, or, equivalently, the pair correlation function $g(\vec{r}_1,\vec{r}_2)$, to the second-order direct correlation function[7].

To derive the OZ equation, we recall that the second-order direct correlation function, $c^{(2)}(\vec{r}_1,\vec{r}_2)$, is defined as the functional derivative of the singlet direct correlation function $c^{(1)}(\vec{r}_1)$:

$$c^{(2)}(\vec{r}_1,\vec{r}_2) = \frac{\delta c^{(1)}(\vec{r}_1)}{\delta\rho(\vec{r}_2)}. \tag{87}$$

The latter represents an effective one-body potential (Eq. 86):

$$c^{(1)}(\vec{r}_1) = \ln[\rho(\vec{r}_1)\Lambda^3] + \beta\varphi(\vec{r}_1) - \beta\mu. \tag{91}$$

Substitution of Eq. 91 into 87 gives:

$$c^{(2)}(\vec{r}_1,\vec{r}_2) = \frac{\delta(\vec{r}_1-\vec{r}_2)}{\rho(\vec{r}_1)} + \frac{\delta\beta\varphi(\vec{r}_1)}{\delta\rho(\vec{r}_2)}. \tag{92}$$

Equation 92 indicates that the second-order direct correlation function includes two parts: one is due to the self-correlation, and the other is from variation of the one-body potential with respect to the density.

According to the inverse relation between functional derivatives:

$$\int \mathrm{d}\vec{r}_3 \frac{\delta\varphi(\vec{r}_1)}{\delta\rho(\vec{r}_3)} \frac{\delta\rho(\vec{r}_3)}{\delta\varphi(\vec{r}_2)} = \delta(\vec{r}_1-\vec{r}_2) \tag{93}$$

the second term on the right side of Eq. 92 is connected with the density–density correlation function (Eq. 78):

$$\chi(\vec{r}_1,\vec{r}_2) = -\frac{\delta\rho(\vec{r}_1)}{\delta\beta\varphi(\vec{r}_2)} = \rho(\vec{r}_1)\rho(\vec{r}_2)h(\vec{r}_1,\vec{r}_2) + \rho(\vec{r}_1)\delta(\vec{r}_1-\vec{r}_2), \tag{94}$$

where $h(\vec{r}_1,\vec{r}_2) \equiv g(\vec{r}_1,\vec{r}_2) - 1$ is the total correlation function. The OZ equation is obtained by substitutions of Eqs. 92 and 94 into Eq. 93:

$$h(\vec{r}_1,\vec{r}_2) = c^{(2)}(\vec{r}_1,\vec{r}_2) + \int \mathrm{d}\vec{r}_3 \rho(\vec{r}_3)\, h(\vec{r}_1,\vec{r}_3)\, c^{(2)}(\vec{r}_3,\vec{r}_2). \tag{95}$$

Eq. 95 suggests that the total correlation function $h(\vec{r}_1,\vec{r}_2)$ includes two parts: one due to the direct correlation represented by $c^{(2)}(\vec{r}_1,\vec{r}_2)$ and the other due to the indirect correlations represented by the convolution integral.

For a uniform system, the one-body density profile is independent of the position, and the direct and total correlation functions vary only with the center-to-center distance r. In that case, the OZ equation becomes:

[7] In some literature, the OZ equation defines the second-order direct correlation function. While such definition is legitimate mathematically, it applies only to the second-order and to some extent it makes the physical meaning of the direct correlation less transparent.

$$h(r) = c(r) + \rho \int \mathrm{d}\vec{r}_3\, h(|\vec{r}_1 - \vec{r}_3|)\, c(|\vec{r}_2 - \vec{r}_3|). \tag{96}$$

In the Fourier space, Eq. 96 can be expressed as:

$$\hat{h}(k) = \hat{c}(k) + \rho\, \hat{h}(k)\hat{c}(k). \tag{97}$$

A combination of Eqs. 97 and 82 gives simple algebraic relations between the static structure factor, the direct correlation function, and the total correlation function:

$$\mathbb{S}(k) = 1 + \rho\, \hat{h}(k) = \frac{1}{1 - \rho\hat{c}(k)}. \tag{98}$$

Based on the static structure factor obtained from neutron or X-ray scattering experiments, Eq. 98 allows us to calculate the radial distribution function $g(r) = h(r) + 1$ and the second-order direct correlation function $c(r)$.

6.2 Closures

The OZ equation provides a convenient starting point to theoretically determine the microscopic structure and correlation functions of a liquid. While it is mathematically exact, the OZ equation alone is insufficient because it involves two unknown functions, viz, the direct and total correlation functions. An additional relation is needed to specify either the direct or the total correlation function. This additional relation is known as the closure, which can be formulated on the basis of physical arguments and/or mathematical approximations.

A generic way to obtain a closure of the OZ equation is by a functional Taylor expansion of the excess intrinsic Helmholtz energy (Eq. 91):

$$\begin{aligned}\beta F^{\mathrm{ex}}[\rho] = \beta F^{\mathrm{ex}}[\rho_0] - \int \mathrm{d}\vec{r}\Delta\rho(\vec{r})c^{(1)}(\rho_0;\vec{r}) - \frac{1}{2} \\ \times \int\int \mathrm{d}\vec{r}_1\mathrm{d}\vec{r}_2\Delta\rho(\vec{r}_1)\Delta\rho(\vec{r}_2)c^{(2)}(\rho_0;\vec{r}_1,\vec{r}_2) + \cdots,\end{aligned} \tag{99}$$

where subscript 0 denotes a reference system with uniform density ρ_0, $\Delta\rho(\vec{r}) = \rho(\vec{r}) - \rho_0$. According the Euler–Lagrange equation (Eq. 70), the equilibrium density profile satisfies:

$$\ln[\rho(\vec{r})\Lambda^3] + \frac{\delta\beta F^{\mathrm{ex}}}{\delta\rho(\vec{r})} + \beta\varphi(\vec{r}) = 0. \tag{100}$$

By using Eqs. 99 and 100, we can find the one-body density profile:

$$\ln[\rho(\vec{r})\Lambda^3] = -\beta\varphi(\vec{r}) + c^{(1)}(\rho_0;\vec{r}) + \int \mathrm{d}\vec{r}' c^{(2)}(\rho_0;\vec{r},\vec{r}')\Delta\rho(\vec{r}') + \cdots. \tag{101}$$

For a uniform system, the singlet correlation function is equal to Eq. 87:

$$c^{(1)}(\rho_0;\vec{r}) = \ln[\rho_0\Lambda^3] - \beta\mu. \tag{102}$$

Substitution of Eq. 102 into Eq. 101 gives:

$$\ln[\rho(\vec{r})/\rho_0] = -\beta v(\vec{r}) + \int \mathrm{d}\vec{r}' c^{(2)}(\rho_0;\vec{r},\vec{r}')\Delta\rho(\vec{r}') + \cdots. \tag{103}$$

Equation 103 is exact provided that the direct correlation functions of the reference system are known. The convergence of the functional Taylor expansion can be controlled by a careful selection of the deviation of the inhomogeneous density from that of the reference, i.e., the magnitude and range of $\Delta\rho(\vec{r})$.

If the direct correlation function is short-ranged and $\Delta\rho(\vec{r})$ is small, Eq. 103 converges rapidly. In that case, the functional Taylor expansion may be truncated after the second-order direct correlation function:

$$\rho(\vec{r})/\rho_0 \approx \exp[-\beta v(\vec{r}) + \int \mathrm{d}\vec{r}' c^{(2)}(\rho_0;\vec{r},\vec{r}')\Delta\rho(\vec{r}')]. \tag{104}$$

Equation 104 is known as the hypernetted-chain (HNC) approximation; it provides a relation between the density distribution function and direct correlation function complementary to the OZ equation.

Another popular selection of the closure, known as the Percus–Yevick (PY) theory [35], can be obtained by a linear expansion of the second exponential term in Eq. 104:

$$\rho(\vec{r}_1)/\rho_0 \approx \exp[-\beta v(\vec{r}_1)]\,[1 + \int \mathrm{d}\vec{r}_2 c^{(2)}(\rho_0;\vec{r}_1,\vec{r}_2)(\rho(\vec{r}_2) - \rho_0)]. \tag{105}$$

The HNC and PY closures are complementary in practical applications of the OZ equation. The former is most accurate for systems with long-range interactions and the latter works best for systems with short-range forces.

Given a pairwise additive interaction potential, the OZ equation, along with a closure, can be numerically solved by using Gillan's modification of the Newton–Raphson method [36]. Once the correlation functions are known, one can calculate all thermodynamic properties using various thermodynamic routes such as the virial, compressibility, and energy equations (to be discussed later). Because of the approximations used in deriving the closure relations, there often exist disagreements between the thermodynamic properties obtained from different thermodynamic routes. This difference is known as the thermodynamic inconsistency of the integral-equation theory. For most cases, the thermodynamic consistency deteriorates as the density or charge of the system increases.

Whereas the OZ equation and its closures are applicable to both uniform and inhomogeneous systems, they are most useful only for the former case where a small local density inhomogeneity can be justified. To apply the density expansion method to a uniform system, we may use the Percus trick, i.e., singling out one tagged molecule and placing it at the origin. Because of the translational invariance

of a uniform system, the location of a tagged molecule is arbitrary. Distribution of the remaining molecules is equivalent to that in an inhomogeneous system where the "external" potential is identical to the pair potential $v(\vec{r}) = \Gamma(\vec{r})$. In that case, the HNC and PY closures become, respectively:

$$\ln[g(r)] \approx -\beta\Gamma(r) + \rho \int d\vec{r}' c(|\vec{r} - \vec{r}'|)h(|\vec{r}'|) \tag{106}$$

and:

$$g(r) \approx \exp[-\beta\Gamma(r)][1 + \rho \int d\vec{r}' c(|\vec{r} - \vec{r}'|)h(|\vec{r}'|)], \tag{107}$$

where $h(r) = \Delta\rho(r)/\rho_0 = g(r) - 1$.

Using the OZ equation (Eq. 96), we can rewrite Eqs. 106 and 107 as:

$$c(r) \approx h(r) - \ln[h(r) + 1] - \beta\Gamma(r) = h(r) - \ln[y(r)](\text{HNC}), \tag{108}$$

$$c(r) \approx g(r) - y(r)(\text{PY}), \tag{109}$$

where $y(r) \equiv g(r)\exp[\beta\Gamma(r)]$ is the cavity correlation function[8]. According to Eq. 109, the radial distribution function $g(r)$ includes approximately a contribution from the direct correlation function $c(r)$ and an "indirect" contribution represented by the cavity correlation function $y(r)$.

For a fluid of hard spheres or sticky hard spheres, the OZ equation with the PY closure can be solved analytically [37, 38]. These analytical solutions have enormous impacts on the early development of the liquid-state theories. Because the PY closure can be obtained by linearization of the HNC closure, one may presume that the HNC closure is superior to the PY closure. While this is true for many cases, surprisingly the thermodynamic properties of hard spheres calculated from the PY closure are more accurate than those from the HNC closure. The success of the PY closure for hard spheres is probably due to cancellation of errors.

For systems satisfying $h(r) << 1$ and $h(r) \approx \ln[1 + h(r)]$ at large value of r, the HNC approximation can be further approximated by:

$$c(r) \approx -\beta\Gamma(r) \quad r > \sigma. \tag{110}$$

As mentioned earlier, Eq. 110 is known as the mean-spherical approximation (MSA). The OZ equation with the MSA approximation can also be solved analytically for ionic systems [39] or, in general, for systems with the hard-core Yukawa potential:

$$\Gamma(r) = \begin{cases} 0 & r < \sigma \\ -\varepsilon \dfrac{e^{-\kappa(r-\sigma)}}{r} & r \geq \sigma \end{cases}, \tag{111}$$

[8] A cavity correlation function describes the correlation between two "cavities" in the fluid. A cavity is a real particle that has no interaction with another cavity particle. Because the potential of mean force ($\beta W(r) = -\ln[g(r)]$) is the overall interaction between two molecules in the system, it follows that $-\ln[y(\vec{r})]$ includes all indirect interactions, or effects of all other molecules on the overall interaction.

where ε and σ are energy and size parameters, respectively, and parameter κ controls the range of the intermolecular interaction. Because of the thermodynamic inconsistency, the MSA closure yields more accurate thermodynamic properties from the energy equation than those from the compressibility or virial equations.

In general, the HNC closure is not accurate for systems with strong local density inhomogeneity or with long-range order. To improve the numerical accuracy, we may use the bridge function $b(r)$, which is defined as all high-order terms neglected in the density expansion of the intrinsic Helmholtz functional (Eq. 99). Mathematically, the bridge function connects the direct correlation function $c(r)$ and the total correlation function $h(r)$:

$$c(r) = h(r) - \ln[y(r)] + b(r). \tag{112}$$

Following the derivation for HNC, we may express $b(r)$ in terms of the density expansion:

$$\begin{aligned} b(r) =& \frac{\rho^2}{2!}\int\int \mathrm{d}\vec{r}_2\mathrm{d}\vec{r}_3 c^{(3)}(|\vec{r}_2-\vec{r}|,|\vec{r}_3-\vec{r}|)h(|\vec{r}_2-\vec{r}|)h(|\vec{r}_3-\vec{r}|) \\ &+ \frac{\rho^3}{3!}\int\int\int \mathrm{d}\vec{r}_2\mathrm{d}\vec{r}_3\mathrm{d}\vec{r}_4 c^{(4)}(|\vec{r}_2-\vec{r}|,|\vec{r}_3-\vec{r}|,|\vec{r}_4-\vec{r}|) \\ &h(|\vec{r}_2-\vec{r}|)h(|\vec{r}_3-\vec{r}|)h(|\vec{r}_3-\vec{r}|)+\cdots. \end{aligned} \tag{113}$$

Because the higher-order correlation functions are rarely known even for a simple fluid, the bridge function is often formulated by a heuristic means, e.g., by using accurate results for a reference system (such as hard spheres) or by imposing the conditions of thermodynamic consistency.

For a uniform hard-sphere fluid, the bridge function has been determined accurately from computer simulations. It can be conveniently correlated with the semi-empirical relation [40]:

$$b(r) \approx \frac{1}{2}\frac{[h(r)-c(r)]^2}{1+(1.1-\rho\sigma^3/3)\,[h(r)-c(r)]}, \tag{114}$$

where σ is the hard-sphere diameter. Figure 9 shows the bridge functions of hard spheres at different densities. While the bridge function is negligible at low density, it becomes more significant as the density increases, in particular at short separations.

Far away from the critical point, the bridge function is not sensitive to the details of the intermolecular potential. As a result, once a bridge function is determined for one particular potential function, it may be applied to other situations. The quasi-universality of the bridge function provides a simple procedure to improve the numerical performance of the HNC closure [41]. For example, the reference hypernetted chain (RHNC) theory is obtained by substituting the exact bridge function by that of a reference system:

$$c(r) - c_0(r) \approx h(r) - h_0(r) - \ln[y(r)/y_0(r)], \tag{115}$$

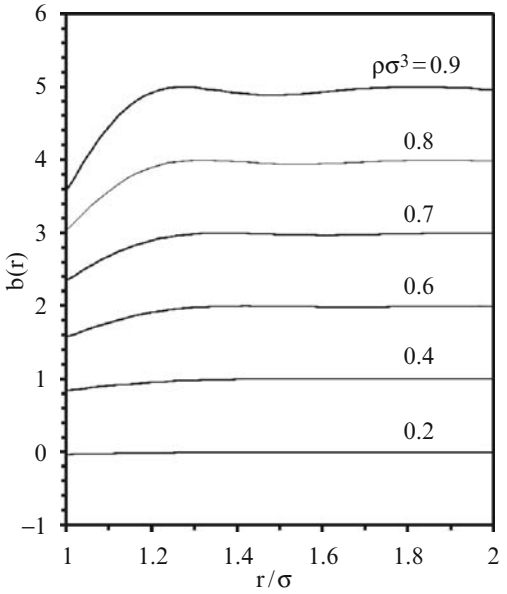

Fig. 9 Bridge functions of uniform hard spheres at different reduced densities. Each high-density curve has been consecutively shifted upward by one unit

where subscript 0 denotes a reference system (usually hard spheres) where the structural properties can be determined accurately. In the modified hypernetted chain (MHNC) theory of Rosenfeld and Ashcroft [42], the bridge function is replaced by that of the hard-sphere fluid:

$$c(r) \approx h(r) - \ln[y(r)] + b^{\mathrm{hs}}(r), \tag{116}$$

where the hard-sphere diameter is chosen such that the predictions of MHNC satisfy the thermodynamic consistency. The RHNC and MHNC theories give accurate representations of both pair distribution functions and thermodynamic properties for a wide choice of pair intermolecular interactions.

The integral equation theories experience tremendous success in representing the structure and thermodynamic properties of uniform fluids. However, it becomes less useful for highly asymmetric mixtures and inhomogeneous systems, where the density inhomogeneity is magnified under an external field. Because the excess intrinsic Helmholtz energy is truncated after the quadratic term, HNC is applicable only when the density deviation is small and is inappropriate to directly describe phase transitions. The same limitation applies to the PY and MSA closures.

7 Thermodynamic Properties of Uniform Fluids

The purpose of statistical mechanics is to provide explicit connections of thermodynamic variables to the underlying intermolecular forces and to the microscopic structure. For uniform systems, such connections are discussed in typical texts [5, 11]. The relations are less known for inhomogeneous fluids. We discuss both cases for completeness. In this section, we present the standard relations between thermodynamic variables and various correlation functions for uniform systems. The next section gives analogous relations for inhomogeneous fluids.

7.1 Internal Energy

The internal energy of a thermodynamic system is defined as the ensemble average of the total molecular energy, which consists of a kinetic term K due to the molecular motions, a potential Γ due to the intermolecular interactions, and a potential energy in the presence of an external field $v(\vec{r})$. With the pairwise additive approximation for the intermolecular potential energy, the internal energy is given by:

$$\begin{aligned} U &= < K > + \frac{1}{2} < \sum_{i \neq j} \Gamma(\vec{r}_i, \vec{r}_j) > + < \sum_{i=1}^{N} v(r_i) >, \\ &= \frac{3 < N >}{2\beta} + \frac{1}{2} \int \mathrm{d}\vec{r} \int \mathrm{d}\vec{r}' \rho(\vec{r}, \vec{r}) \Gamma(\vec{r}, \vec{r}') + \int \mathrm{d}\vec{r} \rho(\vec{r}) v(\vec{r}). \end{aligned} \tag{117}$$

The first term on the right side of Eq. 117 is identical to that in an ideal gas; the second term is for the intermolecular potential where a factor of $1/2$ corrects for double counting of the total number of molecular pairs; and the third term comes from the external potential energy $v(\vec{r})$. In Eq. 117, the expressions for the intermolecular and external energies follow the definitions of the two-body and one-body density distribution functions, $\rho(\vec{r}, \vec{r}')$ and $\rho(\vec{r})$, respectively.

Equation 117 suggests that the internal energy can be calculated from a pairwise additive intermolecular potential $\Gamma(\vec{r}, \vec{r}')$, the one- and two-body density distribution functions $\rho(\vec{r})$ and $\rho(\vec{r}, \vec{r}')$, and the external potential $v(\vec{r})$. For a uniform system free of the external potential, $\rho(\vec{r}) = \rho$ and the two-body density distribution function can be simply expressed as:

$$\rho(\vec{r}, \vec{r}') = \rho^2 g(r), \tag{118}$$

where $r = |\vec{r} - \vec{r}'|$, $g(r)$ is the radial distribution function. In that case, the internal energy becomes:

$$\frac{U}{< N >} = \frac{3}{2} k_{\mathrm{B}} T + 2\pi\rho \int \mathrm{d}r\, r^2 \Gamma(r) g(r). \tag{119}$$

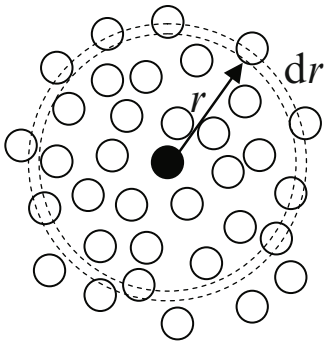

Fig. 10 Schematic distribution of molecules around an arbitrarily tagged molecule

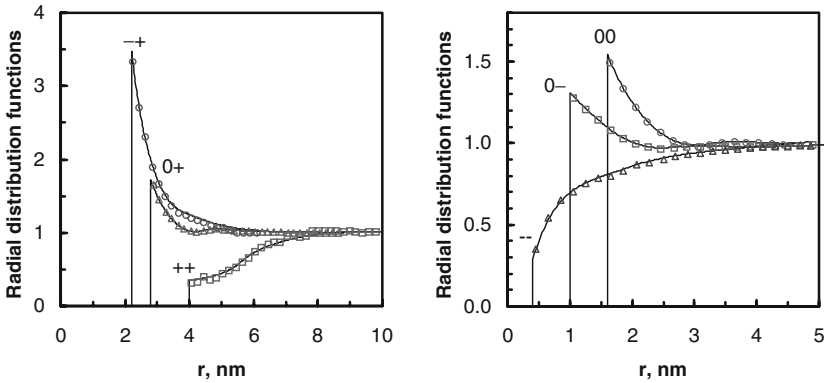

Fig. 11 *Left*: The distributions of counterions (−), neutral particles (0), and macroions (+) around a macromion predicted from DFT (*lines*) and from Monte Carlo simulations (*points*). *Right*: The radial distribution functions around a neutral particle. The diameters of macroions, microions, and neutral particles are 4, 0.4, 1.6 nm, respectively. Each macroion bears six positive charges. The packing density for the macroions is 0.08 and that for neutral particles is 0.25

Because the intermolecular potential $\Gamma(r)$ is significant only when the separation is within the range of a few molecular diameters, the interaction of molecules with their immediate neighbors represent the most important contributions to the non-ideal part of the internal energy.

One may conceive the physical significance of the potential energy due to the intermolecular interactions by considering, as shown in Fig. 10, an arbitrarily tagged molecule interacting with all other molecules in the system. The number of molecules with the center of mass located in a spherical shell of radius r and thickness dr is $4\pi r^2 \mathrm{d}r\,\rho g(r)$, and the total interaction energy from this shell is $4\pi r^2 \mathrm{d}r\,\rho g(r)\Gamma(r)$. Integration of the radius r gives the total potential energy for the tagged molecule. To avoid double counting of the pair interactions we need a factor of $1/2$.

To apply DFT to a uniform system, we first calculate $g(r)$ from the distribution molecules around a tagged molecule, which is equivalent to the one-body density profile in an external potential identical to the pair potential. Figure 11 shows, for

example, the radial distribution functions in a ternary mixture of macromolecules, neutral particles, and small ions predicted from DFT in comparison with simulation results. The system provides a simplistic representation of a cellular environment that contains macromolecules at high packing density. From the radial distribution function, Eq. 119 gives the internal energy in good agreement with simulation data [43].

7.2 Pressure Equations

The pressure of a uniform fluid can be calculated either from the compressibility equation or from the viral equation[9]. The former connects pressure to the density fluctuation and the latter is directly related to the intermolecular forces.

To find a connection between pressure and density fluctuation in a thermodynamic system, we consider a uniform one-component fluid in the grand canonical ensemble. At given temperature T and chemical potential μ, the fluctuation of the number of molecules in a fixed volume V is given by:

$$\begin{aligned}\left(\frac{\partial < N >}{\partial \beta \mu}\right)_{T,V} &= < N^2 > - < N >^2 = < N(N-1) > + < N > - < N >^2, \\ &= < N > + \int \mathrm{d}\vec{r}\mathrm{d}\vec{r}' \rho^{(2)}(\vec{r},\vec{r}') - \left[\int \mathrm{d}\vec{r}\rho(\vec{r})\right]^2, \\ &= < N > + \int \mathrm{d}\vec{r}\mathrm{d}\vec{r}' \rho(\vec{r})\rho(\vec{r}')[g(|\vec{r}-\vec{r}'|)-1], \\ &= < N > \left[1 + \rho \int \mathrm{d}\vec{r} h(r)\right] = < N > [1 + \rho \hat{h}(0)],\end{aligned} \tag{120}$$

where $\hat{h}(k)$ is the Fourier transform of the total correlation function.

Because the total volume is fixed, we can express the left side of Eq. 120 in terms of the average number density $\rho = < N > /V$:

$$(\partial < N > /\partial \beta \mu)_{T,V} = V(\partial \rho / \partial \beta \mu)_{T,V}. \tag{121}$$

Following the Gibbs–Duhem equation:

$$(\partial P/\partial \rho)_T = \rho(\partial \mu / \partial \rho)_T, \tag{122}$$

we obtain:

$$(\partial \rho / \partial \beta P)_T = \rho^{-1}(\partial \rho / \partial \beta \mu)_T = 1 + \rho \hat{h}(0). \tag{123}$$

Equation 123 is known as the compressibility equation; it connects the fluid-structure to the isothermal compressibility:

[9] The concept of virial was first introduced by Clausius; in Latin it means force. The virial equation is not the same as the virial expansion.

$$\kappa_{\mathrm{T}} = \rho^{-1}(\partial\rho/\partial P)_T. \tag{124}$$

Because the total correlation function is related to the static structure factor:

$$\mathbb{S}(0) = 1 + \rho\hat{h}(0), \tag{125}$$

the compressibility equation can be alternatively expressed as:

$$\rho k_{\mathrm{B}} T \kappa_{\mathrm{T}} = \mathbb{S}(0). \tag{126}$$

The compressibility equation predicts the pressure of a thermodynamic system on the basis of the microscopic structure without evoking explicit knowledge of the intermolecular potential.

A second route to calculation of the pressure is by using the virial theorem, which connects the pressure to the intermolecular potential and the pair correlation function. To illustrate this method, we consider a system containing N molecules at fixed temperature and volume. For a given molecule i, Newton's equation of motion gives:

$$m\ddot{\vec{r}}_i = \vec{F}_i^{\text{total}}, \tag{127}$$

where m stands for the molecular mass, $\vec{F}_i^{\text{total}}$ is the total force on the molecule, $\vec{r}_i$ is the molecular position, and $\ddot{\vec{r}} \equiv \mathrm{d}^2\vec{r}/\mathrm{d}t^2$ describes acceleration.

Multiply Eq. 127 by $\vec{r}_i$, and apply the canonical ensemble average:

$$m < \vec{r}_i \cdot \ddot{\vec{r}}_i > = < \vec{r}_i \cdot \vec{F}_i^{\text{total}} > . \tag{128}$$

We can rewrite the left side of Eq. 128 as:

$$< \vec{r}_i \cdot \ddot{\vec{r}}_i > = \mathrm{d} < \vec{r}_i \cdot \dot{\vec{r}}_i > /\mathrm{d}t - < \dot{\vec{r}}_i^2 >, \tag{129}$$

and according to the ergodic assumption, we obtain:

$$< \vec{r}_i \cdot \dot{\vec{r}}_i > = \lim_{\tau\to\infty} \frac{1}{\tau} \int_0^\tau \vec{r}_i \cdot \dot{\vec{r}}_i \mathrm{d}t = \lim_{\tau\to\infty} \frac{\vec{r}_i(\tau)^2 - \vec{r}_i(0)^2}{2\tau}. \tag{130}$$

Equation 130 suggests that $< \vec{r}_i \cdot \dot{\vec{r}}_i >$ is independent of time:

$$\mathrm{d} < \vec{r}_i \cdot \dot{\vec{r}}_i > /\mathrm{d}t = 0. \tag{131}$$

Substituting Eq. 129 into 128 gives:

$$- < \vec{p}_i^2/m > = < \vec{r}_i \cdot \vec{F}_i^{\text{total}} >, \tag{132}$$

where $\vec{p}_i = m\dot{\vec{r}}_i$ is the molecular momentum.

The left side of Eq. 132 is equal to $3k_{\mathrm{B}}T$ according to the average kinetic energy. From Eq. 132, we obtain the virial theorem by a summation of overall molecules:

$$-3Nk_{\mathrm{B}}T = \sum_i < \vec{r}_i \cdot \vec{F}_i^{\text{total}} > . \tag{133}$$

Clausius defined the right side of Eq. 133 as virial, which means force in its Latin origin.

The pressure of a thermodynamic system can be identified from the force per unit area exerted on the system boundary. Near the system boundary, the total force on each molecule $\vec{F}_i^{\text{total}}$ includes a contribution due to all other molecules in the system $\vec{F}_i$, and that due to the container $\vec{F}_i'$. The pressure can be calculated from the ensemble average of the total force exerted on the boundary per unit area. According to Gauss' theorem, the contribution of the force due to the container to the viral is given by:

$$\sum_i < \vec{r}_i \cdot \vec{F}_i' > = \int \mathrm{d}\vec{r} < \delta(\vec{r} - \vec{r}_i)\, \vec{r}_i \cdot \vec{F}_i' > = - \oint \vec{r} \cdot \vec{n} P \, \mathrm{d}A = -P \int \nabla \cdot \vec{r} \mathrm{d}V = -3PV, \tag{134}$$

where dA represents a surface element with a normal in the direction of the unit vector $\vec{n}$, $\vec{r}$ stands for the position of the surface element dA, and the negative sign indicates that the force from the container to a molecule is opposite to that from the molecular to the container. In deriving Eq. 134, we have used the identity $\nabla \cdot \vec{r} = 3$.

From Eqs. 133 and 134, we obtain the virial equation:

$$P = \rho k_{\mathrm{B}} T + \frac{1}{3V} \sum_i < \vec{r}_i \cdot \vec{F}_i >, \tag{135}$$

where $\rho = N/V$ is the average molecular density. With the pairwise additive approximation, the force due to other molecules on molecule i can be written as a sum of the pair interaction forces:

$$\vec{F}_i = \sum_{j \neq i} \vec{F}_{ij} = - \sum_{j \neq i} \partial \Gamma_{ij}(r) / \partial r. \tag{136}$$

Substituting Eq. 136 into 135 gives:

$$\begin{aligned} \sum_i \vec{F}_i \cdot \vec{r}_i &= \sum_i \sum_{j \neq i} \vec{F}_{ij} \cdot \vec{r}_i = \frac{1}{2} \sum_i \sum_{j \neq i} (\vec{F}_{ij} \cdot \vec{r}_i + \vec{F}_{ji} \cdot \vec{r}_j) \\ &= \frac{1}{2} \sum_i \sum_{j \neq i} (\vec{F}_{ij} \cdot \vec{r}_i - \vec{F}_{ij} \cdot \vec{r}_j) = \frac{1}{2} \sum_i \sum_{j \neq i} \vec{F}_{ij} \cdot \vec{r}_{ij}, \end{aligned} \tag{137}$$

where $\vec{r}_{ij} = \vec{r}_i - \vec{r}_j$, the second equality follows the symmetry of indices i and j, and the third equality follows Newton's third law $\vec{F}_{ij} = -\vec{F}_{ji}$.
In terms of the pair correlation function, the virial equation becomes:

$$P = k_{\mathrm{B}} T \rho + \frac{1}{6V} < \sum_i \sum_{j \neq i} \vec{F}_{ij} \cdot \vec{r}_{ij} > = k_{\mathrm{B}} T \rho - \frac{\rho^2}{6} \int \mathrm{d}\vec{r} \frac{\partial \Gamma(r)}{\partial r} r g(r). \tag{138}$$

The virial equation or virial theorem is convenient for practical applications when the information concerning the radial distribution function and the intermolecular potential are readily available. In particular, Eq. 135 is useful for calculation

of pressure from a molecular simulation. Because of the pairwise additive approximation, results from the virial equation can be less accurate than that from the compressibility equation. For practical applications, the virial and compressibility equations are often used together to test the thermodynamic consistency of a liquid-state theory.

7.3 Chemical Potential

Chemical potential can be calculated from the correlation functions according to the compressibility equation (Eq. 123):

$$\rho(\partial\beta\mu/\partial\rho)_{\mathrm{T}} = [1+\rho\hat{h}(0)]^{-1} = 1-\rho\hat{c}(0), \tag{139}$$

where the second equality in Eq. 139 follows the OZ equation. For an ideal gas, the direct correlation function vanishes and an integration of Eq. 139 gives:

$$\beta\mu^{\mathrm{id}} = \ln\rho\Lambda^3, \tag{140}$$

where Λ represents the thermal wavelength.

Alternatively, the chemical potential can be calculated from the virial route by considering the change in the Helmholtz energy. Towards that end, we divide the Helmholtz energy into an ideal part and an excess:

$$F = F^{\mathrm{id}} + F^{\mathrm{ex}}, \tag{141}$$

where F^{id} denotes the Helmholtz energy of an ideal gas at the same (N,T,V), and F^{ex} represents the excess Helmholtz energy that arises from intermolecular interactions. Accordingly, the chemical potential can be expressed as:

$$\mu = \mu^{\mathrm{id}} + \mu^{\mathrm{ex}}, \tag{142}$$

where μ^{id} is the chemical potential of the ideal gas (Eq. 140), and μ^{ex} represents the excess chemical potential.

In the thermodynamic limit ($N\to\infty$), the excess chemical potential μ^{ex} can be calculated from the difference in the excess Helmholtz energy:

$$\mu^{\mathrm{ex}} = \left(\frac{\partial F^{\mathrm{ex}}}{\partial N}\right)_{T,V} = F^{\mathrm{ex}}(N,T,V) - F^{\mathrm{ex}}(N-1,T,V). \tag{143}$$

Equation 143 provides a practical basis for calculating the excess chemical potential by using a coupling parameter method. To fix the ideas, let $0\le\lambda\le 1$ be a coupling parameter for the interaction between a tagged molecule and all other molecules in the system. At a given value of λ, the tagged molecule interacts with any other molecule with a potential $\lambda\Gamma(r)$, where $\Gamma(r)$ is the normal pair interaction potential. When $\lambda = 0$, the tagged molecule does not interact with other molecules, i.e.,

it is uncoupled from the system; when $\lambda = 1$, the tagged molecule becomes identical to other molecules, i.e., it is fully coupled. The excess chemical potential μ^{ex} represents the reversible work to transfer one molecule into a canonical system from an ideal-gas state, which can be obtained by integrating the coupling parameter from $\lambda = 0$ to $\lambda = 1$.

Let $\rho(r,\lambda)$ represent the average number density of other molecules at radial distance r from the tagged molecule. The reversible work to increase λ by $d\lambda$ due to interaction of the tagged molecule with other molecules located in a spherical shell between r and $r + dr$ is:

$$dW = \Gamma(r)d\lambda \cdot \rho(r,\lambda) \cdot 4\pi r^2 dr. \tag{144}$$

The excess chemical potential or the total work corresponds to increase λ from $\lambda = 0$ to $\lambda = 1$ is:

$$\mu^{ex} = \int_0^1 d\lambda \int \Gamma(r)\rho(r,\lambda) \cdot 4\pi r^2 dr. \tag{145}$$

Substitution of Eq. 145 into 142 gives:

$$\mu = k_B T \ln(\rho\Lambda^3) + \int_0^1 d\lambda \int \Gamma(r)\rho(r,\lambda) \cdot 4\pi r^2 dr. \tag{146}$$

Equation 146 indicates that in order to calculate the chemical potential, we need to know the density distribution function $\rho(r,\lambda)$ for $0 \le \lambda \le 1$.

8 Thermodynamic Properties of Inhomogeneous Fluids

As for uniform fluids, we can establish exact statistical–mechanical relations between thermodynamic properties and the microscopic structure for inhomogeneous systems. While the basic ideas for deriving the structure–property relationships are similar, the equations for inhomogeneous systems are necessarily more complicated because, in this case, the thermodynamic properties depend not only on the intermolecular forces and but also on the nonuniform distribution of molecules and on the external potential. These relations provide a foundation for application of DFT to various interfacial phenomena including interfacial tension, adoption, wetting, and solvation.

8.1 Intrinsic Helmholtz Energy Functional

The intrinsic Helmholtz energy functional can be calculated either from the density distribution functions or from the direct correlation functions. These relations are formally exact and provide a useful starting point for developing statistical–mechanical theories of inhomogeneous fluids.

Formally, the intrinsic Helmholtz energy can be separated into an ideal part and an excess. The former is known exactly; and the latter, arising from the intermolecular interactions, can be obtained by a functional integration of the singlet direct correlation function:

$$\beta F^{\mathrm{ex}}[\rho] = \beta F^{\mathrm{ex}}[\rho_0] - \int_0^1 \mathrm{d}\lambda \int \mathrm{d}\vec{r}\Delta\rho(\vec{r})c^{(1)}(\rho_\lambda, \vec{r}), \tag{147}$$

where $\rho_0(\vec{r})$ stands for a reference density distribution, $\Delta\rho(\vec{r}) \equiv \rho(\vec{r}) - \rho_0(\vec{r})$, and $\rho_\lambda(\vec{r}) \equiv \rho_0(\vec{r}) + \lambda\Delta\rho(\vec{r})$, with $0 \leq \lambda \leq 1$ as a coupling parameter that links the density of the reference state, $\rho_0(\vec{r})$, to that of the real system, $\rho(\vec{r})$.

The one-body direct correlation function, in turn, can be expressed as a functional integration of the second-order direct correlation function:

$$c^{(1)}(\rho_\lambda, \vec{r}_1) = c^{(1)}(\rho_0, \vec{r}_1) + \int_0^\lambda \mathrm{d}\lambda' \int \mathrm{d}\vec{r}_2\Delta\rho(\vec{r}_2)c^{(2)}(\rho_{\lambda\prime}, \vec{r}_1, \vec{r}_2). \tag{148}$$

A combination of Eqs. 147 and 148 gives:

$$\begin{aligned}\beta F^{\mathrm{ex}}[\rho] = \beta F^{\mathrm{ex}}[\rho_0] &- \int \mathrm{d}\vec{r}\Delta\rho(\vec{r})c^{(1)}(\rho_0, \vec{r}) \\ &+ \int_0^1 \mathrm{d}\lambda(\lambda - 1)\int\int \mathrm{d}\vec{r}_1\mathrm{d}\vec{r}_2\Delta\rho(\vec{r}_1)\Delta\rho(\vec{r}_2)c^{(2)}(\rho_\lambda, \vec{r}_1, \vec{r}_2).\end{aligned} \tag{149}$$

Since the direct correlation functions are meaningful only for equilibrium systems, the integrations in Eq. 149 are restricted to a single phase region where the derivatives of Helmholtz energy with respect to the density profiles are well-defined.

For a uniform fluid, Eq. 149 becomes:

$$\beta F^{\mathrm{ex}}/V = \rho^2 \int_0^1 \mathrm{d}\lambda(\lambda - 1)\int \mathrm{d}\vec{r}c^{(2)}(\lambda\rho, r). \tag{150}$$

If the direct correlation function is approximated by that of a uniform system independent of the coupling parameter, Eq. 150 becomes:

$$\beta F^{\mathrm{ex}}/V \approx -\frac{\rho^2}{2}\int \mathrm{d}\vec{r}c^{(2)}(\rho, r) = -\frac{\rho^2}{2}\hat{c}(0). \tag{151}$$

Equation 151 provides a reasonable approximation of the excess Helmholtz energy for systems at low density.

For systems with a pairwise additive intermolecular potential $\Gamma(r)$, the intrinsic Helmholtz energy can also be related to the density distribution functions. At a given configuration of molecules, the total potential can be expressed as:

$$\Gamma(\vec{r}^N) = \frac{1}{2}\sum_{i\neq j}\Gamma(\vec{r}_i, \vec{r}_j) = \frac{1}{2}\sum_{i\neq j}\int\int \mathrm{d}\vec{r}_1\mathrm{d}\vec{r}_2\Gamma(\vec{r}_1, \vec{r}_2)\delta(\vec{r}_1 - \vec{r}_i)\delta(\vec{r}_2 - \vec{r}_j). \tag{152}$$

A functional derivative of $\Gamma(\vec{r}^N)$ with respect to the pair interaction potential $\Gamma(\vec{r}_1,\vec{r}_2)$ gives:

$$\frac{\delta\Gamma(\vec{r}^N)}{\delta\Gamma(\vec{r}_1,\vec{r}_2)} = \frac{1}{2}\sum_{i\neq j}\delta(\vec{r}_1-\vec{r}_i)\delta(\vec{r}_2-\vec{r}_j). \tag{153}$$

Applying a grand-canonical ensemble average to both sides of Eq. 153, we obtain:

$$\frac{\delta\Omega}{\delta\Gamma(\vec{r}_1,\vec{r}_2)} = \rho^{(2)}(\vec{r}_1,\vec{r}_2)/2. \tag{154}$$

Because the intrinsic Helmholtz energy F is related to the grand-partition function Ω by the Legendre transformation:

$$F = \Omega - \int \mathrm{d}\vec{r}\varphi(\vec{r})\rho(\vec{r}), \tag{155}$$

where $\varphi(\vec{r}) = v(\vec{r}) - \mu$ is the one-body external potential, Eq. 154 can be rewritten as:

$$\frac{\delta F}{\delta\Gamma(\vec{r}_1,\vec{r}_2)} = \rho^{(2)}(\vec{r}_1,\vec{r}_2)/2. \tag{156}$$

A functional integration of Eq. 156 gives a relation between the intrinsic Helmholtz energy and the two-body density distribution function:

$$F[\rho(\vec{r})] = F_0[\rho(\vec{r})] + \frac{1}{2}\int_0^1 \mathrm{d}\lambda \int\int \mathrm{d}\vec{r}_1\mathrm{d}\vec{r}_2\rho^{(2)}(\Gamma_\lambda,\vec{r}_1,\vec{r}_2)\Delta\Gamma(\vec{r}_1,\vec{r}_2), \tag{157}$$

where subscript "0" stands for a reference system at the system temperature but a different pairwise additive potential $\Gamma_0(\vec{r}_1,\vec{r}_2)$, $\Delta\Gamma(\vec{r}_1,\vec{r}_2) = \Gamma(\vec{r}_1,\vec{r}_2) - \Gamma_0(\vec{r}_1,\vec{r}_2)$, is called the perturbation potential, and the two-body density distribution function $\rho^{(2)}(\Gamma_\lambda,\vec{r}_1,\vec{r}_2)$ corresponds to that of the system with the pair potential:

$$\Gamma_\lambda(\vec{r}_1,\vec{r}_2) = \Gamma_0(\vec{r}_1,\vec{r}_2) + \lambda\Delta\Gamma(\vec{r}_1,\vec{r}_2) \tag{158}$$

with $0 \leq \lambda \leq 1$.

Equation 157 forms a starting point for virtually all perturbation liquid-state theories. In most practical applications, the reference potential is chosen as the short-range repulsion between molecules, and the intermolecular attraction is treated as the perturbation. The former is often further approximated by that between hard spheres:

$$\Gamma_0(\vec{r}_1,\vec{r}_2) = \begin{cases} \infty & r_{12} < \sigma \\ 0 & r_{12} \geq \sigma \end{cases}, \tag{159}$$

where $r_{12} = |\vec{r}_1 - \vec{r}_2|$ is the distance between two spherical centers, and σ stands for an effective hard-sphere diameter. The two-body density correlation function for hard spheres can be obtained from the Percus–Yevick theory [35].

The two-body density distribution function depends on both the properties of the reference fluid and on the coupling parameter λ. To decouple these two factors,

we may use a functional Taylor expansion of $\rho^{(2)}(\Gamma_\lambda,\vec{r}_1,\vec{r}_2)$ with respect to the perturbation potential $\Delta\Gamma(\vec{r}_1,\vec{r}_2)$:

$$\rho^{(2)}(\Gamma_\lambda,\vec{r}_1,\vec{r}_2)=\rho_0^{(2)}(\vec{r}_1,\vec{r}_2)+\lambda\int\int \mathrm{d}\vec{r}_3\mathrm{d}\vec{r}_4\left.\frac{\delta\rho^{(2)}(\Gamma_\lambda,\vec{r}_1,\vec{r}_2)}{\delta\lambda\Delta\Gamma(\vec{r}_3,\vec{r}_4)}\right|_{\lambda=0}\Delta\Gamma(\vec{r}_3,\vec{r}_4)$$
$$+\frac{\lambda^2}{2!}\int\int\int\int \mathrm{d}\vec{r}_3\mathrm{d}\vec{r}_4\mathrm{d}\vec{r}_5\mathrm{d}\vec{r}_6\left.\frac{\delta^2\rho^{(2)}(\Gamma_\lambda,\vec{r}_1,\vec{r}_2)}{\delta\lambda\Delta\Gamma(\vec{r}_3,\vec{r}_4)\delta\lambda\Delta\Gamma(\vec{r}_5,\vec{r}_6)}\right|_{\lambda=0}$$
$$\Delta\Gamma(\vec{r}_3,\vec{r}_4)\Delta\Gamma(\vec{r}_5,\vec{r}_6)+\cdots. \tag{160}$$

A first-order perturbation theory retains only the first term on the right side of Eq. 160; the second-order perturbation keeps the first two terms, and so forth for the higher-order perturbation theories. The convergence of the Taylor expansion depends on how close the reference intermolecular potential is to that of the real fluid, or on the difference between the structure of the reference fluid and that of the real one.

The density expansion and perturbation are two complementary methods for formulation of the intrinsic Helmholtz energy functional. In the density expansion method, the reference system is at the same temperature and chemical potential as the real system; the expansion is most efficient when the system is close to uniform or, equivalently, when there is only a weak inhomogeneity. In the perturbation method, the reference system is at the same temperature and density profile as the real system but with a different intermolecular potential and chemical potential. In general, the perturbation theory is most useful when the structure of the reference system is close to that of the real system.

8.2 Pressure Tensor

In classical thermodynamics, pressure specifies how the system energy varies in response to change in volume. Like other thermodynamic variables, pressure is defined as a scalar for uniform systems.

In classical mechanics, however, pressure refers to the force per unit area. Because both the force and the surface have directions and each entails three spatial components, a complete definition of the pressure requires a second-order tensor[10] to specify three components of the force vector with respect to three components of the surface vector.

For a uniform fluid, pressure is a scalar because the average force on a "test" surface is homogenous and isotropic, independent of the position and orientation of the test surface. For an inhomogeneous system, however, both density and pressure

[10] A second-order tensor is a linear mapping of a vector onto another vector. Here, mapping means an arbitrary arithmetic calculation. For example, the gradient of a vector is a second-order tensor, which specifies the change in this vector with respect to position.

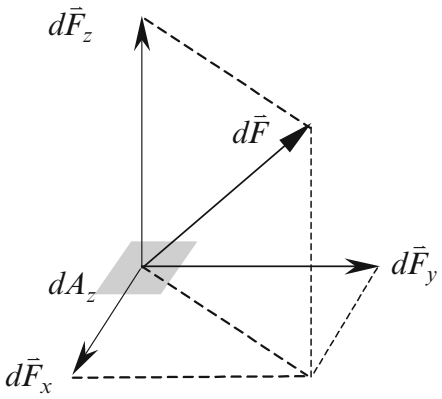

Fig. 12 Three "pressures" can be defined when a force $\mathrm{d}\vec{F}$ is applied to an infestisimal area $\mathrm{d}A_z$, the normal of which is in the z-direction: one is due to the component of the force perpendicular to the surface, and the other two from the components parallel to the surface

tensor are functions of the position. As a result, pressure must be defined as a tensor that includes nine elements, or a 3×3 matrix.

To make the ideas concrete, we consider an arbitrary force, denoted by $\mathrm{d}\vec{F}$, acting on an infinitesimal surface element $\mathrm{d}A_z$ with a normal in the direction of the z-axis. As shown in Fig. 12, the force has three components based on which we can define three scalar "pressures":

$$-\mathrm{d}F_x/\mathrm{d}A_z, -\mathrm{d}F_y/\mathrm{d}A_z, -\mathrm{d}F_z/\mathrm{d}A_z,^{11} \tag{161}$$

where $-\mathrm{d}F_x/\mathrm{d}A_z$ and $-\mathrm{d}F_y/\mathrm{d}A_z$ arise from the components of the force tangential to the surface and $-\mathrm{d}F_z/\mathrm{d}A_z$ is from that in the normal direction.

In general, of course, the normal direction of the surface is not necessarily aligned with the z-axis. For an arbitrary infinitesimal surface, as shown in Fig. 13, the surface area can be projected into three mutually perpendicular components $\mathrm{d}A_x$, $\mathrm{d}A_y$, and $\mathrm{d}A_z$. Subsequently, we can define three "scalar" pressures for each component of the surface. Because both the force and the normal direction of the surface are three-dimensional vectors, we need nine elements to completely specify the pressure. In matrix form, the pressure tensor is defined as:

$$\tilde{P} = -\begin{bmatrix} \dfrac{\mathrm{d}F_x}{\mathrm{d}A_x} & \dfrac{\mathrm{d}F_x}{\mathrm{d}A_y} & \dfrac{\mathrm{d}F_x}{\mathrm{d}A_z} \\ \dfrac{\mathrm{d}F_y}{\mathrm{d}A_x} & \dfrac{\mathrm{d}F_y}{\mathrm{d}A_y} & \dfrac{\mathrm{d}F_y}{\mathrm{d}A_z} \\ \dfrac{\mathrm{d}F_z}{\mathrm{d}A_x} & \dfrac{\mathrm{d}F_z}{\mathrm{d}A_y} & \dfrac{\mathrm{d}F_z}{\mathrm{d}A_z} \end{bmatrix}. \tag{162}$$

[11] We put a negative sign here because, according to the conventional notation, a pressure is defined as the force applied toward a surface per unit area (compression push). In Fig. 12, the force is in the outward direction of the surface (pull, tension).

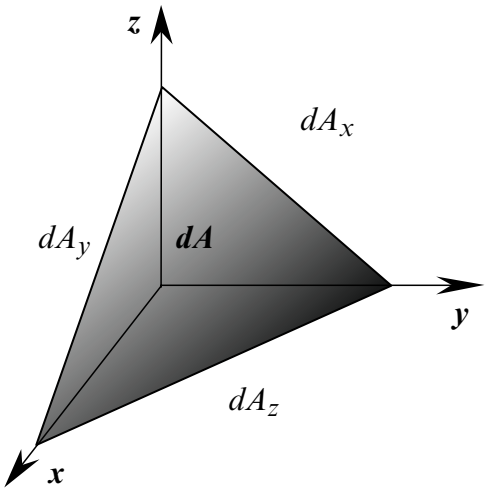

Fig. 13 An arbitrary surface element dA can be decomposed into three mutually perpendicular components dA_x, dA_y, and dA_z

The diagonal elements of the pressure tensor arise from the force components normal to the surface, and the nondiagonal elements are due to the components of the force that are parallel or tangential to the surface. A positive pressure means that the applied force is in the opposite direction to the surface normal direction.[12]

For systems with a pairwise additive intermolecular potential, the pressure tensor can be calculated from the two-body density distribution function $\rho(\vec{r}_1,\vec{r}_2)$. The equation is analogous to the virial equation for bulk fluids. To derive the connection between pressure tensor and $\rho(\vec{r}_1,\vec{r}_2)$ in an inhomogeneous system, we consider an infinitesimal surface element dA_z at position $\vec{r}$ in a one-component fluid. As shown in Fig. 14, the normal vector of dA_z is in the direction of the z-axis. The total force acting toward the normal direction of dA_z includes two contributions: one is due to the kinetic motion of molecules; and the other is due to the intermolecular interactions[13].

Let us first consider the force on dA_z due to the molecular motions. Whenever a molecule of mass m passes through a surface with a velocity v_z in the z-direction, the momentum transferred across the surface dA_z is mv_z. Figure 14 shows that the number of molecules passing through the surface dA_z in an infinitesimal time dt is proportional to the fraction of molecules with a velocity in the z-direction between v_z and $v_z + \mathrm{d}v_z$, the local density $\rho(\vec{r})$, and the volume of a cylinder traveled by the

[12] Pressure tensor is also used to describe the mechanical properties of materials, including strain, stress, and elasticity. Stress is a concept that is equivalent to pressure tensor but defined in a different perspective, $\hat{\tau} = -\hat{P}$. The diagonal elements of a stress tensor are called normal stress. While a positive normal pressure means a force pushing on a surface, a positive normal stress stands for a pulling force out of there surface, or a tension. The nondiagonal elements of a stress tensor are called shear stress.

[13] Here the force due to the external field is not included.

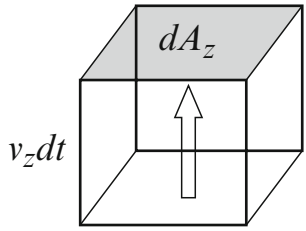

Fig. 14 In a small time $\mathrm{d}t$, the total numer of molecules with a z-directional velocity between v_z and $v_z + \mathrm{d}v_z$ impinging on infinitesimal surface element $\mathrm{d}A_z$ at position $\vec{r}$ is $\rho(\vec{r})v_z \mathrm{d}t\mathrm{d}A_z$, where $\rho(\vec{r})$ is the number density of molecules at position $\vec{r}$

molecules. The cylinder volume is $|v_z|\mathrm{d}t\mathrm{d}A_z$ and the average number of molecules within the cylinder is $\rho(\vec{r})|v_z|\mathrm{d}t\mathrm{d}A_z$.

Following the Maxwell–Boltzmann law for the velocity distribution:

$$p(v_z) = \left\{\frac{k_\mathrm{B}T}{2\pi m}\right\}^{1/2} \mathrm{e}^{-mv_z^2/(2k_\mathrm{B}T)}, \tag{163}$$

we find that the total momentum transferred through $\mathrm{d}A_z$ is:

$$\begin{aligned}\vec{M}_z &= \int_{-\infty}^{\infty} \rho(\vec{r})\,|v_z|\,\mathrm{d}t\mathrm{d}A_z \cdot mv_z p(v_z)\mathrm{d}v_z,\\ &= \rho(\vec{r})\mathrm{d}t\mathrm{d}A_z \int_{-\infty}^{\infty} mv_z^2 p(v_z)\mathrm{d}v_z,\\ &= \rho(\vec{r})k_\mathrm{B}T\,\mathrm{d}t\mathrm{d}A_z.\end{aligned} \tag{164}$$

Newton's equation indicates that the force is equal to the momentum transferred per unit time. Therefore, the kinetic component of the pressure on $\mathrm{d}A_z$, defined as the force per unit area, is:

$$\tilde{P}^K_{z,z} = k_\mathrm{B}T\rho(\vec{r}). \tag{165}$$

As expected, Eq. 165 is identical to that predicted by the ideal-gas law. Because there is no molecular crossing in the tangential directions, the molecular motion makes no contribution to the tangential pressures, i.e., $\tilde{P}^K_{x,z} = 0$ and $\tilde{P}^K_{y,z} = 0$.

For systems with a pairwise additive intermolecular potential, the force acting across the surface element $\mathrm{d}A_z$ can be decomposed into that from the pair interactions. As shown in Fig. 15, two molecules i and j exert a force on $\mathrm{d}A_z$ only if the vector $\vec{s} = \vec{r}_j - \vec{r}_i$ intersects with $\mathrm{d}A_z$. Based on the pair interactions, we can calculate the force arising from interactions of the molecules in the volume $\mathrm{d}V_i = \mathrm{d}A_z \cdot s_z \mathrm{d}\nu$ with those in the volume $\mathrm{d}V_j = \mathrm{d}\vec{s}$ where s_z is the z-component of vector $\vec{s}$ and $0 \le \nu \le 1$. The average number of molecular pairs from volume elements $\mathrm{d}V_i$ and $\mathrm{d}V_j$ is given by the two-body distribution function $\rho^{(2)}(\vec{r}_i, \vec{r}_j)$:

$$\rho^{(2)}(\vec{r}_i, \vec{r}_j)\mathrm{d}V_i\mathrm{d}V_j = \rho^{(2)}(\vec{r} - \nu\vec{s}, \vec{r} - \nu\vec{s} + \vec{s})(\mathrm{d}A_z \cdot s_z \mathrm{d}\nu) \cdot \mathrm{d}\vec{s}. \tag{166}$$

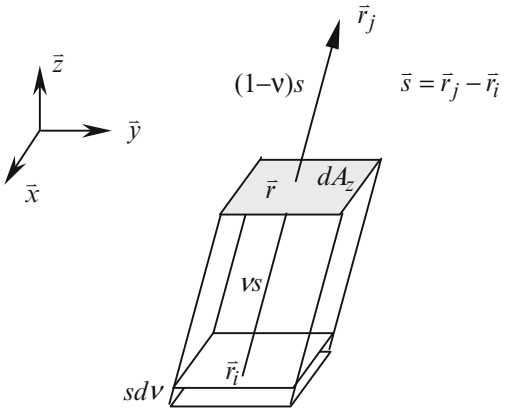

Fig. 15 Molecules at $\vec{r}_i = \vec{r} - \nu\vec{s}$ and $\vec{r}_j = \vec{r} + (1-\nu)\vec{s}$ exert a force across an infinitesimal surface $\mathrm{d}A_z$

Based on Eq. 166, we obtain the force acting across $\mathrm{d}A_z$ due to all the pair interactions from volume elements $\mathrm{d}V_i$ and $\mathrm{d}V_j$:

$$\vec{F}(s) \cdot \rho^{(2)}(\vec{r} - \alpha\vec{s}, \vec{r} - \alpha\vec{s} + \vec{s})(\mathrm{d}A_z \cdot s_z \mathrm{d}\alpha) \cdot \mathrm{d}\vec{s}, \tag{167}$$

where $\vec{F}(s)$ is the interaction force between two molecules.

The total force exerted across $\mathrm{d}A_z$ is obtained by integration of Eq. 167 over $\mathrm{d}\nu$ and $\mathrm{d}\vec{s}$, and the force per unit area defines the z-components of the pressure tensor:

$$\tilde{P}_z^{\mathrm{ex}} = -\frac{1}{2}\int \mathrm{d}\vec{s} \int_0^1 \mathrm{d}\alpha \vec{F}(s) \cdot s_z \rho^{(2)}(\vec{r} - \alpha\vec{s}, \vec{r} - \alpha\vec{s} + \vec{s}), \tag{168}$$

where 1/2 accounts for the fact that each pair interaction involves two molecules. The intermolecular force $\vec{F}(s)$ has components in both perpendicular and parallel directions of the surface. Correspondingly, the pressure tensor has components in both normal and tangential directions.

We can apply a similar procedure to analyze the force in the x- and y-directions of an arbitrary surface element. The final expression for the pressure tensor is obtained by a combination of all components in three directions:

$$\tilde{P} = \rho(\vec{r}) k_{\mathrm{B}} T \tilde{I} + \frac{1}{2}\int \mathrm{d}\vec{s} \int_0^1 \mathrm{d}\alpha \vec{F}\vec{s}\rho^{(2)}(\vec{r} - \alpha\vec{s}, \vec{r} - \alpha\vec{s} + \vec{s}), \tag{169}$$

where $\tilde{I}$ denotes the unit tensor, and $\vec{F}\,\vec{s}$ is the dyadic product:

$$\vec{F}\vec{s} = \begin{pmatrix} F_x s_x & F_x s_y & F_x s_z \\ F_y s_x & F_y s_y & F_y s_z \\ F_z s_x & F_z s_y & F_z s_z \end{pmatrix}. \tag{170}$$

Equation 169 was first derived by Irving and Kirkwood [44].

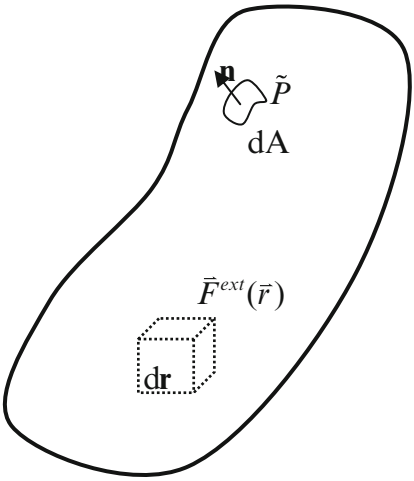

Fig. 16 The hydrostatics equation can be obtained by a force balance between the pressure at the surface and the external force. The pressure tensor contributes to the force at the system boundary and the external potential contributes to the force applied to the system volume

To find the physical significance of a pressure tensor, we consider, as shown in Fig. 16, the momentum balance for a static fluid of an arbitrary volume V and with a boundary A:

$$-\int_A \tilde{P}\cdot\vec{n}\mathrm{d}A+\int_V \rho(\vec{r})\vec{F}^{\mathrm{ext}}(\vec{r})\mathrm{d}\vec{r}=0, \tag{171}$$

where $\vec{F}^{\mathrm{ext}}(\vec{r})$ represents the external force acting on a molecule at $\vec{r}$. The first term on the left side of Eq. 171 represents the total force applied to the fluid of volume V at the boundary, and the second term is the total force due to the external field. These two forces cancel each other in a static fluid.

By applying Gauss' divergence theorem to Eq. 171, we obtain the familiar hydrostatics equation as typically introduced in fluid mechanics:

$$-\nabla\cdot\tilde{P}+\rho(\vec{r})\vec{F}^{\mathrm{ext}}(\vec{r})=0. \tag{172}$$

The hydrostatic pressure for liquid water, for example, can be simply obtained by assuming $\rho(r)$ is constant and the pressure is uniform:

$$\Delta P=\rho mgH, \tag{173}$$

where m is the molecular weight, g is the gravitational constant, and H is the elevation. Following the ideal-gas law, we can also obtain from Eq. 172 the change of molecular density in the atmosphere:

$$\rho=\rho_0\exp(-\beta mgH), \tag{174}$$

where ρ_0 is the molecular density at ground.

For a uniform fluid, the Irving–Kirkwood equation reduces to the viral equation. In that case, the number density is everywhere identical, i.e., $\rho(\vec{r}) = \rho$, and the two-body density distribution function is given by $\rho^{(2)}(\vec{r} - \nu\vec{s}, \vec{r} - \nu\vec{s} + \vec{s}) = \rho^2 g(s)$, where $g(s)$ is the radial distribution function. With these simplifications, Eq. 169 becomes:

$$\tilde{P} = \rho k_B T \tilde{I} - \frac{\rho^2}{2} \int \mathrm{d}\vec{s} \frac{\vec{s}\vec{s}}{s} g(s) \frac{\mathrm{d}\Gamma(s)}{\mathrm{d}s}. \tag{175}$$

Because both $\Gamma(s)$ and $g(s)$ depend only on the intermolecular distance, the nondiagonal elements in the pressure tensor must be zero and the three diagonal elements are the same. As a result, a scalar is sufficient to represent all information contained in the pressure tensor:

$$P = \tilde{P}_{xx} = \tilde{P}_{yy} = \tilde{P}_{zz} = \rho k_B T - \frac{\rho^2}{6} \int \mathrm{d}\vec{s}\, s g(s) \frac{\mathrm{d}\Gamma(s)}{\mathrm{d}s}. \tag{176}$$

For systems with only one-dimensional inhomogeneity, the pressure tensor can be directly used to define the normal and tangential pressures. For example, Fig. 17 shows schematically the vapor–liquid interface of a pure liquid in equilibrium with its vapor. Let the direction perpendicular to the planar interface be the z-direction of the coordinate system. Because of the symmetry in the x- and y-directions, the Irving–Kirkwood equation indicates that only the diagonal elements of the pressure tensor are nonzero.

In the absence of an external field, $\vec{F}^{\mathrm{ext}}(\vec{r}) = 0$, the hydrostatic equation becomes:

$$\nabla \cdot \hat{P} = 0 \tag{177}$$

or equivalently:

$$\frac{\partial P_{xx}}{\partial x} = \frac{\partial P_{yy}}{\partial y} = \frac{\partial P_{zz}}{\partial z} = 0. \tag{178}$$

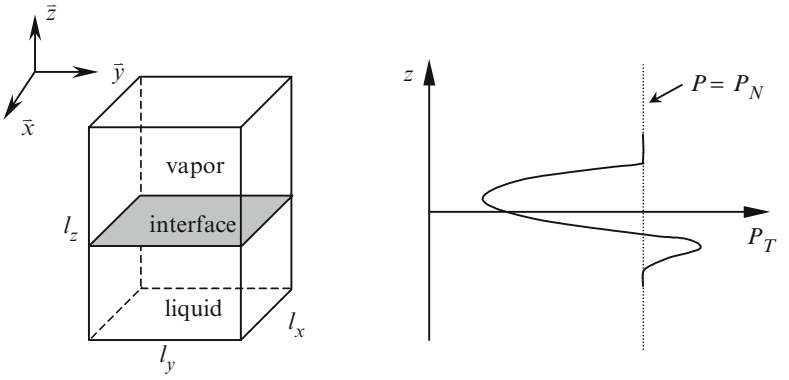

Fig. 17 In a liquid–vapor system with a planar interface, the normal pressure P_N is the same everywhere (left), but the tangential pressure P_T is a function of the coordinate z perpendicular to the interface (right)

The symmetry in the x- and y-directions implies that the two-body density correlation function $\rho^{(2)}(\vec{r}_i,\, \vec{r}_j)$ depends only on z_i and z_j and on the separation, $\left|\vec{r}_i - \vec{r}_j\right|$:

$$\rho^{(2)}(\vec{r} - \nu\vec{s},\, \vec{r} - \nu\vec{s} + \vec{s}) = \rho^{(2)}(z - \nu s_z,\, z - \nu s_z,\, s). \tag{179}$$

Substitute Eq. 179 into 169:

$$P_{\mathrm{T}}(z) \equiv P_{xx} = P_{yy} = \rho(z)k_{\mathrm{B}}T - \frac{1}{2}\int \mathrm{d}\vec{s}\int_0^1 \mathrm{d}\nu \frac{s_x^2}{s}\frac{\partial\Gamma(s)}{\partial s}\rho^{(2)}(z - \nu s_z, z - \nu s_z + s_z, s), \tag{180}$$

$$P_N \equiv P_{zz} = \rho(z)k_{\mathrm{B}}T - \frac{1}{2}\int \mathrm{d}\vec{s}\int_0^1 \mathrm{d}\nu \frac{s_z^2}{s}\frac{\partial\Gamma(s)}{\partial s}\rho^{(2)}(z - \nu s_z, z - \nu s_z + s_z, s), \tag{181}$$

where $P_{\mathrm{T}}(z)$ defines the tangential pressure, i.e., a pressure on a surface that exerts force in the parallel direction; and P_{N} is the normal pressure, i.e., a pressure on a surface that exerts force in the perpendicular direction. Because the normal pressure is independent of z (Eq. 178), it must be uniform across the interface and equal to the bulk pressure. Understanding the difference in normal and tangential pressure provides a good starting point for studying surface properties, especially surface tension.

8.3 Surface Tension

To find the connection between surface tension and the tangential and normal pressures at a planar interface, we consider that a liquid coexists with its saturated vapor, as shown in Fig. 18. The rectangular box has the dimensions of $l_x \times l_y \times l_z$ where the coordinate z is assigned perpendicular to the interface. Imagine that there exists a small opening and a piston located on the vapor side far away from the interface, and that there exists a movable wall and another piston on the opposite side spanning the vapor–liquid interface. The pressure on piston 1 is equal to the saturation pressure P, which is the same in both vapor and liquid phases and equal to the normal pressure P_{N}. Because of the density inhomogeneity at the interface, the pressure on the movable wall depends on the distance from the interface. This pressure is represented by the tangential pressure $P_{\mathrm{T}}(z)$.

We now consider a reversible process where piston 1 on the open side and piston 2 on the movable wall are displaced simultaneously such that the total volume of the system is unchanged. The reversible work includes two opposite contributions, one from piston 1 and the other from piston 2:

$$\mathrm{d}W = -P\mathrm{d}V + l_x\mathrm{d}y \cdot \int P_{\mathrm{T}}(z)\mathrm{d}z = -\mathrm{d}A\int [P - P_{\mathrm{T}}(z)]\,\mathrm{d}z, \tag{182}$$

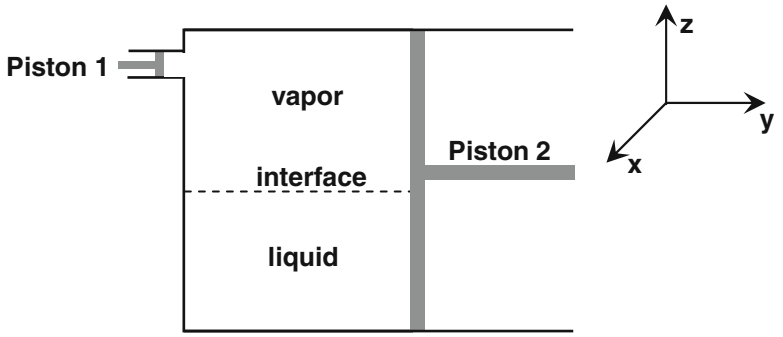

Fig. 18 An imaginary experiment may be performed to relate the surface tension of a vapor–liquid interface to the tangential pressure, i.e., the component of the pressure tensor that is parallel to the planar vapor–liquid interface (see text for discussion)

where $\mathrm{d}V = l_x l_z \mathrm{d}y = \int l_x \mathrm{d}z\mathrm{d}y$ is the displacement volume, and $\mathrm{d}A = l_x \mathrm{d}y$ is the change in interfacial area. The integration limits in Eq. 182 are over the liquid–vapor interface where $[P - P_{\mathrm{T}}(z)]$ is nonzero. At constant temperature, volume, and total number of molecules, this reversible work is equal to the change in the Helmholtz energy $\mathrm{d}F = -\mathrm{d}W$, which in turn, is related to surface tension γ:

$$\mathrm{d}F = -\mathrm{d}W = \gamma \mathrm{d}A. \tag{183}$$

Substituting of Eq. 183 into 182 gives:

$$\gamma = \int [P - P_{\mathrm{T}}(z)]\mathrm{d}z. \tag{184}$$

Equation 184 indicates that the surface tension arises from the difference in the normal and tangential pressures across the interface.

8.4 Contact Value Theorem

The contact value theorem connects the pressure of a fluid in contact with a solid surface to the contact molecular density and to the surface potential. It is an exact relationship, useful for studying the energy of solvation and solvation forces.

We can derive the contact value theorem by integration of the hydrostatics equation given in Eq. 172. For example, near a planar wall located at $z = 0$, the solvent pressure is zero for $z < 0$ and is equal to the bulk pressure P far from the surface. Integration of the normal component of the pressure tensor (i.e., in the z-direction) gives:

$$P = -\int \mathrm{d}z \rho(z) v'(z), \tag{185}$$

where $v'(z) = -\mathrm{d}v(z)/\mathrm{d}z$ represents the surface force in the perpendicular direction. Equation 185 represents the most general form of the contact-value theorem for a planar surface.

Near a hard wall, the external potential is given by:

$$v(z) = \begin{cases} \infty & z < 0 \\ 0 & z \geq 0 \end{cases}, \tag{186}$$

and $\exp[-\beta v(z)]$ is a Heaviside step function. As a result, the surface force becomes:

$$v'(z) = -\beta^{-1} \frac{\mathrm{d}\exp[-\beta v(z)]}{\mathrm{d}z} = -\beta^{-1}\delta(z), \tag{187}$$

where $\delta(z)$ stands for the Dirac delta function. Substituting of Eq. 187 into 185 gives:

$$P = k_{\mathrm{B}} T \rho(0). \tag{188}$$

Alternatively, we can obtain Eq. 188 directly from the Irving–Kirkwood theory, which indicates that the momentum transfer to a flat hard wall at $z = 0$ is equal to the contact value of the solvent density $\rho(0)$ multiplied by $k_{\mathrm{B}}T$. Because solvent molecules exist only on one side of the wall, the intermolecular potential makes no direct contribution to the surface pressure.

Figure 19 shows, for example, the surface pressure as a function of the separation between two parallel hard walls filled with hard spheres in equilibrium with a bulk fluid with the reduced density equal to $\rho_{\mathrm{b}}\sigma^3 = 0.7$. When the separation is infinite, the hard spheres are in contact with a single wall. In that case, the wall pressure is identical to the bulk pressure.

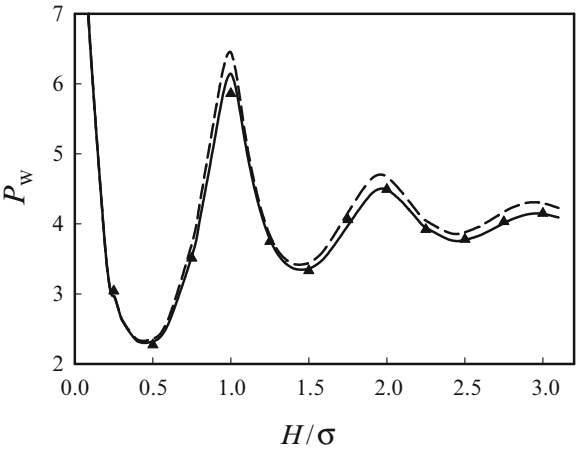

Fig. 19 Surface pressure as a function of the separation between two parallel hard walls filled with hard spheres with the reduced density $\rho_{\mathrm{b}}\sigma^3 = 0.7$ in the bulk. The *points* are from Monte Carlo simulation and the *lines* are predicted from DFT [45]

For a planar hard wall with an additional long-range potential $v_a(z)$, the contact value theorem becomes [46]:

$$P = \rho(0)k_BT - \int dz\rho(z)v_a'(z). \tag{189}$$

If the wall has a surface charge density Q, the surface force of counterions of charge q is:

$$-v_a'(z) = \frac{2\pi qQ}{\varepsilon_D}, \tag{190}$$

where ε_D is the dielectric constant, which is assumed to be identical on both sides of the wall. Because of the charge neutrality:

$$Q + \int dz\rho(z)\,q = 0. \tag{191}$$

Substitution of Eq. 190 into 189 gives:

$$P = \rho(0)k_BT - \frac{2\pi Q^2}{\varepsilon_D}. \tag{192}$$

Whereas for simplicity we consider only counterions near the wall, the second term on the right side of Eq. 192 is valid at arbitrary ionic conditions.

8.5 Solvation Force and Potential of Mean Force

The solvation force refers to the interaction between two (or multiple) solute molecules or solid particles in a solvent. It is a quantity often of concern for understanding solubility or colloidal stability.

When the solute particles are much larger than the solvent molecules, the solvation force can be approximated by that between two parallel walls. The solvation force *per unit area* is related to the differential of the grand potential with respect to the wall separation H:

$$\vec{F}(H)/A = -\left(\frac{\partial\Omega/A}{\partial H}\right)_{T,\mu} - P, \tag{193}$$

where P is the bulk pressure. Equation 193 satisfies the boundary condition $\vec{F}(H = \infty) = 0$. Integration of the solvation force with respect to H gives the change in grand potential or, equivalently, the reversible work for moving the two particles. This reversible work is often referred to as the potential of mean force.

For systems with only one-dimensional inhomogeneity, the density profile $\rho(z)$ is given by a functional derivative of the grand potential with respect to the one-body

potential $\varphi(z) = \nu(z) - \mu$. In terms of the density profile $\rho(z)$, the solvation force is given by:

$$\begin{aligned}\vec{F}(H)/A &= -\left(\frac{\partial \Omega/A}{\partial H}\right)_{T,\mu} - P, \\ &= -\frac{1}{A}\int_0^H \mathrm{d}z \frac{\delta\Omega}{\delta\varphi(z)}\frac{\partial\varphi(z)}{\partial z} - P, \\ &= -\int_0^H \mathrm{d}z \rho(z)\frac{\partial\varphi(z)}{\partial z} - P, \\ &= -\int_0^H \mathrm{d}z \rho(z)\frac{\partial\nu(z)}{\partial z} - P.\end{aligned} \tag{194}$$

Equation 194 is expected because when $H = \infty$, the contact value theorem (Eq. 185) ensures that the solvation force is zero.

If the size of solute particles is comparable to that of the solvent molecules, the connection between the macroscopic pressure and the solvation force becomes slightly more complicated. If the particles are spherical, the solvation force depends only on the center-to-center distance. In that case, it can be calculated from the radial distribution function $g(r)$:

$$\vec{F}(r) = \beta^{-1}\nabla \ln[g(r)]. \tag{195}$$

To derive the above equation, we consider two solute particles fixed at positions $\vec{r}_1$ and $\vec{r}_2$ surrounded by solvent molecules and other solute particles. At a given molecular configuration, the net force between the these two tagged particles is given by the gradient of total potential energy Γ:

$$\vec{F}_v(r) = -\nabla\Gamma(\vec{r}^N), \tag{196}$$

where $r = |\vec{r}_1 - \vec{r}_2|$ is the separation between two particles, and the total potential Γ includes contributions from all solvent and solute interactions. The ensemble average of Eq. 196 gives:

$$\begin{aligned}\vec{F}(r) &= -\frac{\int \mathrm{d}\vec{r}^N \nabla\Gamma \mathrm{e}^{-\beta\Gamma}}{\int \mathrm{d}\vec{r}^N \mathrm{e}^{-\beta\Gamma}} = \beta^{-1}\frac{\nabla\int \mathrm{d}\vec{r}^N \mathrm{e}^{-\beta\Gamma}}{\int \mathrm{d}\vec{r}^N \mathrm{e}^{-\beta\Gamma}}, \\ &= \beta^{-1}\nabla \ln \int \mathrm{d}\vec{r}^N \mathrm{e}^{-\beta\Gamma} = \beta^{-1}\nabla\ln[\rho(\vec{r}_1, \vec{r}_2)],\end{aligned} \tag{197}$$

where $\mathrm{d}\vec{r}^N$ stands for an integration over the position of all free molecules, and the two-body density distribution function is given by

$$\rho(\vec{r}_1, \vec{r}_2) = \frac{\int \mathrm{d}\vec{r}^{N+2} \mathrm{e}^{-\beta\Gamma}\delta(\vec{r}_1 - \vec{r}')\delta(\vec{r}_2 - \vec{r}'')}{\int \mathrm{d}\vec{r}^{N+2}\mathrm{e}^{-\beta\Gamma}} \tag{198}$$

with $\mathrm{d}\vec{r}^{N+2} = \mathrm{d}\vec{r}^N \mathrm{d}\vec{r}'\mathrm{d}\vec{r}''$.

At a finite concentration of solute particles, the two-body density distribution function can be replaced by the radial distribution function $g(r)$. Following Eq. 195, we can obtain a simple expression for the potential of mean force between two spherical particles:

$$W(r) = -\beta^{-1} \ln g(r). \tag{199}$$

Because the radial distribution function approaches unity at large values of r, the potential of mean force vanishes when two the two particles are infinitely apart.

8.6 Potential Distribution Theorem

The potential distribution theorem (PDT) provides a simple way to calculate the potential of mean force between solute particles. It is convenient for practical applications, in particular by combination with a DFT method [47]. PDT is formally exact and can be easily derived from the connection between the singlet direct correlation function and the effective one-body potential.

According to PDT, the potential of mean force between two particles (exclude the direct interaction) is given by:

$$\beta W(r) = c^{(1)}(\infty) - c^{(1)}(r), \tag{200}$$

where $c^{(1)}(r)$ is the singlet direct correlation function of the particle in the inhomogeneous system of the solvent molecules with the other particle fixed at the origin. Following its definition, we can calculate $c^{(1)}(r)$ from the functional derivative of the excess Helmholtz energy functional for the particle–solvent mixture and from the density profile of solvent molecules around a single particle.

We can understand the PDT on the base of the physical significance of $c^{(1)}(r)$. The reversible work to bring two particles together is equivalent to the difference in the work to insert one particle near another fixed at the origin from the work without the fixed particle. Because the reversible work to insert a particle can be conveniently calculated from the excess Helmholtz energy, PDT allows us to predict the potential of mean force between two particles without evoking the anisotropic distribution of solvent molecules.

Figure 20 shows the potential of mean force between two large hard spheres in a solvent of smaller hard spheres. This system provides a simplistic representation of colloids (large particles) dispersed in a solution of polymers (small spheres) in a good solvent. Here the lines are calculated from PDT and the symbols are from molecular simulations [48]. The slight difference between theory and simulation is due to the approximations introduced in calculation of the direct correlation functions.

PDT is applicable to the potential of mean force between identical particles as well as to that between a particle and a surface. Figure 21 shows, for example, the depletion potential (i.e., the potential of mean force due to depletion) of a single big hard sphere inside or outside of a hard spherical cavity immersed in a fluid of small

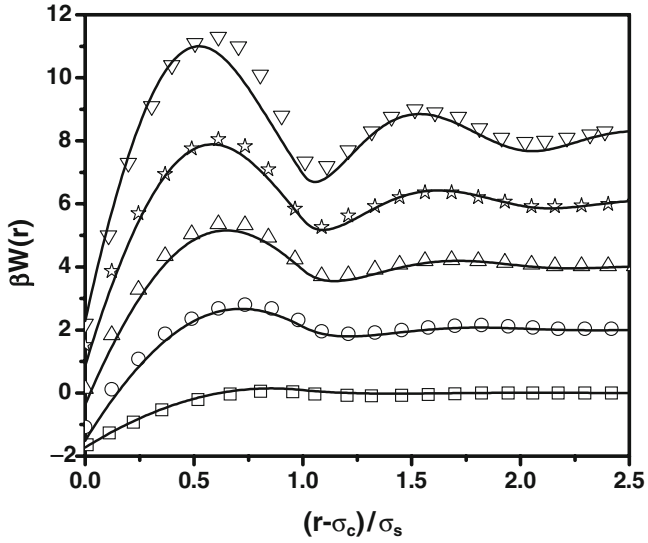

Fig. 20 Reduced depletion potential between two big hard spheres in a solution of small hard spheres with $\sigma_c/\sigma_s = 10$. Here σ_c stands for the diameter of big spheres and σ_s corresponds to that for small sphere. From *bottom to top*, the five *curves* correspond to reduced bulk density $\rho^*_{s,b} = 0.2, 0.4, 0.5, 0.6$, and 0.7. For clarity, the results for $\rho^*_{s,b} = 0.4$, 0.5, 0.6, and 0.7 have been consecutively shifted upward by 2. *Lines* are PDT predictions and *symbols* are simulation results from [48]

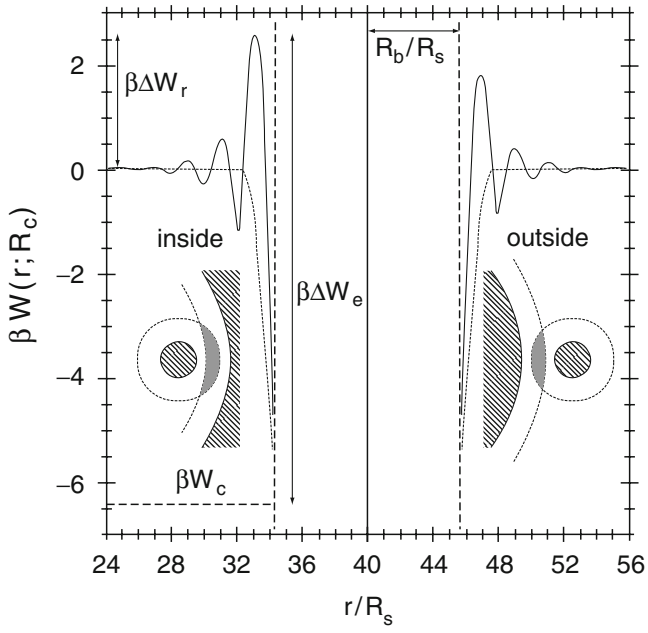

Fig. 21 Depletion potential of a sphere with radius $R_b = 5.7R_s$ inside and outside of a spherical cavity with radius $R_c = 40R_s$ immersed in a hard-sphere solvent with radius R_s and packing density $\eta = 0.3$ [49]. The *dashed lines* show areas not accessible to solvent molecules; an overlap of these areas (*shaded*) leads to an entropic attraction

hard spheres [49]. The system mimics the interactions of macromolecules with a cell membrane. The DFT predicts the potential barrier near the surface arising from the correlation effects of the solvent molecules. The presence of this potential barrier may have pronounced repercussions for the diffusion dynamics of biomacromolecules across the cell membrane.

9 Excess Helmholtz Energy Functionals

Density functional theory (DFT) provides an exact mathematical framework for predicting fluid structure and thermodynamic properties. However, it does not prescribe a generic procedure for formulation of the intrinsic Helmholtz energy as a functional of the molecular density profiles. Development of the thermodynamic functionals is a task essentially equivalent to solving the statistical mechanical problem for the particular system under consideration. The value of DFT is reflected in its efficiency for analyzing thermodynamic properties directly in terms of the molecular density profile, i.e., in the context of the microscopic structure. Towards that end, DFT can be regarded as an extension of classical thermodynamics where the scalar thermodynamic functions are replaced by thermodynamic functionals.

As in applications of classical thermodynamics, the intrinsic Helmholtz energy functional of a nonideal system is conventionally divided into an ideal-gas part and an excess. While the ideal-gas part is known exactly, the excess intrinsic Helmholtz energy is typically formulated on the basis of mathematical expansions in combination with insightful analysis of the physical phenomena under consideration. Because the intermolecular interactions are often expressed in terms of the short-range repulsion, van der Waals attraction, electrostatic forces, electron donor–acceptor interactions, and hydrogen bonding, each component of the intermolecular potential makes a distinct (but not necessarily independent) contribution to the excess intrinsic Helmholtz energy. The approximations introduced in developing these excess intrinsic Helmholtz energy functionals underlie different versions of DFT.

9.1 Intrinsic Helmholtz Energy Functional of an Ideal Gas

We can analytically evaluate the partition function of an ideal-gas system under arbitrary conditions, from which we can formulate the intrinsic Helmholtz energy as a functional of the density profile. In a one-component open system of spherical particles, the grand partition function is given by:

$$\Xi^{\mathrm{id}} = \sum_{N=0}^{\infty} \frac{1}{N!\Lambda^{3N}} \int \mathrm{d}\vec{r}^{N} \mathrm{e}^{-\beta \sum_{i=1}^{N} [v(\vec{r}_i)-\mu]} = \sum_{N=0}^{\infty} \frac{\varpi^N}{N!\Lambda^{3N}} = \exp(\varpi/\Lambda^3), \qquad (201)$$

where $\varpi \equiv \int \mathrm{d}\vec{r}\mathrm{e}^{-\beta[v(\vec{r})-\mu]}$. Correspondingly, the grand potential is:

$$\beta\Omega^{\mathrm{id}} = -\ln\Xi^{\mathrm{id}} = -q/\Lambda^3 = -\int \mathrm{d}\vec{r}\mathrm{e}^{-\beta[v(\vec{r})-\mu]}/\Lambda^3. \tag{202}$$

To find the equilibrium density profile, we note that the energy due to the external potential $v(\vec{r})$ can be expressed as:

$$-\beta\sum_{i=1}^{N}[v(\vec{r}_i)-\mu] = -\int \mathrm{d}\vec{r}\hat{\rho}(\vec{r})\beta\varphi(\vec{r}), \tag{203}$$

where $\hat{\rho}(\vec{r}) = \sum_{i=1}^{N}\delta(\vec{r}-\vec{r}_i)$ is the instantaneous density, and $\varphi(\vec{r}) = v(\vec{r})-\mu$. The equilibrium density profile is thus given by:

$$\rho(\vec{r}) = \langle\hat{\rho}(\vec{r})\rangle = -\frac{\delta\ln\Xi}{\delta\beta\varphi(\vec{r})} = \frac{\delta\int \mathrm{d}\vec{r}\mathrm{e}^{-\beta\varphi(\vec{r})}/\Lambda^3}{\delta\beta\varphi(\vec{r})} = \mathrm{e}^{-\beta\varphi(\vec{r})}/\Lambda^3. \tag{204}$$

Substitution of Eq. 204 into 202 yields:

$$\beta\Omega^{\mathrm{id}} = -\int \mathrm{d}\vec{r}\mathrm{e}^{-\beta\varphi(\vec{r})}/\Lambda^3 = -\int \mathrm{d}\vec{r}\rho(\vec{r}). \tag{205}$$

Equation 205 represents as a generalized ideal-gas law for an inhomogeneous system.

From the grand potential, the intrinsic Helmholtz energy functional is given by:

$$\begin{aligned}\beta F^{\mathrm{id}} &= \beta\Omega^{\mathrm{id}} - \int \mathrm{d}\vec{r}\rho(\vec{r})\beta\varphi(\vec{r}),\\ &= -\int \mathrm{d}\vec{r}\rho(\vec{r}) + \int \mathrm{d}\vec{r}\rho(\vec{r})\ln[\rho(\vec{r})\Lambda^3],\\ &= \int \mathrm{d}\vec{r}\rho(\vec{r})[\ln\rho(\vec{r})\Lambda^3 - 1].\end{aligned} \tag{206}$$

Equation 206 suggests that for an ideal-gas system, the thermodynamic variables depend only on the local density. In other words, the local density approximation (LDA) becomes exact for an ideal-gas system.

9.2 Short-Range Repulsion

In a typical semi-empirical force field, the short-range repulsion between molecules can be represented by an effective the hard-sphere model, which assumes that each particle has a physical volume prohibiting an overlap with other spheres. Such an excluded-volume effect plays a pivotal role in determining the structure and thermodynamic properties of any condensed materials.

Because of its theoretical importance, a number of different versions of DFT have been published for representing the structure and thermodynamic properties of hard spheres [50]. Among them, the fundamental-measure theory (FMT), first proposed by Rosenfeld [51], bears some special merits. First, this geometry-based DFT is built on firm physical and mathematical foundations rather than on empirical approximations. Unlike alternative versions of DFT that rely on the structure of a bulk reference system and weighted density approximations, FMT does not require the bulk properties as the input; instead, it can be reduced to an accurate theory of bulk fluids as an output. Theoretically, FMT provides an exact dimensional crossover, i.e., it is equally applicable to bulk systems (3D), hard spheres confined between surfaces (2D), in a cylindrical pore (1D), and in a cavity (0D) [52]. It is a self-consistent theory directly applicable to one-component and polydisperse mixtures, fluid and solid phases, and systems consisting of nonspherical particles including liquid crystals [53]. From a practical point of view, it performs well at all densities, particularly at high densities where alternative methods may fail. Most importantly, FMT is computationally as efficient as simple versions of DFT.

A number of modifications of FMT have been proposed since it was first published in 1989 [50, 53]. The accuracy of the original FMT is similar to that of scaled-particle theory or Percus–Yevick (PY) theory for uniform hard spheres. Its numerical performance can be further improved by utilizing the equation of state for bulk hard-sphere fluids by Boublik [54], and independently by Mansoori, Carnahan, Starling, and Leland (BMCSL) [55]. According to this version of FMT [45, 56], the excess Helmholtz energy functional is given by:

$$\begin{aligned}\beta F_{\rm hs}^{\rm ex} = \int {\rm d}\vec{r} \Bigg\{ & -n_0 \ln(1-n_3) + \frac{n_1 n_2 - \vec{n}_{V1}\vec{n}_{V2}}{1-n_3} \\ & + \frac{1}{36\pi}\left[n_3 \ln(1-n_3) + \frac{n_3^2}{(1-n_3)^2} \right] \frac{(n_2^3 - 3n_2 \vec{n}_{V2}\vec{n}_{V2})}{n_3^3} \Bigg\},\end{aligned} \tag{207}$$

where $\{n_\alpha\}$ stand for weighted densities defined as:

$$n_\alpha(\vec{r}) = \int \rho(\vec{r}\,') w^{(\alpha)}(\vec{r} - \vec{r}\,') {\rm d}\vec{r}\,'. \tag{208}$$

The weight functions $w^{(\alpha)}(\vec{r})$ characterize the geometry of a hard sphere: two scalar functions are related to, respectively, the volume and the surface area:

$$w^{(3)}(\vec{r}) = \theta(\sigma/2 - r), \tag{209}$$

$$w^{(2)}(\vec{r}) = \delta(\sigma/2 - r), \tag{210}$$

and a surface vector function characterizes the variance across the particle surface:

$$\vec{w}^{(V2)}(\vec{r}\,') = (\vec{r}\,'/r)\delta(\sigma/2 - r). \tag{211}$$

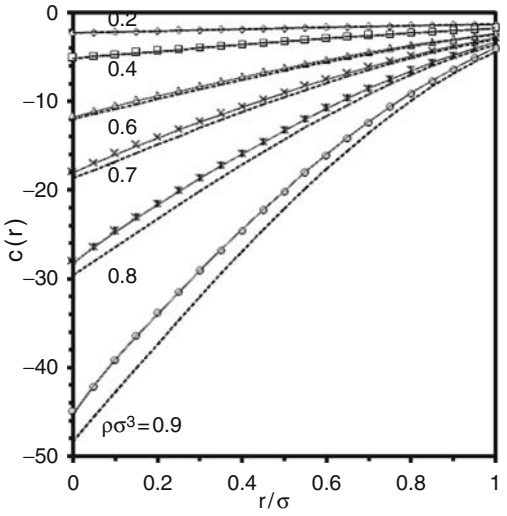

Fig. 22 Direct correlation functions for uniform hard-sphere fluids at different reduced densities. The *solid lines* are from the modified FMT, the *dashed lines* are from the PY theory, and the *symbols* are from simulation [45]

Three additional weight functions are given by:

$$w^{(1)}(\vec{r}) = w^{(2)}(\vec{r})/(2\pi\sigma)\, w^{(0)}(\vec{r}) = w^{(2)}(\vec{r})/(\pi\sigma^2)\, \vec{w}^{(V1)}(\vec{r}) = \vec{w}^{(V2)}(\vec{r})/(2\pi\sigma). \tag{212}$$

In Eqs. 209–212, σ is the hard-sphere diameter, $\delta(r)$ is the Dirac delta function, and $\theta(r)$ is the Heaviside step function. The vector-weighted densities, $\vec{n}_{V1}$ and $\vec{n}_{V2}$, vanish in the limit of a bulk fluid. For a uniform fluid, the vector-weighted densities disappear. In that case, Eq. 207 reduces to the excess Helmholtz energy from the BMCSL equation of state.

While the modified FMT preserves the advantages of the original theory, it improves the numerical performance, in particular, for highly asymmetric hard-sphere systems. For example, Fig. 22 compares the direct correlation functions calculated from the modified FMT with those from Monte Carlo (MC) simulation for a uniform hard-sphere fluid at different reduced densities [57]. The modified FMT is more accurate than the PY theory for all densities. In addition, the modified FMT predicts the radial distribution functions in good agreement with the simulation results. By contrast, the PY theory underestimates the contact values of the radial distribution functions. The FMT has also been generalized to lattice models [58], and to systems with soft and/or nonadditive potentials [59].

9.3 Van der Waals Attraction

Many practical versions of DFT take a mean-field method to account for the contribution of van der Waals attraction to the excess Helmholtz energy functional. As in van der Waals' equation of state, the mean-field theory separates the thermodynamic nonideality from contributions due to the attractive and repulsive components of the intermolecular potential, and neglects the effect of intermolecular correlations.

In van der Waals' square-gradient theory, for example, the repulsive part is represented by that of a hard-sphere reference system in terms of the local-density approximation (LDA):

$$F_0[\rho] = F_{\rm hs}[\rho] \approx \int {\rm d}\vec{r} f_{\rm hs}(\rho), \tag{213}$$

where $f_{\rm hs}(\rho)$ is the Helmholtz energy density of a uniform hard-sphere fluid at density $\rho(\vec{r})$. The LDA ignores the short-range intermolecular correlations.

With the mean-field approximation, the two-body density-distribution function in the perturbation expansion of the Helmholtz energy functional (Eq. 157) is simply given by:

$$\rho^{(2)}(\Gamma_\lambda;\vec{r}_1,\vec{r}_2) \approx \rho(\vec{r}_1)\rho(\vec{r}_2). \tag{214}$$

As a result, the excess intrinsic Helmholtz energy functional becomes:

$$F^{\rm ex}(\rho) = \int {\rm d}\vec{r} f_{\rm hs}(\rho) + \frac{1}{2}\int\int {\rm d}\vec{r}_1 {\rm d}\vec{r}_2 \rho(\vec{r}_1)\rho(\vec{r}_2)\Gamma_A(\vec{r}_1,\vec{r}_2). \tag{215}$$

Accordingly, the Euler–Lagrange equation is given by:

$$\mu = \nu(\vec{r}) + \mu_{\rm hs}[\rho(\vec{r})] + \int {\rm d}\vec{r}'\rho(\vec{r}')\Gamma_A(\vec{r},\vec{r}'). \tag{216}$$

Given a chemical potential μ and an external field $\nu(\vec{r})$, we can calculate the equilibrium density profile $\rho(\vec{r})$ by solving Eq. 216. From$\rho(\vec{r})$, we can further calculate all pertinent thermodynamic properties.

The mean-field intrinsic Helmholtz energy function yields a direct correlation function:

$$c^{(2)}(\vec{r}_1,\vec{r}_2) = \left[-\beta f''_{\rm hs}(\rho) + \frac{1}{\rho(\vec{r}_1)}\right]\delta(\vec{r}_1-\vec{r}_2) - \beta\Gamma_A(r_{12}), \tag{217}$$

where the double prime denotes the second derivative with respect to the density. While Eq. 217 gives the correct asymptotic behavior as $r_{12}\to\infty$, it yields an unphysical Dirac-δ function at short separation. This caveat can be avoided by incorporating short-range correlations in the reference system.

In general, the mean-field theory gives fair predictions of vapor–liquid interfacial properties, adsorption isotherms, wetting, and phase transitions in confined fluids [60]. However, they are at most semiquantitative, as one would anticipate from the van der Waals equation of state. To surmount the numerical deficiencies of the

mean-field approximation, a number of theoretical improvements and ad hoc empirical corrections have been proposed [61]. A simple yet efficient way toward the improvement is by using a quadratic density expansion of the excess Helmholtz energy functional relative to that for a uniform fluid [62]:

$$F_A^{\mathrm{ex}} = F_A^{\mathrm{ex}}(\rho^0) + \mu_A^{\mathrm{ex}} \int \mathrm{d}\vec{r}\Delta\rho(\vec{r}) - \frac{k_\mathrm{B}T}{2}\int\int \mathrm{d}\vec{r}\mathrm{d}\vec{r}' c_A(\left|\vec{r}-\vec{r}'\right|)\Delta\rho(\vec{r})\Delta\rho(\vec{r}'), \quad (218)$$

where $F_A^{\mathrm{ex}}(\rho^0)$ is the attractive part of the excess Helmholtz energy of the reference bulk fluid with density ρ^0. This "semiquadratic" approach requires the excess chemical potential μ_A^{ex} and the direct correlation function $c_A(r)$ of a uniform atomic fluid as input. Towards that end, the analytical correlation functions derived from the first-order mean-spherical approximation (FMSA) are particularly useful [63].

The long-range part of an intermolecular potential can be expressed in form of the double-Yukawa function:

$$\Gamma_A(r) = -\varepsilon_1 \mathrm{e}^{-\kappa 1(r-\sigma)}/r + \varepsilon_2 \mathrm{e}^{-\kappa_2(r-\sigma)}/r, \quad r > \sigma, \quad (219)$$

where $\varepsilon_{\alpha=1,2}$ and $\kappa_{\alpha=1,2}$ are energy and range parameters, respectively. Equation 219 is convenient to represent either the long-range repulsion or attraction between molecules. For example, it can be mapped to the Lennard-Jones (LJ) potential by letting the parameters relate to σ_{LJ} and $\varepsilon_{\mathrm{LJ}}$:

$$\sigma = \frac{1+0.2977T^*}{1+0.33163T^*+1.047710^{-3}T^{*2}}\sigma_{\mathrm{LJ}},\ T^* = k_\mathrm{B}T/\varepsilon_{\mathrm{LJ}}, \quad (220)$$

$$\varepsilon_1 = k_0\varepsilon_{\mathrm{LJ}}\mathrm{e}^{\kappa_1(\sigma_{\mathrm{LJ}}-\sigma)},\ \varepsilon_2 = k_0\varepsilon_{\mathrm{LJ}}\mathrm{e}^{\kappa_2(\sigma_{\mathrm{LJ}}-\sigma)}, \quad (221)$$

$$k_0 = 2.1714\sigma_{\mathrm{LJ}},\ \kappa_1 = 2.9637/\sigma \text{and}\ \kappa_2 = 14.0167/\sigma. \quad (222)$$

According to FMSA, the direct correlation function due to long-range interactions is given by:

$$c_\mathrm{A}(r) = c_{\mathrm{FMSA}}(T_1^*, \kappa_1\sigma, r/\sigma) - c_{\mathrm{FMSA}}(T_2^*, \kappa_2\sigma, r/\sigma), \quad (223)$$

where $T_1^* = T^*\sigma\varepsilon_{\mathrm{LJ}}/\varepsilon_1$, $T_2^* = T^*\sigma\varepsilon_{\mathrm{LJ}}/\varepsilon_2$, and:

$$rc_{\mathrm{FMSA}}(T^*,z,r) = \begin{cases} \dfrac{\mathrm{e}^{-\kappa(r-1)}}{T^*}, & r > 1 \\ \dfrac{\mathrm{e}^{-\kappa(r-1)}}{T^*} - \dfrac{1}{(1-\eta)^4\kappa^6 Q_0{}^2(\kappa)T^*}\times & \\ \left\{\begin{array}{l} S_0^2(\kappa)\mathrm{e}^{-\kappa(r-1)} + 144\eta^2 L_0^2(\kappa)\mathrm{e}^{\kappa(r-1)} \\ -12\eta^2\left[(1+2\eta)^2\kappa^4 + (1-\eta)(1+2\eta)\kappa^5\right]r^4 \\ +12\eta\left[S_0(\kappa)L_0(\kappa)\kappa^2 - (1-\eta)^2(1+\eta/2)\kappa^6\right]r^2 \\ -24\eta\left[(1+2\eta)^2\kappa^4 + (1-\eta)(1+2\eta)\kappa^5\right]r + 24\eta S_0(\kappa)L_0(\kappa) \end{array}\right\}, & r \le 1 \end{cases} \quad (224)$$

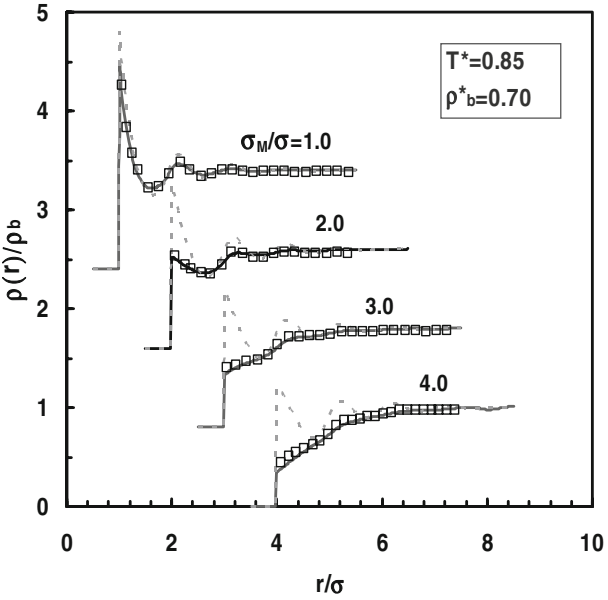

Fig. 23 Density profiles of a Lennard-Jones fluid around colloid particles of different diameters (σ_M). Here ρ_b stands for the bulk concentration, $\rho^*b = \rho_b\sigma 3$ and $T^* = kBT/\varepsilon$. The *symbols* are the computer simulation data. The *solid* and *dashed lines* are the predictions of FMSA and MFT, respectively [62]. To enhance visual clarity, the profiles of $\sigma_M/\sigma = 1$, 2, and 3 are shifted upward by 2.4, 1.6, and 0.8, respectively

with:

$$Q_0(t) = \frac{S_0(t) + 12\eta L_0(t)e^{-t}}{(1-\eta)^2 t^3}, \tag{225}$$

$$S_0(t) = (1-\eta)^2 t^3 + 6\eta(1-\eta)t^2 + 18\eta^2 t - 12\eta(1+2\eta), \tag{226}$$

$$L_0(t) = \left(1 + \frac{\eta}{2}\right)t + 1 + 2\eta, \quad \eta = \pi\rho\sigma^3/6. \tag{227}$$

With the analytical expressions for both the excess chemical potentials and direct correlation functions the numerical implementation and computational cost of Eq. 218 are very comparable to those for a mean-field theory.

Figure 23 compares the distributions of Lennard-Jones (LJ) molecules around isolated hard-sphere particles of different sizes calculated from a mean-field theory, from FMSA, and from molecular simulations [62]. Close to a particle with size comparable to that of a LJ molecule, the density profile is highly oscillatory. With the increase of particle size, however, the oscillation rapidly fades away and a drying layer with a vapor-like density is formed around the particle surface. If the particle is large enough, the recovery from the drying layer to the bulk density over space can be essentially monotonous. While the FMSA is able to account for the drying process with increasing particle size, the density profiles from the mean-field theory

are highly oscillatory for all cases, with the first peak occurring at contact. It is incapable of reproducing the depletion around hard spheres.

9.4 Association and Hydrogen Bonding

Another important component in a conventional force field is to account for formation of chemical or hydrogen bonds in associating fluids. For fluid-phase-equilibrium calculations, the statistical associating fluid theory (SAFT) [64] provides a unique equation of state applicable to a wide variety of fluids and mixtures including aqueous mixtures and electrolytes, amphiphilic systems, liquid crystals, polymers, and petroleum fluids [65]. By incorporation of the basic concepts from DFT, various extensions of SAFT have been applied to inhomogeneous associating fluids near a hard-wall, in slit pores, and at vapor–liquid or liquid–liquid interfaces [66–74].

A relatively simple version of the excess Helmholtz energy functional can be derived by introducing the scalar- and vector-weighted densities of FMT into the SAFT equation of state:

$$\beta F_{\text{ass}}^{\text{ex}} = \sum_A \int \mathrm{d}\vec{r}\, n_0 \zeta \left[\ln \chi_0^{(A)} - \chi_0^{(A)}/2 + 1/2 \right], \tag{228}$$

where the summation applies to all association sites A, and the inhomogeneous factor ζ is defined by using Rosenfeld's weighted densities:

$$\zeta = 1 - \vec{n}_{V2} \cdot \vec{n}_{V2}/n_2^2 \tag{229}$$

and $\chi_0^{(A)}$ is the local fraction of associating site A not bonded.

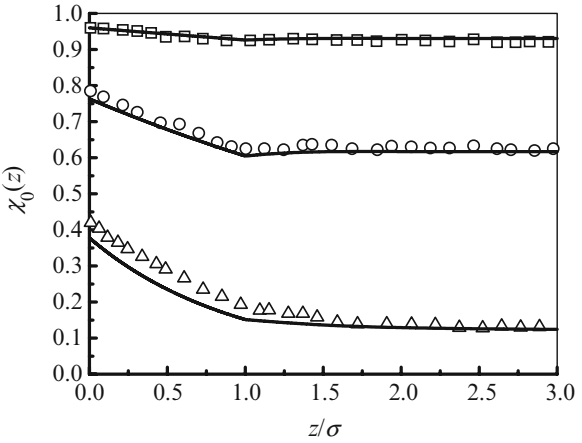

Fig. 24 Local monomer fraction for the associating hard-sphere fluid near a hard wall. The *symbols* represent simulation data and *solid lines* represent the extended FMT results [69]. The *curves* are for $\rho_b^* = 0.1977$, $1/T^* = 3$ (*squares*); $\rho_b^* = 0.1994$, $1/T^* = 5$ (*circles*); and $\rho_b^* = 0.2112$, $1/T^* = 7$ (*triangles*). Again ρ_b^* is reduced density and T^* is reduced temperature

Equation 228 provides a good description of chemical bonding for inhomogeneous associating fluids, including water-like molecules. For example, Fig. 24 shows the local fraction of unbonded associating hard spheres as a function of the distance from the hard wall at three combinations of density and association energy [69]. Because some bonding sites are restricted near the hard surface, the monomer fraction falls monotonically away from the wall. If a molecule sits at $z < \sigma$, its association with a second molecule on the wall side is restricted by the excluded volume effect; while if it is far away from the wall ($z > \sigma$), the wall has essentially little effect on intermolecular bonding and $\chi_0(z)$ is almost constant.

9.5 Electrostatics

For systems with Coulomb interactions, we may formulate the excess Helmholtz energy functional by a quadratic density expansion with respect to that of a bulk fluid. Similar to Eq. 218, the excess chemical potential and the direct correlation functions in this "semiquadratic" expansion are obtained from an integral-equation theory, mostly the analytical solutions from the mean-spherical approximations (MSA) [39].

If the system contains cations and anions of the same hard-sphere diameter σ, MSA provides an analytical expression for the direct correlation function due to the Coulomb interactions:

$$\Delta C_{ij}^{\mathrm{el}}(r) = \begin{cases} -\dfrac{q_i q_j \beta}{\varepsilon_{\mathrm{D}}} \left[\dfrac{2B}{\sigma} - \left(\frac{B}{\sigma}\right)^2 r - \dfrac{1}{r} \right] & r < \sigma \\ -\dfrac{\beta q_i q_j}{\varepsilon_{\mathrm{D}} r} & r > \sigma \end{cases}, \tag{230}$$

where q stands for electrostatic charge, ε_{D} is the dielectric constant, and:

$$B = \Gamma\sigma/(1+\Gamma\sigma), 2\sigma\Gamma = \sqrt{2\kappa\sigma+1} - 1, \kappa^2 = (4\pi\beta/\varepsilon_{\mathrm{D}}) \sum_{i=1}^{N} \rho_i^{\mathrm{b}} q_i^2. \tag{231}$$

Unlike a typical mean-field theory derived from variations of the Poisson–Boltzmann (PB) equation, the quadratic approximation is often sufficient to capture a number of counter-intuitive electrostatic phenomena observed in solutions containing multivalent ions, such as charge inversion of macroions and attraction between like charges. The major limitation of the PB equation arises from its neglect of the size of small ions and the correlation of charge distributions.

Figure 25 shows the ζ-potential of latex particles predicted from DFT in comparison with the experimental data [75]. In the DFT calculations, the diameters of K^+ and Br^- are taken as the Pauling diameter of the counterions (Br^-), with $\sigma = 0.390\,\mathrm{nm}$. The ζ-potential is defined by the electrostatic potential at the shear plane, which is approximately located at $\sigma + 0.1/\kappa$. The diffuse layer potential is the electrostatic potential at the colloidal surface. If the latex surface is smooth and

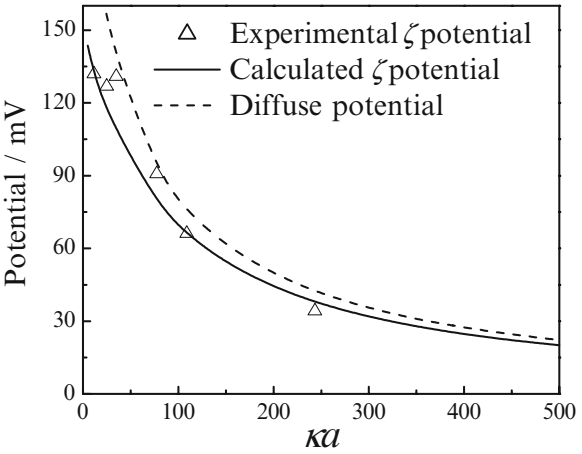

Fig. 25 ζ -Potential and diffuse potential of the latex particles (radius $a = 630\,\text{nm}$, surface charge density $Q = 0.0126\,\text{C}\,\text{m}^{-2}$) as a function of the reduced electrokinetic radius κa in aqueous KBr solutions at $pH = 6.1$ and $T = 298\,\text{K}$ [75]

if there are no organic impurities and polyelectrolytes adsorbed on the latex surface, diffuse layer potential is a good approximation to the ζ-potential. However, the surface roughness of the charged polystyrene particles results in a large value for the location of the shear plane [76]. DFT quantitatively predicts the decrease of the ζ-potential with the increase of the electrokinetic radius (or the concentration of KBr).

We close this section by pointing out that there are numerous versions of DFT in the literature but none is universally applicable to arbitrary thermodynamic systems. The wide diversity of DFT reflects the wide variety and complexity of natural phenomena, in contrast to the universality of thermodynamics laws. The selection of a particular version of DFT for a particular system depends on several factors, including not only the numerical performance but also the underlying physical model for the problems of interest.

10 Summary

In this chapter, we have discussed the basic concepts of the density functional theory (DFT) for thermodynamic systems. The theoretical foundation of DFT is essentially the same as its counterpart for electronic systems, i.e., the Hohenberg–Kohn theorem. Instead of solving for the electronic energy, DFT for classical systems focuses on the intrinsic Helmholtz energy as a functional of the one-body density profile. Minimization of the Helmholtz energy functional provides a mathematical framework en route to the microscopic structure and all relevant thermodynamic properties. In addition to thermodynamic properties, DFT provides an effective means of calculating the density distribution and correlation functions.

While the formalism of DFT is exact, the thermodynamic functionals are essentially unknown for most systems of practical concern. Regrettably, no universal procedure is available for formulation of a density functional, which is equivalent to solving the statistical mechanics for the particular system under investigation. The value of DFT is reflected in its physical clarity and computational efficiency for analyzing thermodynamic properties directly in terms of the molecular density profile or, equivalently, in terms of the microscopic structure. Indeed, DFT extends the scope of classical thermodynamics from the scalar thermodynamic functions to functionals.

As conventionally practiced in classical thermodynamics, a viable procedure in application of DFT is to divide the Helmholtz energy functional into an ideal part and an excess part representing, respectively, the contributions of an ideal gas (where all intermolecular interactions are neglected) and that due to intermolecular interactions. The ideal part of the Helmholtz energy functional is known exactly; the excess part, on the other hand, can be effectively taken into account by considering the details of intermolecular forces following the perturbation or density expansion methods. Because the intermolecular forces are conventionally represented by a short-range repulsion, van der Waals attractions, electrostatic forces, and electron donor–acceptor interactions, the major task of DFT consists of the development of theoretical models that can faithfully represent different components of the excess free energy functional.

The short-range repulsion between molecules can be conveniently represented by the hard-sphere model, which asserts that each molecule has a physical volume prohibiting overlap with other molecules. This so-called excluded-volume effect often dominates the structure of a condensed fluid and makes a vital contribution to thermodynamic functionals. The structure and thermodynamic properties of a hard-sphere fluid are conventionally determined by the Ornstein–Zernike integral equation theory with the Percus–Yevick closure. For practical applications, a quasi-exact equation of state is also available by combination of different statistical mechanical approaches. We have discussed a geometry-based density functional approach named fundamental measure theory (FMT) developed by Rosenfeld and others. At a similar level of numerical accuracy as for the bulk systems, FMT is able to represent the structure and thermodynamic properties of hard-sphere fluids and solids in the bulk as well as under confinement. Most remarkably, the same formulism is applicable to one-component systems, mixtures, and systems containing polydisperse hard spheres.

Van der Waals attraction represents another essential component of intermolecular interactions in all thermodynamic systems. Traditionally, this part of the free energy functional is formulated using the mean-field approximation. Just as in the van der Waals equation of state, the mean-field approach captures the essential physics but its performance is only qualitative or at most semiquantitative. We discussed an improvement towards more quantitative representation of the free energy functional due to van der Waals interactions that that utilizes accurate analytical correlation functions derived from the first-order mean-spherical approximation.

A conventional theory for modeling systems with charges is based on the Poisson–Boltzmann (PB) equation, which can be readily derived in the context of DFT by neglecting the size of small ions and the correlation of charge distributions. Despite its simplicity and apparent theoretical limitations, the PB equation remains a workhorse in virtually every aspect of applied colloid science and biophysics. DFT provides a powerful alternative to the PB equation for systems with electrostatic interactions. It holds major advantages, not only because it accounts for the ion size and density correlations that are ignored in the PB equation but, more important, because it provides a systematic approach to incorporate the specific properties of ions and solvent molecules beyond the primitive model.

Finally, DFT provides an essential theoretical foundation for development of molecular theories of dynamic processes. Impressive progress has already been made over the past decade on the time-dependent density functional theory (TDDFT) for classical systems [8]. We expect that TDDFT will be fruitful for application to the kinetics of self-assembly, nucleation, nanoparticle formation, and glass transitions.

Acknowledgments The author is grateful to Prof. John Prausnitz for reading many sections of this chapter and to Prof. Lloyd Lee for helpful comments. The research is sponsored by the US Department of Energy (DE-FG02-06ER46296) and uses the computational resources of the National Energy Research Scientific Computing Center (NERSC), which is supported by the Office of Science of the US Department of Energy under contract no. DE-AC03-76SF00098.

References

1. Rowlinson JS (1979) J Stat Phys 20:197
2. van der Waals JD (1893) Verh K Akad Wet Amsterdam 1:8
3. Mezger M, Reichert H, Schoder S, Okasinski J, Schroder H, Dosch H, Palms D, Ralston J, Honkimaki V (2006) Proc Natl Acad Sci USA 103:18401
4. Frenkel D (2006) Science 314:768
5. Hansen JP, McDonald IR (2006) Theory of simple liquids, 3rd edn. Elsevier, London
6. Evans R (1992) Density functionals in the theory of nonuniform fluids. In: D Henderson (ed) Fundamentals of inhomogeneous fluids. Dekker, New York, p 85
7. Davis HT (1996) Statistical mechanics of phases, interfaces, and thin films, VCH, New York
8. Wu JZ, Li ZD (2007) Annu Rev Phys Chem 58:85
9. Wu JZ (2006) AIChE J 52:1169; Hu Y, Liu HL, Wang WC (2002), Fluid phase equilibria 194(97).
10. Gibbs JW (1876) Trans Conn Acad 3:108; 343
11. Rowlinson JS, Widom B (1982) Molecular theory of capillarity, Clarendon Press, Oxford
12. Cahn JW, Hilliard JE (1958) J Chem Phys 28:258
13. Landau LD, Lifschitz L (1935) Phys Z Sowjetunion 8:153
14. Mitsui T, Furuichi J (1953) Phys Rev 90:193
15. Bonn D, Ross D (2001) Rep Prog Phys 64:1085
16. de Mello EVL, Caixeiro ES (2006) J Phys Chem Solids 67:165
17. Gameiro M, Mischaikow K, Wanner T (2005) Acta Material 53:693
18. Carnahan NF, Starling KE (1969) J Chem Phys 51:635
19. Fu D, Wu J (2005) Ind Eng Chem Res 44:1120
20. Cornelisse PMW, Peters CJ, Arons JD (1997) J Chem Phys 106:9820

21. Trokhymchuk A, Alejandre J (1999) J Chem Phys 111:8510
22. Dominik A, Tripathi S, Chapman WG (2006) Ind Eng Chem Res 45:6785
23. Dee GT, Sauer BB (1998) Adv Phys 47:161
24. Geerlings P, De Proft F, Langenaeker W (2003) Chem Rev 103:1793
25. Thomas LH (1927) Proc Cambridge Philos Soc 23:542
26. Fermi E (1928) Z Phys 48:73
27. Hohenberg P, Kohn W (1964) Phys Rev 136:B864
28. Kohn W, Sham LJ (1965) Phys Rev 140:A1133
29. Parr RG, Yang W (1989) Density-functional theory of atoms and molecules. Oxford University Press, New York
30. Ebner C, Saam WF, Stroud D (1976) Phys Rev A 14:2264
31. Evans R (1979) Adv Phy 28:143
32. Mermin ND (1965) Phys Rev 127:A1441
33. Narten AH, Levy D (1971) J Chem Phys 55:2263
34. Okhulkov AV, Demianets YN, Gorbaty YE (1994) J Chem Phys 100:1578
35. Percus JK, Yevick GJ (1958) Phys Rev 110:1
36. Lee LL (1988) Molecular thermodynamics of nonideal fluids. Butterworths, Boston
37. Wertheim M (1963) Phys Rev Lett 10:321
38. Baxter RJ (1968) J Chem Phys 49:2770
39. Blum L (1975) Mol Phys 30:1529
40. Malijevsky A, Labik S, Smith WR (1991) Mol Phys 72:193
41. Caccamo C (1996) Phys Rep 274:1
42. Rosenfeld Y, Ashcroft NW (1979) Phys Rev A (Gen Phys) 20:1208
43. Li ZD, Wu JZ (2005) Macromol Symp 219: 51
44. Irving JH, Kirkwood JG (1950) J Chem Phys 18:817
45. Yu YX, Wu JZ (2002) J Chem Phys 117:10156
46. Henderson D, Blum L, Lebowitz JL (1979) J Electroanal Chem 102:315
47. Roth R, Evans R, Dietrich S (2000) Phys Rev E 62:5360
48. Biben T, Bladon P, Frenkel D (1996) J Phys Condens Matter 8:10799
49. Roth R, Gotzelmann B, Dietrich S (1999) Phys Rev Lett 83:448
50. Cuesta JA, Martinez-Raton Y, Tarazona P (2002) J Phys Condens Matter 14:11965
51. Rosenfeld Y (1989) Phys Rev Lett 63:980
52. Tarazona P (2002) Physica A 306:243
53. Rosenfeld Y (2002) J Phys Condens Matter 14:9141
54. Boublik T (1970) J Chem Phys 53:471
55. Mansoori GA, Carnahan NF, Starling KE, Leland TW, Jr. (1971) J Chem Phys 54:1523
56. Roth R, Evans R, Lang A, Kahl G (2002) J Phys Condens Matter 14:12063
57. Groot RD, van der Eerden JP, Faber NM (1987) J Chem Phys 87:2263
58. Lafuente L, Cuesta JA (2003) J Chem Phys 119:10832
59. Schmidt M (1999) Phys Rev E 60:R6291
60. Winkelmann J (2001) J Phys Condens Matter 13:4739
61. Tang YP, Wu JZ (2003) J Chem Phys 119:7388
62. Tang YP, Wu JZ (2004) Phys Rev E 70:011201
63. Tang YP (2003) J Chem Phys 118:4140
64. Chapman WG, Gubbins KE, Jackson G, Radosz M (1989) Fluid Phase Equil 52:31
65. Muller EA, Gubbins KE (2001) Ind Eng Chem Res 40:2193
66. Segura CJ, Chapman WG, Shukla KP (1997) Mol Phys 90:759
67. Segura CJ, Vakarin EV, Chapman WG, Holovko MF (1998) J Chem Phys 108:4837
68. Segura CJ, Zhang J, Chapman WG (2001) Mol Phys 99:1
69. Yu YX, Wu JZ (2002) J Chem Phys 116:7094
70. Paricaud P, Galindo A, Jackson G (2002) Fluid Phase Equil 194:87
71. Tripathi S, Chapman WG (2003) J Chem Phys 118:7993
72. Pizio O, Patrykiejew A, Sokolowski S (2000) J Chem Phys 113:10761
73. Malo BM, Huerta A, Pizio O, Sokolowski S (2000) J Phys Chem B 104:7756
74. Huerta A, Pizio O, Bryk P, Sokolowski S (2000) Mol Phys 98:1859
75. Yu YX, Wu JZ, Gao GH (2004) Chin J Chem Eng 12:688
76. Chow RS, Takamura K (1988) J Colloid Interface Sci 125:226

Struct Bond
DOI:10.1007/430_2008_2

Thermodynamic Modeling of Complex Systems

Matthias Kleiner, Feelly Tumakaka, and Gabriele Sadowski

Abstract The thermodynamic behavior of complex pure fluids and mixtures is strongly affected by specific interactions like association (hydrogen bonding) and electrostatic interactions of permanent or induced dipoles. The modeling of those systems requires a physical model that is able to explicitly account for these specific interactions. This contribution describes the state of the art in modeling of complex fluids using analytical equations of state. Many applications demonstrate that those models can successfully be applied to describe and even to predict the phase behavior of a whole variety of substances ranging from small gas molecules up to organic solvents and polymeric systems.

Keywords: Copolymers · Pharmaceutical · Phase equilibria · Polymers

Contents

M. Kleiner, F. Tumakaka, and G. Sadowski(✉)
Dortmund University of Technology, Laboratory of Thermodynamics,
Emil-Figge-Str. 70, 44227 Dortmund, Germany
e-mail: gabriele.sadowski@bci.tu-dortmund.de

1 Introduction

The ability to predict and to correlate thermodynamic properties and phase equilibria is essential for the simulation of chemical processes and thus for process development and optimization. For industrial as well as for academic applications, the applied models should possess a sufficient accuracy over a wide range of conditions using a minimum of adjustable and easily accessible parameters.

Significant progress towards this type of model was made by applying the approach of perturbation theories from statistical mechanics. These theories are based on the fact that the thermodynamic properties of a system are mainly determined by the repulsive interactions of the molecules. Thus, these theories typically choose a reference system that shows only repulsive interactions. An often used reference systems is a system of "hard spheres," which have a fixed volume and no other interactions than repulsion. Starting from that, the influence of any deviation of a real system from the reference system to the thermodynamic behavior is described as a perturbation of the repulsive reference system. These deviations might be van der Waals attractive interactions, specific interactions like association, polar or quadrupolar interactions as well as the non-spherical shape of the molecules. Usually, these perturbations are assumed to be additive and independent of each other.

A whole series of models of this kind is based on the statistical associating fluid theory (SAFT) [1–4], which considers a molecule as a chain of tangent spherical segments. Starting from the Helmholtz energy of a hard-sphere reference system A^{hs}, different perturbation contributions are considered. These are namely the hard-sphere chain formation of m segments (A^{chain}), which accounts for the non-spherical shape of molecules, non-specific attractive interactions (A^{disp}) of the m (non-bonded) spherical segments, and very strong, short-range attractive interactions, like association (A^{assoc}).

Thus, the total Helmholtz energy of a system can be written as:

$$A^{\mathrm{res}} = mA^{\mathrm{hs}} + mA^{\mathrm{disp}} + A^{\mathrm{chain}} + A^{\mathrm{assoc}}. \tag{1}$$

Within the SAFT model, the Helmholtz energy of the reference A^{hs} is described using the Carnahan–Starling expression [5]; the segment–segment dispersion contribution to the Helmholtz energy A^{disp} is described using a fourth-order perturbation term [6, 7]. The contribution of chain formation as well as the association term are accounted for, based on the work of Wertheim [8].

Subsequently, several models were suggested that differ in the use of the various perturbation expressions. Examples are the perturbed hard-sphere-chain theory (PHSC) [9], as well as the models proposed by Chang and Sandler [10], Gil-Villegas et al. [11], and Hino and Prausnitz [12].

Each of these models considers the non-spherical shape of a molecule on one-hand side and the attractive interaction on the-other-hand side as independent perturbations of the reference system. Several attempts have been made to overcome this deficiency. Various models were suggested that use attractive square-well spheres

(e.g., [11, 13, 14]) or Lennard-Jones spheres (e.g., [15–17]) rather than hard spheres as reference to modify the chain contribution A^{chain}.

The perturbed-chain SAFT (PC-SAFT) model [18, 19] adopts the opposite idea: here, a perturbation theory of second order is applied to the reference system of hard chains instead of hard spheres to develop a dispersion term A^{disp}. Whereas the contributions to describe the hard-chain formation as well as the association are identical to those of the original SAFT model, the dispersion term was modified to account for the influence of the non-spherical shape of the molecule on the number of intermolecular interactions, and is therefore a function of segment number m:

$$A^{\text{res}} = A^{\text{hc}} + A^{\text{disp}}(m) + A^{\text{assoc}}. \tag{2}$$

The PC-SAFT model was successfully applied to a wide variety of systems, demonstrating that the modeling results could be improved for more systems than just for chain molecules like polymers. Even for small non-spherical substances, the modeling results could be improved considerably compared to the original SAFT model [18–21].

In addition to dispersive interactions, the phase behavior of pure fluids and mixtures is strongly affected by specific intermolecular interactions like association (hydrogen bonding) or dipolar interactions. Müller and Gubbins [22] gave a detailed review of different approaches to describe the contribution of association interactions to the Helmholtz energy A^{assoc} of a system, and discussed numerous examples of its application to real fluids and mixtures.

To account for dipolar interactions, various theories based on statistical mechanics were developed. In these theories, the dipole moment is assumed to be positioned at the center of a sphere, whereas the diameter of the sphere is chosen to preserve the molecular volume [23–31]. This treatment, however, does not explicitly account for the non-spherical shape, which becomes important in many real dipolar fluids, and thus its application is limited to simple fluids and mixtures. To account for the non-spherical shape of dipolar molecules, Jog and Chapman [32] proposed a theory that considers polar molecules as chains of non-polar and dipolar spherical segments. Another way to account for the non-spherical shape of dipolar molecules was followed by Gross and Vrabec [33], who assumed a two-center Lennard–Jones fluid as reference fluid. The model constants were adjusted to simulation data of two-center Lennard–Jones molecules having different molecular elongations from spheres up to dimers. The model was applied with PC-SAFT and is referred to as perturbed-chain polar SAFT (PCP-SAFT).

An alternative route to the perturbation theories was followed by Saager and Fischer [34] and Saager et al. [35] who constructed a dipolar contribution to the Helmholtz free energy on the basis of computer simulation results by fitting empirical expressions to simulation data of two-center Lennard–Jones molecules.

However, all these dipole expressions do not account for the polarizability of molecules that allows the induction of a dipolar moment in a molecule. To account for the non-additive induction interactions due to the polarization of molecules, Kleiner and Gross [36] applied the renormalized perturbation theory of Wertheim

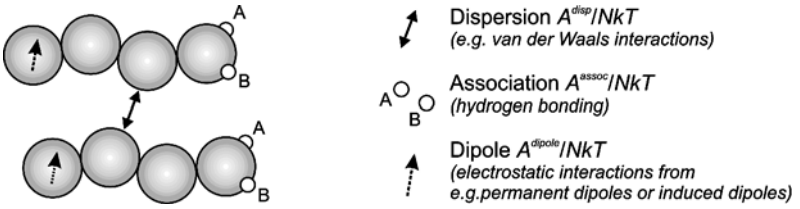

Fig. 1 Molecular picture of the PC-SAFT equation of state and its extension to dipolar fluids (e.g., PCP-SAFT, PCIP-SAFT). Illustration of the perturbation contributions to account for dispersion interactions, association interactions, and dipolar interactions

[37, 38] in combination with the dipolar expression of Gross and Vrabec. The equation of state contribution was applied with PC-SAFT to real fluids and mixtures and the model is referred to as perturbed-chain induced-polar SAFT (PCIP-SAFT).

The underlying molecular picture of the PC-SAFT equation of state, as well as of its extensions to dipolar and polarizable fluids (e.g., PCP-SAFT, PCIP-SAFT), is depicted in Fig. 1.

Thus, the Helmholtz energy using PC-SAFT based models finally reads as:

$$A^{\mathrm{res}} = A^{\mathrm{hc}} + A^{\mathrm{disp}}(m) + A^{\mathrm{assoc}} + A^{\mathrm{dipole}}. \tag{3}$$

Many applications of PC-SAFT as well as of its extensions for polar and polarizable fluids (PCP-SAFT and PCIP-SAFT) demonstrated that these models can successfully be applied to a broad range of substances and mixtures including simple fluids without specific interactions, associating fluids as well as to dipolar components and their mixtures. The model was applied to aqueous electrolyte solutions [39] as well as to solutions of aqueous amino acids and polypeptides [40]. An excellent performance of the PC-SAFT model was also shown for various polymer as well as copolymer systems.

This contribution summarizes the state of the art in modeling using PC-SAFT-based models. Due to the wide variety of compounds and the resulting mixtures, the focus lies on the modeling of phase equilibria of very asymmetric mixtures that exhibit complex intermolecular interactions.

2 PC-SAFT Equation of State

According to Eq. 3, different contributions to the Helmholtz energy are considered in PC-SAFT. They are briefly described below. The detailed expressions for each contribution can be found in the appendix.

2.1 Hard-Chain Contribution A^{hc}

The hard-chain reference fluid consists of spherical segments that do not show any attractive interactions. It is defined by two parameters, namely the number of segments m and the diameter of segments σ. The Helmholtz energy of this reference system is described by an expression developed by Chapman et al. [41], which is based on Wertheim's first-order thermodynamic perturbation theory [42–44].

2.2 Dispersion Contribution A^{disp}

To determine the contribution of dispersive attractions to the Helmholtz energy of a system, PC-SAFT applies the perturbation theory of Barker and Henderson [45, 46] to the hard-chain reference system instead of the hard-sphere system. Thus, the influence of the non-spherical shape of molecules on the attractive dispersion interactions is explicitly considered.

In addition to the above-mentioned parameters, segment number m and segment diameter σ, one additional parameter is required for describing the segment–segment interaction: the dispersion energy parameter ε/k. All three parameters are determined by simultaneously fitting to liquid density and vapor-pressure data of a pure component. The parameter-estimation approach for non-volatile substances, such as solids or polymers, is later described in the solid–liquid equilibria (Sect. 4) and polymer (Sect. 5) sections, respectively.

To model mixtures, conventional Berthelot–Lorentz combining rules are applied:

$$\sigma_{ij} = \frac{1}{2}(\sigma_i + \sigma_j), \tag{4}$$

$$\varepsilon_{ij} = \sqrt{\varepsilon_i \varepsilon_j} \cdot (1 - k_{ij}). \tag{5}$$

Equation 5 contains one adjustable binary interaction parameter k_{ij}, which is used to correct the dispersion energy in the mixture. If needed, this is determined from fitting to phase-equilibrium data of the binary mixture. Parameter k_{ij} will remain the only parameter that is fitted to binary data and is usually independent of temperature. For the description of ternary of higher systems it is assumed that the system is dominated by two-molecule interactions and thus no parameters other than the binary parameters are required.

2.3 Association Contribution A^{assoc}

The contribution due to short-range association interactions (hydrogen bonding) A^{assoc} is considered by an association model that was proposed by Chapman et al.

[2,41] based on Wertheim's first-order thermodynamic perturbation theory (TPT1). Within this theory, a molecule is assumed to have one or more association sites that can form hydrogen bonds. This is shown exemplarily in Fig. 1 for molecules with two association sites A and B. The association between two association sites is characterized by two additional parameters: the association energy $\varepsilon^{A_iB_i}/k$ and the effective volume of an association interaction $\kappa^{A_iB_i}$. Therefore, an associating compound is characterized by five pure-component parameters.

The number of association sites of a molecule and the possible site–site interactions have a profound effect on the fluid structure, and therefore on the phase behavior, and should thus be chosen carefully. Examples are given later in this contribution (see Sect. 3.3).

The strength of cross-association interactions between two different associating compounds can be determined using simple combining rules of the pure-component parameters, as suggested by Wolbach and Sandler [47] without introducing binary parameters:

$$\varepsilon^{A_iB_j} = \frac{1}{2}\left(\varepsilon^{A_iB_i} + \varepsilon^{A_jB_j}\right), \tag{6}$$

$$\kappa^{A_iB_j} = \sqrt{\kappa^{A_iB_i}\kappa^{A_jB_j}}\left(\frac{\sqrt{\sigma_{ii}\sigma_{jj}}}{1/2\,(\sigma_{ii}+\sigma_{jj})}\right)^3. \tag{7}$$

2.4 Dipole/Polarizability Contribution A^{dipole}

Long-range electrostatic interactions of dipolar and polarizable fluids A^{dipole} are taken into account by the expression of Kleiner and Gross (PCIP-SAFT). It is based on the renormalized perturbation theory for polarizable polar fluids of Wertheim [37,38], which was applied to the dipole contribution for non-spherical molecules of Gross and Vrabec. Since tabulated values for the dipole moments and average molecular polarizabilities are available, no additional adjustable parameters are required.

For non-polarizable components, the dipolar expression of Gross and Vrabec is recovered and, thus, the PCIP-SAFT equation of state simply reduces to PCP-SAFT.

3 Modeling of Low Molecular Weight Systems

The PC-SAFT equation of state can successfully be applied to correlate or even to predict the thermodynamic properties of a broad range of low molecular weight substances (e.g., [18, 20]). For systems without specific interactions (e.g., alkane mixtures) the phase behavior as well as the heat of mixing can usually even be predicted ($k_{ij} = 0$) in good agreement with experimental data. This is illustrated in Fig. 2 for the mixture of hexane and hexadecane.

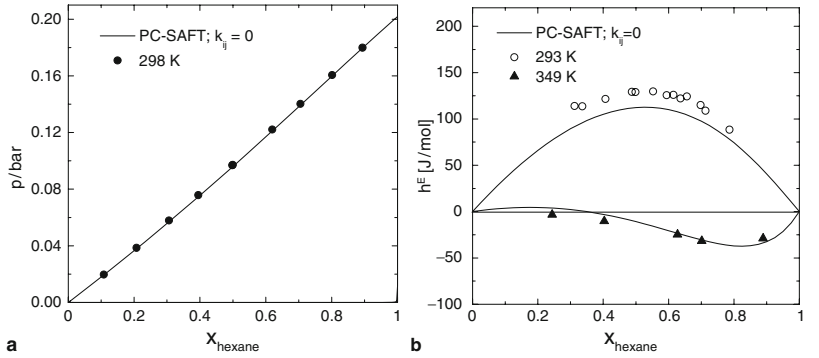

Fig. 2 PC-SAFT predictions ($k_{ij} = 0$) (*lines*) of thermodynamic properties of the mixture hexane/hexadecane at different temperatures in comparison to experimental data (*symbols*). **a** Vapor–liquid equilibrium at $T = 298\,\mathrm{K}$ (*filled circles* experimental data from Shen et al. [48]). **b** Excess enthalpies at two temperatures (*open circles* experimental data from McGlashan and Morcom [49], *filled triangles* experimental data from Holleman [50])

However, modeling of strongly asymmetric mixtures and mixtures exhibiting complex intermolecular interactions is much more challenging and will be discussed in the following section.

3.1 Mixtures of Strongly Polar and Non-polar Fluids

Mixtures containing polar as well as non-polar components often exhibit a strong deviation from ideality, and thus often show an azeotropic behavior. It was shown in several investigations that these mixtures can only be described accurately when the specific electrostatic interactions are explicitly taken into account.

The PCIP-SAFT model is applied here to model the thermodynamic behavior of strongly dipolar fluids and their mixtures with non-polar compounds, both of which are polarizable. An example of such a mixture is the binary system *N*,*N*-dimethylformamide and 1-butene, which is shown in Fig. 3. In order to assess the effect of the polarizability, the results are compared to the PCP-SAFT model where only permanent dipoles are considered. Moreover, the results are compared to the original PC-SAFT model where the electrostatic interactions are not explicitly accounted for. It becomes obvious that both PCIP-SAFT and PCP-SAFT are in good agreement with the experimental data, while the non-polar PC-SAFT model reveals a false temperature-behavior in describing a non-physical liquid–liquid demixing at lower temperatures.

Moreover, the physically more realistic models PCIP-SAFT and PCP-SAFT require a much lower value of the binary parameter than the non-polar PC-SAFT, while providing a superior description of the experimental data.

Another example for the strong influence of dipolar interactions on the thermodynamic properties is the mixture butyronitrile and *n*-heptane. The vapor–liquid equilibrium of this mixture at $T = 318\,\mathrm{K}$ is depicted in Fig. 4a. When a binary interaction

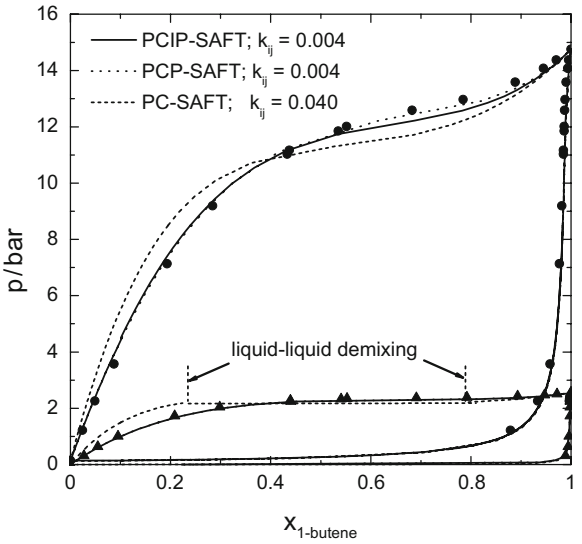

Fig. 3 Vapor–liquid equilibrium of the mixture *N*,*N*-dimethylformamide/1-butene at two temperatures (*filled circles* 363 K, *filled triangles* 293 K). Comparison of experimental data from Wilding et al. [51]to correlation results of PCIP-SAFT, of PCP-SAFT, and of PC-SAFT

parameter of the non-polar PC-SAFT model is adjusted, the model is not capable of reproducing the vapor–liquid equilibrium. Taking into account the polarity of butyronitril as well as the polarizibility of the two components, the PCIP-SAFT model provides a good representation of the experimental data, while the binary interaction parameter is almost zero. Although the binary interaction parameter is somewhat higher for the PCP-SAFT model, it is in almost as good agreement with the data. This is substantiated in Fig. 4b, where the predicted excess enthalpies of PCIP-SAFT and PCP-SAFT are in qualitative good agreement with the experimental data, compared to the non-polar PC-SAFT model.

It can be concluded that when considering this type of mixture, the inclusion of dipolar interaction and induced dipolar interactions due to the molecule's polarizability usually leads to lower (absolute) values of the required binary interaction parameter. Thus, the predictive abilities of the model are significantly improved when the physics of the molecules is considered. In particular, the consideration of the dipole moments in PCP-SAFT leads to a remarkable improvement of the modeling results compared to the non-polar PC-SAFT model. An additional accounting for the molecular polarizabilities in PCIP-SAFT usually leads to a further improvement of the modeling compared to PCP-SAFT.

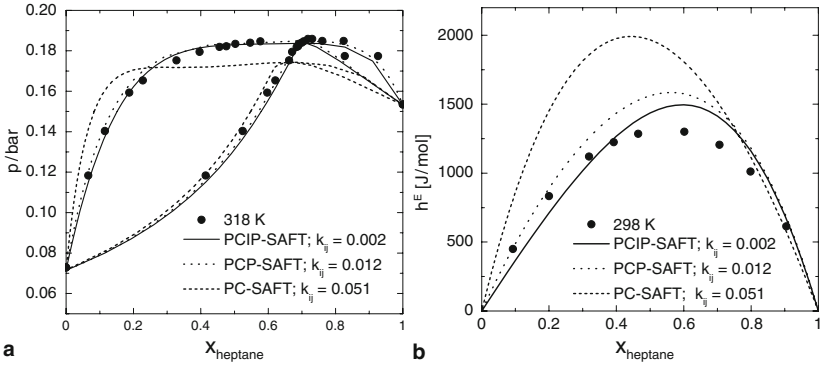

Fig. 4 Thermodynamic properties of the mixture butyronitrile/*n*-heptane. **a** Vapor–liquid equilibrium at $T = 318\,\mathrm{K}$. Comparison of experimental data from Artal et al. [52] (*filled circles*) to correlation results of PCIP-SAFT, of PCP-SAFT, and of PC-SAFT. **b** Excess enthalpies of mixing at 298 K. Predictions of PCIP-SAFT, of PCP-SAFT, and of PC-SAFT and comparison to experimental data from Akamatsu et al. [53] (*filled circles*). Binary interaction parameters were adjusted to VLE data as shown in **a**

3.2 Mixtures of Polar and Associating Fluids

The modeling of mixtures containing polar as well as associating components is very challenging for any equation of state. This is due to the fact that classical combining rules do not allow for the consideration of cross-interactions of molecules showing unlike interactions as pure components. Here, mixtures of a self-associating component (e.g., water) in a mixture with a component that does not self-associate but can act as either proton donor (e.g., chloroform) or proton acceptor (e.g., acetone) are considered. In those mixtures, cross-association interactions may occur: the polar compound does not self-associate but is able to associate with the associating compound. This type of interaction is here referred to as induced association to distinguish from mixtures of two self-associating compounds for which the combining rules (Eqs. 6 and 7) can directly be applied. However, using a simple but physical meaningful approach it is possible to account for the induced cross-association only from the knowledge of the pure-component parameters [54].

This approach is based on the following assumptions:

1. The association-energy parameter $\varepsilon^{\mathrm{A}_i\mathrm{B}_i}$ of the non-self-associating (polar) component is set to zero
2. The association-volume parameter $\kappa^{\mathrm{A}_i\mathrm{B}_i}$ of the non-self-associating component is assumed to be equal to the value of the associating component in the mixture

As a consequence of the first assumption, association of the polar substance is considered only if the mixture contains at least one associating component. Based on these assumptions, the cross-association parameters in the mixture can simply be calculated by applying the combining rules of Wolbach and Sandler (Eqs. 6 and 7).

The advantage of this approach is that the cross-association parameters are easily accessible and that no additional adjustable parameters are required.

Some applications of the proposed approach to model vapor–liquid as well as liquid–liquid equilibria of mixtures will be presented. Any effects due to polarizability are not explicitly considered here since they were found to have a minor influence on the phase behavior in these mixtures and, thus, the PCP-SAFT model is used for the polar compounds. All results are compared with calculations using PCP-SAFT and the classical approach where induced-association interactions are not considered.

Figure 5 shows the error bars of predicted ($k_{ij} = 0$) bubble-point pressures for different mixtures of alcohols with polar compounds. The grey bars show predictions using the classical approach where the induced-association interactions are not considered. The black bars represent predictions where the induced association between the associating and the polar component is explicitly accounted for. It can be seen that the deviations of the experimental and calculated bubble-point pressures can be drastically reduced especially for the mixtures containing methanol or ethanol. Since the influence of the OH-groups decreases with increasing chain length of the alcohols, the influence of the induced association also decreases. Nevertheless, the bubble-point predictions can still be improved for longer alcohols when the proposed approach for induced association is applied.

The phase behavior of a mixture of water and methyl methacrylate at atmospheric pressure is depicted in Fig. 6. This system shows heteroazeotropic behavior with a vapor–liquid equilibrium at higher temperatures and a liquid–liquid demixing at lower temperatures. Using the classical approach, the heteroazeotropic behavior in this mixture cannot be described quantitatively even using a very high binary interaction parameter. When the induced association is considered, the phase equilibrium can even be predicted setting the binary interaction parameter to zero.

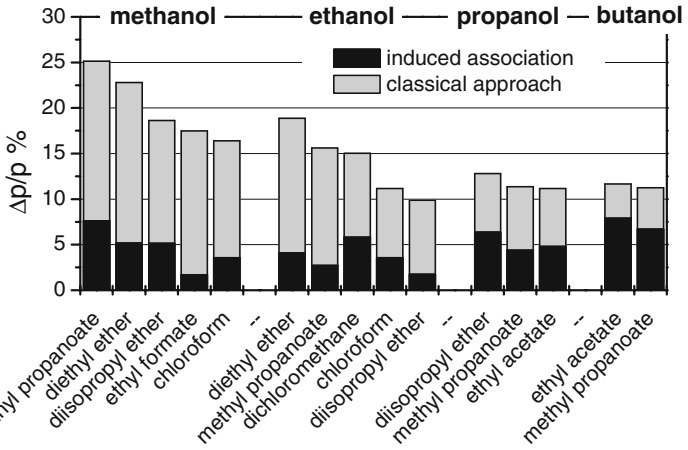

Fig. 5 Error bars of predicted bubble-point pressures for different alcohols in mixtures with a second component, which is polar

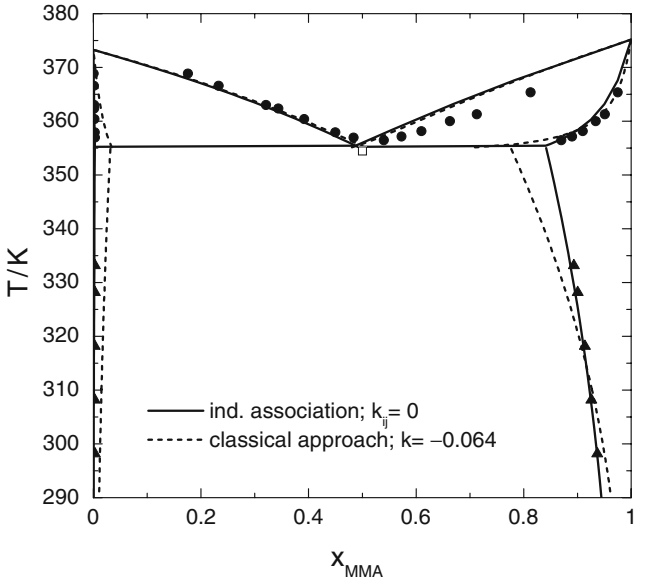

Fig. 6 Liquid–liquid and vapor–liquid equilibrium of the mixture methyl methacrylate (MMA)/water at $p = 1$ bar (*filled circles* Danov et al. [55], *open square* Frolova et al. [56], *filled triangles* Fu et al. [57]). *Dashed lines*: correlation results of PCP-SAFT using the classical approach. *Solid lines*: PCP-SAFT predictions considering the induced association

The approach can also be extended to ternary mixtures. Figure 7 shows the liquid–liquid equilibrium of the ternary mixture water/furfural/ethyl acetate as an example of a mixture with one associating component that may form cross-associates with the two polar compounds furfural and ethyl acetate. The binary interaction parameters for water/furfural and water/ethyl acetate are taken from the binary subsystems and the k_{ij} for the system ethyl acetate/furfural is set to zero. Thus, the ternary liquid–liquid equilibrium is predicted using only the binary information of the subsystems water/furfural and water/ethyl acetate, respectively. It becomes obvious that again the predicted results are in very good agreement with experimental data when the induced association is considered, whereas the classical approach is not able to properly describe the ternary-mixture phase behavior.

This is substantiated in Fig. 8 for the system water/methanol/methyl methacrylate. The classical approach underestimates the miscibility gap, even if a binary interaction parameter is used for the water/methyl methacrylate binary system, whereas the liquid–liquid equilibrium can be well predicted when applying the approach for the induced association.

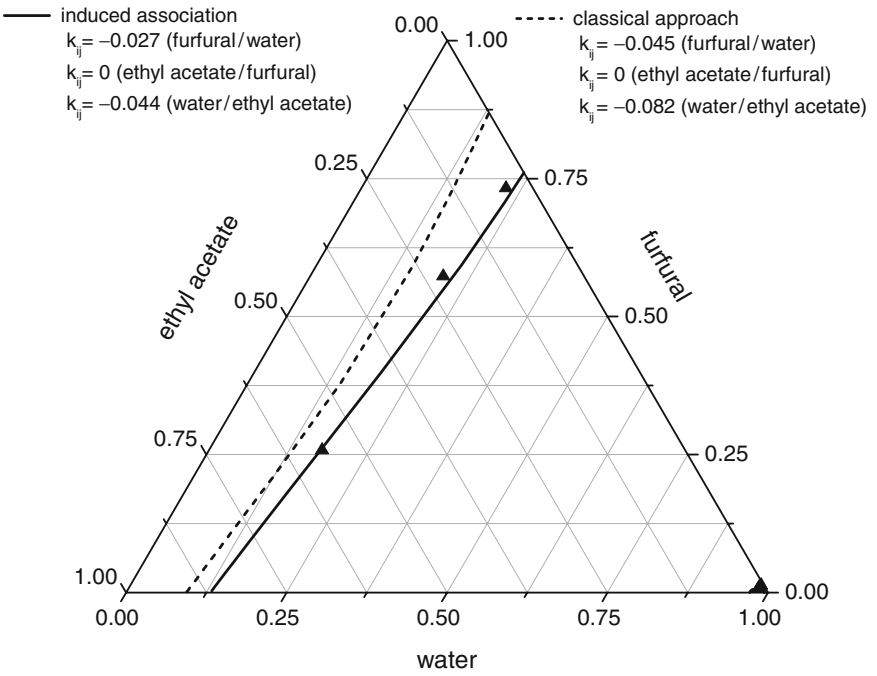

Fig. 7 Liquid–liquid equilibrium of the ternary mixture water/furfural/ethyl acetate for $T = 298\,\mathrm{K}$ (*filled triangles* Lloyd et al. [58]). *Dashed line*: predictions of PCP-SAFT using the classical approach. *Solid line*: PCP-SAFT predictions considering the induced association

3.3 Mixtures with Carboxylic Acids

In general, carboxylic acids are well described using two different association sites: a donor site at the oxygen and an acceptor site at the OH-group [20,61]. This corresponds to the 2B-association scheme as suggested by Huang and Radosz [3].

However, particularly small carboxylic acids show a specific thermodynamic behavior (e.g., very high boiling points), which is caused by two hydrogen bonds formed between the carboxylic groups of two acid molecules (see Fig. 9).

Therefore, these acid molecules appear as cyclic dimers even in the vapor phase.

This behavior can be captured using PC-SAFT by allowing for only one association site per molecule (1A-association scheme). A schematic picture of the 1A- and 2B-association schemes and the possible site–site interactions of the association sites are depicted in Fig. 10. As can be seen from Fig. 10a, the 1A-association enables the formation of only dimers whereas the 2B-scheme would also allow the formation of clusters with more than two molecules.

Investigations of pure-component properties of different carboxylic acids (from formic acid up to decanoic acid) showed that using a one-site association scheme gives an improved representation of liquid-density data and in particular of vapor-pressure data. For example, the unweighted average of all individual AAD values

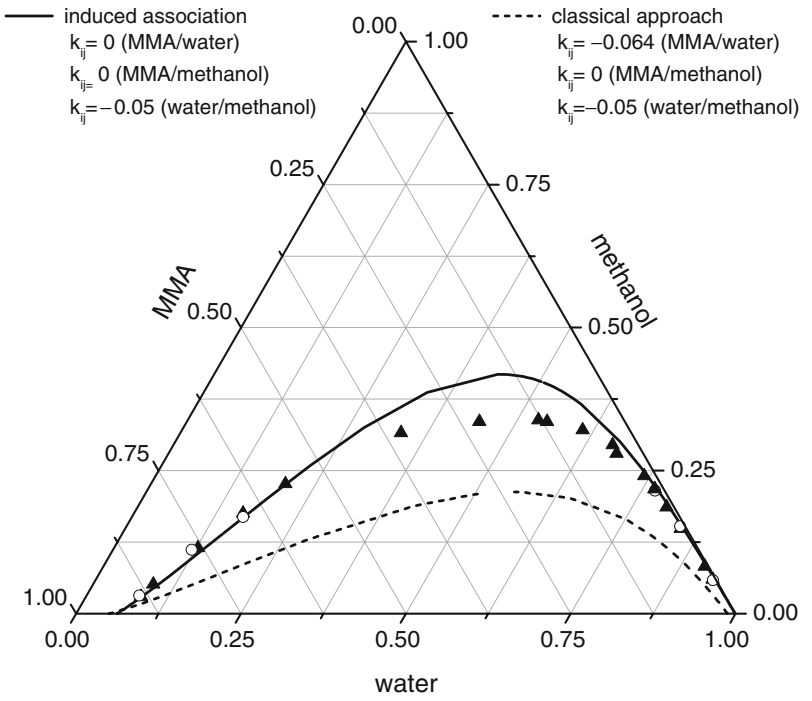

Fig. 8 Liquid–liquid equilibrium of the ternary mixture water/methanol/methyl methacrylate (MMA) for $T = 298\,\mathrm{K}$ (*open circles* Clausse et al. [59], *filled triangles,* Chubarov et al. [60]). *Dashed line*: predictions of PCP-SAFT using the classical approach. *Solid line*: PCP-SAFT predictions considering the induced association

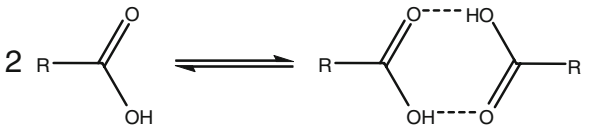

Fig. 9 Dimerization of carboxylic acids

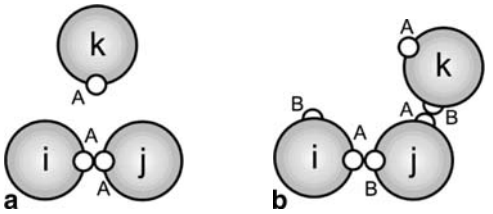

Fig. 10 Site–site interactions assumed by two different association schemes as suggested by Huang and Radosz [3]

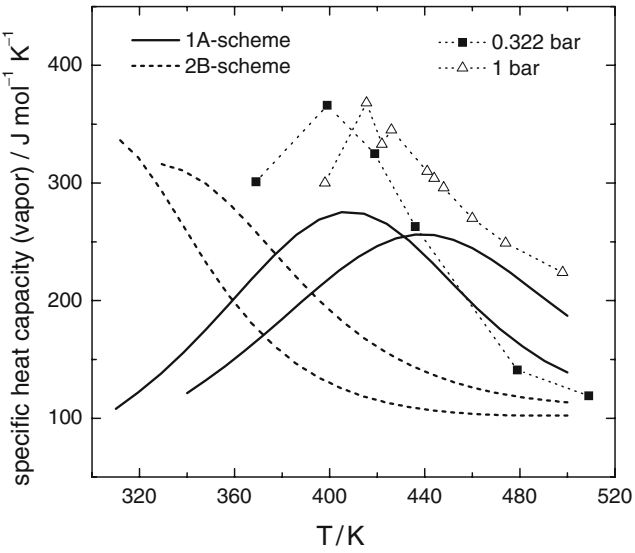

Fig. 11 Specific heat capacities (vapor phase) for acetic acid at two pressures (*filled squares* for $p = 0.332$ bar, *open triangles* for $p = 1$ bar). *Dashed lines*: Predictions via PC-SAFT using the 2B-association scheme. *Solid lines*: PC-SAFT predictions using the 1A-association scheme. Experimental data are taken from Weltner [62]

for vapor pressure data are 1.08% for the 1A scheme and 3.24% for the 2B scheme. For the liquid densities, average errors of 0.93% and of 1.28% were obtained for the 1A- and 2B-association schemes, respectively.

The specific heat capacities of acetic acid in the vapor phase are depicted in Fig. 11 at 0.33 bar and 1 bar, respectively. The experimental data show a maximum of the heat capacity. As can be seen, the predictions using the 1A scheme also follow this behavior and are in qualitative agreement to the experimental data, whereas the results obtained with the 2B scheme do not show this trend in the respective temperature range. This is quite remarkable because the heat capacities were not used for the determination of the acid pure-component parameters. These results reveal the good performance of the 1A scheme for the modeling and even prediction of pure-component properties of carboxylic acids.

The 1A- and 2B-association schemes are also compared for modeling the phase behavior of binary mixtures with acetic acid. The mixture of acetic acid with the non-polar cyclohexane as depicted in Fig. 12 is an example of a mixture in which the acid does not cross-associate but is only able to form self-associates. The dashed line indicates correlations using the 2B-association scheme where dimerization is not accounted for. It can be seen that the correlations are in poor agreement with the experimental data. If the dimerization is considered by applying the 1A-association scheme, the quality of the correlations can be improved considerably.

Considering the system acetic acid/carbon dioxide (Fig. 13), the carbon dioxide molecule may form weak hydrogen bonds with the carboxyl group of acetic acid.

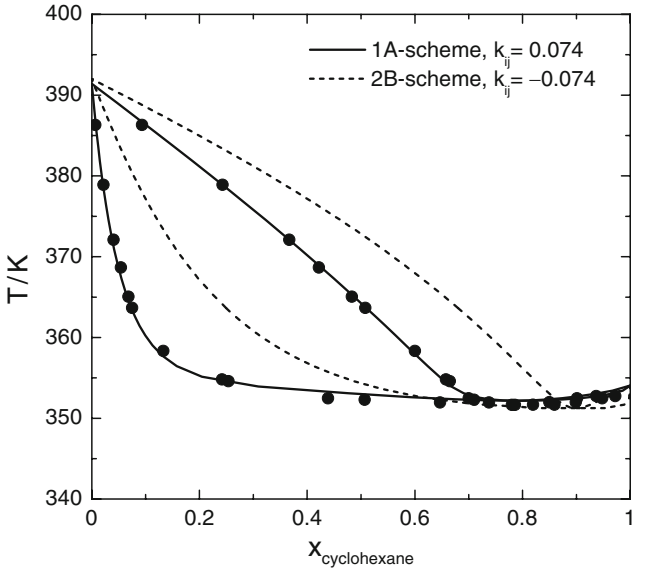

Fig. 12 Vapor–liquid equilibrium of the mixture cyclohexane/acetic acid at $p = 1\,\text{bar}$. *Dashed lines*: correlation results of PC-SAFT using the 2B-association scheme. *Solid lines*: PC-SAFT correlations considering using the 1A-association scheme. Experimental data taken from Miyamoto et al. [63]

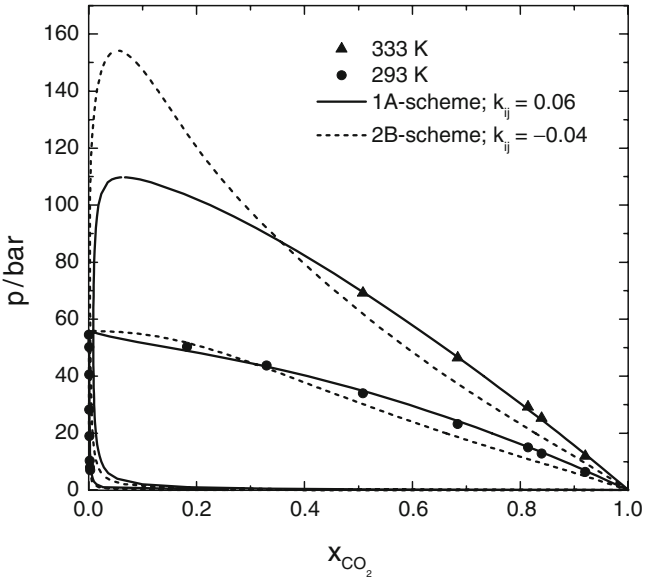

Fig. 13 Vapor–liquid equilibrium of the acetic acid/CO_2 mixture at two temperatures (*filled circles* for $T = 293.2\,\text{K}$, *filled triangles* for $T = 333.2\,\text{K}$). *Dashed lines*: correlations via PC-SAFT using the 2B-association scheme. *Solid lines*: PC-SAFT correlations using the 1A-association scheme. Experimental data are from Laugier et al. [64]

However, investigations have shown that accounting for the cross-association interactions have a minor influence on the phase behavior modeling and, thus, these interactions are not explicitly considered here. It can be seen that again the results using the 2B-association scheme for acetic acid cannot be brought into good agreement with experimental data, even using a binary interaction parameter k_{ij}. In the case of the 1A scheme, where the dimerization is considered, the correlation results are in excellent agreement with experimental data.

The mixture of acetic acid with ethyl acetate represents a system containing an associating and a polar compound in which induced association may occur, as described in the previous section. Modeling results for the vapor–liquid equilibrium of this mixture are presented in Fig. 14 using the 1A- and 2B-association schemes, respectively. It can be seen that the results are poorly represented using the 2B scheme, even applying a very high binary interaction parameter where the model calculates an azeotropic behavior. Again, the results are improved considerably when the dimerization is considered by the 1A scheme, even requiring a much smaller value for the binary interaction parameter k_{ij}.

It becomes obvious that the applied association scheme strongly affects the modeling results. Despite its simplicity, for carboxylic acids the 1A scheme leads to a reasonable description of mixture phase behavior containing compounds with different functionalities.

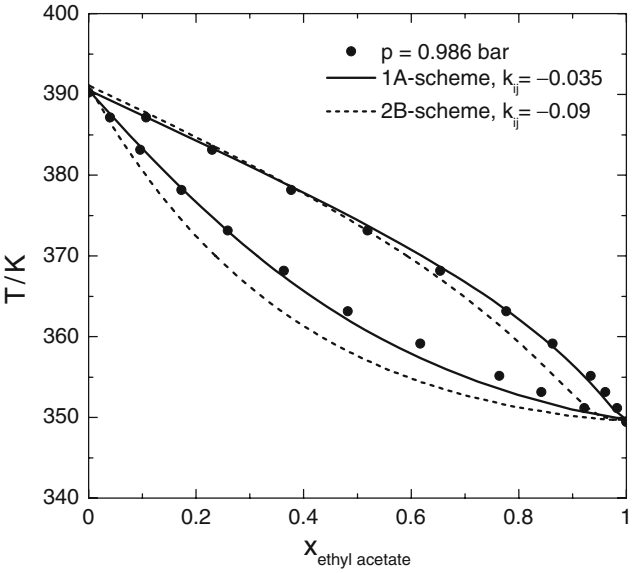

Fig. 14 Vapor–liquid equilibrium of the mixture acetic acid/ethyl acetate mixture at $p = 0.986$ bar. *Dashed lines*: correlations via PC-SAFT using the 2B-association scheme. *Solid lines*: PC-SAFT correlations using the 1A-association scheme. Experimental data are taken from Kato [65]

4 Modeling of Solid–Liquid Equilibria

PC-SAFT can also be applied to describe the solubility of solid solutes. This knowledge is particularly crucial for the study of crystallization, which is an important purification technique for many pharmaceutical and biological compounds.

Assuming pure solid phases, and neglecting the influence of the heat-capacity differences in the solid and liquid state, the solubility of a compound i at atmospheric pressure can be calculated as:

$$x_i^{\mathrm{L}} = \frac{\phi_{0i}^{\mathrm{L}}}{\phi_i^{\mathrm{L}}} \cdot \exp\left[-\frac{\Delta h_{0i}^{\mathrm{SL}}}{RT}\left(1 - \frac{T}{T_{0i}^{\mathrm{SL}}}\right)\right]. \tag{8}$$

Here, x_i^L represents the mole fraction of substance i in the liquid (L) phase. Δh_{0i}^{SL} and T_{0i}^{SL} are the enthalpy of melting and temperature of melting of pure substance i, respectively. They can be measured independently, e.g., using differential scanning calorimetry (DSC). In the case of compounds that decompose during melting (e.g., amino acids), the two pure-component properties can be treated as adjustable parameters [66]. The PC-SAFT model can be used to calculate the fugacity coefficients of substance i in the mixture (φ_i^L) and as pure component (φ_{0i}^L). The ratio of the fugacity coefficient in the mixture to the fugacity coefficient of pure component gives the activity coefficient γ_i^L.

To estimate the pure-component PC-SAFT parameters for solid solute compounds, binary solubility data in one solvent can be used since usually neither liquid-density nor vapor-pressure data of the pure solute are available.

The applicability of the PC-SAFT model to calculate and estimate organic-solute solubility is demonstrated here for the drug substance paracetamol which is commonly used for the relief of fever, headaches, and other minor aches and pains. There exist extensive sets of experimental solubility data for paracetamol in pure solvents and in solvent mixtures. The experimentally measured melting temperature of 441.2 K and the melting enthalpy of 26 kJ/mol from Manzo and Ahumada [67] were used for the solubility calculations. The original PC-SAFT model with association term was applied to calculate the solubility of paracetamol in different solvents and solvent mixtures. Paracetamol is modeled as an associating compound with two different types of association sites (A and B), each of them having two sites. Both types were assumed to be of equal strength. Hence, five pure-component parameters had to be determined for paracetamol: segment number, segment diameter, dispersion energy, association energy, and association volume. These parameters for paracetamol, as well as the binary parameter k_{ij} of paracetamol/water, were identified from its experimental solubility data in water from [68].

Using these parameters and the binary parameter k_{ij} for each paracetamol/solvent system, solubilities in other solvents such as acetone, ethanol, and toluene can also be modeled. The correlation results and the comparison to experimental data are shown in Fig. 15. The results reveal the ability of the PC-SAFT model to provide a description of the solubility of a complex molecule like paracetamol in different solvents that is remarkably consistent with the experiments.

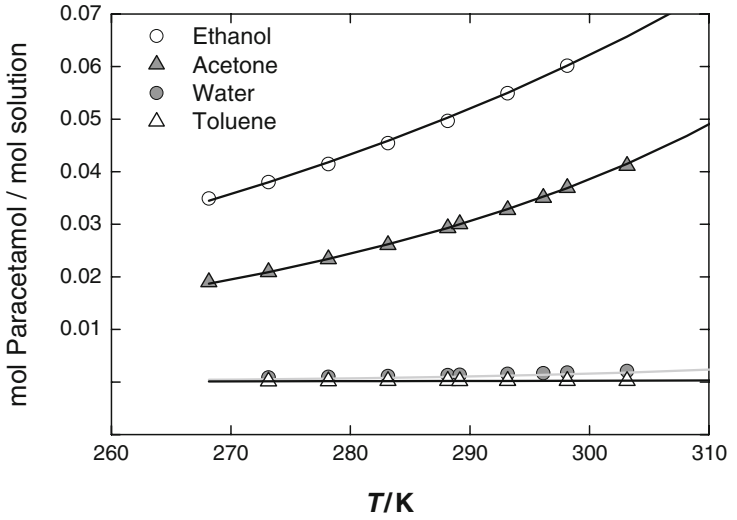

Fig. 15 Solubility of paracetamol in different pure solvents. *Symbols* are experimental data from [68]. *Solid lines* represent correlation results of PC-SAFT

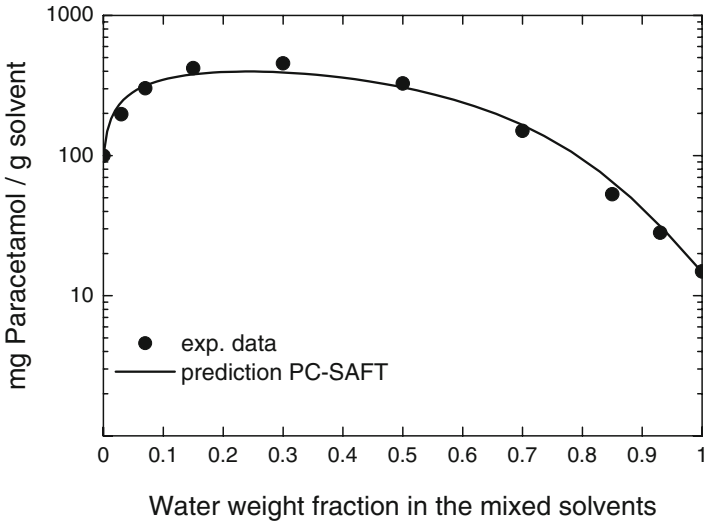

Fig. 16 Solubility of paracetamol in water/acetone mixtures of different compositions at 25°C. *Symbols* are experimental data from [69] and the *solid line* represents the model prediction with PC-SAFT

Based on the modeling of the solubility in pure solvents and the determined binary parameters, the solubility in mixed solvents can be predicted. Figure 16 shows the prediction results for the paracetamol solubility in a solution of water and acetone at 25°C as an example for a mixture of one polar and one hydrophilic solvent.

The experimental data exhibit a non-linear and non-monotonic solubility behavior. Starting from the binary system paracetamol/acetone (solubility about 100 mg paracetamol/g acetone) the solubility increases extremely as a small amount of water is added (up to 450 mg paracetamol/g mixed solvent at a water weight fraction of 0.3 in the solvent mixture). This happens although paracetamol is much less soluble in pure water (about 15 mg/g water) than in acetone. PC-SAFT predicts this behavior without fitting any parameters to the ternary mixture, as shown in Fig. 16.

The non-linear and non-monotonic behavior is also observed for the solubility of adipic acid in solvent mixtures of 1-propanol and 1,4-dioxane at different temperatures in the range 25–60°C. 1-propanol is a much worse solvent for adipic acid than 1,4-dioxane. Nevertheless, adding of 1-propanol to 1,4-dioxane up to a concentration of about 25% enhances the adipic-acid solubility, which is also predicted by PC-SAFT, as depicted in Fig. 17. A further increasing amount of 1-propanol, however, results in the decline of the adipic acid solubility, which is again also predicted by PC-SAFT. Given that the adipic acid solubilities in the mixed solvents are predicted using the parameters identified from solubility data in the pure solvents, the results for adipic-acid solubility are considered to be very satisfactory.

To account for pH effects on the solubility of, e.g., amino acids in water, a simple approach can be applied, as proposed by Gupta and Heidemann [70], using the pK_a values of the respective amino acids to calculate the solubility at different pH:

$$x_i^{\mathrm{L}} = x_{i,\,\mathrm{isoelectric}}^{\mathrm{L}} \cdot \left(1 + \frac{10^{-\mathrm{pH}}}{K_{a1}} + \frac{K_{a2}}{10^{-\mathrm{pH}}}\right). \tag{9}$$

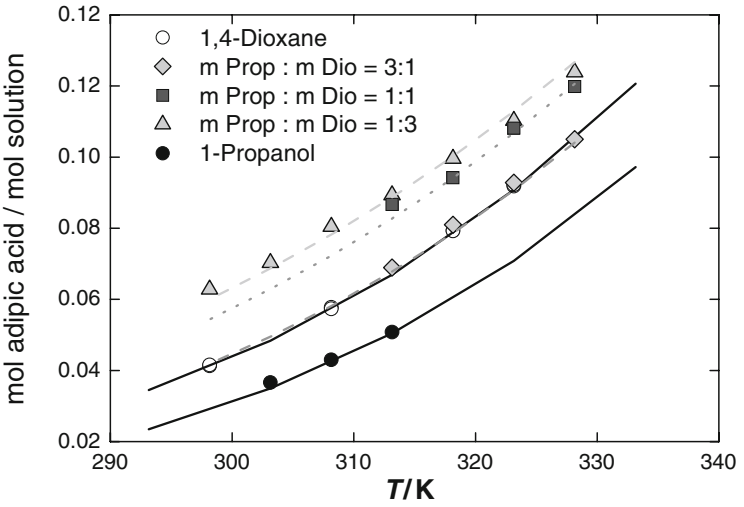

Fig. 17 Solubility of adipic acid in 1-propanol, 1,4-dioxane, and in mixtures of 1-propanol and 1,4-dioxane. *Solid lines* are modeling results using PC-SAFT. *Dashed lines* are PC-SAFT predictions

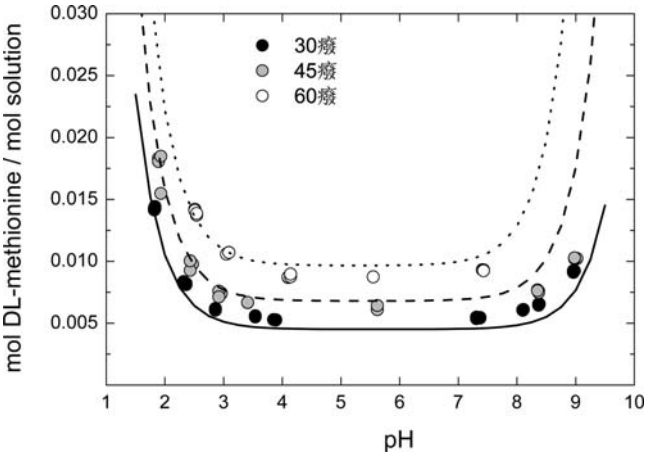

Fig. 18 Solubility of DL-methionine in aqueous solutions as a function of pH values. *Symbols* represent experimental data from [66], and *lines* represent PC-SAFT calculation results

The solubility at the isoelectric point $x_i^{\mathrm{L},\ \mathrm{isoelectric}}$ at different temperatures can be calculated using PC-SAFT according to Eq. 8. In Fig. 18 the experimental data and calculation results for the solubility of the amino acid DL-methionine at three different temperatures and altered pH values are presented [66]. Using the pK_a values of DL-methionine, the calculation results of the solubility in HCl/NaOH solutions show good agreement in the isoelectrical band and also in basic and acidic environments.

Considering solid–liquid equilibria, melting systems can show solid complexes, which are formed due to strong hydrogen-bonding interactions between the participating species. Such complexes are often referred to as intermolecular compounds, adducts (or addition compounds), hydrates (in aqueous systems), or solvates (in non-aqueous systems). These complexes usually exist only in the solid phase. To describe the solubility of such hydrates and solvates, the complex formation can be treated like a chemical reaction between the liquid species (e.g., A and B) and described by the corresponding equilibrium constants [71]:

$$|\nu_A| A^{(L)} + |\nu_B| B^{(L)} \Leftrightarrow A_{|\nu_A|} B_{|\nu_B|}{}^{(S)}. \tag{10}$$

Assuming again a pure solid complex, the equilibrium constant for the reaction in Eq. 10 can be expressed as a function of liquid concentrations and activity coefficients according to:

$$K_a = \prod_i a_i^{\nu_i} = (x_A \gamma_A)^{\nu_A} (x_B \gamma_B)^{\nu_B}. \tag{11}$$

Here, the activity coefficient of component A and B, respectively, can again be calculated as the ratio of the fugacity coefficient of the component in the mixture and the fugacity coefficient of the pure component, both of which are again calculated with PC-SAFT.

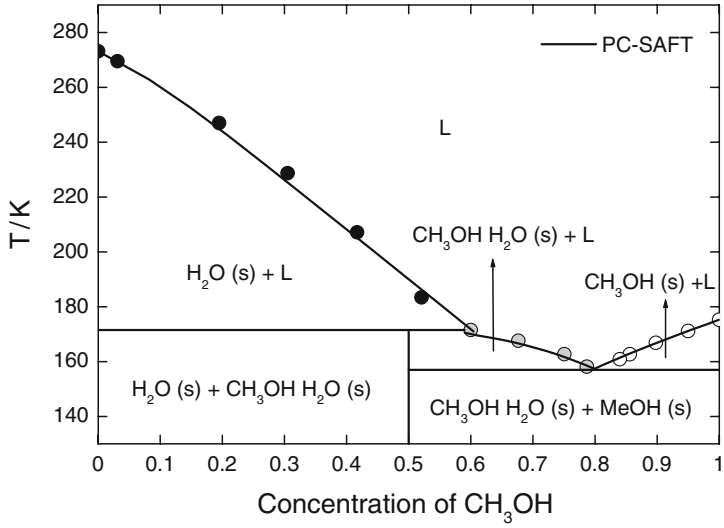

Fig. 19 Melting phase diagram of methanol/water with monohydrate formation. *Symbols* are experimental data from [72, 73]. *Solid lines* are calculation results of PC-SAFT

The equilibrium constant K_a is determined using the pseudo-melting properties of the solid complex as described in [71]. To calculate the solubility of the solid complex, Eq. 11 has to be solved iteratively.

Figure 19 illustrates the power of this approach to describing solid–liquid equilibria with solid-complex formation for the example methanol–water. In addition to the crystallization of pure methanol and of pure water, this system forms a 1:1 complex [methanol monohydrate $CH_3OH \cdot H_2O(s)$]. The various phase regions are indicated in the phase diagram. The calculated lines characterize the phase boundaries of solid–liquid and solid–solid equilibrium. The type of solid (either pure component or complex) is also identified. As can be seen, using the same set of parameters to calculate the solubility of the two pure components methanol and water, the crystallization curve of the monohydrate could also be modeled in a very good agreement with experimental data.

The excellent match with experiments is also confirmed for the ternary system bisphenol A (BPA)/phenol/water, as depicted in Fig. 20 for a water concentration of 30 mol%. In this system, BPA and phenol form a solid 1:1 complex. The symbols represent the literature data from Kwok et al. [74] and the lines are calculation results using PC-SAFT for the solubilities of pure BPA, pure phenol, and BPA/phenol complex. Again, PC-SAFT is able to describe the solubility of pure solids and of solid complex in a very good agreement with the experimental data.

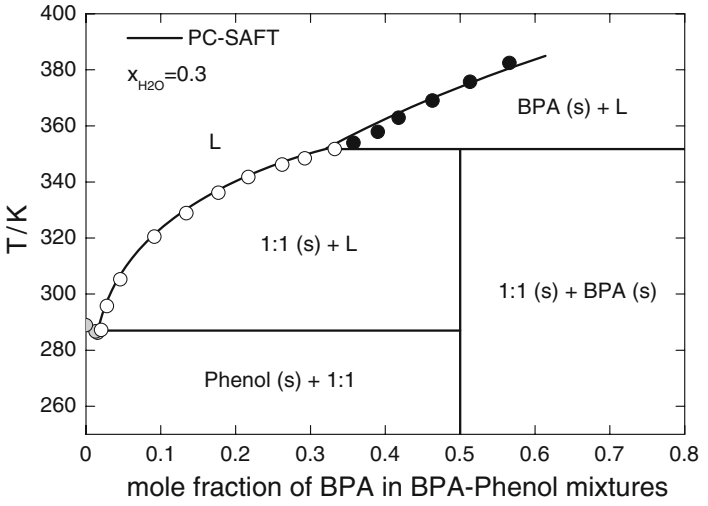

Fig. 20 Phase diagram of the ternary BPA/phenol/water system at a water concentration of 30 mol%. Comparison of experimental data (*symbols*) from [74] with modeling results using PC-SAFT (*lines*)

5 Polymer Systems

Due to the large differences in molecular size of polymers and solvents, and due to the molar-mass distribution of a polymer, modeling of polymer systems is always challenging. The PC-SAFT model is based on the hard-chain reference system and thus explicitly considers the attractive interactions of chain molecules instead of those of the unbonded segments. Therefore, PC-SAFT is particularly suitable for describing polymer systems [19, 61, 75–84].

Compared to low molecular weight substances, the determination of pure-component parameters for polymers is more difficult because polymer vapor-pressure data are not accessible. A methodology for the identification of pure-component parameters for polymers is the simultaneous fitting of liquid densities and phase-equilibrium data of one binary system [19, 76]. It has been shown in many applications that the so-determined pure-component parameters are suitable for different mixtures and can thus be regarded as characteristic for a specific polymer. For example, the pure-component parameters for low-density polyethylene (LDPE) were determined by fitting the liquid densities of LDPE and the experimental binary data of LDPE/ethene. The same pure-component parameters of LDPE were then subsequently used to model the cloud points of 5 wt.% LDPE in different solvents (ethane, propane, propene, 1-butene, and *n*-butane) using one k_{ij} for each respective binary system [85]. The correlation results and the comparison to the experimental data from [86] are depicted in a pressure–temperature diagram in Fig. 21, which shows on the one hand the good agreement between the modeling results and experimen-

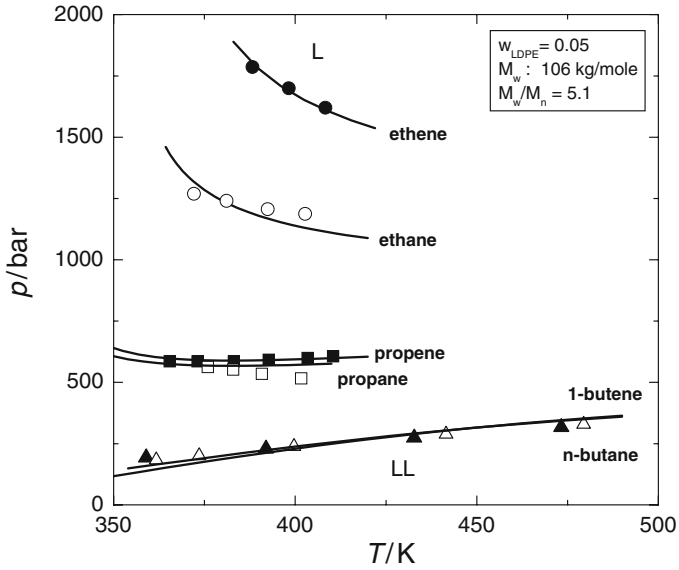

Fig. 21 High-pressure equilibrium for mixtures of low-density polyethylene (LDPE) with varying solvents: ethene, ethane, propene, propane, 1-butene, and *n*-butane. Comparison of experimental cloud-point measurements [86] to calculation results of the PC-SAFT equation of state. (LDPE-1-butene *open triangles*)

tal data and proves on the other hand the applicability of the described method for determination of the pure-component parameters of polymers.

Furthermore, the influence of molecular weight on phase behavior can be taken into account when applying PC-SAFT. By only varying the segment number proportional to the molecular weight, the solubility of various polyethylene samples in ethene can be predicted by PC-SAFT, as presented in Fig. 22 for four molecular weights ranging from 19 to 129 kg/mol.

The phase behavior of copolymers is influenced by the nature of the different monomers as well as by the monomer composition within the copolymer backbone. An extension of the PC-SAFT equation of state to heterosegment molecules also allows the composition of the different monomers in the copolymer chain to be accounted for and, to a certain extent, the arrangement of the monomers also [85]. The underlying molecular model of a copolymer consisting of α-segments and β-segments is shown in Fig. 23. The modeling of a copolymer–solvent mixture requires the appropriate pure-component parameters of the respective homopolymer segments and of the solvent. The binary parameters of the homopolymer–solvent systems ($k_{\alpha-S}$, $k_{\beta-S}$) can be determined from fitting the phase equilibrium data of the respective homopolymers/solvent systems. To describe the copolymer system, if necessary, one additional binary interaction parameter can be fitted to binary copolymer data, which accounts for the dispersive interactions between the unlike homopolymer segments ($k_{\alpha-\beta}$) in the copolymer solution.

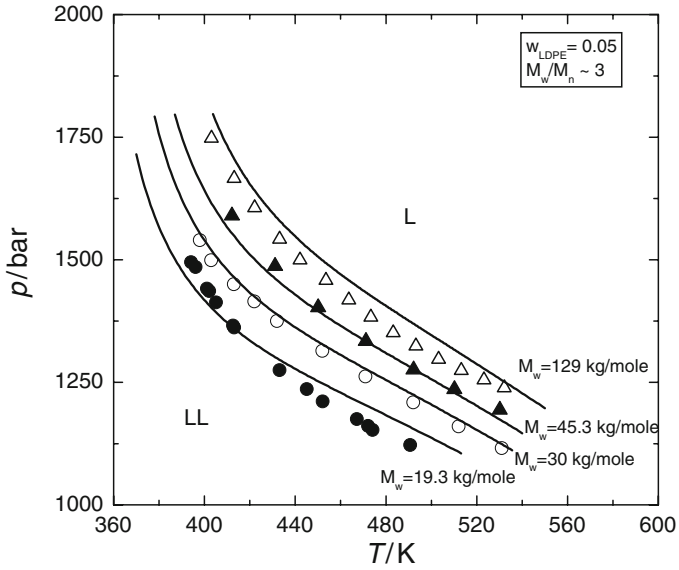

Fig. 22 Experimental cloud-point data (*symbols*) of polyethylene samples with different molecular weights [87] compared to the prediction results using PC-SAFT (*lines*)

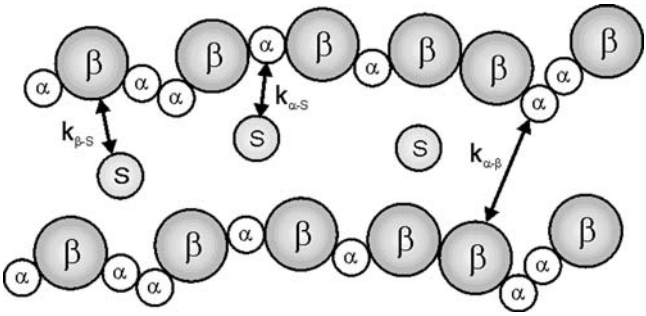

Fig. 23 Molecular model for a copolymer of type poly(α-*co*-β), composed of segments α and β in interaction with a solvent S. There exist three types of interactions α-β, α-S, as well as β-S, which are described by three binary interaction parameters

Applications of the PC-SAFT equation of state to polyolefin copolymers [85], branched polyolefins [80], copolymers and terpolymers of ethylene, and carboxylic acid esters [76, 78, 88] revealed the strength of this methodology.

This is illustrated in Fig. 24 for the solubility of poly(ethylene-*co*-ethyl acrylate) [poly(E-*co*-EA)] in ethene, which compares experimental cloud-point-pressure data to modeling results of PC-SAFT. Starting from the homopolymer polyethylene, an increasing ethyl-acrylate content in the copolymer backbone first leads to an increasing solubility of the poly(E-*co*-EA) copolymers and thus to lower cloud-point pressures. After passing through a minimum at an EA content of about 30 mol% in the polymer backbone, the solubility again decreases with rising EA content.

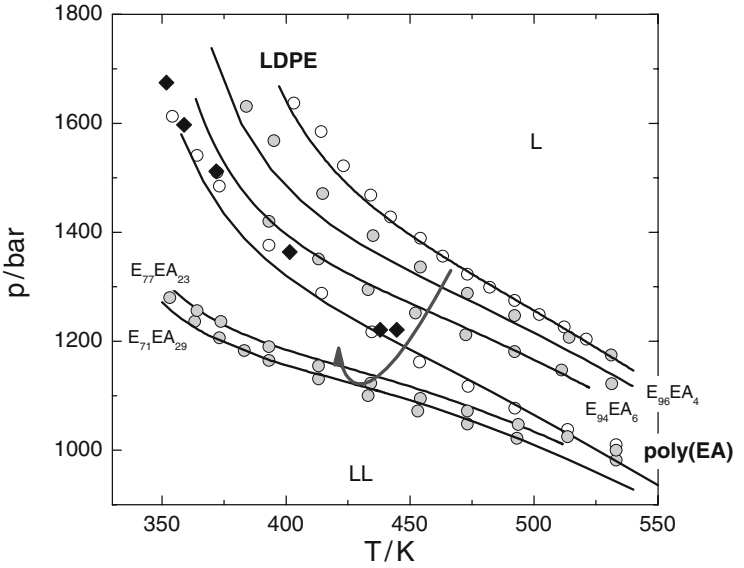

Fig. 24 Cloud-point pressure curves for mixtures of ethene and poly(E-*co*-EA) for various monomer compositions. Comparison of experimental data (*symbols*) from Lora et al. [89] and calculations obtained with the PC–SAFT model (*lines*). Indices give the ethylene and ethyl-acrylate compositions (mol%) in the copolymer molecules, respectively

The remarkably good agreement of experimental data and the PC-SAFT calculations for the different copolymer/solvent mixtures is obtained using only the information of homopolymer systems as well as one additional binary interaction parameter $k_{\alpha\beta}$. However, even without fitting the binary parameter $k_{\alpha\beta}$, PC-SAFT did qualitatively predict the non-monotonic solubility behavior. None of the parameters is dependent on temperature or copolymer composition. Thus, PC-SAFT allows for the estimation and, to a certain extent, even predicts the cloud-point behavior of copolymer systems for a wide range of pressures, temperatures, and copolymer compositions.

The parameter identification for copolymer systems might be challenging if experimental data for the respective homopolymers is scarce or not available. This is the case, e.g., for methacrylic acid copolymers where no experimental phase-equilibrium data for the homopolymer poly(methacrylic acid) [poly(MAA)] in any solvent is available. Poly(ethylene-*co*-methacrylic acid) [poly(E-*co*-MAA)] is an example of a copolymer that consists of one non-polar-monomer group (ethylene) and one associating monomer group (methacrylic acid). The methacrylic acid (MAA) content in the copolymers in Fig. 25 varies from 1% to 10.3 mol% and the copolymer molecular weights M_w range from 32 to 63 kg/mol, with a polydispersity index of about 3.3. To characterize the homopolymer poly(MAA), five pure-component parameters are required. These parameters can be determined from fitting the cloud-point data of one copolymer/solvent system,

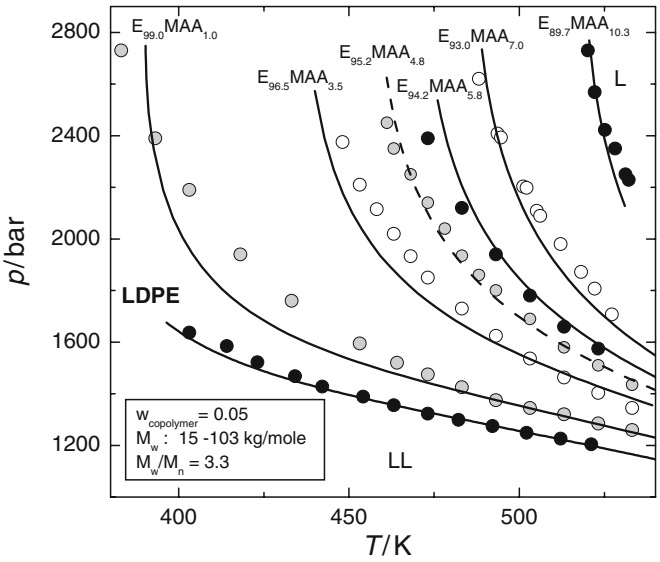

Fig. 25 Cloud-point pressure curves for mixtures of ethene and poly(E-*co*-MAA). The dashed line represents correlation results from the parameter determination of PC-SAFT. Experimental data taken from Buback and Latz [90] (*circles*) are compared with PC-SAFT predictions (*solid lines*). *Indices* give the ethylene and methacrylic-acid content (mol%) in the copolymer samples

e.g., poly($E_{95.2} - co$-$MAA_{4.8}$)/ethene. Moreover, the polydispersity of the polymers has also a profound effect on the phase behavior. To account for that, the polydisperse poly(E-*co*-MMA) copolymers were characterized by two representative pseudo-components [61]. Using that approach, the solubility of a whole series of these copolymers having different comonomer compositions and molecular weights could be predicted in very satisfactory agreement with the experimental cloud-point pressures. This demonstrates that reasonable model parameters can be obtained for complex polymeric systems, even if experimental data for the homopolymers is scare or not available.

When the parameters of the homopolymers as well as the required binary parameters are known, even more complex polymers (e.g., terpolymers) can be modeled. Figure 26 shows the cloud-point pressure curves for terpolymers that consist of monomers that have very different functionalities: the non-polar ethylene, the polar butyl methacrylate (BMA), and the associating monomer methacrylic acid, poly(E-*co*-BMA-*co*-MAA). The solvent is again ethene. The lines represent pure predictions of the phase behavior using the PC-SAFT parameters obtained for the binary homopolymer/ethene systems and the respective copolymer/ethene systems without any additional parameter fitting or readjustment. It can be seen that the experimentally observed effects of the terpolymer composition on solubility are well predicted by the PC-SAFT model.

Finally, the influence of cosolvents can also be predicted by PC-SAFT. Figure 27 illustrates a typical example of a mixture that consists of the copolymer

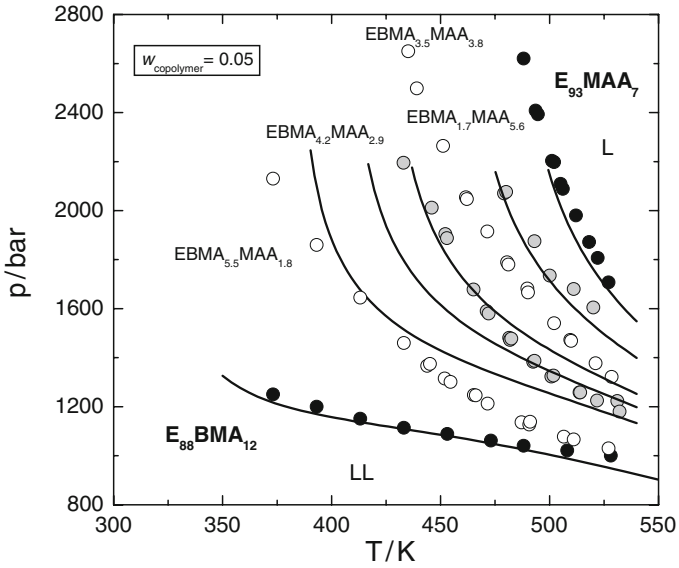

Fig. 26 Cloud-point pressure curves for the copolymers poly(E-*co*-BMA) and poly(E-*co*-MAA), as well as for the terpolymers poly(E-*co*-BMA-*co*-MAA) in ethene. Comparison of experimental data from [61, 78, 90] and predictions obtained by PC-SAFT

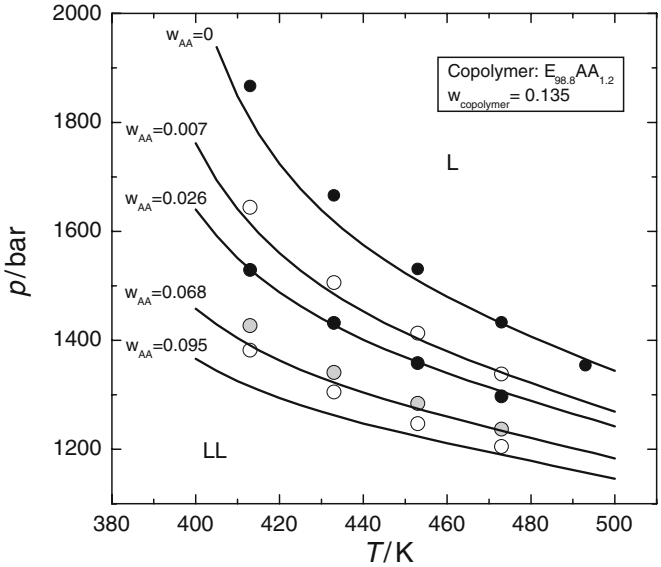

Fig. 27 Influence of acrylic acid (AA) on the cloud-point pressures of poly(ethylene-*co*-acrylic acid) in ethene**.** Ethylene content in the copolymer backbone is 98.9%. w_{AA} denotes the acrylic-acid weight fraction in the polymer-free system. Experimental data from Wind [91] (*symbols*) are compared with predictions via PC-SAFT (*solid lines*)

poly(ethene-*co*-acrylic acid) (EAA), ethene and different concentrations of the cosolvent acrylic acid (AA). Although all model parameters were previously determined from pure-component and binary data, the influence of the cosolvent is adequately predicted by PC-SAFT. Again, all parameters used are independent of temperature and concentration. The very good agreement of the experimental data and the predictions demonstrate that the PC-SAFT model is also capable of almost quantitatively predicting the influence of a cosolvent/comonomer on polymer solubility.

6 Summary

State-of-the-art thermodynamic models have a sound physical basis. As shown for the PC-SAFT equation of state they can be successfully applied to a whole variety of substances ranging from small gas molecules up to organic solvents and polymeric systems. Recent developments and modifications further extended the physical basis by explicitly accounting for complex intermolecular interactions such as association, polar interactions, and induced interactions that only occur in mixtures but not in the pure components. These achievements ensured a remarkably improved ability of the models to correlate and even to predict thermodynamic properties of very asymmetric and complex mixtures over a wide range of component properties and system conditions.

References

1. Chapman WG, Gubbins KE, Jackson G,Radosz M (1989) Fluid Phase Equilibr 52:31
2. Chapman WG, Gubbins KE, Jackson G, Radosz M (1990) Ind Eng Chem Res 29:1709
3. Huang SH, Radosz M (1990) Ind Eng Chem Res 29:2284
4. Huang SH, Radosz M (1991) Ind Eng Chem Res 30:1994
5. Carnahan NF, Starling KE (1969) J Chem Phys 51:635
6. Alder BJ, Young DA, Marx MA (1972) J Chem Phys 56:3013
7. Chen SS, Kreglewski A (1977) Ber Bunsen Phys Chem 81:1048
8. Wertheim MS (1987) J Chem Phys 87:7323
9. Song YH, Lambert SM, Prausnitz JM (1994) 10. Ind Eng Chem Res 33:1047
10. Chang J, Sandler SI (1994) Mol Phys 81:745
11. Gil-Villegas A, Galindo A, Whitehead PJ, Mills SJ, Jackson G, Burgess AN (1997) J Chem Phys 106:4168
12. Hino T, Prausnitz JM (1997) Fluid Phase Equilib 138:105
13. Banaszak M, Chiew YC, Radosz M (1993) Phys Rev E 48:3760
14. Tavares FW, Chang J, Sandler SI (1997) Fluid Phase Equilibr 140:129
15. Chapman WG (1990) J Chem Phys 93:4299
16. Muller EA, Vega LF, Gubbins KE (1994) Mol Phys 83:1209
17. Blas FJ, Vega LF (1997) Mol Phys 92:135
18. Gross J, Sadowski G (2001) Ind Eng Chem Res 40:1244
19. Gross J, Sadowski G (2002) Ind Eng Chem Res 41:1084
20. Gross J, Sadowski G (2002) Ind Eng Chem Res 41:5510
21. Tumakaka F, Sadowski G (2004) Fluid Phase Equilib 217:233

22. Muller EA, Gubbins KE (2001) Ind Eng Chem Res 40:2193
23. Gubbins KE, Gray CG (1972) Mol Phys 23:187
24. Cotterman RL, Prausnitz JM (1986) AIChE J 32:1787
25. Cotterman RL, Prausnitz JM (1986) AIChE J 32:1799
26. Walsh JM, Jin G, Donohue MD (1991) Fluid Phase Equilibr 65:209
27. Kraska T, Gubbins KE (1996) Ind Eng Chem Res 35:4727
28. Kraska T, Gubbins KE (1996) Ind Eng Chem Res 35:4738
29. Xu K, Li Y, Liu W (1998) 142:55
30. Tang Y, Wang Z, Lu BY (2001) Mol Phys 99:65
31. Sear RP (1996) Phys Rev Lett 76:2310
32. Jog PK, Chapman WG (1999) Mol Phys 97:307
33. Gross J, Vrabec J (2006) AIChE J 52:1194
34. Saager B, Fischer J (1992) Fluid Phase Equilibr 72:67
35. Saager B, Fischer J, Neumann M (1991) Molec Simul 6:27
36. Kleiner M, Gross J (2006) AIChE J 52:1951
37. Wertheim M (1977) Mol Phys 34:1109
38. Wertheim M (1979) Mol Phys 37:83
39. Cameretti LF, Sadowski G, Mollerup JM (2005) Ind Eng Chem Res 44:3355
40. Cameretti LF, Sadowski G (2007) Chem Eng Proc 47:1018
41. Chapman WG, Jackson G, Gubbins KE (1988) Mol Phys 65:1057
42. Wertheim MS (1984) J Stat Phys 35:19
43. Wertheim MS (1984) J Stat Phys 35:35
44. Wertheim MS (1986) J Chem Phys 85:2929
45. Barker JA, Henderson D (1967) J Chem Phys 47:2856
46. Barker JA, Henderson D (1967) J Chem Phys 47:4714
47. Wolbach JP, Sandler IS (1998) Ind Eng Chem Res 37:2917
48. Shen SB, Wang YR, Shi J, Benson GC, Lu BCY (1990) J Chem Thermodyn 22:387
49. Mcglashan M, Morcom KW (1961) T Faraday Soc 57:581
50. Holleman T (1965) Physica 31:49
51. Wilding WV, Wilson LC, Wilson GM (1987) Fluid Phase Equilibr 36:67
52. Artal M, Embid JM, Marras G, Velasco I, Otin S (1995) J Chem Eng Data 40:1154
53. Akamatsu Y, Ogawa H, Murakami S (1987) Thermochim Acta 113:141
54. Kleiner M, Sadowski G (2007) J Phys Chem C 111:15544
55. Danov SM, Obmelyukhina TN, Chubarov GA, Balashov AL, Dolgopolov AA (1990) J Appl Chem USSR 63:566
56. Frolova EA, Ershova TP, Stepanova VA, Pavlov SY (1979) Osnov Organ Sintez i Neftekhimiya 11:90
57. Fu J, Wang K, Hu Y (1988) J Chem Ind Eng China 39:64
58. Lloyd BA, Thompson SO, Ferguson JB (1937) Can J Research 15B:98
59. Clausse D, Lambert JP, Guigon P, Boudehen-Boiveaut A (1988) Calorim Anal Therm 19: C21.1
60. Chubarov GA, Danov SM, Brovkina GV, Kupriyanov TV (1978) J Appl Chem USSR 51:434
61. Kleiner M, Tumakaka F, Sadowski G, Latz H, Buback M (2006) Fluid Phase Equilibr 241:113
62. Weltner W (1955) J Am Chem Soc 77:3941
63. Miyamoto S, Nakamura S, Iwai Y, Arai Y (2000) J Chem Eng Data 45:857
64. Laugier S, Richon D, Renon H (1990) Fluid Phase Equilibr 54:19
65. Kato M (1988) J Chem Eng Data 33:499
66. Fuchs D, Fischer J, Tumakaka F, Sadowski G (2006) Ind Eng Chem Res 45:6578
67. Manzo RH, Ahumada AA (1990) J Pharm Sci 79:1109
68. Granberg RA, Rasmuson AC (1999) J Chem Eng Data 44:1391
69. Granberg RA, Rasmuson AC (2000) J Chem Eng Data 45:478
70. Gupta RB, Heidemann RA (1990) AIChE J 36:333
71. Tumakaka F, Prikhodko IV, Sadowski G (2007) Fluid Phase Equilibr 260:98
72. Miller GA, Carpenter DK (1964) J Chem Eng Data 9:371
73. Ott JB, Goates JR, Waite BA (1979) J Chem Thermodyn 11:739

74. Kwok KS, Chan HC, Chan CK, Ng KM (2005) Ind Eng Chem Res 44:3788
75. Cheluget EL, Bokis CP, Wardhaugh L, Chen CC, Fisher J (2002) Ind Eng Chem Res. 41:968
76. Tumakaka F, Gross J, Sadowski G (2002) Fluid Phase Equilibr 194:541
77. Lindvig T, Michelsen ML, Kontogeorgis GM (2004) Ind Eng Chem Res 43:1125
78. Becker F, Buback M, Latz H, Sadowski G, Tumakaka F (2004) Fluid Phase Equilibr 215:263
79. Arce P, Aznar M (2005) Fluid Phase Equilibr 238:242
80. Dominik A, Chapman WG (2005) Macromolecules 38:10836
81. van Schilt MA, Wering RM, van Meerendonk WJ, Kemmere MF, Keurentjes JTF, Kleiner M, Sadowski G, de Loos TW (2005) Ind Eng Chem Res 44:3363
82. Hungenberg KD, Nieken U, Zollner K, Gao J, Szekely A (2005) Ind Eng Chem Res 44:2518
83. Spyriouni T, Economou IG (2005) Polymer 46:10772
84. Arce P, Mattedi S, Aznar M (2006) Fluid Phase Equilibr 246:52
85. Gross J, Spuhl O, Tumakaka F, Sadowski G (2003) Ind Eng Chem Res 42:1266
86. Hasch BM, Lee SH, McHugh MA (1996) J Appl Polym Sci 59:1107
87. Latz H (2004) Kinetische und thermodynamische Untersuchungen der Hochdruck-Copolymerisation von Ethen mit (Meth)Acrylsäureestern. Georg-August-Universität zu Göttingen, Göttingen
88. Tumakaka F, Sadowski G, Latz H, Buback M (2007) J Supercrit Fluid 41:461
89. Lora M, Rindfleisch F, McHugh MA (1999) J Appl Polym Sci 73:1979
90. Buback M, Latz H (2003) Macromol Chem Physic 204:638
91. Wind RW (1992) Untersuchungen zum Phasenverhalten von Mischungen aus Ethylen, Acrylsäure und Ethylen-Acrylsäure-Copolymeren unter hohem Druck. TH Darmstadt, Darmstadt

Appendix

This section provides a summary of the equation of state contributions to the residual Helmholtz energy according to PC-SAFT (Eq. 3).

Hard-Chain Reference Contribution

The Helmholtz energy of the hard-chain reference term is given as:

$$\frac{A^{\mathrm{hc}}}{NkT} = \bar{m} \cdot \frac{A^{\mathrm{hs}}}{N_s kT} - \sum_i x_i (m_i - 1) \cdot \ln g_{ii}^{\mathrm{hs}}(d_{ii}), \tag{12}$$

where x_i is the mole fraction of chains of component i, m_i is the number of segments in a chain and the mean segment number in the mixture is defined as:

$$\bar{m} = \sum_i x_i m_i. \tag{13}$$

The Helmholtz energy for the hard-sphere segments A^{hs}/NkT in Equ. 12 is given on a per-segment basis as:

$$\frac{A^{\mathrm{hs}}}{N_s kT} = \frac{1}{\zeta_0}\left[\frac{3\zeta_1\zeta_2}{(1-\zeta_3)} + \frac{\zeta_2^3}{\zeta_3(1-\zeta_3)^2} + \left(\frac{\zeta_2^3}{\zeta_3^2} - \zeta_0\right) \cdot \ln(1-\zeta_3)\right], \tag{14}$$

where N_s is related to the number of hard-spheres, the radial pair distribution function for the hard-sphere fluid is given by:

$$g_{ij}^{\mathrm{hs}}(d_{ij}) = \frac{1}{(1-\zeta_3)} + \left(\frac{d_i d_j}{d_i + d_j}\right)\frac{3\zeta_2}{(1-\zeta_3)^2} + \left(\frac{d_i d_j}{d_i + d_j}\right)^2 \frac{2\zeta_2^2}{(1-\zeta_3)^3}, \tag{15}$$

and ζ_n is defined as:

$$\zeta_n = \frac{\pi}{6}\cdot\rho\sum_i x_i m_i d_i^n \qquad n = \{0,1,2,3\}. \tag{16}$$

The temperature-dependent segment diameter is obtained as:

$$d_i = \sigma_i\left(1 - 0.12\cdot\exp\left(-3\cdot\frac{\varepsilon_i}{kT}\right)\right), \tag{17}$$

where σ_i is the temperature-independent segment diameter and ε_i/k is the depth of the pair-potential.

Dispersion Contribution

The dispersion contribution to the Helmholtz energy is given by:

$$\begin{aligned}\frac{A^{\mathrm{disp}}}{NkT} &= -2\pi\rho\cdot I_1(\eta,\bar{m})\cdot\sum_i\sum_j x_i x_j m_i m_j\left(\frac{\varepsilon_{ij}}{kT}\right)\sigma_{ij}^3 \\ &-\pi\rho\cdot\bar{m}\cdot C_1\cdot I_2(\eta,\bar{m})\cdot\sum_i\sum_j x_i x_j m_i m_j\left(\frac{\varepsilon_{ij}}{kT}\right)^2\sigma_{ij}^3\end{aligned} \tag{18}$$

with

$$\begin{aligned}C_1 &= \left(1 + Z^{hc} + \rho\frac{\partial Z^{hc}}{\partial\rho}\right)^{-1} \\ &= \left(1 + \bar{m}\frac{8\eta - 2\eta^2}{(1-\eta)^4} + (1-\bar{m})\frac{20\eta - 27\eta^2 + 12\eta^3 - 2\eta^4}{[(1-\eta)(2-\eta)]^2}\right)^{-1}.\end{aligned} \tag{19}$$

The power series I_1 and I_2 depend only on density and segment number according to:

$$I_1(\eta,\bar{m}) = \sum_{i=0}^{6} a_i(\bar{m})\cdot\eta^i, \tag{20}$$

$$I_2(\eta,\bar{m}) = \sum_{i=0}^{6} b_i(\bar{m})\cdot\eta^i, \tag{21}$$

where the coefficients $a_i(m)$ and $b_i(m)$ are functions of the segment number:

$$a_i(\bar{m}) = a_{0i} + \frac{\bar{m}-1}{\bar{m}} a_{1i} + \frac{\bar{m}-1}{\bar{m}} \frac{\bar{m}-2}{\bar{m}} a_{2i}, \tag{22}$$

$$b_i(\bar{m}) = b_{0i} + \frac{\bar{m}-1}{\bar{m}} b_{1i} + \frac{\bar{m}-1}{\bar{m}} \frac{\bar{m}-2}{\bar{m}} b_{2i}. \tag{23}$$

The universal model constants in Eqs. 22 and 23 are given in the work of Gross and Sadowski [18].

Association Contribution

The association contribution to the Helmholtz energy is given as:

$$\frac{A^{\text{assoc}}}{NkT} = \sum_i x_i \sum_{\mathrm{A}_i=1}^{n\text{site}} \left(\ln X^{\mathrm{A}_i} - \frac{X^{\mathrm{A}_i}}{2} + \frac{1}{2} \right). \tag{24}$$

It is important to note that the summation runs over all association sites of the molecule i where X^{A_i} is the fraction of the free molecules i that are not bonded at the association site A:

$$X^{\mathrm{A}_i} = \left(1 + \rho \cdot \sum_j x_j \sum_{\mathrm{B}_j}^{n\text{sites}} X^{\mathrm{B}_j} \cdot \Delta^{\mathrm{A}_i \mathrm{B}_j} \right)^{-1} \tag{25}$$

with

$$\Delta^{\mathrm{A_j B_j}} = g_{ij}^{\mathrm{hs}}(d_{ij}) \cdot \kappa^{\mathrm{A_i B_j}} \cdot \sigma_{\mathrm{ij}}^3 \left(\exp\left(\frac{\varepsilon^{\mathrm{A_i B_j}}}{kT} \right) - 1 \right), \tag{26}$$

where $g_{\mathrm{ij}}^{\mathrm{hs}}(d_{\mathrm{ij}})$ is the pair distribution function of hard spheres given in Eq. 15.

Dipolar Contribution

The Helmholtz energy contribution from dipolar interactions of induced dipoles is given as:

$$\frac{A^{\text{dipole}}}{NkT} = \frac{A'^{\text{dipole}}}{NkT} + \frac{1}{2} kT \sum_{\mathrm{i}} x_{\mathrm{i}} \alpha_{\mathrm{i}} \left(\frac{1}{x_{\mathrm{i}}} \frac{\partial}{\partial \mu_{\mathrm{i}}^{\mathrm{eff}}} \left(\frac{A'^{\text{dipole}}}{NkT} \right) \right)^2_{\rho,T}, \tag{27}$$

where α_i is the molecular polarizability and the term A'^{dipole}/NkT is defined as:

$$\frac{A'^{\text{dipole}}}{NkT} = \left(\frac{A_2'}{NkT} \left[1 - \frac{A_3'}{A_2'} \right]^{-1} \right). \tag{28}$$

The first-order and second-order perturbation terms in Eq. 28 are given as:

$$\frac{A_2'}{NkT} = -\pi \frac{\rho}{(kT)^2} \sum_{\mathrm{i}} \sum_{\mathrm{j}} x_{\mathrm{i}} x_{\mathrm{j}} \frac{\left(z_i^{\mathrm{A}} z_j^{\mathrm{A}} - z_i^{\mathrm{B}} z_j^{\mathrm{B}} \right)}{\sigma_{\mathrm{ij}}^3} \frac{n_{\mu,i}}{m_i} \frac{n_{\mu,j}}{m_j} J_{2,ij}^{DD}, \tag{29}$$

$$\frac{A_3'}{NkT} = -\frac{4}{3}\pi^2 \frac{\rho^2}{(kT)^3} \sum_i \sum_j \sum_k x_i x_j x_k \frac{\left(z_i^{\mathrm{A}} z_j^{\mathrm{A}} z_k^{\mathrm{A}} - z_i^{\mathrm{B}} z_j^{\mathrm{B}} z_k^{\mathrm{B}} \right)}{\sigma_{ij}\sigma_{ik}\sigma_{jk}} \frac{n_{\mu,i}}{m_i} \frac{n_{\mu,j}}{m_j} \frac{n_{\mu,k}}{m_k} J_{3,ijk}^{DD}, \tag{30}$$

where $n_{\mu,i}$ is the number of dipolar segments in the molecule and z_i^A and z_i^B are defined as:

$$z_{\mathrm{i}}^{\mathrm{A}} = (\mu_i^{\mathrm{eff}})^2 + 3kT\,\alpha_i, \tag{31}$$

$$z_i^B = 3kT\,\alpha_i. \tag{32}$$

In Eqs. 29 and 30, the expressions $J_{2,ij}^{DD}$ and $J_{3,ijk}^{DD}$ are given by simple power functions of the dimensionless density η as:

$$J_{2,ij}^{DD} = \sum_{n=0}^{4} \left(a_{n,ij} + b_{n,ij} \frac{\varepsilon_{ij}}{kT} \right) \eta^n, \tag{33}$$

$$J_{3,ijk}^{DD} = \sum_{n=0}^{4} c_{n,ijk} \eta^n \tag{34}$$

with the coefficients:

$$a_{n,ij} = a_{0n} + \frac{(m_i m_j)^{1/2} - 1}{(m_i m_j)^{1/2}} a_{1n} + \frac{(m_i m_j)^{1/2} - 1}{(m_i m_j)^{1/2}} \cdot \frac{(m_i m_j)^{1/2} - 2}{(m_i m_j)^{1/2}} a_{2n}, \tag{35}$$

$$b_{n,ij} = b_{0n} + \frac{(m_i m_j)^{1/2} - 1}{(m_i m_j)^{1/2}} b_{1n} + \frac{(m_i m_j)^{1/2} - 1}{(m_i m_j)^{1/2}} \cdot \frac{(m_i m_j)^{1/2} - 2}{(m_i m_j)^{1/2}} b_{2n}, \tag{36}$$

$$c_{n,ijk} = c_{0n} + \frac{(m_i m_j m_k)^{1/3} - 1}{(m_i m_j m_k)^{1/3}} c_{1n} + \frac{(m_i m_j m_k)^{1/3} - 1}{(m_i m_j m_k)^{1/3}} \cdot \frac{(m_i m_j m_k)^{1/3} - 2}{(m_i m_j m_k)^{1/3}} c_{2n}. \tag{37}$$

The universal model constants in Eqs. 35–37 are given in the work of Gross and Vrabec [33].

The effective dipole moments μ_i^{eff} is obtained by the implicit equation:

$$\mu_i^{\mathrm{eff}} = \mu_i - kT\alpha_i \left(\frac{1}{x_i} \frac{\partial}{\partial \mu_i^{\mathrm{eff}}} \left(\frac{A'^{\mathrm{dipole}}}{NkT} \right) \right)_{\rho,T}, \tag{38}$$

which has to be solved iteratively using Eq. 28.

If the molecular polarizability α_i is set to zero, the second term in Eq. 38 vanishes and the permanent dipole moment is used instead of the induced dipole moment. The second term in Eq. 27 also vanishes and thus, the dipolar term of Gross and Vrabec [33] is recovered, neglecting any effects due to the polarizability of the induced dipoles.

Density

The density at a given system pressure P^{sys} must be determined iteratively by adjusting the reduced density η until $P^{\text{calc}} = P^{\text{sys}}$. The number density of molecules ρ is calculated from η through:

$$\rho = \frac{6}{\pi}\eta \cdot \left(\sum_i x_i m_i d_i^3\right)^{-1}. \tag{39}$$

Pressure

Equations for the compressibility factor will be derived using the thermodynamic relation:

$$Z = 1 + \rho \left(\frac{\partial (A^{\text{res}}/nRT)}{\partial \rho}\right)_{T,n_{\text{i}}}, \tag{40}$$

where to n_i the number of moles of component i and and $nRT = NkT$.
The pressure can be calculated in units of $\text{Pa} = \text{N}/\text{m}^2$ by applying the relation:

$$P = Z \cdot kT\rho \cdot \left(10^{10}\frac{\mathring{A}}{m}\right)^3. \tag{41}$$

Fugacity Coefficient

The fugacity coefficient $\varphi_{\text{k}}(T,P)$ is related to the residual chemical potential according to:

$$RT \ln \phi_{\text{i}} = \left(\frac{\partial A^{\text{res}}}{\partial n_{\text{i}}}\right)_{T,V,n_{k\neq i}} - RT \ln Z. \tag{42}$$

Struct Bond
DOI:10.1007/430_2008_1

Phase Equilibria, Morphologies of Microphase Separation, and Interfacial Structures of Polymer Systems Studied by Equations of State

Honglai Liu, Hui Xu, Houyang Chen, Changjun Peng, and Ying Hu

Abstract Polymer blends or copolymers have multiscale complex structures that can be used as templates to prepare various complex materials. To regulate the mesoscale structures of these polymer blends or copolymers, there are three fundamental problems: What is the physical condition of the microphase separation needed to form materials with desired compositions and mesoscale structures in different domains? How do these compositions and mesoscale structures evolve during the preparation period? How does the morphology change in the interfacial region? Many experimental measurements, computer simulation methods, and theories have been developed. However, most of them are only suitable for individual tasks. In recent years, we have developed theoretical methods based on equations of state that can be used comprehensively to study the multiscale structure of polymer systems, including the phase diagrams, the morphologies and evolution of microphase separation, the densities and composition profiles in different domains, and the molecular configurations in the interfacial region. The molecular parameters of the equation of state or the Helmholtz function model can be determined from the pressure, volume, temperature, and miscibility data of polymers, which ensures the practical applicability of the methods.

Keywords: Density functional theory · Dynamic density functional theory · Microphase separation · Molecular thermodynamics · Non-uniform fluid · Polymer system

H. Liu(✉), H. Xu, H. Chen, C. Peng, and Y. Hu
State Key Laboratory of Chemical Engineering and Department of Chemistry,
East China University of Science and Technology,
Shanghai 200237, China
e-mail: hlliu@ecust.edu.cn

Contents

1 Introduction

In engineering practice, many new functional materials are required to have not only the assigned compositions, but also special mesoscale structures; the latter is always decisive. To design and control the manufacturing processes of such materials, it is crucial to gain insight into the formation mechanisms of the mesoscale structures and to study the effects on those structures of different engineering factors such as changes in the flow field, temperature gradient, and external field. We take as an example the copolymers, which have typical multiscale complex structures and can be used as templates to prepare various complex materials [1–4], To regulate the mesoscale structure of copolymer materials, there are three fundamental problems: What is the physical condition of the microphase separation needed to form materials with desired compositions and mesoscale structures in different domains? How do these compositions and mesoscale structures evolve during the preparation period? What are the morphology changes in the interfacial region that might determine the stability and the properties of the material? The first problem can be solved by the phase equilibrium theory, which is usually approached by introducing an equation of state (EOS) or a mixing Helmholtz function for complex systems [5], or by computer simulation methods such as Monte Carlo (MC) and molecular dynamics (MD) [6], Solving the second problem involves the dynamics of mesostructure evolution, which can be worked out by field-based theories combined with the appropriate Helmholtz functional. The relevant approaches include the time-dependent Ginzburg–Landau equation (TDGL) [7], the self-consistent-field theory (SCFT) [8], the dynamic density functional theory (DDFT) [9], the cell dynamics system method (CDS) [10, 11], and the dissipative particle dynamics method (DPD) [12]. The last problem concerns distributions or composition profiles leading to the change of

mesostructures from one microdomain to a neighboring domain, which can be studied by density functional theory (DFT) [13] and SCFT [14], and also by MC and MD simulations [15, 16].

Here, we will introduce part of the work completed in this laboratory concerning the above problems. We first developed an EOS for chain-like fluids based on the association theory of statistical mechanics, which can be used to describe accurately the experimental pressure, volume, and temperature (pVT) data, vapor–liquid equilibria (VLE), liquid–liquid equilibria (LLE), and solid–liquid equilibria (SLE) for systems composed of non-polar, polar, and associating molecules, as well as chain-like polymers. Combining this EOS with the Langevin equation and the weighted density approximation (WDA), we then developed a dynamic density functional theory based on the equation of state (EOS-based DDFT), which can describe the mesoscale structures and their evolution for copolymer systems. The effect of pressure on the mesophase separation can be successfully predicted. Further applying this EOS to DFT for heterogeneous fluids and combining with the WDA and the simulation technique, we could describe the density distribution of polymer in the interfacial region. The microscale information about polymers, such as the radius of gyration, is also obtained.

2 Equation of State for Polymer Systems

In the last two decades, much attention has been given to the development of equations of state for an assembly of chain-like molecules in free space (off-lattice) [17–25]. We have made efforts in the same line and developed a HSCF equation [26] through the r-particle cavity-correlation function of sticky hard spheres, based on the model of Stell, Cummings, and Zhou [27, 28]. The HSCF equation has a simple form similar to the Carnahan–Starling equation and has been satisfactorily tested by computer simulation results for chain fluids covering a wide range of chain length. Later, we developed a practical equation of state [29, 30] for ordinary fluids and fluid mixtures by combining the HSCF equation with a square-well (SW) perturbation term from the work of Alder et al. [31]. For associating systems such as carboxylic acids, alcohols, phenols, amides, water, and their mixtures, as well as some mixtures of non-associating substances such as acetone and chloroform, self-association or cross-association occurs between molecules due to hydrogen bonding. In these cases, the statistical mechanical theory of association based on a shield-sticky model [28] were used to calculate the contribution due to association. The HSCF equation has also been extended to fluids containing associated molecules [32–34].

2.1 Theoretical Framework

We consider a system composed of species S, which can form a linear r-mer associate by the reaction $r\mathrm{S} \Rightarrow \mathrm{S}_r$. For each nearest-neighbor pair $\mathrm{S}_i - S_j$, there are

m different interaction configurations. Each configuration is characterized by an intersegment distance vector $\boldsymbol{L}_k$, $k = 1 - m$, originated from a definite number of interaction sites. The corresponding mode is L, irrespective of k.

By adopting the sticky-point model of Cummings and Stell [27] for each nearest-neighbor pair, statistical-mechanical derivation gives an analytical expression for the Helmholtz function as:

$$\frac{\beta[A(\alpha) - A(\alpha = 0)]}{N_0} = -\frac{1}{r}\left[\alpha - \int_{\alpha=0}^{\alpha=\alpha} \alpha d \ln y^{(r)}(L)\right], \tag{1}$$

where $\beta = 1/kT$, α is the degree of association, N_0 is the total number of monomers (both unassociated and associated), $y^{(r)}(\boldsymbol{L})$ is the r-particle cavity-correlation function (CCF) where $\boldsymbol{L}$ represents all $\boldsymbol{L}_k$. The CCF is defined by:

$$y^{(r)} = \exp(\beta \varepsilon^{(r)}) g^{(r)}, \tag{2}$$

where $\varepsilon^{(r)}$ is the attractive energy for an r-particle assembly, and $g^{(r)}$ is the r-particle radial distribution function. From Eq. 1, the thermodynamic gives an equation of state:

$$p = (r\rho_0)^2 \left(\frac{\partial(A/N_0)}{\partial(r\rho_0)}\right)_{T,\tau^{-1}} = r\rho_0^2 \left(\frac{\partial(A/N_0)}{\partial \rho_0}\right)_{T,\tau^{-1}}, \tag{3}$$

where ρ_0 is the total number density of monomers, both unassociated and associated.

As shown in Eq. 1, to obtain the Helmholtz function and then the equation of state, we need the information of the r-particle CCF for an r-mer chain with a special configuration. Unfortunately, at present it is almost impossible to obtain it theoretically for polymers. Zhou and Stell [28] adopted a linear approximation and simplified the r-particle CCF by the nearest-neighbor two-particle CCF, but raising it to an empirical power. In this work, enlightened by the Kirkwood superposition rule, the r-particle CCF is approximated by a product of two contributions: a chemical contribution $(1 - \alpha)^r$ dependent on the degree of association, and a physical contribution expressed by the product of nearest-neighbor effective two-particle CCFs $y^{(2e)}_{S_iS_{i+1}}$ and the product of next-to-nearest-neighbor effective two-particle CCFs $y^{(2e)}_{S_iS_{i+2}}$. The correlations between two particles apart by more than one particle are reasonably neglected:

$$y^{(r)}(\mathbf{L}) = (1 - \alpha)^r \prod_{i=1}^{r-1} y^{(2e)}_{S_iS_{i+1}} \prod_{i=1}^{r-2} y^{(2e)}_{S_iS_{i+2}}. \tag{4}$$

Substitution into Eqs. 1 and 3 yields:

$$\beta[A(\alpha) - A(\alpha = 0)]/N_0 = \ln(1 - \alpha) + \alpha(r - 1)/r, \tag{5}$$

$$\frac{\beta[p(\alpha) - p(\alpha = 0)]}{r\rho_0} = -\frac{\alpha}{r}\left[r - 1 + \rho_0 \sum_{i=1}^{r-1} \frac{\partial \ln y^{(2e)}_{S_iS_{i+1}}}{\partial \rho_0} + \rho_0 \sum_{i=1}^{r-2} \frac{\partial \ln y^{(2e)}_{S_iS_{i+2}}}{\partial \rho_0}\right]. \tag{6}$$

Equations 5 and 6 are the generalized Helmholtz function and equation of state for a fluid where some of the monomers are associated r-mer associates. When the degree of association α equals one, they are the generalized equations for a chain fluid. If we have a density dependence of those nearest-neighbor and next-to-nearest-neighbor effective two-particle CCFs, and the equation of state for the corresponding monomers ($\alpha = 0$), we can obtain an equation of state for a chain fluid ($\alpha = 1$). For a homonuclear chain molecule, we designate the total number of nearest-neighbor segment pairs as $r_{S_iS_{i+1}}$, and the total number of next-to-nearest-neighbor segment pairs as $r_{S_iS_{i+2}}$, then the equation of state and the residual Helmholtz function can be expressed as:

$$Z = \frac{\beta p}{\rho_0} = rZ(\alpha = 0) - \left[(r-1) + r_{S_iS_{i+1}} \eta \frac{d \ln y^{(2e)}_{S_iS_{i+1}}}{d\eta} + r_{S_iS_{i+2}} \eta \frac{d \ln y^{(2e)}_{S_iS_{i+2}}}{d\eta} \right], \tag{7}$$

$$\frac{\beta A^r}{N} = r \frac{\beta A^r(\alpha = 0)}{rN} - r_{S_iS_{i+1}} \ln y^{(2e)}_{S_iS_{i+1}} - r_{S_iS_{i+2}} \ln y^{(2e)}_{S_iS_{i+2}}, \tag{8}$$

where $r_{S_iS_{i+1}} = r - 1$ and $r_{S_iS_{i+2}} = r - 2$ for a linear chain fluid, and A^r is the residual Helmholtz function.

2.2 Equation of State for Pure Fluids

Real fluids can be approximated by a square-well-chain fluid with association between molecules. The residual Helmholtz function A^r and corresponding compressibility factor Z can be expressed as sums of hard-sphere chain fluid, square-well-perturbation, and association terms:

$$A^r = A^{r(\mathrm{HSCF})} + \Delta A^{(\mathrm{SW})} + \Delta A^{(\mathrm{ASS})}, \tag{9}$$

$$Z = Z^{(\mathrm{HSCF})} + Z^{(\mathrm{SW})} + Z^{(\mathrm{ASS})}. \tag{10}$$

2.2.1 HSCF Reference Term

The residual Helmholtz function and the compressibility factor for homonuclear HSCFs has been derived through the r-particle CCF based on a sticky-point model for chemical association. The r-particle CCF is approximated by a product of effective two-particle CCFs, accounting for correlations in nearest-neighbor and next-to-nearest-neighbor segment pairs. The density dependence of the effective two-particle CCF $y^{(2e)}_{S_iS_{i+1}}$ for the nearest-neighbor pair is derived from the rigorous Tildesley–Streett equation [35]. The density dependence of the effective two-particle CCF $y^{(2e)}_{S_iS_{i+2}}$ for the next-to-nearest-neighbor pair is obtained by fitting computer simulation data of compressibility factors for linear homonuclear

hard-sphere trimers. The Carnahan–Starling equation is used for the corresponding monomer system. The final residual Helmholtz function and the compressibility factor for HSCFs are:

$$\frac{\beta A^{r(\mathrm{HSCF})}}{N_0} = \frac{(3+a-b+3c)\eta-(1+a+b-c)}{2(1-\eta)}+\frac{1+a+b-c}{2(1-\eta)^2}+(c-1)\ln(1-\eta), \tag{11}$$

$$\frac{\beta p}{\rho_0} = \frac{1}{(1-\eta)^3}+\frac{a\eta}{(1-\eta)^3}+\frac{b\eta^2}{(1-\eta)^3}-\frac{c\eta^3}{(1-\eta)^3}, \tag{12}$$

where $\eta = \pi\rho_0 r\sigma^3/6$ is the reduced density; a, b, and c are functions of chain length:

$$a = r\left(1+\frac{r-1}{r}a_2+\frac{r-1}{r}\frac{r-2}{r}a_3\right), \tag{13}$$

$$b = r\left(1+\frac{r-1}{r}b_2+\frac{r-1}{r}\frac{r-2}{r}b_3\right), \tag{14}$$

$$c = r\left(1+\frac{r-1}{r}c_2+\frac{r-1}{r}\frac{r-2}{r}c_3\right), \tag{15}$$

$$a_2 = 0.45696 \quad b_2 = 2.10386 \quad c_2 = 1.75503, \tag{16}$$

$$a_3 = -0.74745 \quad b_3 = 3.49695 \quad c_3 = 4.83207. \tag{17}$$

As shown from these equations, the HSCF equation has a simple form similar to the Carnahan–Starling equation. It can excellently predict compressibility factors and second viral coefficients for homonuclear HSCFs, including ring and branch molecules covering a wide range of chain length as well as for HSCF mixtures [26, 29, 30, 36, 37].

2.2.2 SW Perturbation Term

For the perturbation, we can directly use the power series obtained by Alder et al. [31] for a square-well fluid. The Helmholtz function and the compressibility factor contributed by square-well interactions between segments are given by:

$$\frac{\beta\Delta A^{(\mathrm{SW})}}{N_0} = r\sum_m^9\sum_n^4 A_{mn}\left(3\sqrt{2}/\pi\right)^m\eta^m\tilde{T}^{-n}, \tag{18}$$

$$Z^{(\mathrm{SW})} = r\sum_m^9\sum_n^4 mA_{mn}\left(3\sqrt{2}/\pi\right)^m\eta^m\tilde{T}^{-n}, \tag{19}$$

where $\tilde{T} = kT/\varepsilon$ is the reduced temperature, ε is the depth of the square well, and A_{mn} are numerical coefficients. If we account for the contributions of square-well attractive interaction to the effective two-particle CCF for the nearest-neighbor pair

and next-to-nearest-neighbor pairs, the obtained EOS can excellently describe the compressibility factors for SWCFs with different chain lengths and different temperature ranges [38] compared with molecular simulation results [39–41].

2.2.3 Association Term

Assuming that associated dimers with bond length $L = \sigma$ are formed between molecules, the corresponding contribution to Helmholtz function and compressibility factor are given by [32–34]:

$$\beta \Delta A^{(\mathrm{ASS})}/N_0 = \ln(1-\alpha) + \alpha/2, \tag{20}$$

$$Z^{(\mathrm{ASS})} = -\frac{1}{2}\alpha\left(1+\eta\frac{\partial \ln y^{(2e)}_{S_iS_{i+1}}}{\partial \eta}\right), \tag{21}$$

where the degree of association α is expressed as:

$$\alpha = \left[(2\rho_0\Delta+1) - \sqrt{1+4\rho_0\Delta}\right]/2\rho_0\Delta, \tag{22}$$

$$\Delta = \pi\omega\sigma^3\tau^{-1}y^{(2e)}_{S_iS_{i+1}}/3, \tag{23}$$

where the sticky parameter $\tau^{-1} = e^{\beta\delta\varepsilon} - 1$, $\delta\varepsilon$ is the sticky or association energy, ω is a surface-fraction parameter responsible for association, and $y^{(2e)}_{S_iS_{i+1}}$ is the effective nearest-neighbor correlation function calculated by:

$$\ln y^{(2e)}_{S_iS_{i+1}} = \frac{(3-a_2+b_2-3c_2)\eta-(1-a_2-b_2+c_2)}{2(1-\eta)} + \frac{1-a_2-b_2+c_2}{2(1-\eta)^2} - (1+c_2)\ln(1-\eta). \tag{24}$$

Equations 20 and 21 have been satisfactorily tested by computer simulation data [42] for an associated hard-sphere dumbbell fluid (a mixture of hard-sphere dimers and linear hard-sphere quadrimers) at different associating strengths [32].

2.2.4 Molecular Parameters

There are three molecular parameters in this model for non-associating pure substances, namely, chain length r, cube of segment diameter σ^3, and square-well interaction energy between segments ε/k. They are regressed from vapor pressures and saturated liquid volumes of pure fluids [29,30]. For polymers, the ratio of chain length and molar mass r/M is taken to replace the chain length r. Parameters of pure polymers are estimated from densities of melting polymers at different temperatures and pressures [29,30]. For associating pure substances, there are four molecular parameters that should be regressed, namely, chain length r, square-well interaction

energy between segments ε/k, surface-fraction parameter ω, and association energy $\delta\varepsilon/k$. The cube of segment diameter σ^3 is set equal to 19.0×10^{-3} L mol^{-1}, referring to alkanes [32, 34].

2.3 Equation of State for Fluid Mixtures

2.3.1 HSCF Reference Term

For fluid mixtures, Eqs. 11 and 12 are still valid with $\eta=\sum_i \pi\rho_{i0}r_i\sigma_i^3/6$. Parameters a, b, and c are calculated by the following mixing rules:

$$a=\sum_i x_i r_i\left(1+\frac{r_i-1}{r_i}a_2+\frac{r_i-1}{r_i}\frac{r_i-2}{r_i}a_3\right), \tag{25}$$

$$b=\sum_i x_i r_i\left(1+\frac{r_i-1}{r_i}b_2+\frac{r_i-1}{r_i}\frac{r_i-2}{r_i}b_3\right), \tag{26}$$

$$c=\sum_i x_i r_i\left(1+\frac{r_i-1}{r_i}c_2+\frac{r_i-1}{r_i}\frac{r_i-2}{r_i}c_3\right), \tag{27}$$

The Mansoori–Carnahan–Starling–Leland equation [43] was used in our earlier works [26, 29, 30] for the hard-sphere reference, especially for the heterogeneous hard-sphere chain fluids. The merit is that no mixing rule is needed for HSCF mixtures. However, the final equation is then more tedious.

2.3.2 SW Perturbation Term

For fluid mixtures, Eqs. 10 and 11 are used with the van der Waals one-fluid mixing rules for the reduced temperature and the corresponding parameters:

$$\tilde{T}^{-1}=\sum_{i=1}^{K}\sum_{j=1}^{K}\phi_i\phi_j(\varepsilon_{ij}/kT)\sigma_{ij}^3/\sum_{i=1}^{K}\sum_{j=1}^{K}\phi_i\phi_j\sigma_{ij}^3, \tag{28}$$

$$\varepsilon_{ij}=(1-k_{ij})(\varepsilon_i\varepsilon_j)^{1/2}, \tag{29}$$

where, k_{ij} and l_{ij} are adjustable binary interaction parameters, and ϕ_i is the segment fraction of component i:

$$\phi_i=x_i r_i/r,\ r=\sum_i x_i r_i. \tag{30}$$

2.3.3 Association Term

For mixtures, contributions to the Helmholtz function and the compressibility factor due to association can be derived through chemical association theory as follows:

$$\beta \Delta A^{(\mathrm{ASS})}/N_0 = \sum_i x_i [\ln X_i + (1 - X_i)/2]. \tag{31}$$

$$Z^{(\mathrm{ASS})} = \sum_i x_i \left(\frac{1}{X_i} - \frac{1}{2}\right) \rho_0 \left(\frac{\partial X_i}{\partial \rho_0}\right), \tag{32}$$

where:

$$X_i = \left(1 + \sum_j \rho_{j0} X_j \Delta_{ij}\right)^{-1}, \tag{33}$$

$$\rho_{j0} \Delta_{ij} = \pi \omega_{ij} T_{ij}^{-1} \sigma_{ij}^3 \rho_{j0} y_{\mathrm{S}_i \mathrm{S}_{i+1}}{}^{(2e)}/3, \tag{34}$$

$$\rho_0 \left(\frac{\partial X_i}{\partial \rho_0}\right) = -X_i^2 \left\{ \sum_j \rho_{j0} \Delta_{ij} \left[\rho_0 \left(\frac{\partial X_j}{\partial \rho_0}\right) + X_j \left(1 + \eta \frac{\partial \ln y_{\mathrm{S}_i \mathrm{S}_{i+1}}^{(2e)}}{\partial \eta}\right)\right]\right\}, \tag{35}$$

Mixing rules should be used for the cross-association between molecules of different kinds:

$$\omega_{ij} = (\omega_{ii} + \omega_{jj})/2, \quad \delta\varepsilon_{ij} = (\delta\varepsilon_{ii} \delta\varepsilon_{jj})^{1/2}, \quad \sigma_{ij} = (1 - l_{ij})(\sigma_i + \sigma_j)/2. \tag{36}$$

2.4 Applications

The EOS obtained has been applied to various systems containing different molecules: from spherical small molecules to chain-like molecules [29, 30, 33], homopolymers [29, 30, 33, 34] and copolymers [44–46], from non-polar to polar [29, 30, 33], associating substances [32–34, 47, 48], and ionic liquids [49, 50]. Volumetric properties [29, 30, 34, 46, 49, 51], vapor–liquid equilibria [29, 30, 32, 33, 45, 47, 48, 52], mixing excess enthalpy [33], liquid–liquid equilibria [34, 44], solid–liquid equilibria [53], solubility of gases in polymer melts [54], and ionic liquids [49] can be described satisfactorily. Figures 1–6 show some examples for the predicted or correlated results of compressibility factors, pVT, vapor–liquid equilibria and liquid–liquid equilibria for chain-like fluids and their mixtures.

Equations 28 and 29 are the most widely used mixing rules and are capable of representing vapor–liquid equilibria, usually with one or two binary adjustable parameters. Generally, they give good results for non-polar or slightly polar systems; however, they do not always yield reasonable results for polar or strongly polar systems, especially for asymmetrical systems. The reason lies in the fact that the one-fluid theory is based on the assumption of completely random mixing. A mixing rule based on the two-fluid theory developed by Whiting and Prausnitz [55] has been introduced to consider the non-random mixing of species in the calculation of VLE for systems containing non-associated segments and associated segments [56]. For asymmetrical systems with large polar difference between different molecules,

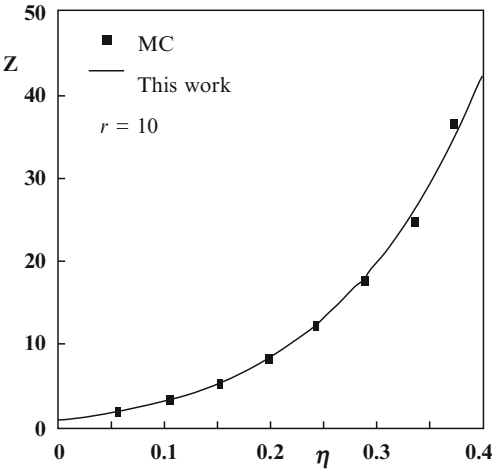

Fig. 1 Compressibility factors of three-arm homonuclear HSCF [37]

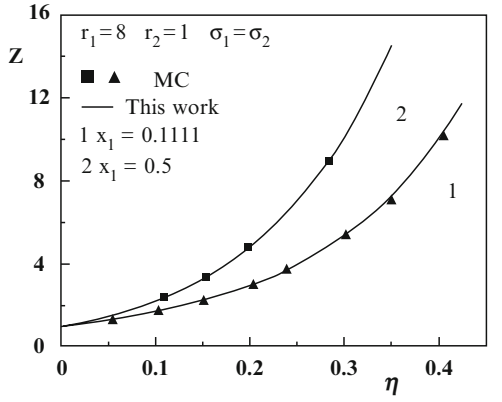

Fig. 2 Compressibility factors of HSCF mixture [29, 30]

or for systems with only self-association, results obtained by using two-fluid theory are obviously better than those by one-fluid theory because of the notable non-randomness. For symmetrical systems, the superiority of the two-fluid theory is not as evident as expected. However, for systems with cross-association as well as self-association, the difference between the results using the two mixing rules is again not serious. In this case, because the A–A, A–B, and B–B interactions are all very strong, the non-randomness effect may be weakened.

Coupled with the scaled particle theory, the EOS mentioned above has been employed to calculate the surface tensions of binary and ternary mixtures, including non-associating, self-associating, and cross-associating fluids; and the theoretical results are in good agreement with experimental data. The salient feature is that the molecular parameters used in this work are general and can be used for calculation

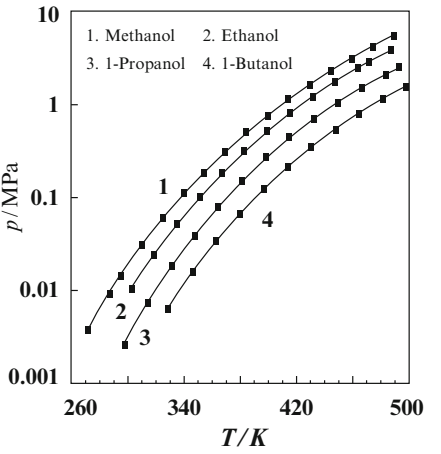

Fig. 3 Vapor pressures of alcohols [32]

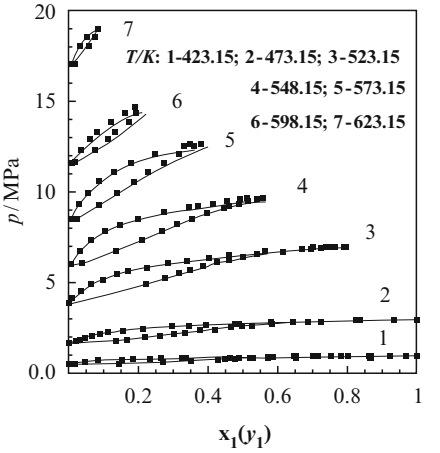

Fig. 4 Vapor–liquid equilibria of ethanol–water mixture at high pressure [48]

of other thermo-physical properties [57]. Combining with Eyring's absolute rate theory, this EOS has also been used to calculate the viscosity of liquids and mixtures at atmospheric and higher pressures [58–60].

Equations 7 and 8 can also be used to develop the EOS and residual Helmholtz function for chain fluids other than hard-sphere chains and square-well chains with different segment–segment interaction potential, such as Yukawa chain fluids [61], polyelectrolyte solutions [62–65] and polyampholyte solutions [66, 67]. Good agreement between predicted results and computer simulation results of volumetric properties, liquid–liquid equilibria, and osmotic coefficients can be obtained. Experimental osmotic coefficients and activity coefficients of polyelectrolyte solutions can be satisfactorily correlated.

Recently, the above method for the development of an EOS for chain fluids based on the free-space model has been extended to a lattice model for polymer systems.

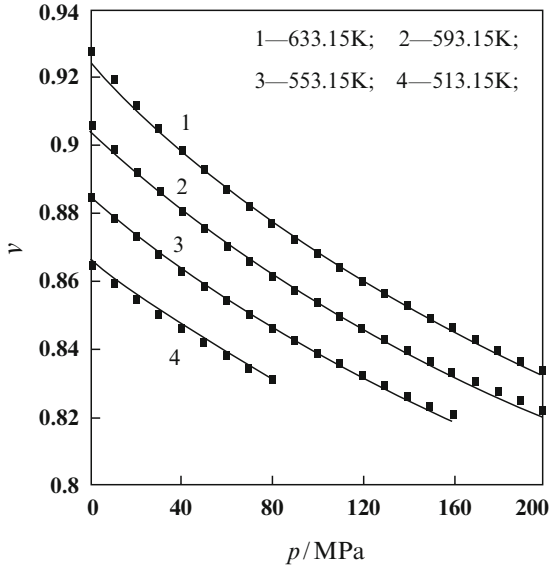

Fig. 5 *pVT* of poly(sulfone) [29, 30]

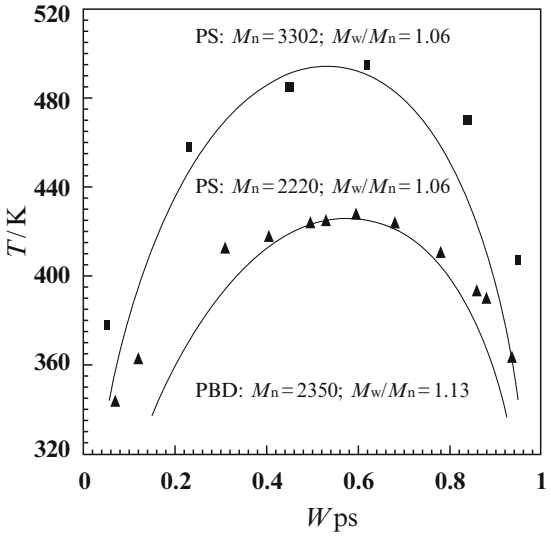

Fig. 6 Liquid–liquid equilibria of PS-PBD blend [33]

A molecular thermodynamic model for polymers based on a lattice model with concise and accurate expressions for the Helmholtz energy of mixing and other thermodynamic properties has been established. Computer simulation results are combined with the statistical mechanical derivation to obtain the expressions. The predicted critical temperatures and critical compositions, spinodals and coexistence curves, as well as internal energies of mixing for systems with various chain lengths are in satisfactory agreement with the computer simulation results and experimental data, indicating the superiority of this model over other theories [68–75].

The above-mentioned molecular thermodynamic approach has general significance. In developing a theoretical model, statistical mechanics is generally a first choice. However, its power is always limited because of the mathematical difficulties. Molecular thermodynamics seeks to overcome this limitation. Usually, semiempirical approaches based on concepts from statistical mechanics, on ideas from molecular physics, and on information from molecular structures are adopted. However, their reliability is always doubted when compared with rigorous results. Directly introducing molecular simulation results in constructing models, as shown in this work, gives us new impetus to solve this problem and to develop more accurate models. The method developed retains the rigor of statistical mechanics. First, an analytical expression from statistical mechanical derivations is obtained; however, it may contain unknown functions or coefficients because of the mathematical difficulty or because of the simplifications introduced. The form of the unknown functions or unknown coefficients is then determined by a few computer simulations [76]. The models obtained are then very reliable and the obtained expressions are extremely simple in appearance, suitable for engineering and application. This method has great potential.

3 Microphase Separation of Polymer Systems by a Dynamic Density Functional Theory Based on Equations of State

Polymer materials with special mesostructures can be applied in various fields such as microelectronics, optics, novel membranes, and so on [77–79]. Among, block copolymers comprised of chemically different blocks have attracted special attention. Owing to the chemical connectivity, macroscopic phase separation of different blocks cannot take place. Instead, due to the immiscibility between different blocks, microphase separation occurs in the melt and different mesophase structures (such as lamellar, hexagonal, and body-centered cubic microphases) form along with the changes of volume fraction and other physical parameters [1]. The macroscopic behavior of these systems is determined, not only by their microscopic properties (such as bonding, chain connectivity and flexibility, intersegment interactions, and excluded volume effect) but, more directly and decisively, by their mesoscale structures. At least three scales, micro-, meso- and macro-, exist simultaneously in these systems. The multiscale approach, especially building bridges between these scales, is essential in understanding the behavior of these systems. Many theoretical and

simulation methods have been developed to study the microphase separation of block copolymer and polymer blends, such as the time-dependent Ginzburg–Landau equation (TDGL) [7], the self-consistent-field theory (SCFT) [8], the dynamic density functional theory (DDFT) [9], the cell dynamics system method (CDS) [10, 11], the dissipative particle dynamics method (DPD) [12], and the Monte Carlo (MC) method [80]. Here we introduce a new mesoscale simulation method, dynamic density functional theory based on equation of state (EOS-based DDFT) [81]. It is quite different to the traditional DDFT. By employing the fluid EOS and the bonding potential, not only can EOS-based DDFT study the evolution of the morphologies by using the experimental pVT data (Xu et al., unpublished results), but also can investigate the pressure-induced phase behavior of polymer systems [82].

3.1 Theory and Model

The following is a brief description of the EOS-based DDFT. Detail information of the theory is given in [81].

The polymer molecule is modeled as a tangentially connected square-well chain with bead diameter σ and chain length N in a compressible system of volume V and pressure p. The component is indexed by $I.\rho_I(r)$ and $\mu_I(r)$ are the density field and the chemical potential of bead I at position r, respectively.

For a given density field, the free-energy functional $F\{\rho\}$ can be expressed as follows:

$$F\{\rho\} = \beta^{-1}\sum_I \int \rho_I(\mathbf{r})[\ln\rho_I(r) - 1]\mathrm{d}\mathbf{r} + \sum_{s=1}^{N-1}\int \rho_s(\mathbf{r})v_b(|\mathbf{r}'_{s+1} - r_s|)\mathrm{d}\mathbf{r} + F^{\mathrm{nid}}\{\rho\}, \tag{37}$$

where the first term is the ideal gas contribution. The second term takes into account the chain connectivity, where $v_b(|\mathbf{r}'_{s+1} - \mathbf{r}_s|)$ is the bonding potential between the beads of s at $\boldsymbol{r}$, and $s+1$ at $\mathbf{r}'$. The non-ideal free-energy functional $F^{nid}\{\rho\}$ contains the excluded volume and the cohesive interactions.

The chemical potential field $\mu_I(\boldsymbol{r})$ is defined by the functional derivative of the free-energy functional:

$$\mu_I(\mathbf{r}) = \beta^{-1}\ln\rho_I(\mathbf{r}) - \beta^{-1}\ln\left(\exp[-\beta\mu_I^{\mathrm{nid}}(\mathbf{r})]\prod_{s=1}^{N-1}\delta_{\mathrm{Is}}^{\mathrm{K}}\frac{\delta(|r'_{s+1} - r_s| - \sigma)}{4\pi\sigma^2}\right), \tag{38}$$

where δ_{Is}^{K} is the Kronecker delta function, with a value of 1 when bead s is of type I and 0 otherwise.

Assuming that the local distribution of the density field can be depicted by the EOS for a square-well chain fluid, then:

$$\beta\mu_I^{\mathrm{nid}}(\mathbf{r})=\frac{8\eta(\mathbf{r})-9\eta(\mathbf{r})^2+3\eta(\mathbf{r})^3}{(1-\eta(\mathbf{r}))^3}-\left[\frac{(a+c)\eta(\mathbf{r})}{1-\eta(\mathbf{r})}+\frac{a\eta(\mathbf{r})^2}{2(1-\eta(\mathbf{r}))^2}+\frac{b\eta(\mathbf{r})}{(1-\eta(\mathbf{r}))^3}-c\ln(1-\eta(\mathbf{r}))\right]+\sum_m^9\sum_n^4(1+m+2n\cdot L_I(\mathbf{r}))A_{mn}\left(\frac{3\sqrt{2}}{\pi}\right)^m\eta(\mathbf{r})^m\tilde{T}(\mathbf{r})^{-n}, \tag{39}$$

where A_{mn} are the numerical coefficients of the square-well interaction. The reduced bead density is $\eta(\mathbf{r})=\tilde{p}(\mathbf{r})/Z(\mathbf{r})\tilde{T}(\mathbf{r})$. The compressibility factor is:

$$Z(\mathbf{r})=1+N\eta(\mathbf{r})\left(\frac{4-2\eta(\mathbf{r})}{(1-\eta(\mathbf{r}))^3}\right)-N\eta(\mathbf{r})\left(\frac{c+a/2}{1-\eta(\mathbf{r})}+\frac{a\eta(\mathbf{r})-b}{2(1-\eta(r))^2}+\frac{b}{(1-\eta(\mathbf{r}))^3}\right)+N\sum_m^9\sum_n^4 mA_{mn}\left(\frac{3\sqrt{2}}{\pi}\right)^m\eta(\mathbf{r})^m\tilde{T}(\mathbf{r})^{-n}, \tag{40}$$

where:

$$a=a_{20}(N-1)/N+a_{30}(N-1)(N-2)/N^2,\ \ a_{20}=-0.61819,\ \ a_{30}=-10.25181, \tag{41}$$

$$b=b_{20}(N-1)/N+b_{30}(N-1)(N-2)/N^2,\quad b_{20}=0.19421,\quad b_{30}=2.08257, \tag{42}$$

$$c=c_{20}(N-1)/N+c_{30}(N-1)(N-2)/N^2,\quad c_{20}=2.75503,\quad c_{30}=4.83207, \tag{43}$$

$$\tilde{T}(\mathbf{r})^{-1}=\frac{\sum_I\sum_J\phi_I(\mathbf{r})\phi_J(\mathbf{r})(\varepsilon_{IJ}/kT)\sigma^3}{\sum_I\sum_J\phi_I(\mathbf{r})\phi_J(\mathbf{r})\sigma^3}, \tag{44}$$

$$L_I(\mathbf{r})=\left(\frac{\sum_J\phi_J(\mathbf{r})(\varepsilon_{IJ}/kT)\sigma^3}{\sum_J\sum_K\phi_J(\mathbf{r})\phi_K(\mathbf{r})(\varepsilon_{JK}/kT)\sigma^3}-\frac{\sum_J\phi_J(\mathbf{r})\sigma^3}{\sum_J\sum_K\phi_J(\mathbf{r})\phi_K(\mathbf{r})\sigma^3}\right), \tag{45}$$

$\phi_I(\mathbf{r})=\rho_I(\mathbf{r})\Big/\sum_J\rho_J(\mathbf{r})$, ε_{IJ} is the interaction parameter between the beads of type I and J, the reduced pressure $\tilde{p}=p\pi\sigma^3/6\varepsilon$, and the energy parameter $\varepsilon=\sum_I\sum_J\phi_I\phi_J\varepsilon_{IJ}/\sum_I\sum_J\phi_I\phi_J$.

To make the locally applied EOS complementary with DDFT, a weighted density approximation (WDA) should be introduced. Here, the simplest Heaviside step function is adopted:

$$\tilde{\rho}(\mathbf{r})=\int\rho(\mathbf{r}')w(|\mathbf{r}-\mathbf{r}'|)\,\mathrm{d}\mathbf{r}', \tag{46}$$

$$w(r)=\frac{3\Theta(\sigma-r)}{4\pi\sigma^3}, \tag{47}$$

where w is the weight function, and Θ is the Heaviside step function. During the calculation, the weighted density functional is discretized as:

$$\tilde{\rho}(x,y,z) = \frac{4}{7}\rho(x,y,z) + \frac{1}{14}\begin{pmatrix} \rho(x+1,y,z)+\rho(x,y+1,z)+\rho(x,y,z+1) \\ +\rho(x-1,y,z)+\rho(x,y-1,z)+\rho(x,y,z-1) \end{pmatrix}. \tag{48}$$

We assume that the time evolution of the density field can be given by a time-dependent Ginzburg–Landau type equation:

$$\frac{\partial \rho_I(\mathbf{r},t)}{\partial t} = \nabla \cdot M\rho_I \nabla \mu_I + \xi_I, \tag{49}$$

where M is the mobility coefficient, and ξ_I is the stochastic noise, which is distributed according to the fluctuation-dissipation theorem:

$$\langle \xi_I(\mathbf{r},t)\rangle = 0, \quad \langle \xi_I(\mathbf{r},t)\xi_J(\mathbf{r}',t')\rangle = 2\beta^{-1}M\rho_I\delta(\mathbf{r}-\mathbf{r}')\delta(t-t'). \tag{50}$$

For the convenience of numerical calculation, the following dimensionless parameters are introduced:

$$\tau \equiv \beta^{-1}Mh^{-2}t, \quad d \equiv \sigma h^{-1}, \tag{51}$$

where τ is the dimensionless time, h is the mesh size, $\beta^{-1}M$ is the diffusion coefficient, and d is the grid scaling.

3.2 Applications

3.2.1 Pressure Effect on the Microphase Separation of Diblock Copolymer Melts

The ordered morphologies depend on the temperature, volume fraction, and pressure. The effects of the former two factors on the microphase separation of block copolymers have been studied in detail both experimentally and theoretically. The impact of pressure on the microphase separation of block copolymer has also been experimentally investigated by Hajduk et al. [83, 84], Pollard et al. [85], Ruzette et al. [86], and Schwahn et al. [87], but the theoretical aspect still remains relatively untouched. Probably this is because the earlier theoretical treatments of block copolymer usually regard it as an incompressible system, in which the local density of the copolymer remains constant. Although some recent theories and simulations have introduced the assumption of a compressible system, leading to a local volume change, the total size of the whole system still remains unchanged. This is not in agreement with experimental data [84], which indicate a slight but definite increase in volume accompanying the order–disorder transition (ODT). In this work, the bead number of the whole system is not held as a constant, but is a variable that can be accurately calculated from the EOS by the given pressure, volume, and temperature.

For the diblock copolymer melts with different volume fractions, the following parameters are set for the numerical calculations: the copolymer chain length

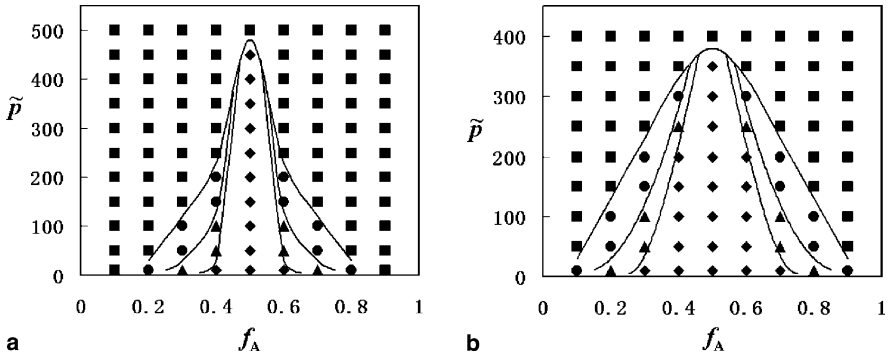

Fig. 7 Phase diagrams for the diblock copolymer melts under different reduced temperatures: **a** $T_r^{-1} = 5$, **b** $T_r^{-1} = 10$. Symbols *filled square*, *filled circle*, *filled triangle*, and *filled diamond* refer to the disordered, spherical, rod-like, and bicontinuous mesostructures, respectively

$N = 10$, the noise parameter $\xi_0 = 0.1$, the grid scaling $d = 1$, the reference interaction parameters $\varepsilon_{AA}/kT_0 = \varepsilon_{BB}/kT_0 = 0.10$ and $\varepsilon_{AB}/kT_0 = \varepsilon_{BA}/kT_0 = 0.04$, the dimensionless time step $\Delta\tau = 0.02$. All calculations are performed in a box of size $20 \times 20 \times 20$, and the total time is 1000 dimensionless time steps. The start configuration is a homogeneous profile, i.e., $\theta_I(r) = N_I/N$.

Figure 7 shows the phase diagrams of diblock copolymer under the reduced temperature $T_r^{-1} = 5$ and $T_r^{-1} = 10$. It can be seen that with the application of high pressure, the morphologies of diblock copolymers transform from ordered to disordered states. In the microphase-separated region, pressurization induces the order–order transition (OOT) of asymmetrical diblock copolymers. Especially for A_4B_6, the OOT from bicontinuous to rod-like, and then to spherical morphology can be observed. This is a very special and interesting result, and there has been no relevant experimental research published up to the present. Because A_4B_6 is nearly symmetrical, the repulsive effect is important; therefore, a possible explanation for this special phenomenon is that, due to the increase in the degree of segregation, the transition from bicontinuous morphology to sphere would happen upon pressurization.

Figure 8 plots reduced order–disorder transition temperature, $T_{r,ODT}$, as a function of reduced pressure for diblock copolymer A_5B_5. The relation can be fitted as $T_{r,ODT} = 0.2705 \times \tilde{p}^{0.1652}$. It can be found from Fig. 8 that at the lower pressure range ($\tilde{p} < 50$), $T_{r,ODT}$ increases quickly with increasing pressure, and at the higher pressure range ($\tilde{p} > 50$), the increase tendency of $T_{r,ODT}$ slow down due to the decrease of free volume under high pressure.

As mentioned above, for a system with given pressure, volume, and temperature, the total number of molecules is not independent, but is determined according to the EOS. Here we introduce an average reduced bead density to describe the change of total number in the evolution. It is defined as follows:

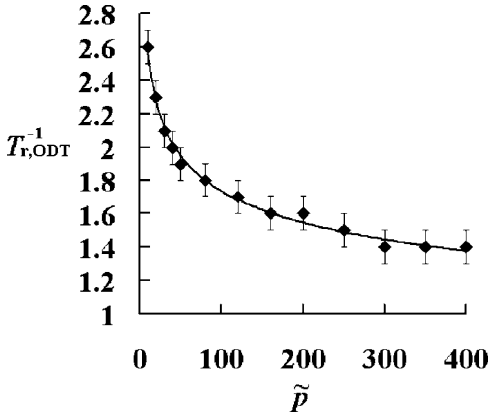

Fig. 8 $T_{r,ODT}$ as a function of reduced pressure for the block copolymer A_5B_5. *Filled diamonds* are the simulation results, and the *solid line* is the fitting curve

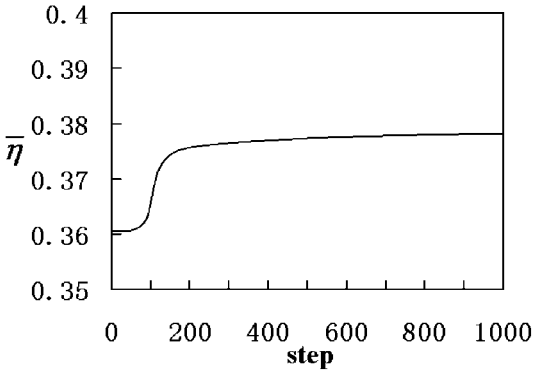

Fig. 9 Time evolution of the average reduced bead density $\bar{\eta}$ of A_5B_5 with $\tilde{p} = 10$ and $T_r^{-1} = 6$

$$\bar{\eta} = \frac{1}{V}\int_V \eta(\mathbf{r})\mathrm{d}\mathbf{r}. \tag{52}$$

Figure 9 describes the time evolution of average reduced bead density $\bar{\eta}$ of diblock copolymer A_5B_5 for the case of $\tilde{p}$ = 10 and T_r^{-1} = 6. At the beginning of evolution, the system keeps disordered state and $\bar{\eta}$ remains constant. When the microphase separation of diblock copolymer occurs, the bicontinuous morphology is obtained and $\bar{\eta}$ increases, from 0.361 to 0.376, in a short time. In the late stage of microphase separation, the bicontinuous morphology keeps stable, the increase in $\bar{\eta}$ slows down and finally stops. It should be mentioned that when $\tilde{p} < 100$, the time evolution of average reduced bead density is consistent with that of the order parameter, which is always used to reflect the microphase separation in most theories and simulations. When $\tilde{p} > 200$, the change of $\bar{\eta}$ is not obvious.

The increase in $\bar{\eta}$ indicates that, for the system with given pressure, volume, and temperature, the total number of molecules of the whole system increases when the microphase separation occurs. This is in accordance with the experimental data measured by Hajduk et al. [84], which prove that there is a slight but definite and measurable increase in volume accompanying the transition from the microphase-separated to disordered state. In most simulation methods, to distinguish them from the incompressible treatments of block copolymer phase behavior, the local density fluctuation is introduced to represent the compressibility of block copolymer at the ODT. However, the total bead number of whole system throughout the evolution still remains unchanged, regardless of the phase state. The results presented here, from a simulation aspect, indicate that such a compressibility correction is insufficient to describe the pressure dependence of block copolymer phase behavior at the ODT. A proper description of ODT in the compressible treatment should incorporate the volume change, i.e., the change of total bead number during the transition.

3.2.2 Quantitative Study of Real Polymer Systems

Despite the success of the qualitative applications, quantitative study of real polymer systems by mesoscale simulation methods is rare. The key is to improve the accuracy of the structure parameters of the coarse-grained bead. In most mesoscale simulations, the structure parameters are arbitrarily set, judged by the morphologies obtained. No direct and reliable relationship for the real systems has been established. To improve the accuracy of the structure information, one approach is to use the molecular force field [88, 89] to calculate the parameters through the positions of atoms or molecules. However, the number of force field parameters required are always several tens, or even hundreds, leading to great inconvenience. In this work, a simpler and more convenient approach is introduced where the parameters are regressed from experimental pVT data through the fluid EOS based on statistical and molecular thermodynamics.

In the EOS-based DDFT, the model parameters relevant to the structure information of the real polymers include the coarse-grained chain length N, the bead diameter σ, and the energy parameter ε. For the sake of simplicity, they are replaced by N/M_w, σ^3, and ε/k, respectively, where M_w is the weight-average molecular weight of polymer, and k is the Boltzmann constant. These parameters can be obtained from regression of the pVT data of pure polymers.

Take the blends of polystyrene (PS) and polybutadiene (PBD) with different weight-average molecular weights as an example. Besides the model parameters in the EOS, the following parameters are set for the simulation: pressure $p = 1$ bar, noise parameter $\xi_0 = 0.1$, grid scaling $d = 1$, and dimensionless time step $\Delta\tau = 0.02$. All simulation are performed in a box of size $20 \times 20 \times 20$. The total time is 5000 dimensionless time steps. In some conditions near the coexistence curve, the total time steps increase up to 10,000 or more to assure the stability of structures. The start configuration is a homogeneous profile, i.e., $\theta_I(\mathbf{r}) = N_I/N$. In addition, to obtain the interaction parameters between different beads, a combining rule should be added

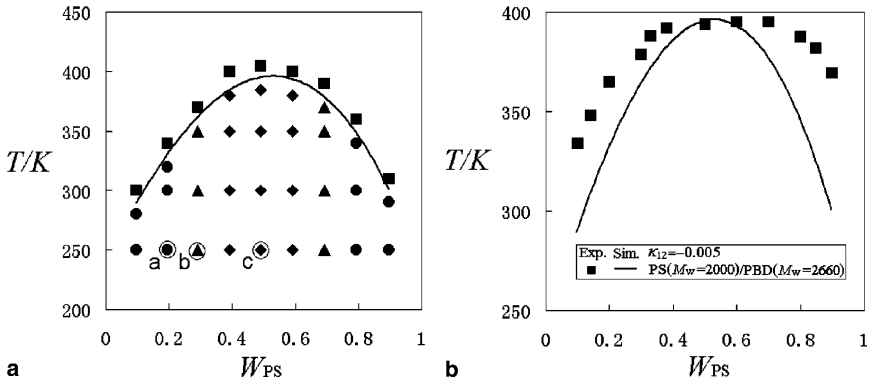

Fig. 10 **a** Detailed phase diagram of PS($M_w = 2000$)/PBD($M_w = 2660$) blend. Symbols *filled square*, *filled circle*, *filled triangle*, and *filled diamond* refer to the disordered, spherical, cylindrical, and bicontinuous mesostructures, respectively. The morphologies of the marks *a*, *b*, and *c* are shown correspondingly in Fig. 11. **b** Comparison of simulated coexistence curve with experiments

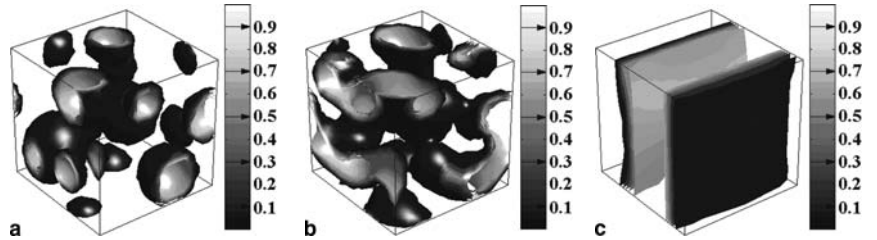

Fig. 11 Morphologies of PS($M_w = 2000$)/PBD($M_w = 2660$) with different simulation conditions: **a** $W_{PS} = 0.194$, $T = 250$ K; **b** $W_{PS} = 0.292$, $T = 250$ K; **c** $W_{PS} = 0.490$, $T = 250$ K

to the square-well energy parameter. In this work, the combining rule adopted is:

$$\varepsilon_{IJ} = (1 - \kappa_{IJ})\sqrt{\varepsilon_I \varepsilon_J}, \tag{53}$$

where κ_{IJ} is an adjustable binary parameter.

Figure 10 depicts the phase diagram of PS ($M_w = 2000$)/PBD ($M_w = 2660$). Part a shows the simulated results and part b shows the corresponding comparison of the simulated coexistence curve with experiments [90]. The binary parameter is $\kappa_{IJ} = -0.005$. Figure 11 shows the mesostructures at different compositions of the blend. It can be seen from Fig. 10 that the simulation results are in agreement with the experiments, especially in the region near critical composition; the error between simulated T_{ODT} and the experimental T_{ODT} is less than 10°C. In the region far from the critical composition, the agreement is deteriorated because of the mean-field approximation used in the model.

To check the reliability of the parameters, another two PS/PBD blends with different weight-average molecular weights, PS($M_w = 2400$)/PBD($M_w = 2660$)

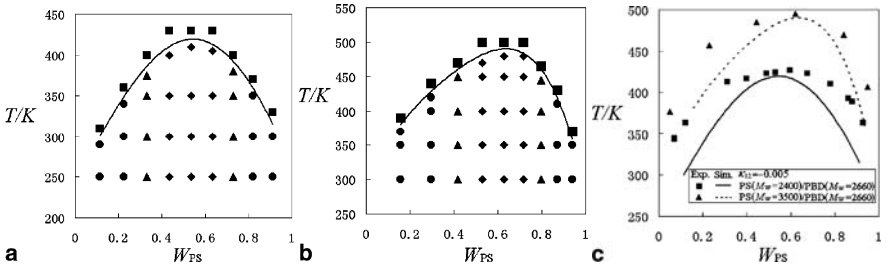

Fig. 12 **a** Detailed phase diagram of PS($M_w = 2400$)/PBD($M_w = 2660$) blend. **b** Detailed phase diagram of PS($M_w = 3500$)/PBD($M_w = 2660$) blend. Symbols *filled square*, *filled circle*, *filled triangle*, and *filled diamond* refer to the disordered, spherical, cylindrical, and bicontinuous mesostructures, respectively. **c** Comparisons of simulated coexistence curves with experiments

and PS($M_w = 3500$)/PBD($M_w = 2660$) [91], were simulated. All parameters including the binary parameter κ_{IJ} are the same as those adopted in the PS($M_w = 2000$)/PBD($M_w = 2660$) blend. Figure 12 shows the phase diagrams of the two blends and the corresponding comparisons of simulated coexistence curves with experiments. It can be seen that the simulation results are still in good accord with the experiments, especially in the region near the critical composition.

To improve the consistency between simulated and experimental results, the adjustable binary interaction parameter κ_{IJ} can be expressed as a function of the temperature. Here we assume that κ_{IJ} is described by:

$$\kappa_{IJ}(T) = -0.08 + 29.625/T. \tag{54}$$

Figure 13 shows the comparisons of simulated coexistence curves with experiments for the PS($M_w = 2000$)/PBD($M_w = 2660$) blend. The solid line and dashed line refer to $\kappa_{IJ} = -0.005$ and $\kappa_{IJ}(T) = -0.08 + 29.625/T$, respectively. It can be found that after expanding the binary parameter as a linear function of the reverse temperature, the agreement between simulation and experiment in the full range of the composition is enhanced remarkably. However, in this case, for the blends with different molecular weights, the coefficients of Eq. 54 will be different.

The method can be extended to other systems, including multicomponent copolymer mixtures, surfactant solutions, copolymer films, and so on. The method provides a new effective means to study the dynamic properties of the free energy in the systems. It provides the connection between microscopic properties and the mesostructures, which is crucial to the multiscale approach for complex fluids. The real advantage of this method relies heavily on the accuracy of the EOS, and also on the reliability of the weighted density approximation. Therefore, there is still room for improvement by adopting more accurate EOS and more reliable WDA. Besides, building the bridge between mesostructures and the macroscopic properties merits more attention.

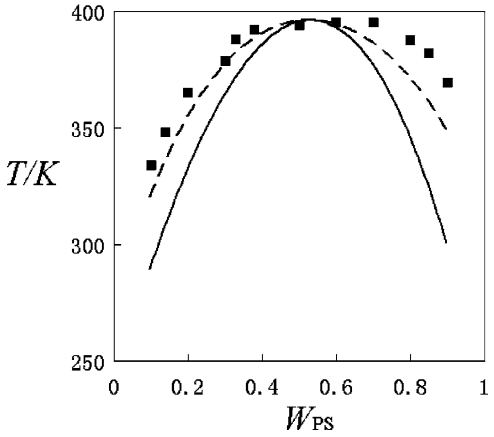

Fig. 13 Comparisons of simulated coexistence curves with experiments for PS(M_w = 2000)/PBD(M_w = 2660) blend. The *solid line* refers to $\kappa_{IJ} = -0.005$, the *dashed line* refers to $\kappa_{IJ}(T) = -0.08 + 29.625/T$, and *filled squares* are experimental data

4 Density Functional Theory for Heterogeneous Fluids

Density functional theory (DFT) has been widely used to investigate the structural and thermodynamic properties of confined fluids. As an extension of the reference-interaction-site model (RISM) for simple atomic fluids [92], DFT for molecular fluids was developed by Chandler, McCoy, and Singer (CMS) [93–96]. The weighted density approximation (WDA) for molecular systems was first built by Woodward [97] and later by Kierlik and Rosinburg (KR) [98]. In WDA, all the intra- and intermolecular correlations are included in the excess free energy functional with a coarse-graining approximation and a simple weighting function. For polymer mixtures, Nath et al. [99] proposed a DFT from the PRISM-based framework of CMS. By introducing a partial excess free energy functional, Cai et al. [100, 101] extended the EOS- based DFT to the hard-sphere chain mixtures, and, later, Ye et al. [102–105] developed square-well fluid of the EOS-based DFT. Yu and Wu [106] developed a new DFT by combining Rosenfeld's FMT [107] for excluded-volume effect with Wertheim's TPT1 [17] for chain connectivity. More recently, Tripathi and Chapman [108] combined the statistical-association-fluid theory (SAFT) [109] with FMT [107] and developed another new DFT for polymer mixtures.

In this section, we summarize the DFT developed in this laboratory.

4.1 Theoretical Framework

4.1.1 Helmholtz Energy Functional

The Helmholtz free energy functional $F[\rho_M(R)]$ for the system can be decomposed into an ideal part and an excess part:

$$F[\rho_{\mathrm{M}}(\mathbf{R})] = kT\sum_{l=1}^{K}\int\{\rho_{\mathrm{M},l}(\mathbf{R}_l) - [\ln\rho_{\mathrm{M},l}(\mathbf{R}_l) - 1 + \beta U_{\mathrm{M},l}(\mathbf{R}_l) + \beta V_{\mathrm{M},l}(\mathbf{R}_l)]\}\,\mathrm{d}\mathbf{R}_l + F^{ex}[\rho_{\mathrm{M}}(\mathbf{R})], \tag{55}$$

where $\rho_{\mathbf{M}}(\mathbf{R})$ is the chain density and a function of positions R. R_l, $\rho_{\mathrm{M},l}$, $U_{\mathrm{M},l}$, and $V_{M,l}$ are the position, density profile, external-field potential, and intramolecular interaction of component l, respectively.

For hard-sphere chains, $F^{\mathrm{ex}} = F^{\mathrm{ex}}_{\mathrm{hs}}$. For square-well chains, the excess Helmholtz free energy functional can be expressed by [102, 110, 111]:

$$F^{\mathrm{ex}} = F^{\mathrm{ex}}_{\mathrm{hs}} + F^{\mathrm{ex}}_{\mathrm{attr}}, \tag{56}$$

where the subscript "hs" represents the hard-sphere repulsive contribution, and the subscript "attr" denotes the contribution of square-well attractive interaction between segments. The following weighted density approximations are adapted for these two contributions:

$$F^{\mathrm{ex}}_{\mathrm{hs}}[\rho_{\mathrm{M}}] = \sum_{i=1}^{K}\int\rho_i(\mathbf{r})f^{(i)}_{\mathrm{hs}}\,[\bar{\rho}^{(i)}_{\mathrm{hs}}(\mathbf{r})]\mathrm{d}\mathbf{r}, \tag{57a}$$

$$F^{\mathrm{ex}}_{\mathrm{attr}}[\rho_{\mathrm{M}}] = \sum_{i=1}^{K}\int\rho_i(\mathbf{r})f^{(i)}_{\mathrm{attr}}\,[\bar{\rho}^{(i)}_{\mathrm{attr}}(\mathbf{r})]\,\mathrm{d}\mathbf{r}, \tag{57b}$$

where $f^{(i)}_{\mathrm{hs}}[\bar{\rho}]$ is the partial excess free energy functional of a hard-sphere chain i at a given weighted density profile $\bar{\rho}^{(i)}_{\mathrm{hs}}(\mathbf{r})$, which accounts for the excluded-volume effect. $f^{(i)}_{\mathrm{attr}}(\bar{\rho})$ is the difference between the partial excess free energy of a square-well chain and that of a hard-sphere chain. Expressions of $f^{(i)}_{\mathrm{hs}}$ and $f^{(i)}_{\mathrm{attr}}$ can be found elsewhere [102]. $F^{\mathrm{ex}}_{\mathrm{hs}}$ and F^{ex}_{attr} are calculated by the corresponding equation of state. $\bar{\rho}(\mathbf{r})$ is the weighted density profile given by:

$$\bar{\rho}_{\mathrm{hs}}(\mathbf{r}) = \int\rho(\mathbf{r}')w_{\mathrm{hs}}(|\mathbf{r}-\mathbf{r}'|)\,\mathrm{d}\mathbf{r}', \tag{58a}$$

$$\bar{\rho}_{\mathrm{attr}}(\mathbf{r}) = \int\rho(\mathbf{r}')w_{\mathrm{attr}}(|\mathrm{r}-\mathrm{r}'|)\,\mathrm{d}\mathbf{r}', \tag{58b}$$

where $w_{\mathrm{hs}}(\mathbf{r})$ and $w_{\mathrm{attr}}(\mathbf{r})$ are the weighting functions for hard-sphere and attractive square-well contributions, respectively. The weighting functions satisfy the normalization condition:

$$\int w_{hs}(\mathbf{r})\mathrm{d}\mathbf{r} = \int w_{\mathrm{attr}}(\mathbf{r})\,\mathrm{d}\mathbf{r} = 1 \tag{59}$$

with:

$$w_{\mathrm{hs}}(\mathbf{r}) = 3\Theta(\sigma - \mathbf{r})/4\pi\sigma^3, \tag{60a}$$

$$w_{\mathrm{attr}}(\mathbf{r}) = 3\Theta(L\sigma - \mathbf{r})/4\pi(L\sigma)^3, \tag{60b}$$

where $L\sigma$ is the width of square-well and $L = 1.5$ is selected.

4.1.2 Euler–Lagrange Equation

In DFT, the grand potential functional Ω can be expressed as a single functional of density $\Omega = \Omega[\rho]$. Let $\boldsymbol{R} = \{r_1, \ldots, r_m\}$ denotes the position of m segments of a polymer chain, and r_i is the spatial position of the ith segment. Molecular density is correspondingly written as $\rho_{\mathrm{M},l}(\mathbf{R})$. The grand potential functional $\Omega[\rho_{\mathrm{M},l}]$ can be expressed as:

$$\Omega[\rho_{\mathrm{M},l}] = F[\rho_{\mathrm{M},l}] + \int U_{M,l}(\mathbf{R})\rho_{\mathrm{M},l}(\mathbf{R})\mathrm{d}\mathbf{R} - \mu \int \rho_{\mathrm{M},l}(\mathbf{R})\mathrm{d}\mathbf{R}, \tag{61}$$

where μ is the chemical potential.

Following the variational principles, the stationary condition of the grand potential satisfies:

$$\delta\Omega/\delta\rho_{\mathrm{M},l}(\mathbf{R}) = 0. \tag{62}$$

The segment density is given by:

$$\rho_l(\mathbf{r}) = \int \sum_{j=1}^{m_l} \rho_{\mathrm{M},l}(\mathbf{R}_l)\,\delta(\mathbf{r} - \mathbf{r}_j)\,\mathrm{d}\mathbf{R}_l, \tag{63}$$

where ρ_l is the segment density profile of molecule l with length m_l, and $\mathbf{r}$ is the segment coordinate.

Therefore, the segment density profile can be written as:

$$\rho_l(\mathbf{r}) = \int \sum_{j=1}^{m_l} \delta(\mathbf{r} - \mathbf{r}') \exp\left[\beta\mu_{\mathrm{M},l} - \beta U_{\mathrm{M},l} - \beta V_{M,l} - \sum_{i=1}^{m_l} \lambda_l(\mathbf{r}_i)\right] \mathrm{d}\mathbf{R}_l, \tag{64}$$

where:

$$\lambda_{\mathrm{hs}}^{(l)}(\mathbf{r}) = \beta f_{\mathrm{hs}}^{(l)}[\bar{\rho}_{\mathrm{hs}}^{(l)}(\mathbf{r})] + \sum_{\mathrm{i}=1}^{L}\sum_{k=1}^{L} \int \rho_i(\mathbf{r}') \frac{\delta\beta f_{\mathrm{hs}}^{(i)}[\bar{\rho}_{\mathrm{hs}}^{(i)}(r)]}{\delta\bar{\rho}_{\mathrm{hs}}^{(k)}(\mathbf{r}')} \frac{\delta\bar{\rho}_{\mathrm{hs}}^{(k)}(\mathbf{r}')}{\delta\rho_l(\mathbf{r})}\,\mathrm{d}\mathbf{r}', \tag{65a}$$

$$\lambda_{\mathrm{attr}}^{(l)}(\mathbf{r}) = \beta f_{\mathrm{attr}}^{(l)}[\bar{\rho}_{\mathrm{attr}}^{(l)}(\mathbf{r})] + \sum_{\mathrm{i}=1}^{L}\sum_{k=1}^{L} \int \rho_i(\mathbf{r}') \frac{\delta\beta f_{\mathrm{attr}}^{(i)}[\bar{\rho}_{\mathrm{attr}}^{(i)}(\mathbf{r})]}{\delta\bar{\rho}_{\mathrm{attr}}^{(k)}(\mathbf{r}')} \frac{\delta\bar{\rho}_{\mathrm{attr}}^{(k)}(\mathbf{r}')}{\delta\rho_l(\mathbf{r})}\mathrm{d}\mathbf{r}'. \tag{65b}$$

Equation 64 can be used to solve the segment density profile. However, we need to know the intramolecular interaction $V_{\mathrm{M},l}$, which can be obtained by a single-chain

MC simulation. Subsequently, the density profiles are calculated by:

$$\rho_l(\mathbf{r}) = \exp(\beta\mu_{\mathrm{M},l}) \left\langle \int \sum_{j=1}^{m_l} \delta(\mathbf{r}-\mathbf{r}') \exp\left[-\beta U_{\mathrm{M},l} - \sum_{i=1}^{m_l} \lambda_l(\mathbf{r}_i)\right] \mathrm{d}\boldsymbol{R}_l \right\rangle, \tag{66}$$

where $\langle \ldots \rangle$ is the ensemble average for a single chain.

Besides single-chain MC simulation method, the intramolecular interaction is also approximately given by:

$$V_{\mathrm{int}\,ra}(\mathbf{R}) \approx \sum_{i=1}^{m-1} v_b(|\mathbf{r}_{i+1} - \mathbf{r}_i|), \tag{67}$$

where v_b is the bonding potential. We consider the tangentially connected square-well chains whose bonding potential is given by:

$$\exp(-\beta v_\mathrm{b}(|\mathbf{r}-\mathbf{r}'|)) = \frac{1}{4\pi\sigma^2}\delta(|r-\mathbf{r}'|-\sigma). \tag{68}$$

Then, the density profile of segments can be expressed as:

$$\rho(\mathbf{r}) = \exp(\beta\mu_\mathrm{M}) \sum_{i=1}^{m} \exp(-\beta\Psi_i(\mathbf{r})) G_L^i(r) G_R^i(r), \tag{69}$$

where $\Psi(r) = U_\mathrm{ext}(r) + \lambda(r)$ and G is the Green propagator:

$$G_L^i(r) = \int \mathrm{d}r' \exp[-\beta\Psi_{i-1}(r')] \frac{\delta(|r-r'|-\sigma)}{4\pi\sigma^2} G_L^{i-1}(r'), \tag{70a}$$

$$G_R^j(r) = \int \mathrm{d}r' \exp[-\beta\Psi_{j+1}(r')] \frac{(\delta|r-r'|-\sigma)}{4\pi\sigma^2} G_R^{j+1}(r'), \tag{70b}$$

for $i = 2, \ldots, m$ and $j = 1, \ldots, m-1$, with $G_L^1(r) = 1$ and $G_R^m(r) = 1$.

We can use both Eqs. 66 and 69 to solve density profiles of segments.

4.2 Application to Hard-Sphere Chains and their Mixtures

4.2.1 Hard-Sphere Chains

Density functional theory (DFT) for non-uniform systems containing chain-like molecules based on the EOS of HSCF developed by Hu et al. [26] is presented by Cai et al. [112]. Chain-like molecules confined between two planes are treated as tangent-jointed hard-sphere chains with intermolecular and intramolecular attraction between the spheres. The Helmholtz free energy is expressed by two parts: the ideal gas part and the excess part, both are functionals of the density distribution. The excess part is calculated from the *m*-particle cavity correlation function.

A single chain MC simulation is adopted to compute the density profile of the chain beads. This method is also used for the calculation of density profiles of hard-sphere chain fluid near the hard-sphere particle [113]. Later, Chen et al. [114] used this method to study the density profile, the chain conformation, and the pattern transfer parameter (PTP) of polymer confined between two nanopatterned walls, where the interaction between strip-like wall and chain segment is given by:

$$\beta u(r_{\mathrm{i-wall}}) = \begin{cases} 0 & r_{\mathrm{i-wall}} \geq 0 \\ \infty & r_{\mathrm{i-wall}} < 0 \end{cases} \tag{71a}$$

for repulsive stripes, and:

$$\beta u(r_{\mathrm{i-wall}}) = \begin{cases} 0 & \sigma < r_{\mathrm{i-wall}} \\ -\lambda & \sigma \geq r_{\mathrm{i-wall}} \geq 0 \\ \infty & r_{\mathrm{i-wall}} < 0 \end{cases} \tag{71b}$$

for attractive stripes. λ is the square-well energy parameter.

Figure 14 shows the pattern transfer parameter (PTP) as a function of z, the distance from the wall. The number of stripes (Ns) at the patterned surface in a simulation box is two. PTP is defined as:

$$\mathrm{PTP(z)} = \frac{\int\limits_{x_D,y_D} \Phi^a(x,y,z)/A_D - \int\limits_{x_C,y_C} \Phi^a(x,y,z)/A_C}{\int\limits_{x,y} \Phi^a(x,y,z)/(A_C + A_D)}, \tag{72}$$

where $\Phi^a(x,y,z)$ is the volume fraction of the adsorbing species at location (x,y,z). A_C and A_D denote the surface areas of C and D domains on the surface, respectively.

It is found that the strength of the segment-wall interaction has a notable effect on the recognition ability, as expected. On the other hand, the effect of segment-wall interaction on PTP increases moderately when the chain length increases. It is also shown that the PTP decreases as the packing density increases. At lower bulk

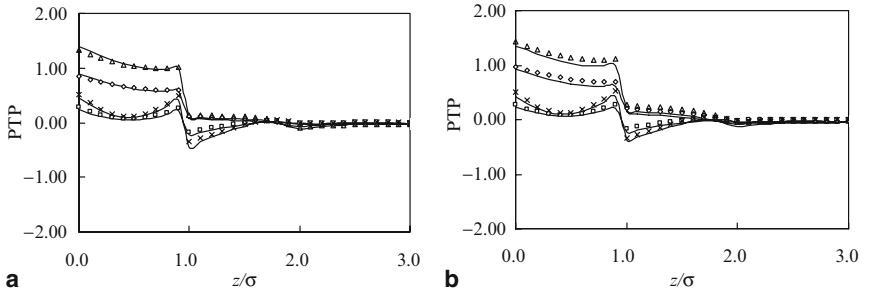

Fig. 14 Pattern transfer parameter of **a** 6-mers and **b** 12-mers when Ns = 2. *Lines* represent theoretical results; *symbols* MC data; *open diamonds* $\eta = 0.1$, $\lambda = 0.5$; *open squares* $\eta = 0.3$, $\lambda = 0.5$; *open triangles* $\eta = 0.1$, $\lambda = 1.0$; *times* $\eta = 0.3$, $\lambda = 1.0$

density, the segment-wall attraction is predominant. At higher bulk density, the segment-wall attraction has to compete with the exclude-volume effect.

Figure 14 also reveals that polymer chains can not only recognize the surface, but also invert the surface when $1.0 \leq z/\sigma \leq 2.0$ at a higher packing fraction. The inversion recognition phenomenon has also been found by Semler et al. [115]. At a higher packing fraction, more polymer chains are adsorbed due to the segment-wall attraction. However, more polymers or segments move to the next stripe (non-adsorbing region) because of the packing effect.

Generally, we have a discontinuity at $z/\sigma = 1.0$, expressed as an interrupted peak originated from the square-well nature of the segment-wall attraction. Furthermore, near $z/\sigma = 2.0$ there is a second weak trough at higher packing fraction due to the packing effect.

4.2.2 Hard-Sphere Chain Mixtures

The mixtures including two kinds of hard-sphere chains confined in a slit of width 10 σ were calculated [100]. The predicted values of monomer density profiles of mixtures are in good agreement with those by simulation. At higher bulk densities, the density profiles of hard-sphere chain fluids (HSCFs) is similar to that of simple hard-sphere fluids, which has a high peak near the wall. At lower bulk densities, the density profiles exhibits a smaller peak at about 1 σ instead of a high peak near the wall. As the bulk density further decreases, the peak tends to disappear. The variation of bead density near the wall results from the competition between the configurational entropic effect and the bulk packing effect. For HSCFs, the loss in configurational entropy promotes depletion of beads near the surface, while the packing of chains against the surface promotes enrichment. At lower densities, the configurational entropic effect plays a key role. At high densities, the bulk packing effect dominates to utilize the available free volume more efficiently.

4.3 Application to Square-Well Chains and their Mixtures

The interaction between the segment and the solid wall is depicted by the square-well potential:

$$u(r_{i-\text{wall}}) = \begin{cases} 0 & r_{i-\text{wall}} > \sigma \\ -\lambda_{i-W} & 0 < r_{i-\text{wall}} < \sigma \\ \infty & r_{E-\text{wall}} < 0 \end{cases} . \tag{73}$$

The equation of state of HSCF developed by Hu et al. [26] is used to calculate the partial molecular excess free energy of the repulsive part. The SAFT-VR equation of Gil-Villegas et al. [24] is used to calculate the partial molecular excess free energy of the attractive part.

4.3.1 Square-Well Chains

Based on the theory of Cai et al. [112], Zhang et al. [116] studied the square-well fluid confined between two parallel planar wall. The calculated results of density profile are satisfactory at higher temperature but are poor at lower temperature.

Ye et al. [102] developed another simple weighting function for the attractive part to construct the excess free energy. Generally, the results for short chains are in good agreement with the simulation data over the entire density region. For long chains, except at low packing fraction and at low temperature, the results are in good agreement with the simulation data. The density profiles for square-well chains are influenced by the competition between the single-chain configuration and many-chain packing effects, and also by the competition between segment–segment attraction and segment-wall attraction, i.e., the density profiles of the chains are governed by the entropic effect and the energetic effect. At lower packing fractions, chains are apt to be in the bulk region for larger configurationally entropy. However, at high packing fractions, chains prefer to keep away from bulk regions for more free volume. The depletion of chain density near the wall becomes stronger when the segment–segment attraction increases (i.e., the temperature decreases). In contrast, the segment-wall attraction causes higher chain density near the wall.

Recently, the hybrid density functional theory (HDFT) (Chen et al., unpublished results), which combines a single chain MC simulation for the ideal gas free energy functional with two weighted density approximations, developed respectively by Yethiraj et al. [110] and by Ye et al. [102] for the excess free energy functional, has been extended and applied to a selective nanoslit.

Figure 15 shows the comparison between theoretical predictions and simulation data for the segmental density profiles of square-well copolymer with

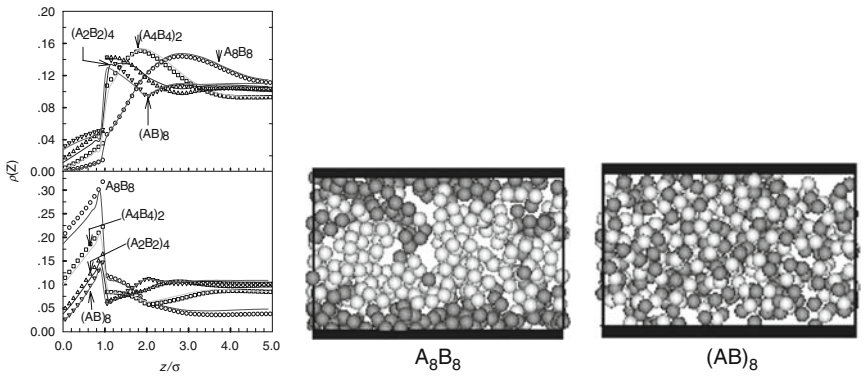

Fig. 15 Comparison between theoretical predictions (*solid lines* this work) and simulation data (*symbols*) for the segmental density profiles of square-well copolymer chains with different chemical sequences in a selective slit: *circles* A_8B_8, *squares* $(A_4B_4)_2$, *triangles up* $(A_2B_2)_4$, *triangles down* $(AB)_8$. The reduced surface energies are $\lambda_{AW} = -1.0$ and $\lambda_{BW} = 1.0$. *Upper graph* segments A; *lower graph* segments B. Corresponding snapshots of A_8B_8(*middle*) and $(AB)_8$ (*right*)

different chemical sequences of copolymer in a selective surface when $\lambda_{AW} = -1.0$ and $\lambda_{BW} = 1.0$. The theoretical predictions catch the primary characteristics of simulations.

Segments A of all copolymers, which have repulsive interaction with the surface, show a depletion layer near the surface, and then come to a peak due to the chain connectivity. The exact position of the maximum is determined mainly by the length of the A block; as the length of block A increases, the maximum site appears farther from the surfaces. Furthermore, for $(AB)_8$, after the peak there is one trough due to the packing effect.

Segments B of all copolymers show an adsorption layer near the surface. As expected, the density profile of B segments with an attractive well is always bigger than that of A segments. The discontinuity of square-well causes a discontinuity at the boundary of the square-well range. Similar behavior has been observed in a selective slit [117] and for other monomeric square-well fluids near a square-well wall [118, 119].

Fixing the length of chain as a constant; as the length of block x decreases, the phase separation becomes indiscernible. The experimental results of Velankar et al. [120] also showed that the degree of microphase separation increases with increasing block length. It was also shown that for the same chain length, the microphase separation of alternate copolymers is difficult while that of diblock copolymer is easier. Two snapshots from MC simulations are shown in Fig. 15. The rich domains of segments A and B of diblock polymer are clearer than that of alternate polymer. Compared with diblock copolymers, alternate copolymers become more coiled and folded. In other words, copolymers possess more homopolymer character as the length of block x decreases.

4.3.2 Square-Well Chain Mixtures

The density functional theory for square-well sphere homopolymer mixtures has also been developed by Ye et al. [103] and Chen et al. [105]. Configurations were also studied by DFT.

Generally, we can find that there is a peak or a cusp at $z = \sigma$ the latter occurs when the segment density on the wall surface is very low. This is similar to the behavior of the corresponding hard-sphere mixture. At higher bulk density, the segment density is enhanced on the wall surface; the density profile has a maximum at $z = 0$ on the wall surface and the maximum value decreases with the increase of chain length. At lower bulk density, the segment density is depleted on the wall surface; the depletion of density near the wall is strengthened with an increase of chain length. It seems that the properties of chains are governed by the chain connectivity at low packing fractions; therefore, the longer chains do not reach the surface as easily as the shorter chains. At high packing fractions, the properties are governed by the excluded volume effect.

Adsorption configurations can be typically classified into three types: tail, loop, and train. A sequence of successive segments is referred to as *tail* if it starts from the

head or the end of a chain to the first segment in contact with surface. It is referred to as *loop* if the sequence is between two nearest segments that are in contact with surface. It is referred to as *train* if the successive segments of a sequence are in contact with the surface. Consequently, the lengths of tail, loop, and train are in the range between 1 and $m_l - 1, m_l - 2, m_l$, respectively. Additionally, bridge is also observed for sufficiently long polymer chains adsorbed simultaneously on both surfaces. This type of configuration is closely related to the stability of colloidal suspensions.

The probability $P_q(i)$ of finding a configuration with i beads is defined as [114, 121, 122]:

$$P_q(i) = N_q(i) / \sum N_q(i), \tag{74}$$

where $q =$ tail, loop, train, or bridge. $N_q(i)$ is the total number of a configuration q with i beads. The average size of a configuration is given by:

$$< i >_q = \sum_i i P_q(i) / \sum_i P_q(i). \tag{75}$$

The percentage S_q of a configuration is defined as [114]:

$$S_q = \sum_i i \times N_q(i) / \sum_q \sum_I i \times N_q(i). \tag{76}$$

Figures 16 shows the average sizes and percentages of tail, loop, and train in B_6 of A_3/B_6 mixture in a selective slit with $\lambda_{AW} = -0.5$ and different λ_{BW}. With increasing adsorption energy between segment B and the surface (i.e., increasing λ_{BW}), more B_6 molecules are adsorbed. As a consequence, $<i>_{tail}$ in B_6 decreases, while $<i>_{loop}$ and $<i>_{train}$ increase (Fig. 16a), S_{tail} decreases, while S_{loop} increases (Fig. 16b). Nevertheless, the extent of decrease or increase is not pronounced. Because the surface is repulsive to segment A, A_3 is much less adsorbed than B_6. Furthermore, λ_{BW} has little effect on the configurations in A_3. Upon increasing λ_{BW}, the $<i>_{tail}$, $<i>_{loop}$, and $<i>_{train}$ in A_3 nearly remain the same, approximately equal to 1.75, 1.00, and 1.03, respectively.

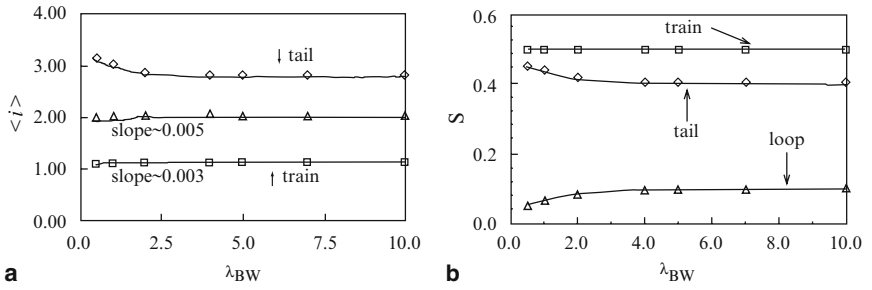

Fig. 16 **a** Average sizes and **b** percentages of tail, loop, and train in B_6 of A_3/B_6 mixture in a selective slit ($\lambda_{AW} = -0.5$ and various λ_{BW}): *open diamond* tail, *open triangle* loop, *open square* train. *Lines* indicate predictions, *symbols* simulations

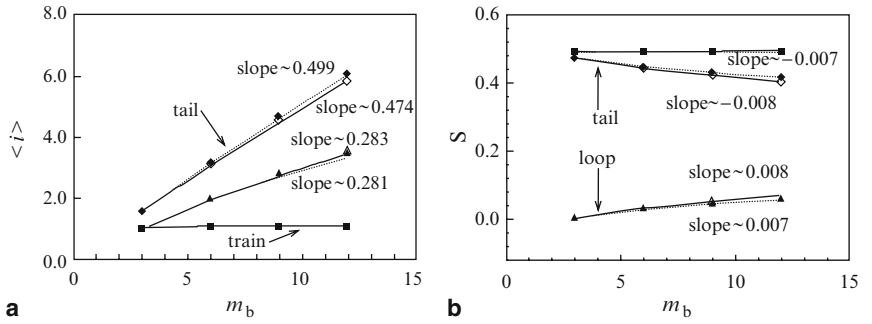

Fig. 17 **a** Average sizes and **b** percentages of tail, loop, and train in B_{mb} of A_3/B_{mb} (m_b = 3, 6, 9, 12) mixture in a selective slit ($\lambda_{AW} = -0.5$ and $\lambda_{BW} = 0.5$): *open diamond* tail, *open triangle* loop, *open square* train; and in a non-selective slit ($\lambda_{AW} = \lambda_{BW} = 0.5$): *filled diamond* tail, *filled triangle* loop, *filled square* train. *Lines* indicate predictions, *symbols* simulations

Figures 17 shows the average sizes and percentages of tail, loop, and train in B_{mb} of A_3/B_{mb} (m_b = 3, 6, 9, 12) mixture in a selective slit with $\lambda_{AW} = -0.5$ and $\lambda_{BW} = 0.5$, and in a non-selective slit with $\lambda_{AW} = \lambda_{BW} = 0.5$. In the selective slit, with increasing chain length of B_{mb}, while the relative amount of B_{mb} in the mixture decreases because the total packing fraction is fixed at 0.1, the average sizes and percentages of the three configurations increase, except for S_{tail}. The lengths of tail, loop, and train are primarily governed by chain length, and a longer chain leads to longer configurations. Though not shown, the average sizes of configurations in A_3 remain almost constant. Similar chain-length dependences of the configurations were previously predicted by the Scheutjens–Fleer lattice theory [123] and observed in a detailed atomistic simulation for polyethylene melt adsorbed on graphite [124]. For even longer B_{mb} chain (e.g., m_b = 16), bridges form connecting the two slit surfaces with a very small percentage $\sim 10^{-6}$. Upon further increasing m_b to 24, both the size and percentage of bridge are enhanced to 18.5 and 10^{-4}, respectively.

Closely similar configurational behavior is found in the non-selective slit. The average sizes of the three configurations in $A_3$are nearly constant, in which $<i>_{tail}$ is about 1.60 slightly smaller than that in the selective slit, and $<i>_{loop}$ and $<i>_{train}$ are approximately the same as those in the selective slit.

5 Conclusion

A theoretical method based on equation of state or Helmholtz function model has been developed in this laboratory that can be used to study the multiscale structure of polymer systems, including the phase diagram, morphology evolution of microphase separation, density and composition profile, and molecular configuration in the interfacial region between different phases. The molecular parameters in the model can be determined from the pVT data and miscibility of the polymer, which enhances the possibility of practical applications.

Acknowledgments This work is supported by the National Natural Science Foundation of China (project nos. 20736002, 20490200), the Doctoral Research Foundation sponsored by the Ministry of Education of China (project no. 20050251004), Program for Changjiang Scholars and Innovative Research Team in University (no. IRT0721), the 111 Project (no. B08021) and E-institute of Shanghai High Institution Grid (no. 200303).

References

1. Bates FS (1991) Science **251**:898
2. Park M, Harrison C, Chainkin PM, Register RA, Adamson DH (1997) Science **276**:1401
3. Xia Y, Rogers JA, Paul KE, Whitesides GM (1999) Chem Rev **99**:1823
4. Li H, Huck WTS (2002) Curr Opin Solid State Mater **6**:3
5. Prausnitz JM, Lichtenthaler RN, de Azevedo EG (1999) Molecular thermodynamics of fluid-phase equilibria, 3rd edn. Prentice-Hall PTR, Englewood Cliffs
6. Sadus RJ (1999) Molecular simulation of fluids, theory, algorithms and object-orientation. Elsevier, Amsterdam
7. Chaikin PM, Lubensky TC (1995) Principles of condensed matter physics. Cambridge University Press, Cambridge
8. Matsen MW, Barrett C (1998) J Chem Phys **109**:4108
9. Fraaije JGEM (1993) J Chem Phys **99**:9202
10. Oono Y, Shiwa Y (1987) Moden Phys Letter B **1**:49
11. Oono Y, Puri S (1988) Phys Rev A **38**:434; 1542
12. Groot RD, Warren PB (1997) J Chem Phys **107**:4423
13. Chandler D, McCoy JD, Singer SJ (1986) J Chem Phys **85**:5971
14. Scheutjens JMHM, Fleer GJ (1979) J Phys Chem **83**:1619
15. Sun L, Peng CJ, Liu HL, Hu Y, Jiang JW (2007) J Chem Phys **126**:094905
16. Feng J, Liu HL, Hu Y (2005) Mol Simul **31**:731
17. Wertheim MS (1987) J Chem Phys **87**:7323
18. Chapman WG, Gubbins KE, Jackson G, Radosz M (1990) Ind Eng Chem Res **29**:31
19. Huang SH, Radosz M (1990) Ind Eng Chem Res **29**:2284
20. Huang SH, Radosz M (1991) Ind Eng Chem Res **30**:1994
21. Chiew YC, Mol Phys (1990) **70**:129
22. Chang J, Sandler SI (1994) Chem Eng Sci **49**:2777
23. Song YH, Lambert S.M, Prausnitz JM (1994) Ind Eng Chem Res **33**:1047
24. Gil-Villegas A, Galindo A, Whitehead PJ, Mills SJ, Jackson G, Burgess AN (1997) J Chem Phys **106**:4168
25. Gross J, Sadowski G (2001) Ind Eng Chem Res **40**:1244
26. Hu Y, Liu HL, Prausnitz JM (1996) J Chem Phys **104**:396
27. Cummings PT, Stell G (1985) Mol Phys **55**:33
28. Zhou Y, Stell G (1992) J Chem Phys **96**:1504
29. Liu HL, Hu Y (1996) Fluid Phase Equilibria **122**:75
30. Liu HL, Hu Y (1997) Fluid Phase Equilibria **138**:69
31. Alder BJ, Young DA, Mark MA (1972) J Chem Phys **56**:3013
32. Liu HL, Zhou H, Hu Y (1997) Chinese J Chem Eng **5**:193
33. Liu HL, Hu Y (1998) Ind Eng Chem Res **37**:3058
34. Peng CJ, Liu HL, Hu Y (2001) Chinese J Chem **19**:1165
35. Tildesley DJ, Streett WB (1980) Mol Phys **41**:85
36. Liu HL, Rong ZM, Hu Y (1995) J East China Univers Sci Techn **21**:619 (in Chinese)
37. Liu HL, Hu Y (1996) J Chem Eng Chinese-Univers **10**:337 (in Chinese)
38. Liu HL, Rong ZM, Hu Y (1996) Chinese J Chem Eng **4**:95
39. Yethiraj A, Hall CK (1991) J Chem Phys **95**:1999
40. Yethiraj A, Hall CK (1991) J Chem Phys **95**:8494

41. Yethiraj A, Hall CK (1991) Mol Phys **72**:619
42. Ghonasgi D, Chapman WG (1993) Mol Phys **80**:161
43. Mansoori GA, Carnahan NF, Starling KE, Leland TW (1971) J Chem Phys **54**:1523
44. Peng CJ, Liu HL, Hu Y (2002) Fluid Phase Equilibria **201**:19
45. Peng C.J, Liu HL, Hu Y (2002) Fluid Phase Equilibria **202**:67
46. Peng CJ, Liu HL, Hu Y (2003) Fluid Phase Equilibria **206**:147
47. Zhou H, Liu HL, Hu Y (1998) J Chem Ind, Eng.(China) **49**:1 (in Chinese)
48. Zhou H, Liu HL, Hu Y (1998) J East China Univers Sci Techn **24**:209 (in Chinese)
49. Wang TF, Peng CJ, Liu HL, Hu Y (2006) Fluid Phase Equilibria **250**:150
50. Wang TF, Peng CJ, Liu HL, Hu Y, Jiang JW (2007) Ind Eng Chem Res **46**:4323
51. Peng CJ, Liu HL, Hu Y (2003) Fluid Phase Equilibria **206**:127
52. Peng CJ, Liu HL, Hu Y (2002) Ind Eng Chem Res **41**:862
53. Peng CJ, Liu HL, Hu Y (2001) Fluid Phase Equilibria **180**:299
54. Peng CJ, Liu HL, Hu Y (2001) Chem Eng Sci **56**:6967
55. Whiting WB, Prausnitz JM (1982) Fluid Phase Equilibria **9**:119
56. Wang SL, Peng CJ, Shi JB, Liu HL, Hu Y (2003) Fluid Phase Equilibria **213**:99
57. Li JL, Ma J, Peng CJ, Liu HL, Hu Y, Jiang JW (2007) Ind Eng Chem Res **46**:7267
58. Zhou YX, Peng CJ, Qiu DL, He EC, Liu HL (2006) J East China Univers Sci Techn **32**:953 (in Chinese)
59. Zhou YX, Peng CJ, He EC, Liu HL (2006) Petrochem Techn **35**:1063 (in Chinese)
60. Xuan AG, Wu YX, Peng CJ, Ma PS (2006) Fluid Phase Equilibria **240**:15
61. Feng J, Liu HL, Hu Y (2003) J Chem Ind, Eng.(China) **54**:881 (in Chinese)
62. Jiang JW, Liu HL, Hu Y, Prausnitz JM (1998) J Chem Phys **108**:780
63. Jiang JW, Liu HL, Hu Y (1999) J Chem Phys **110**:4952
64. Zhang B, Cai J, Liu HL, Hu Y (2002) Chinese J Chem Eng **10**:311
65. Yang JY, Liu N, Yu DH, Peng CJ, Liu HL, Hu Y, Jiang JW (2005) Ind Eng Chem Res **44**:8120
66. Jiang JW, Feng J, Liu HL, Hu Y (2006) J Chem Phys **124**:144908
67. Feng J, Liu HL, Hu Y (2006) Mol Simul **32**:51
68. Yang JY, Peng CJ, Liu HL, Hu Y, Jiang JW (2006) Fluid Phase Equilibria **244**:188
69. Yang JY, Yan QL, Liu HL, Hu Y (2006) Polymer **47**:5187
70. Yang JY, Peng CJ, Liu HL, Hu Y (2006) Ind Eng Chem Res **45**:6811
71. Yang JY, Peng CJ, Liu HL, Hu Y (2006) Fluid Phase Equilibria **249**:192
72. Liu HL, Yang JY, Xin Q, Hu Y (2007) Fluid Phase Equilibria **261**:281
73. Huang YM, Jin XC, Liu HL, Hu Y (2008) Fluid Phase Equilibria **263**:96
74. Xu XC, Liu HL, Peng CJ, Hu Y (2008) Fluid Phase Equilibria **265**:112
75. Xin Q, Peng CJ, Liu HL, Hu Y (2008) Fluid Phase Equilibria **267**:163
76. Hu Y, Liu HL (2006) Fluid Phase Equilibria **241**:248
77. Park M, Harrison C, Chainkin PM, Register RA, Adamson DH (1997) Science **276**:1401
78. Xia Y, Rogers JA, Paul KE, Whitesides GM (1999) Chem Rev **99**:1823
79. Li HW, Huck WTS (2002) Curr Opin Solid State Mater Sci **6**:3
80. Feng J, Cai J, Liu HL, Hu Y (2000) J East China Univers Sci Techn **26**:421 (in Chinese)
81. Xu H, Liu HL, Hu Y (2007) Chem Eng Sci **62**:3494
82. Xu H, Liu HL, Hu Y (2007) Macromol Theory Simul **16**:262
83. Hajduk DA, Urayama P, Gruner SM, Erramilli S, Register RA, Brister K, Fetters LJ (1995) Macromolecules **28**:7148
84. Hajduk DA, Gruner SM, Erramilli S, Register RA, Fetters LJ (1996) Macromolecules **29**:1473
85. Pollard M, Russell TP, Ruzette AV, Mayes AM, Gallot Y (1998) Macromolecules **31**:6493
86. Ruzette AVG, Mayes AM, Pollard M, Russell TP, Hammouda B (2003) Macromolecules **36**:3351
87. Schwahn D, Frielinghaus H, Mortensen K, Almdal K (1998) Physica B **241**–243:1029
88. Sun H (1998) J Phys Chem B **102**:7338
89. Sato F, Hojo S, Sun H (2003) J Phys Chem A **107**:248
90. Park DW, Roe RJ (1991) Macromolecules **24**:5324
91. Roe RJ, Zin WC (1980) Macromolecules **13**:1221

92. Ladanyi BM, Chandler D (1975) J Chem Phys **62**:4308
93. Chandler D, McCoy JD, Singer SJ (1986) J Chem Phys **85**:5971
94. Chandler D, McCoy JD, Singer SJ (1986) J Chem Phys **85**:5977
95. McCoy JD, Singer SJ, Chandler D (1987) J Chem Phys **87**:4853
96. Hooper JB, Pileggi MT, McCoy JD, Gurro JG, Weinhold JD (2000) J Chem Phys **112**:3094
97. Woodward CE (1991) J Chem Phys **94**:3183
98. Kierlik E, Rosinberg ML (1994) J Chem Phys **100**:1716
99. Nath SK, Nealey PF, de Pablo JJ (1999) J Chem Phys **110**:7483
100. Cai J, Liu HL, Hu Y (2002) Fluid Phase Equilibria **194–197**:281
101. Zhang SL, Cai J, Liu HL, Hu Y (2004) Mol Simul **30**:143
102. Ye ZC, Cai J, Liu HL, Hu Y (2005) J Chem Phys **123**:194902
103. Ye ZC, Chen HY, Cai J, Liu HL, Hu Y (2006) J Chem Phys **125**:124705
104. Ye ZC, Chen HY, Liu HL, Hu Y, Jiang JW (2007) J Chem Phys **126**:134903
105. Chen HY, Ye ZC, Cai J, Liu HL, Hu Y, Jiang J (2007) J Phys Chem B**111**:5927
106. Yu YX, Wu JZ (2002) J Chem Phys **117**:2368
107. Rosenfeld Y (1989) Phys Rev Lett **63**:980
108. Tripathi S, Chapman WG (2005) J Chem Phys **122**:094506
109. Chapman WG, Jackson G, Gubbins KE (1988) Mol Phys **65**:1057
110. Yethiraj A, Woodward CE (1995) J Chem Phys **102**:5499
111. Patra CN, Yethiraj A (2000) J Chem Phys **112**:1579
112. Cai J, Liu HL, Hu Y (2000) J East China Unvers Sci Techn **26**:100 (In Chinese)
113. Ye ZC, Zhang SL, Cai J, Liu HL, Hu Y (2006) J Chem Eng Chinese Univers **20**:18 (in Chinese)
114. Chen HY, Ye ZC, Peng CJ, Liu HL, Hu Y (2006) J Chem Phys **125**:204708
115. Semler JJ, Genzer J (2003) J Chem Phys **119**:5274
116. Zhang SL, Cai J, LIu HL, Hu Y (2002) J East China Unvers Sci Techn **28**:274 (in Chinese)
117. Cao DP. Wu JZ (2005) Macromolecules **38**:971
118. Zhou SQ (2003) J Phys Chem B **107**:3585
119. Henderson JR, van Swol F (1988) J Chem Phys **89**:5010
120. Velankar S, Cooper SL (1998) Macromolecules **31**:9181
121. Jeon J, Dobrynin AV (2003) Phys Rev E **67**:061803
122. Chen HY, Peng CJ, Ye ZC, Liu HL, Hu Y, Jiang JW (2007) Langmuir **23**:2430
123. Scheutjens JMHM, Fleer GJ (1985) Macromolecules **18**:1882
124. Daoulas KC, Harmandaris VA, Mavrantzas VG (2005) Macromolecules **38**:5780

Struct Bond
DOI:10.1007/430_2008_5

Ionic Liquids and Relative Process Design

S. Zhang, X. Lu, Y. Zhang, Q. Zhou, J. Sun, L. Han, G. Yue, X. Liu, W. Cheng, and S. Li

Abstract Ionic liquids have gained increasing attention in recent years due to their significant advantages, not only as alternative solvents but also as new materials and catalysts. Until now, most research work on ionic liquids has been at the laboratory or pilot scale. In view of the multifarious applications of ionic liquids, more new knowledge is needed and more systematic work on ionic liquids should be carried out deeply and broadly in order to meet the future needs of process design. For example, knowledge of the physicochemical properties is indispensable for the design of new ionic liquids and for the development of novel processes. The synthesis and application of ionic liquids are fundamental parts of engineering science, and the toxicity and environmental assessment of ionic liquids is critical importance for their large scale applications, especially for process design. These research aspects are closely correlated to the industrial applications of ionic liquids and to sustainable processes. However, material process design in the industrial applications of ionic liquids has hardly been implemented. Therefore, this chapter reviews several essential issues that are closely related to process design, such as the synthesis, structure-property relationships, important applications, and toxicity of ionic liquids.

Keywords: Ionic liquids · Process design · Synthesis · Properties · Applications · Toxicity

Contents

S. Zhang(✉), X. Lu, Y. Zhang, Q. Zhou, J. Sun, L. Han, G. Yue, X. Liu, W. Cheng, and S. Li
Key Laboratory of Green Process and Engineering, Institute of Process Engineering, Chinese Academy of Sciences, Beijing 100080, People's Republic of China
e-mail: sjzhang@home.ipe.ac.cn

1 Introduction

Increasingly, stringent environmental legislation has generated a pressing need for cleaner methods of chemical production, i.e., technologies that reduce or eliminate the generation of waste and avoid the use of toxic or hazardous reagents and solvents [1–4]. This strategy is directed at the design of products with high process efficiency, acceptable costs, and low toxic potential for man and the environment. Ionic liquids (ILs), as important constituents of green solvents, have the potential to improve existing processes and new developments in a multitude of fields in chemistry and chemical technology [3–5].

The first ionic liquid, ethylammonium nitrate, described by Walden, seems to have generated little interest. In 1948, the physical and chemical properties of pyridinium aluminium tetrachloride were investigated. In 1992, this was followed by the discovery that several tetraalkylammonium salts form air- and moisture-stable ILs. From then, the subject of ILs became much hotter. In order to meet the needs of industry, task-specific ILs have been synthesized and employed as solvents for catalysis, synthesis, and electrochemistry [6].

The growing interest in ILs is primarily due to their specific properties (fluid over a broad temperature range, non-flammable, non-explosive, non-coordinating, non-solvating, not very corrosive, extremely low vapor pressure, miscibility or non-miscibility with water and other solvents, high electrochemical stability), which can be tuned by an appropriate choice of anion and cation. ILs can be considered "designer solvents" that can be synthesized rather easily, and many ILs are already available commercially [7]. There are estimated to be hundreds of thousands of simple ion combinations to make ILs, and a near endless (10^{18}) number of potential IL mixtures. The development of reactions in ILs is not only important on the laboratory scale but also for industrial applications, although very few have come to execution. Several processes that use an IL are at pilot scale, and only BASF's BASIL process is realized industrialization.

Commercial applications of ILs need related process design. Chemical process engineering utilizes chemical property and thermodynamic data to design the process and build the equipment required to produce chemical products. Since both the thermodynamics and kinetics of reactions carried out in ILs are different from those in conventional media, they offer new and novel opportunities for multifarious reaction/separation processes and also new challenges for the process designs. When ILs could significantly benefit the chemical industry by providing more efficient synthesis and processing systems, the design problems originating in the new markets are discovered [8].

Process design of ILs requires researchers to not only develop fundamental understanding of IL synthesis and properties, but to impart these liquids with the chemical processing features needed for important industrial applications. Synthesis of ILs in a controlled and predictable way for application-driven research will be required by process design of ILs. Emphasis should be focused on developing ILs with practical industrial needs in mind: economic synthetic pathways, minimizing the costs of raw materials, extended lifetimes of the ILs, minimum toxicity, and increased contaminant tolerability.

Modeling and computational science can greatly aid in the prediction of properties and performance of ILs. Modeling capabilities will provide greater flexibility for validating fundamentals based on experimentation. It is necessary to measure and develop physical and thermodynamic properties of ILs from fundamental understanding at the molecular level. This is required to allow "tunable" synthesis of ILs and to understand the reaction mechanisms involving ILs in chemical processes.

Many of the IL studies to date have been performed at the laboratory scale under conditions that do not adequately represent operating conditions for full-scale industrial applications. In many cases, researchers do not give a complete answer to process design; the process engineer must use experience and judgment to combine various sources of information into practical solutions. Engineering-scale studies and pilot plant demonstrations are the principal tools that provide the basis for experience and for judgment decisions on the process design of new technologies. So, from the application research on ILs we can obtain fundamental information for IL process designs. In this chapter we also present the important applications of ILs, such as in catalysis, materials, and electrochemistry.

ILs have no detectable vapor pressure and do not emit the volatile organic compounds (VOC) associated with many organic solvents. However, each IL is likely to be classified as a "new chemical" and may require a significantly sound, science-based understanding of their environmental, safety and health imports prior to widespread use. It is necessary to establish safety guidelines for IL research, production, and commercial application.

The following sections discuss issues closely related to process design (synthesis, structure–property relationships, typical applications, toxicity) and identify the research that would help the process design of ILs in the chemical industry.

2 Synthesis of ILs

ILs are composed entirely of ions that are fluid around or below 100°C. In comparison to only about 600 molecular solvents, there are potentially at least a million binary ILs, and 10^{18} ternary ILs [9]. Most ILs have an organic cation and an inorganic or polyatomic anion. Typical formulations of ILs rely mostly on quaternary nitrogen or phosphorus cations such as 1-alkyl-3-methylimidazolium, *N*-alkylpyridinium, tetraalkylammonium, tetraalkylphosphonium, and anions such as Cl^-, Br^-, $[BF_4]^-$, $[PF_6]^-$, $[HSO_4]^-$, $[AlCl_4]^-$, $[CH_3COO]^-$, $[CF_3COO]^-$, $[CF_3SO_3]^-$, $[N(CF_3SO_2)_2]^-$, and so on. With the rapid advancement in studies on ILs, synthesis of ILs, especially functional ILs, has gained more and more attention so that an ever-growing volume of literature describing novel ILs has appeared. To accelerate commercialization of ILs and ensure reasonable process design, it is necessary to prepare ILs in a controlled and predictable way. Also, the synthesis routes should be low-cost and green. So, this section will summarize the different methods of ILs synthesis.

2.1 Two-Step Synthesis

Two-step synthesis of ILs is the most widely applied to prepare the desired ILs, which includes the formation of cations and the anion exchange (shown in Scheme 1).

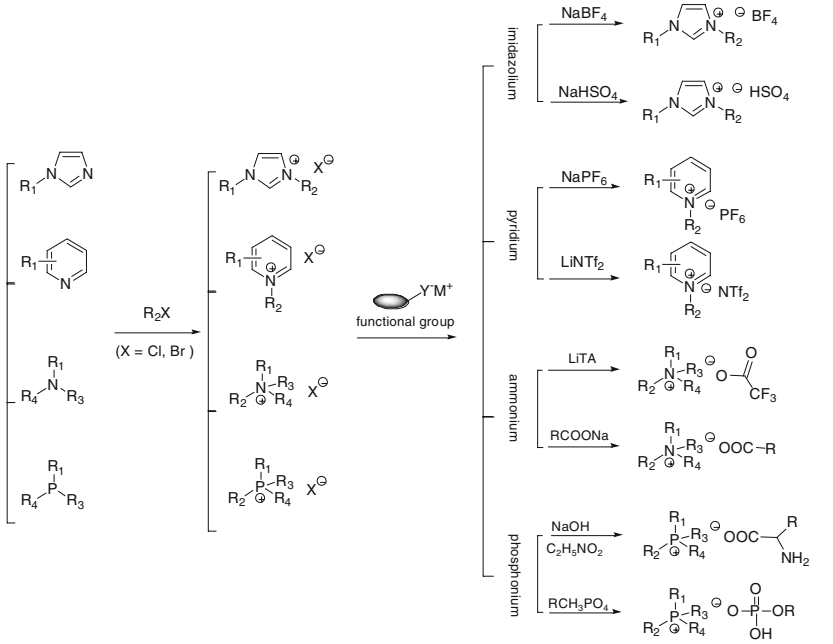

Scheme 1 Two-step synthesis of ILs

Cations are mainly prepared either by protonation with a free acid, or by quaternization of an amine or a phosphine, most commonly with a haloalkane [10–13]. In general, the quaternization reactions are simple: an amine or a phosphine is mixed with the haloalkane, and then the mixture is stirred and heated. The reaction conditions, such as reaction temperature and time, are very dependent on the haloalkane employed and become steadily more gentle in the order chloroalkane $<$ bromoalkane $<$ iodoalkane, as expected for nucleophilic substitution reactions. The reactivity of halocanes generally decreases with the increase of alkyl chain length. However, fluoride salts cannot be formed in this manner. The obtained ILs precursors, commonly halide salts, are generally solid at room temperature, for example 1-alkyl-3-methylimidazolium halide, which can be purified effectively by recrystallization from a mixture of dry acetonitrile and ethyl acetate. The precursors are then used for anion metathesis with Lewis acids or metal salts. The direct treatment of halide salts with Lewis acids is generally a fairly exothermic reaction. The build-up of excess local heat can lead to decomposition and discoloration of the ILs so that great care should be taken when adding one component to the other in small portions, to allow the heat to dissipate. For anion metathesis, a range of silver salts such as $AgNO_3$, $AgNO_2$, $AgBF_4$, $Ag[CO_2CH_3]$, and Ag_2SO_4, in methanol or aqueous methanol solutions is firstly utilized to prepare the relatively air- and water-stable ILs based on 1,3-dialkylimidazolium cations. Later, a solution of sodium salts, potassium salts, or acids of the desired anions are widely used in preparation of ILs. The resulting mixtures form either a biphasic system or a homogeneous phase with water, which depends mainly on the anions selected. For water-immiscible ILs (if the anion is $[PF_6]^-$ or $[N(CF_3SO_2)_2]^-$), they are washed with water to remove the halide and obtain halide-free ILs. If the resulting ILs form a homogeneous solution with water, they should be extracted with organic solvents (e.g., dichloromethane), washed with water to remove the halide, and vaporized under reduced pressure to remove of residual volatile substances.

The two-step synthesis of ILs has many advantages:

- A wide range of cheap haloalkanes is available
- The quaternization reactions generally occur smoothly at reasonable temperatures
- The anion metathesis can always be achieved at mild performance conditions

However, this process of ILs synthesis is not very green nor atom-efficient. Firstly, excessive haloalkanes are needed for quaternization of an amine or a phosphine to get a reasonable yield of the corresponding ILs precursor. Secondly, excessive metal salts with desirable anions are needed to increase the metathesis rate, and an equimolar amount of waste MX acids or salts is produced. Thirdly, many volatile organic compounds (VOCs), such as dichloromethane, acetonitrile, hexy1 acetate, and so on, are commonly used to prepare and purify ILs. As a result, it is critically necessary to develop other effective processes for IL synthesis.

2.2 One-Pot Synthesis

One-pot synthesis of ILs is a strategy to improve the efficiency of quaternization reactions and to obtain the desired ILs in just one reactor. This is highly desirable because it avoids a lengthy separation process and purification of the intermediate chemical compounds, while increasing ILs yield. Many halide-free ILs without salt-forming metathesis have been achieved using one-pot synthesis [14–19].

For example, the mixture of dialkylimidazolium tetrafluoroborate ($[R_1R_2im][BF_4]$) ILs can be obtained by the one-pot reaction of glyoxal, methylamine, *n*-butylamine, formaldehyde, and tetrafluoroboric acid. New, low cost 1,3-dialkylimidazolium ILs containing methyl- and ethyl-sulfate anions have been prepared by alkylation of the appropriate imidazole with dimethyl sulfate or diethyl sulfate. Also, several direct, solvent-free, halide-free routes to phosphonium ILs via the quaternization of tertiary phosphines with dialkylsulfates, trialkylphosphates, and alkylphosphonates have been reported. By a similar route, phosphonium tosylates, the relatively novel anions, have been also prepared.

Another straightforward synthesis of ILs in one-pot is based on simple acid–base chemistry, which is a typical atom-economic reaction without any poisonous by-product. For example, 23 new chiral ILs have been achieved in high yield and purity by the reaction of amino acids or chiral carboxylic acids with tetrabutylammonium hydroxide in water. Also, two families of ILs, in which the chiral cations are directly derived from naturally occurring α-amino acids and α-amino acid ester salts, have been obtained via a simple protonation reaction carried out by mixing the correct molar ratio of amino acid and the appropriate strong acid in water, followed by evaporation of the water under vacuum.

2.3 Cleaner Large-Scale Production

ILs are mainly synthesized in small quantities in laboratories, which leads to the price of ILs being as high as US $10 per gram, even for the common ILs. The high price of ILs has heavily blocked their applications in industry. On the other hand, synthesis of ILs in this way has caused plenty of wastes that may cause a host of negative effects, including insecure quality and purity, and environmental problems. It requires, in the majority of cases, the rethinking and redesign of the IL synthesis process.

With the first integrated process for production of ILs on a large-scale, (Scheme 2) developed in the Henan Lihua Pharmaceutical Co. by the Institute of Process Engineering of the Chinese Academy of Sciences, the problems mentioned above have almost been solved. The cleaner production of ILs is concerned with the more cost-effective use of starting materials and reduction of wastes to zero.

According to this process (producing about 200 tons per year), the waste bromine aqueous solution produced in the Lihua Pharmaceutical Co. is fully exploited to produce haloalkanes, which are the primarily materials for IL synthesis. Considering

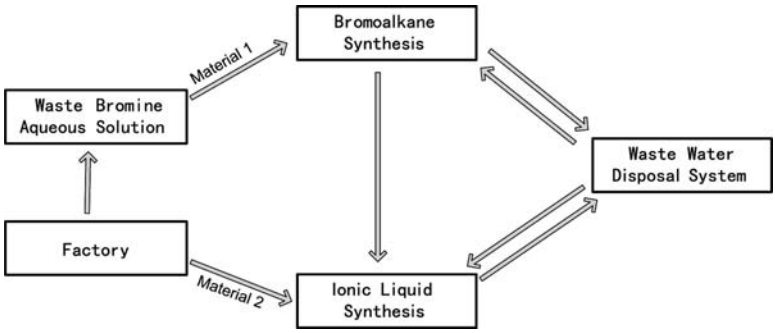

Scheme 2 Integrated process for production of ILs on a large-scale

the different operating conditions required, the process is well developed to be fit for producing a number of series of ILs. With volatile organic solvents recycled (such as acetonitrile, hexy1 acetate, and dichloromethane) and waste-water reused after proper treatment, the whole integrated process is nearly zero-emission. Its implementation has led to economic benefit and a cleaner environment.

3 Structures and Properties of ILs

Property measurement and prediction is essential both for guiding synthesis and for developing applications. It is important that there is a fundamental understanding of ILs at the molecular level in order to tune their physical and thermodynamic properties and further explain the reaction mechanisms involved in chemical processes. Modeling and computational science could greatly aid in prediction of the properties and performance of ILs. Structure–property relationships of ILs will be employed in process design. This section introduces molecular simulation and the common physical–chemical properties of ILs.

3.1 Molecular Simulations of ILs

3.1.1 Research Status and Progress

Molecular simulation is a way to study the thermodynamics, dynamic properties, and microstructures of a system by analyzing the interaction between atoms and molecules. Molecular simulation, especially for multiscale modeling (which focuses on the fundamental modeling and computational principles underlying various multiscale methods), bridges the growing gap in understanding the system at the levels of the atom, molecule, cluster, and in the industrial reactor. Molecular

simulations have played an important role in developing our understanding of the relationship between microscopic and macroscopic properties of ILs. Molecular dynamics (MD), Monte Carlo (MC), transition state, and rare event simulation techniques have been used to study the IL-related processes. It is the objective of this section to highlight these advances and to show that molecular simulations can provide new insights not available from experiments and that they can provide clues to the development of novel separation and reaction processes [20–24].

Since the 1990s, the amount of research on ILs has expanded rapidly. However, designing functional ILs with different applications by experiment is boring, as the possible choices of cation and anion of ILs are numerous. Moreover, experimental data are very scarce, and this scarcity is due to the expensive synthesizing process. In order to interpret the experimentally observed properties from the large scale production processes, we need insights into the energetics and siting of intermediate molecular species formed during the reaction; such information is impossible to obtain from experiments. Fortunately, they can be tailored by judicious selection of cations and anions through molecular simulation [25–32].

3.1.2 Simulation Methods and Research Status

Molecular simulation, including quantum mechanics (QM), MD simulation and MC, can be used for studying the mechanism of chemical reactions and the relationships between the macroproperties and microstructures for ILs. QM is based on the Schrödinger equation, while QM/MC is based on the atomic or molecular interactions. To bridge the electronic, atomistic/molecular and mesoscopic scales across several orders of magnitude in length and time, the ab initio molecular dynamic simulation and coarse-graining molecular simulation are performed on the way. A description of the multiscale in molecular simulation can be found in Fig. 1.

The electronic structures (such as molecular orbital, electron density, and charge population) and properties (such as molecular energy, polarization, and active site) were systematically investigated at the electronic scale. The formation of hydrogen bonds between cations and anions is a key step for Lewis acid–base reactions, a typical example being amino-appended ILs capturing CO_2 [33]. Imidazolium ILs,

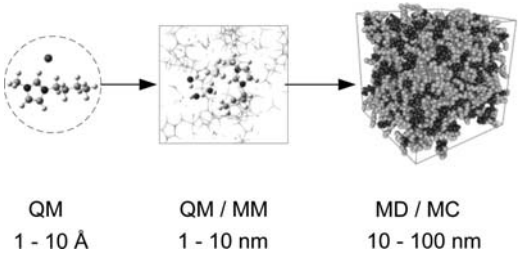

Fig. 1 Multiscale in molecular simulation

which are functionalized by introducing NH_2, have been found to be excellent solvents for CO_2 capture and electrophile separation; however, the relatively high viscosities limit their eventual large-scale applications. To understand the influences of amino addition on the properties of ILs and promote their applications, the microstructure and interionic interaction in two selected amino-functionalized imidazolium ILs, 1-aminoethyl-3-methylimidazolium hexafluorophosphate and 1-aminopropyl-3-butylimidazolium tetrafluoroborate, were studied both for bulk liquid (by using molecular dynamics simulations) and for isolated ion pair (by using ab initio calculations). Calculations show that such terminal amino-associated interaction reduces the flexibility of alkyl side chains and increases the cation–anion interaction. Based on the above results, some ILs with lower viscosities were designed, and the structures for two of them are shown in Fig. 2 [34, 35].

Hydrogen-bond networks were found to extensively exist in imidazolium-, guanidinium-, and phosphonium-based ILs. Intra- and interinteractions among cations and anions, especially the existing hydrogen bonds, strongly affect the physical properties of ILs. The hydrogen-bond network in [emim]Cl is shown in Fig. 3 [36].

At the atomic/molecular scale, precision of the corresponding results for MD and MC simulations are based on the force field to a large extent. The success of molecular simulation in accurately predicting various properties depends on the quality of inter- and intramolecular potential functions. Several force fields, including AMBER, CHARMM, and OPLS, have been developed and applied successfully in a

Fig. 2 Structures for two of the ILs with lower viscosities

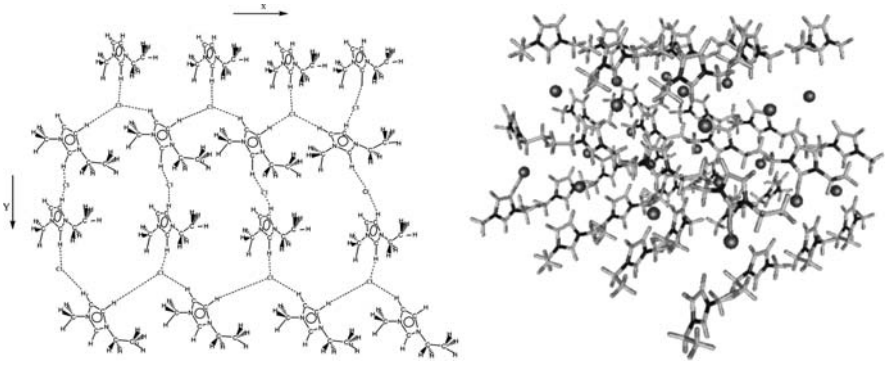

Fig. 3 Hydrogen-bond network in [emim]Cl

variety of systems. However, little research on the force field specific for ILs has been reported in a systematic way. In the work of S. Zhang, the force field parameters were determined for a number of the ILs, such as guanidinium-based ILs and tetrabutylphosphonium amino acid ILs, and the thermodynamic and transport properties of the ILs were obtained by MD. Figure 4 shows the structures and atom types of two of the typical ILs: 1,1,3,3-tetramethylguanidinium perchlorate (TMGP) and tetrabutylphosphonium glutamic acid ($[P(C_4)_4][Glu]$). Radial distribution functions (RDFs) and space distribution functions (SDFs) were investigated to depict the microscopic structures of the ILs. RDFs and SDFs for TMGP are shown in Fig. 5. For

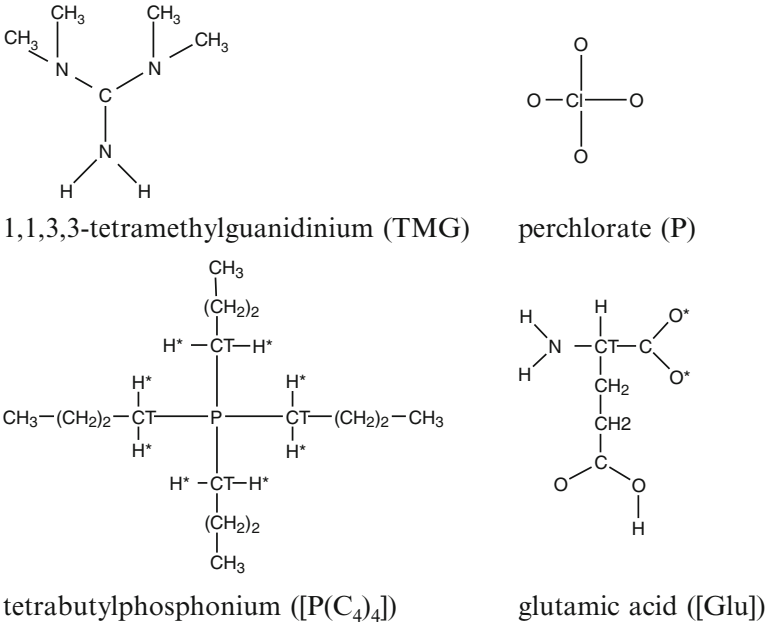

Fig. 4 Structures and atom types of TMGP and $[P(C_4)]$

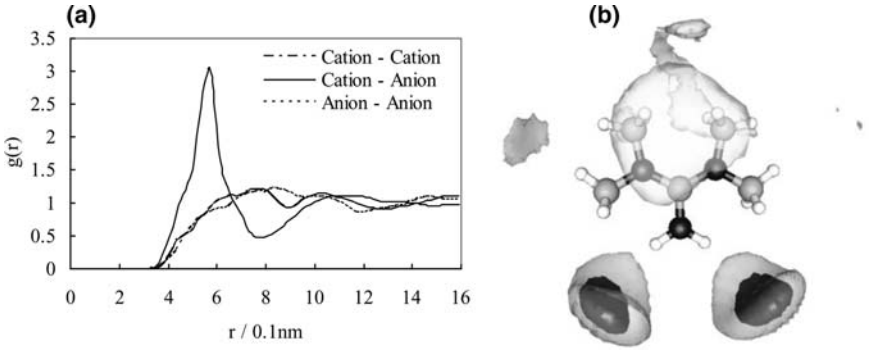

Fig. 5 RDFs (**a**) and SDF (**b**) for guanidinium-based ILs

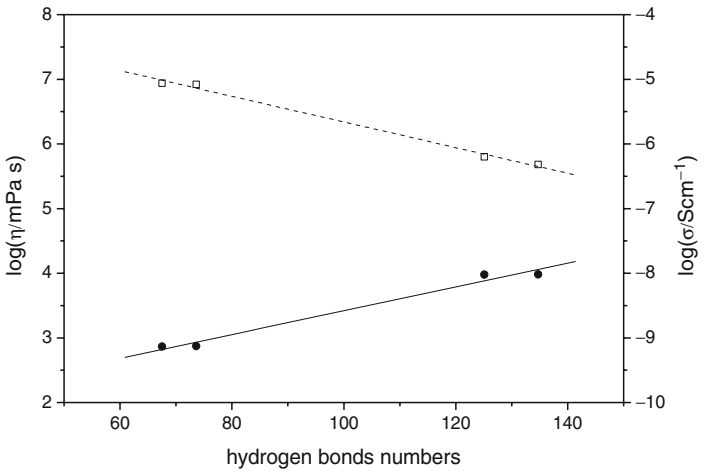

Fig. 6 Experimental conductivities (*squares*) and viscosities (*points*) as a function of hydrogen bond numbers

the $[P(C_4)_4][Glu]$, RDFs of $H^* - O^*$ reveal that H^* in the tetrabutylphosphonium can form hydrogen bonds with O^* in different anions. The hydrogen bonds explain to some extent the low electrical conductivities and high viscosities of the studied tetrabutylphosphonium amino acid ILs. Figure 6 shows the experimental conductivities and viscosities of four kinds of tetrabutylphosphonium-based ILs as a function of the hydrogen bond numbers [37–40].

As Joan F. Brennecke and Edward J. Maginn said, ILs offers the opportunity for chemical engineers to revolutionize the way we do business [25]. How to design the functional ILs becomes the most urgent requirement for industrial application. However, that requires fundamental knowledge of how the nature of the cation, anion, and substituents affect the chemical and physical properties. This fundamental knowledge can be developed in experimentation or through molecular simulations. Because the experimental data for ILs are extremely scarce, molecular simulations are being performed to probe the properties of ILs and solutions containing ILs. Three aspects, QM, QM/MD, and MM, should be considered in order to depict the relationships between properties and structures at multiscale. A maximum amount of information on ILs will be obtained by molecular simulations, and the information will be helpful in designing new functional ILs with the desired properties.

3.2 Properties of ILs

According to the typical cations, ILs are mainly divided into imidazolium, pyridinium, ammonium, phosphonium, pyrrolidinium, guanidinium, sulfonium, and other ILs. The potential for fine-tuning various physicochemical properties of ILs

by structural modification within the anionic and cationic parts distinguishes them from conventional molecular solvents. Knowledge of structure–property relationships is critically necessary for the rational design of ILs with specific applications. To obtain the underlying principles of fundamental physicochemical properties, the structural factors of cations and anions (size, symmetry, charge density, chain length, functional groups, etc.) are needed for a better understanding. As 1-alkyl-3-methylimidazolium ILs have been fully investigated, they will be mainly taken as examples to illustrate the structure–property relationships of ILs.

3.2.1 Melting Point

Effect of Cation Structure on Melting Point

Melting points are dominated by electrostatic forces for ILs with shorter alkyl chains, and by the short-range van der Waals interactions for ILs with longer alkyl chains [10, 41–44]. The competition of the factors yields the u-shape plot shown in Fig. 7. The melting points of imidzolim ILs decrease rapidly when n = 2–4, remain nearly constant when n = 6–8, and increase gradually when n = 9–18 with the increasing chain length.

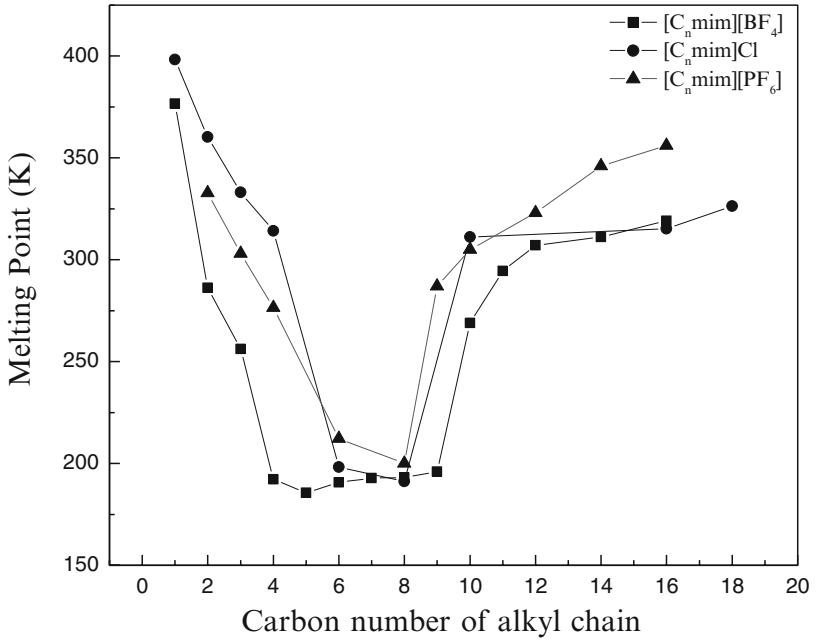

Fig. 7 Change in melting points with alkyl chain length for imidazolium ILs

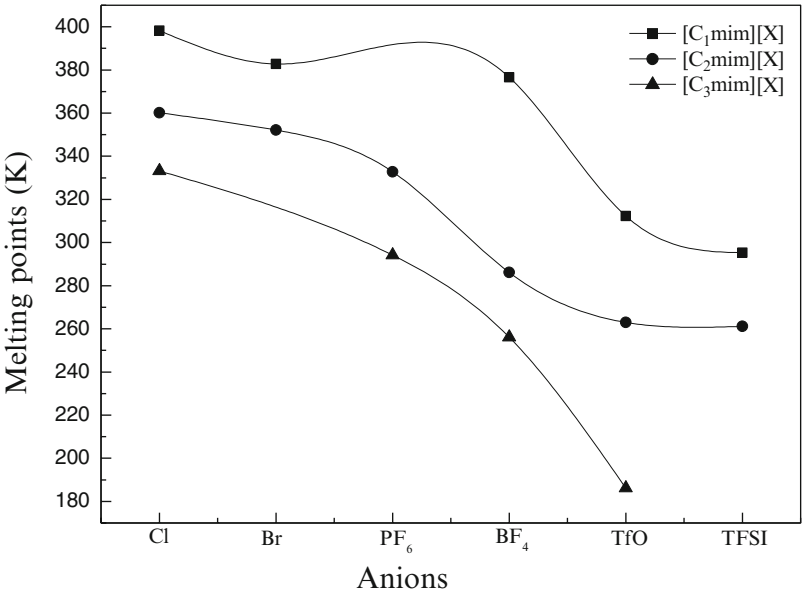

Fig. 8 Change in melting points with anions for imidazolium ILs

Effect of Anion Structure on Melting Point

Increase in anion size generally gives rise to decrease in the melting points of ILs, mainly because of reduction of the Coulombic attraction to the lattice energy of crystal and the increase of the covalency of ions [41, 45–47], as can be seen from Fig. 8. The melting points of ILs follow the order

$$Cl^- > Br^- > [PF_6]^- > [BF_4]^- > [TfO]^- > [TFSI]^-.$$

3.2.2 Glass Transition Point, Clearing Point, and Freezing Point

The solid–liquid transitions of many ILs are relatively complex. A typical IL being heated from the solid state usually cannot become liquid directly since there may be several phase change points such as glass transition point (T_g), melting point (T_m) and clearing point (T_c) [17, 48, 49]. ILs with a long alkyl chain length can form a mesomorphic state whose lower critical point is T_m and upper critical point is T_c (shown in Fig. 9). The gap between T_m and T_c becomes bigger with the increase in alkyl chain length.

Theoretically, freezing point (T_f) should be consistent with melting point (T_m). However, ILs may form supercooled liquids during the solid–liquid transitions. 1-Ethyl-3-methylimidazolium ILs exhibit obvious supercooled phenomena, and the gap between T_f and T_m is as wide as 40–90 K, as shown in Fig. 10.

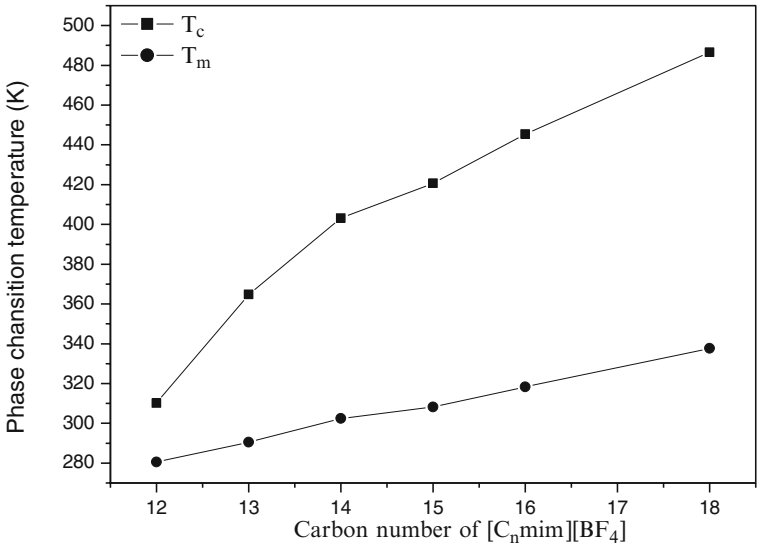

Fig. 9 Change in T_m and T_c with increase in alkyl chain length of cations

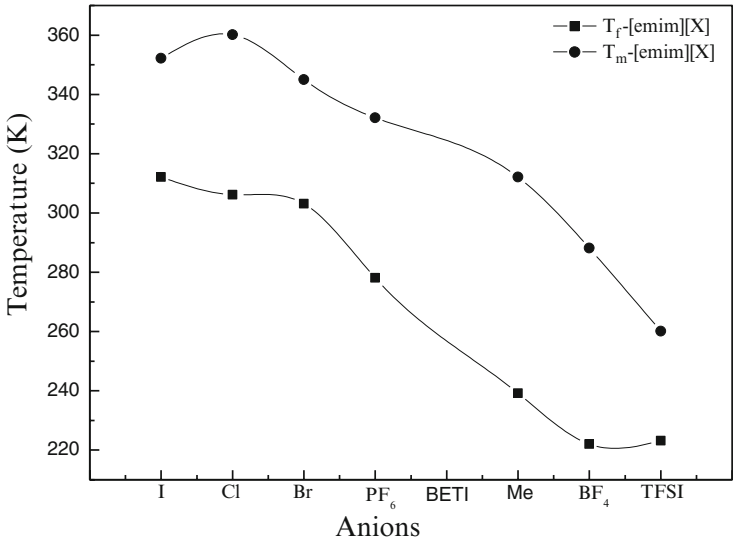

Fig. 10 Change in T_f and T_m with anions

3.2.3 Thermal Stability and Decomposition Point

As ILs are composed entirely of ions, they usually have good thermal stability. On the other hand, ILs contain organic cations, which restricts their upper stability temperature, defined by the decomposition point (T_d). The decomposition points of ILs

are usually determined by thermogravimetric analysis (TGA) under a N_2 protective atmosphere. The thermal stability of ILs is dominated by the charge density, acidic proton, and expansionary force of cations and anions [13, 40, 44, 50–53]. Imidazolium ILs are more stable than the corresponding ammonium and pyridinium ILs because the charge density of the imidazolium cation is lower. Moreover, methylation on the imidazolium ring increases the thermal stability of the cations. Substitution of the C(2)–H has the largest effect because of the greater acidity of this proton. As can be seen from TGA data for ILs (Table 1), the decomposition points vary with anion types and follow the general stability order $[Tf_2N]^- > [BF_4]^- > [EtSO_4]^- > Br^- > [CH_3CO_2]^- > [CF_3CO_2]^-$, which indicates that ILs containing weakly coordinating anions are mostly stable to high-temperature decomposition.

3.2.4 Density

Densities are perhaps the most straightforwardly determined and unambiguous physical properties of ILs. Given a quality analytical balance and good volumetric glassware, the density of an IL can be obtained. The densities of imidazolium ILs

Table 1 Decomposition temperatures of ILs

IL	T_{onset}/K	T_{start}/K
[epy][$EtSO_4$]	576	483
[empy][$EtSO_4$]	554	486
[emmpy][$EtSO_4$]	570	482
[bpy]Br	510	467
[bmpy]Br	508	472
[bmpy][Tf_2N]	670	590
[bmpy][BF_4]	637	506
[bmmpy]Br	512	471
[hpy]Br	511	468
[hpy] [Tf_2N]	665	605
[hmpy]Br	510	472
[hmpy] [Tf_2N]	672	603
[hmmpy]Br	512	474
[hmmpy] [Tf_2N]	678	613
[hemmpy] [Tf_2N]	657	601
[hpeepy] [Tf_2N]	654	598
[hDMApy]Br	561	525
[hDMApy] [Tf_2N]	716	649
[opy]Br	509	460
[ompy]Br	506	459
[ompy] [Tf_2N]	667	605
[ompy] [BF_4]	647	547
[bmim] [CH_3CO_2]	493	446
[bmim] [CF_3CO_2]	443	415
[hmim] Br	549	492
[hmim] [Tf_2N]	700	620
[hmim] [BF_4]	631	556
[hmmim] [Tf_2N]	710	633

Table 2 Densities of 1-ethyl-3-methylimidazolium ILs

emim	$[F(HF)_n]^-$	$[BF_4]^-$	$[CF_3COO]^-$	$[CF_3SO_3]^-$	$[N(CF_3CO_2)_2]^-$
Density ($g\,cm^{-3}$)	1.13	1.24	1.285	1.38	1.50

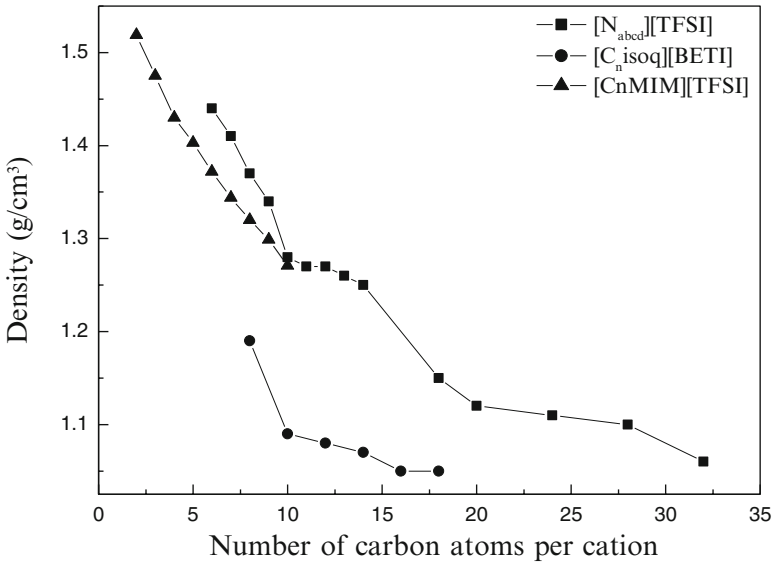

Fig. 11 Change in density with increase in alkyl chain length

vary between 1.1 and 1.6 $g\,cm^{-3}$. Besides temperature, the densities of ILs strongly depend on the structures of cations and anions. In general, IL densities increase with the decrease in cation size [54,55]. Moreover, the types of anions have obvious effect on the densities of ILs, as shown in Table 2.

Densities can be further tuned by regulating the cation structures [56]. The change in density with alkyl chain length is shown in Fig. 11. It can be clearly seen that the densities of the three series of ILs all decrease with the increase in alkyl chain length.

3.2.5 Viscosity

ILs are commonly more viscous than molecular solvents. Their viscosities at room temperature range from 10 cP to more than 500 cP [56, 57]. Unlike densities, viscosities are sensitive to the water and impurity contents so that ILs must be purified and dried completely before viscosity measurements are made [58, 59].

Temperature has the biggest effect on viscosity. In Fig. 12, it can be seen that the viscosities of ILs decrease rapidly at low temperature, and then show no obvious decrease with an increase in temperature.

The viscosities of 22 ILs at between 283 and 343 K, are shown in Table 3. For all the pyridinium ILs, their viscosities increase with an increase in cation alkyl

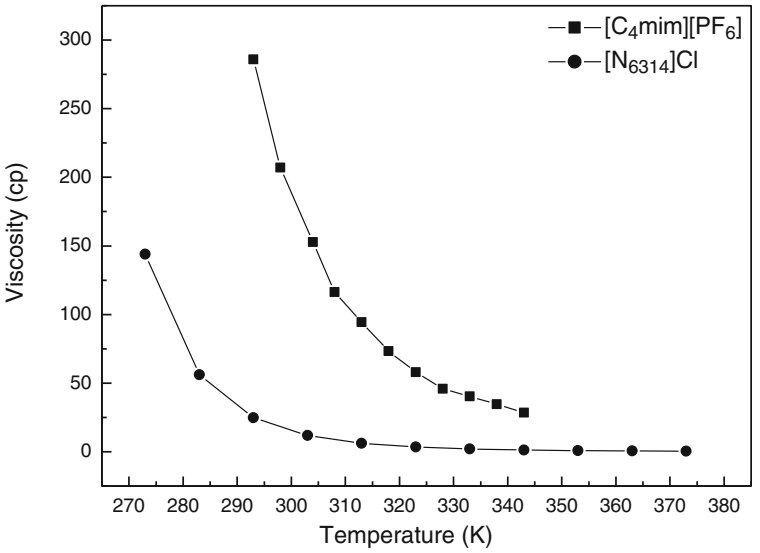

Fig. 12 Change in viscosity with temperature

Table 3 Viscosities of 22 ILs at different temperatures

IL	η (mPa s)								Water content
	283 K	293 K	298 K	303 K	313 K	323 K	333 K	343 K	(ppm)
[epy][$EtSO_4$]	356	183	137	105	66	43	31	23	683
[empy][$EtSO_4$]	414	204	150	114	70	45	32	23	256
[Et_2Nic][$EtSO_4$]	19,610	5675	3173	1986	846	405	221	130	659
[bmpy][Tf_2N]	138	80	63	51	34	24	18	14	28
[bmpy][BF_4]	517	246	177	132	78	48	33	23	327
[b_2Nic][Tf_2N]	1830	774	531	379	203	117	73	48	40
[hpy] [Tf_2N]	189	106	80	64	42	29	21	16	107
[hmpy] [Tf_2N]	197	110	85	67	44	30	22	16	152
[hmmpy] [Tf_2N]	251	136	104	81	52	35	24	18	30
[hemmpy] [Tf_2N]	708	338	245	182	106	64	42	29	258
[hpeepy] [Tf_2N]	579	281	206	155	91	57	39	27	132
[hDMApy] [Tf_2N]	285	146	111	86	54	36	25	15	68
[hmDMApy][Tf_2N]	278	148	112	87	55	37	26	19	33
[ompy] [Tf_2N]	268	146	112	88	56	27	26	19	70
[emim] [Tf_2N]	52	36	32	26	19	15	12	9	204
ECOENG 41M	4070	1676	1033	731	392	228	146	98	831
[bmim] [CH_3CO_2]	1630	646	440	309	165	97	62	42	11,003
[bmim] [CF_3CO_2]	155	89	70	53	35	24	18	13	2246
[hmim] [Tf_2N]	148	86	68	55	37	26	19	15	31
[hmmim] [Tf_2N]	317	171	131	101	63	42	30	22	13
[N_{4444}][doc]			12,100	7560	3180	1470	755	411	
ECOENG 500	10,240	2780	2790	1910	964	511	300	187	1044

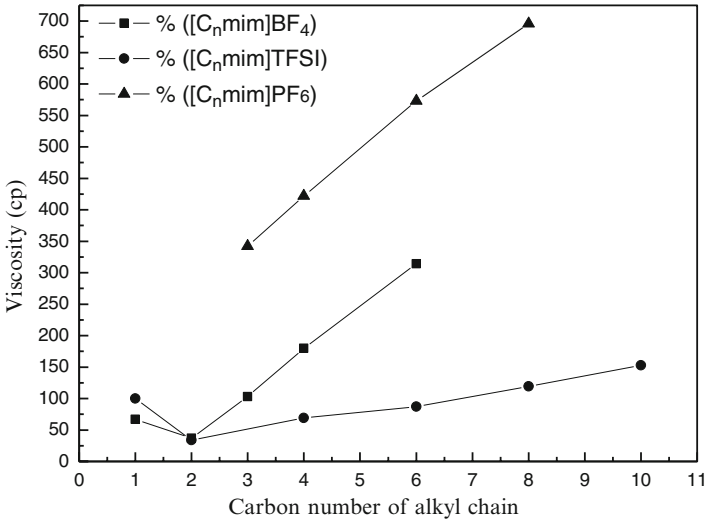

Fig. 13 Change in viscosity with alkyl chain length

chain length. Comparing $[bmpy][NTf_2]$, $[bmpy][BF_4]$, and $[empy][EtSO_4]$ it can be seen that the order of ILs viscosities is $[NTf_2]^- < [BF_4]^-$ and $[EtSO_4]^-$. From $[hpy][NTf_2]$, $[hmpy][NTf_2]$, and $[hmmpy][NTf_2]$, it can be seen that the viscosities increase as more methyl is added onto the pyridine ring. Moreover, the viscosities of imidazolium ILs show similar trends to those of the pyridinium ILs, shown in Fig. 13. This implies that their viscosities are governed by van der Waals interactions.

4 Applications of ILs

Since both the thermodynamics and kinetics of reactions carried out in ionic liquids are different from those in conventional organic solvents, ILs offer new and novel opportunities for catalytic reactions, separations, electrochemistry, and combined reaction/separation processes. Because ILs are being utilized in many research fields, the objective of this section is to discuss typical applications of ILs, particularly in catalytic reactions, materials, and electrochemistry.

4.1 ILs in Catalytic Reactions

In recent years, significant progress has been made in the application of ILs in catalytic processes because ILs have the advantages of undetectable vapor pressure,

wide liquid temperature range, special solubility for many organic or inorganic compounds, and the feasibility of design due to their unusual properties as compared with traditional molecular solvents or medias [27]. Comprehensive information about this field may be found in recent reviews [21, 23, 60–62]. Among the topics to be discussed is the question: what potential do ILs have for catalysis? A simple answer is that they have potential for green catalysis.

Advances have been made in the application of ILs to meet the demands of the industrial catalytic process, such as to take the place of organic solvents, to take the place of liquid acids, and to be immobilized for fix-bed reactors. The applications include the fixation of CO_2 using ILs, dimerization reactions, Heck reactions and hydroformylation, alkylation reactions, and Friedel–Crafts reactions. Based on the key steps involved, we suggest that these reactions can be divided into three types:

1. Hydrogen addition and rearrangement reactions
2. C–C and C–O cleavage reactions
3. C–C or C–heteroatom coupling reactions

4.1.1 Fixation of CO_2 Using ILs

Carbon dioxide (CO_2) produced by combustion of fossil fuels is regarded as the most significant greenhouse gas; the increasing accumulation of CO_2 in the atmosphere with the fast industrial development has attracted worldwide attention. On the other hand, CO_2 is one of the most naturally abundant, inexpensive, nonflammable and non-toxic C1 resources. Recalling the history of the chemical industry, we can find many applications of CO_2 in the production of valuable products and materials such as carbonated drinks, urea, polycarbonates, and so on [63–67]

In order to utilize CO_2 as C1 feedstock or sequestrate CO_2 for reduction of greenhouse effect, the investigation of efficient methods for capturing CO_2 from flue gas (in which CO_2 concentration varies from 3 to 14%) is critically important. One of the most commercially applied technologies is the chemical absorption of CO_2 by aqueous amines to form carbamates [68]. This technology, however, has shown serious disadvantages, such as the fact that the uptake of water into the gas stream requires an additional drying process and causes serious corrosion. The loss of volatile amines increases the operation cost and other difficulties, and the evaporation of water for the release of CO_2 upon heating requires an excessive cost in energy. Also, the amines used for post-combustion CO_2 separation are known to decompose, causing an environmental problem due to waste. Therefore, a novel solvent that could facilitate the separation of CO_2 from gas mixtures without concurrent loss of the capture solvent into the gas stream is highly required. In this regard, ILs show great potential as an alternative for such applications [69].

The negligible volatility of ILs results in a non-contaminated target gas and makes it especially attractive in absorption of CO_2. More interesting is that CO_2 can significantly dissolve in the ILs, as compared to conventional organic solvents, even in the case of physical absorption [70, 71]. Such higher solubilities show the

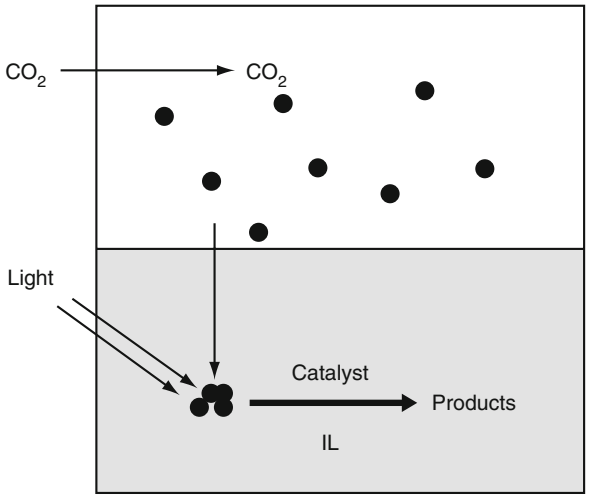

Fig. 14 Proposed integrative fixation–conversion process of CO_2 in ILs

great potential of ILs not only as good absorbents for CO_2 capture, but also as good solvents or catalysts for CO_2 reaction with other compounds such as epoxides. This is because the higher concentration of CO_2 in the ILs phase is a substantially positive factor for promoting the reaction of CO_2. Based on the above-mentioned merits of ILs as both absorbents and reaction media, we can draw a fascinating picture like Fig. 14, which shows an in-situ fixation–conversion coupling process of CO_2 in ILs.

A number of investigations have shown that as CO_2 is remarkably soluble in ILs, it can be advantageous for reactions. According to the structural features and fixation/absorption mechanisms, the ILs can be classified into two categories: conventional ILs and task-specific ILs. The conventional ILs can absorb/fix less CO_2 because of the physical interactions between CO_2 and ILs. The task-specific ILs with alkaline groups can sequester larger amounts of CO_2 than the conventional ILs because of the chemical interactions or reactivities between CO_2 and the alkaline groups of the ILs.

Fixation of CO_2 Using Conventional ILs

There are several reported works on the fixation/absorption of CO_2 in conventional imidazolium-type ILs [71–76],which are composed of 1-alkyl-3-methylimidazolium ($[rmim]^+$) cations and anions such as $[BF_4]^-$, $[PF_6]^-$, $[NTf_2]^-$, $[NO_3]^-$, and $[EtSO_4]^-$. Kazarian et al. [77] found that there was evidence of a weak Lewis acid–base interaction between CO_2 and PF_6^- or BF_4^- anions using ATR-IR spectroscopy. In order to further understand the interaction between ILs and CO_2, a image of the equilibrium state of CO_2 in [bmim]PF_6 (Fig. 15) was described by the method of molecular dynamic simulation in our group [38]. The simulations were performed at 298 K and 1 atm for a system composed of 192 molecules of [bmim]PF_6 and ten molecules of CO_2, with the standard periodical

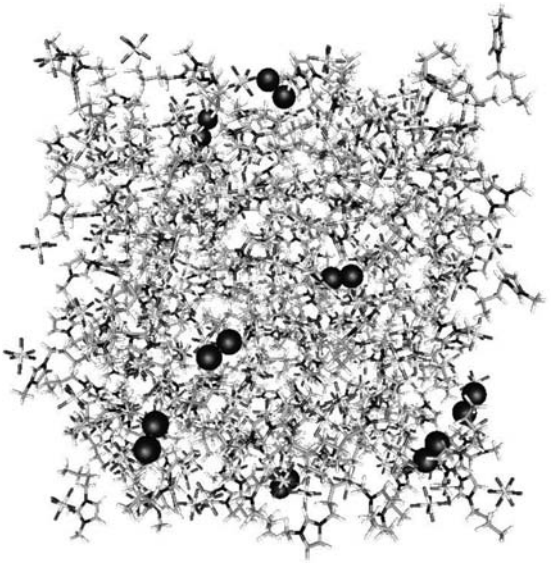

Fig. 15 Image of the equilibrium state of CO_2 in [bmim][PF_6] by molecular dynamic simulation

boundary conditions. In the obtained equilibrium state it can be seen that the molecules of CO_2 disperse well in the [bmim]PF_6 ILs. These microscopic studies provide valuable information for understanding the solubility behavior of CO_2 in the conventional imidazolium-type ILs.

Since ILs/CO_2 biphasic solutions have been used for a variety of homogeneously catalyzed reactions, an understanding of the phase behavior of CO_2 with ILs is necessary to design extraction/separation and reaction processes in industrial applications. Aiming to these purpose, Brennecke and coworkers systematically studied the high-pressure phase behavior of CO_2 in a series of imidazolium-type ILs [71,73,78]. According to the different solubilities of CO_2 and methane, ILs have the potential to be utilized in separation of CO_2 from natural gas. Anthony et al. [71] found that CO_2 solubility in [rmim][PF_6] is much higher than other gases such as CO, CH_4, H_2, N_2, and CH_3CH_3. This suggests that [rmim][PF_6] might be potentially applied as absorbent for separation of CO_2 from a coal steam gas mixture.

But, in industrial process design, high cost of ILs is still a key problem limiting their large scale utilization. Recently there have been some reported works on the solubility of CO_2 in sulfonate ILs. Since sulfonate ILs are more stable with thermal treatment and water, and can be synthesized easily from inexpensive raw materials, Zhang et al. [79] determined the solubility of CO_2 in trihexyl (tetradecyl) phosphonium dodecylbenzenesulfonate ([$P_{666,14}$][$C_{12}H_{25}PhSO_3$]) and trihexyl (tetradecyl) phosphonium methylsulfonate ([$P_{666,14}$][$MeSO_3$]) at temperatures of 305–325 K and pressures of 4–9 MPa. At a given temperature, the magnitude of the Henry constant for CO_2 follows the sequence [$P_{666,14}$][MePh-SO_3] > [$P_{666,14}$][$MeSO_3$] > [bmim][BF_4], which indicates that the solubility of CO_2 in sulfonate ILs is generally lower than that in imidazolium-type ILs.

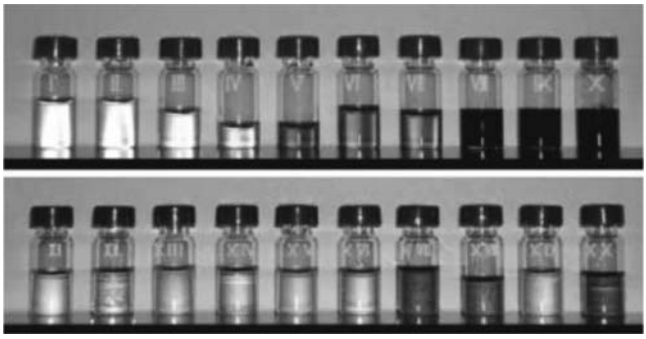

Fig. 16 Phosphonium-amino acid ILs

Fixation of CO_2 Using Task-Specific ILs

Due to the unique "self-designable" character of ILs, alkaline groups, such as $-NH_2$, can be attached to conventional ILs to give a task-specific ILs so as to overcome the limitations of aqueous amine and the conventional ILs. Recently, Zhang et al. [80] reported a new kind of task-specific IL, tetrabutylphosphonium amino acids ($[P(C_4)_4][AA]$). Tetrabutylphosphonium bromide $[P(C_4)_4]Br$ was transformed into tetrabutylphosphonium hydroxide $[P(C_4)_4][OH]$ by anion exchange resin and neutralized by amino acids such as glycine, L-alanine, L-β-alanine, L-serine, and L-lysine to produce $[P(C_4)_4][AA]$ (Fig. 16). To increase the absorption/fixation rate of CO_2 in these highly viscous ILs, the $[P(C_4)_4][AA]$ ILs were coated on porous silica gel to form a thin film. Four cycles of sorption–desorption proved their stable, fast and reversible behavior as compared to bubbling CO_2 through bulk ILs ,which usually takes more than 3 h. The saturated molar ratio between CO_2 and $[P(C_4)_4][AA]$ reached a level of 1:2 at room temperature and atmospheric pressure. Interestingly, in the presence of a small amount of water, the $[P(C_4)_4][AA]$ ILs could adsorb equal molar amounts of CO_2, i.e., the absorption/fixation capability of these ILs was double that in the case without water.

It is worthwhile noting that not all the ILs containing an $-NH_2$ group can absorb/fix CO_2 effectively. Our experimental studies [81] showed that guanidine ILs, e.g., 1,1,3,3-tetramethylguanidium lactate (TMGL), can only absorb/fix 0.25 wt% CO_2. This is much lower than the expected amount according to the absorption molar ratio of 1:2 between the CO_2 and $-NH_2$ group, if it follows the same mechanism as $[pabim][BF_4]$ and $[P(C_4)_4][AA]$. The underlying reason is the large FMO energy gap (9.53 eV) between HOMO-5 of TMGL and LUMO of CO_2, which is much larger than the energy gap (6.07 eV) between HOMO of $[pabim][BF_4]$ and LUMO of CO_2. It is the carbocation that lowers the HOMO-5 energy of TMGL and weakens its nucleophilicity; as a result, TMGL cannot effectively interact with CO_2.

4.1.2 Significant Examples of the Use of ILs in Catalysis

Hydrogen Addition and Rearrangement Reactions

Many attempts have been made to develop biphasic processes for homogeneous hydrogenation catalyzed by transition metal complexes. However some disadvantages in traditional aqueous–organic solvent systems, e.g., modification of the ligands to dissolve in water is generally necessary in order to enhance the catalytic activity, which causes a high cost; and the volatilization of organic solvent causes an environmental pollution. ILs could provide the opportunity to combine the advantages of both homogeneous and heterogeneous processes in a single system [21, 27]. The first successful hydrogenation reactions in ILs were studied by the group of de Souza and Chauvin in 1995 [21]. And the first reported hydrogenation catalysts used in ILs were based on rhodium complexes such as $RuCl_2(PPh_3)_3$, RhCl-$(PPh_3)_3$, and $[Rh(cod)_2][BF_4]$ or $[bmim]_3[Co(CN)_5]$ in $[bmim][BF_4]$ [21, 61]. The low interfacial tension and structural organization of ILs are believed to be effective for preparing small nanoparticles and for controlling extended ordering of nanoscale structures [82]. In addition, evidence has been found relating to the fact that imidazolium-based ILs are good stabilizers for transition-metal nanoparticles [83]. Dupont et al. [84], demonstrated for the first time that $[bmim][PF_6]$ IL is not only a suitable medium for the preparation and stabilization of transition-metal nano-particles, but also ideal for the generation of recyclable biphasic hydrogenation systems. Thus, metal nanoparticles formed in ILs were used directly as catalysts for the hydrogenation of olefins in biphasic liquid systems [84, 85]. Huang and co-workers reported that metal nanoparticles formed in ILs could be used directly as catalysts for the hydrogenation of olefins in biphasic liquid system [85].

Although the advances in developing homogenous hydrogenation catalysts are significant, one of the main problems with homogeneous catalysis is that it is difficult to separate the reaction product from the dissolved catalyst and any solvent. That is why supported IL catalysts (SILCAs), with a catalytic amount of IL immobilized on a solid surface, represent a noteworthy alternative from an industrial point of view. There are many significant works on the supported ILs for this kind of reaction. Huang et al. developed Pd nanoparticles immobilized on molecular sieves by 1,1,3,3-tetramethylguanidinium lactate (TMGL) ILs for solvent-free hydrogenation, and achieved unprecedented activity and stability [86]. And the catalyst can be separated easily from the products.

Zhao et al. [87] reported that rhodium nanoparticles stabilized by the IL-like copolymer poly[(*N*-vinyl-2-pyrrolidone)-*co*-(1-vinyl-3-butylimidazolium chloride)] could be used to catalyze the hydrogenation of benzene and other arenes in ILs. The nanoparticle catalysts can endure forcing conditions at 75°C and 40 bar H_2, resulting in high reaction rates and high conversions for the hydrogenation of arenas. Compared to other nanoparticles that operate in ILs. The hydrogenation of benzene attained record total turnovers of 20,000, and the products were easily separated without being contaminated by the catalysts.

Recently, the use of $Rh(acac)(CO)_2/[bmim][PF_6]$/silica and $Rh(acac)(CO)_2/[bmim][n-C_8H_{17}OSO_3]$/silica catalysts for fixed-bed gas-phase hydroformylation

was first reported by Anders Riisager et al. [88]. They found that the Rh–sulfoxantphos supported ionic liquid-phase catalyst proved to be more regioselective than catalysts without ligand and the analogous ILs-free catalysts, giving up to 96% linear product. The steady performance of the catalysts obtained could be last for 4–5 h, and prolonged use time resulted in a decrease in catalytic activity and selectivity. Hydrogenation of 1-pentene with isomerization to 2-pentene using rhodium catalyst has been investigated by Chauvin et al. [89].

Zulfiqar and Kitazume have reported the formation of 2-methyl-2,3-dihydrobenzo[*b*]furan in 62% yield via the $Sc(OTf)_3$-catalysed Claisen rearrangement/cyclization sequential reaction of allyl phenyl ether in 8-ethyl-1,8-diazabicyclo[4,5,0]-7-undecenium trifluoromethanesulfonate ([EtDBU][OTf]) (Scheme 3) [90]. Similar results were gained using *o*- and *p*-tolyl analogs. Reuse of the catalyst/ILs mixture was achieved with no apparent decrease in activity over three cycles. Among the ILs employed, [EtDBU][OTf] IL showed the most activity, and 91% yield could be obtained using this IL for allyl *o*-tolyl ether. When the reaction was carried out in $[bmim][PF_6]$ and $[bmim][BF_4]$ much lower yields were obtained, indicating that the nature of the cation has a pronounced effect on the reaction rate in this system.

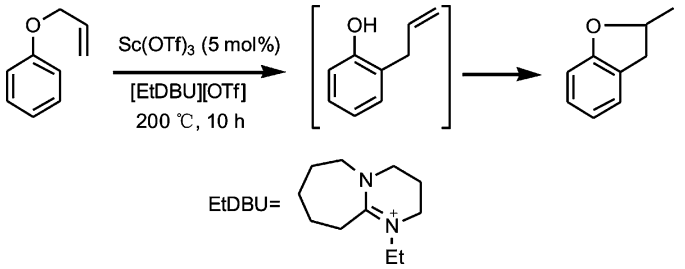

Scheme 3 Claisen rearrangement reactions catalyzed by a mixture of $Sc(OTf)_3$ in [EtDBU][OTf]

Table 4 C–C and C–O cleavage reactions

Reaction	Reaction description	ILs	References
Catalytic cracking of polyethylene	Catalytic cracking of high/low density polyethylene to give light alkanes	[emim]Cl/$AlCl_3$, [*N*-butylpyridine]Cl/$AlCl_3$, [bmim]Cl/$AlCl_3$, LiCl/$AlCl_3$	[91]
Acylative cleavage of a series of cyclic and acyclic ethers	Acylative cleavage of a series of cyclic and acyclic ethers to afford ester	[emim]I–$AlCl_3$	[92]
Dissolution of kerogen and heavy oil	Cleavage of heterocyclic compounds	[bmim]Cl/$AlCl_3$, $[PF_6]$	[93]
Asymmetric ring opening reaction	Ring opening reactions of epoxides catalyzed by Cr(salen)	[bmim]$[PF_6]$/$[SbF_6]$/$[BF_4]$/[OTf]	[94]

C–C and C–O Cleavage Reactions

The details of C–C and C–O cleavage reactions can be seen in Table 4 [91–94].

C–C or C–Heteroatom Coupling Reactions

Friedel–Crafts Reactions

Friedel–Crafts acylation reactions are of great importance in the industrial manufacture of aryl ketones, and are used extensively in the production of pharmaceuticals such as the non-steroidal antiinflammatory drugs Ibuprofen and Naproxen [95]. In general, this type of reaction is catalyzed by $AlCl_3$, H_2SO_4, HF and other acid catalysts, which causes corrosive and difficult recyling of catalysts in industrial processes. ILs based on Lewis acids such as $AlCl_3$ have been applied to the Friedel–Crafts reactions [96]. More recently, there have been a number of reports of reactions utilizing neutral ILs in combination with Lewis acids, in some cases with extremely large effects on reactivity and selectivity. Boon and co-works reported the mixtures of 1-methyl-3-ethylimidazoliumc chloride and Lewis acids (e.g., $AlCl_3$) IL system for the Friedel–Crafts reactions [96]. They found that Friedel–Crafts acylations of aromatic compounds could be promoted by the [emim]C1-AlC1 IL. In 1999, Stark et al., reported Friedel–Crafts acylations of ferrocene in 1-ethyl-3-methylimidazolium halogenoaluminate ionic liquids, [emim]I–$(AlCl_3)_x$ [97]. And the effect of varying the "bulk" Lewis acidity of the ionic liquids used as solvents in these reactions was studied. The use of [emim]I–$(AlCl_3)_x$ ILs as both solvent and catalyst makes some progress for the acetylation of ferrocene since a large excess of the acylating agent (i.e. acetic anhydride or acetyl chloride) is often used in the traditional methods. $Sc(OTf)_3$ in the 1,3-dialkylimidazolium based hydrophobic IL (e.g., [emim][PF_6] and [bmim][SbF_6]), can also efficient catalyze Friedel-Crafts alkylation between aromatic compounds and alkenes with easy catalyst/solvent recycling [98]. Considerable isomerization of the hex-1-ene starting material was observed in these reactions, as indicated by the formation of two different isomeric products in solvent-dependent ratios of between 1.5:1 and 2:1 (Scheme 4). Surprisingly, in water miscible ILs based on the $[BF_4]^-$ and $[OTf]^-$ anions, as well as a range of conventional solvents, no reaction was observed at all. The catalytic activity of $Sc(OTf)_3$ was strongly influenced by the nature of the IL anion. The reaction between cyclohexene and benzene was carried out using the same ILs/$Sc(OTf)_3$ system three times, with no decrease in yield.

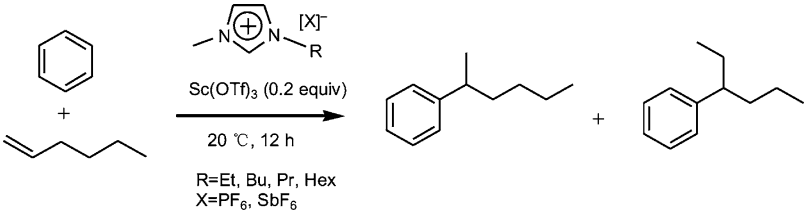

Scheme 4 IL/$Sc(OTf)_3$ catalytic system for the Friedel–Crafts reaction

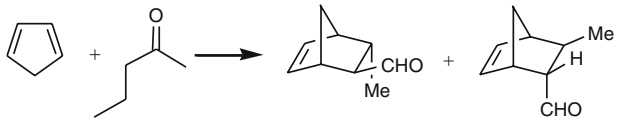

Scheme 5 Diels–Alder reactions using $[BF_4]$-based ILs

Diels–Alder Reactions

Aqueous solutions used as reaction solvents may dramatically affect some Diels–Alder reaction rate constants and stereoselectivities [99]. However, the use of water still has some limitations: Water may be coordinating toward the active metal center or may react with the metal–carbon bond. Additionally, the potential applications are limited by the solubility of the reactants in water. Thus, the technique of aqueous biphasic catalysis has been extended to other solvents. In many cases, when an IL is used, the reaction rate is further enhanced; for example, reaction of cyclopentadiene with methylvinyl ketone is faster in $[BF_4]^-$-based ILs than in water or CH_2Cl_2 at room temperature [100]. Moreover, the ILs can be used as additives for reaction of crotonaldehyde with cyclopentadiene (Scheme 5) [101]. Abbott and co-works demonstrated that the ionic liquids formed from choline chloride and MX_2 (M = Zn or Sn) in 1:2 ratio are effective media for some Diels–Alder reactions [102]. High endo:exo ratios were observed as well as high yields. In this case, the products could be decanted from the ILs and the catalyst system reused. In addition, the ILs are not moisture sensitive which means that no specialist apparatus is required for their synthesis or use and aqueous work-up can be used if necessary.

Few asymmetric Diels–Alder reactions performed in ILs have been reported to date. In 2003, for the first time, Meracz and Oh observed high stereoselectivities for substrate and reagent controlled asymmetric Diels–Alder reactions in imidazolium based ILs [103]. They observed that the use 1% $ZnCl_2/[bbim][BF_4]$ at room temperature resulted in 55–97% yields and high *endo-exo* selectivities for the cycloadducts of the chiral dienophiles. However, $Zn(OAc)_2$ or $ZnCl_2$ in CH_2Cl_2 or Et_2O gave trace amounts or no product even in addition of diene. They also found an ee of 96% for the Diels–Alder reaction of 3-(2-butenoyl)-2-oxazolidinone and cyclopentadiene at room temperature using a chiral catalyst Cu(II)OTf with a yield of 65% in [bbim][BF_4] IL. This was compared with dichloromethane, which showed only 76% ee with a yield of only 4% [103]. Doherty et al. also reported that ILs can increase the ee and yield for the reaction between oxazolidinones and cyclopentadiene using platinum complexes of BINAP as well as conformationally flexible NUPHOS-type diphosphines [104]. Even at $-20°C$, the ee of 88% is still slightly lower than that of 93% obtained in ionic liquid at room temperature, which highlights the beneficial influence of ionic liquids over CH_2Cl_2. Significant enhancements in the enantioselectivity ($\Delta ee \approx 20\%$) as well as reaction rate were achieved in ILs compared with the organic media, even when the IL was in biphasic conditions with diethyl ether in a volume ratio of 1:10 (IL:ether). In addition, the IL allowed the catalyst to be recycled in air without hydrolysis or oxidation of the phosphine ligand.

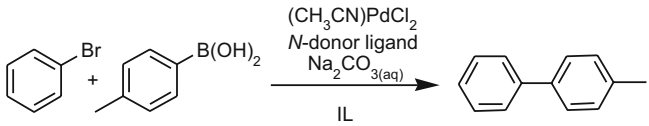

Scheme 6 Palladium(II) imidazole complex-catalyzed Suzuki coupling reactions in ILs

Suzuki Reactions

Although Palladium-catalyzed cross-coupling reactions represent another alternative for formation of C–C bonds, they suffer from a number of disadvantages, such as low catalytic activities, poor catalyst solubility and catalyst decomposition, which limit its application [60–63]. Palladium(II) imidazole complexes have been used as catalyst precursors for the Suzuki coupling reactions in ILs leading to an air-stable catalyst system [105, 106]. For example, Mathews and co-workers also systematically investigated the effect of different ILs on the Palladium(II)/N-donor ligand or Palladium(0, or II)/P-donor ligand catalytic systems [106, 107]. To obtain a good reaction, preactivation of the catalyst was needed in the IL prior to reaction by reacting the catalyst precursor $[(CH_3CN)PdCl_2]$ with a range of *N*-coordinating ligands, including alkylimidazoles, giving an active system for reaction of bromobenzene and tolylboronic acid. Furthermore, the stability of the catalyst in the ILs was strongly dependent on the choice of ligand employed as well as on the IL anion and cation, as a result, the $[(CH_3CN)PdCl_2]$/bmim catalytic system was found to be highly active in $[C_4mim][BF_4]$ IL (Scheme 6) [106, 107].

Recently, Shreeve group reported that Palladium catalyzed Heck and Suzuki cross-coupling reactions were performed successfully in ILs. The *N*-heterocyclic carbene Pd(II) complex {[Pd(Me)(3-mesityl-1-(pyrazolyl-methylene)-imidazolium)] chloride} exhibited high activity for Suzuki and Heck coupling reactions $[bmim][PF_6]$ [108]. Using a butylimidazoletethered $[bbim]^+$ -based IL that could coordinate to $PdCl_2$ dissolved in the system afforded the same results [108–110].

Biphasic IL–water or toluene systems have also been shown to act as a good reaction medium for Suzuki and Heck couplings [111]. In this case, two alkylpiperidinium tetrafluoroborate melts were used in conjunction with $PdCl_2$, giving comparable activity with phosphine-stabilized phosphine palladium catalysts.

Fewer studies have been reported using heterogeneous catalysts for the Suzuki–Miyaura cross-coupling reaction in ILs. Corma et al. have shown that supporting imidazolium modified carbapalladacycle catalyst on Al/MCM-41 is a viable methodology to increase the activity and reusability of the palladium catalyst in Suzuki cross-coupling reactions [112]. The Al/MCM-41 not only makes catalytic system be separated easily, but also enhances the activity of the catalyst. However, the activity of this catalyst–ILs system was poor with yields below 30%.

Heck Reaction

Homogeneous catalysis. The palladium catalyzed Heck reaction involving the coupling of alkenes/alkynes with aryl and vinyl halides is of major importance in

organic chemistry and is widely used industrially. The reactions are commonly carried out at critical conditions (8–72 h, 80–140°C) in polar solvents such as DMF and N-methyl-2-pyrrolidinone (NMP). In addition, low stability of the catalysts caused by the precipitation of palladium black in these conventional organic solvents is urgent to be resolved for industrial applications. Nanoparticles of palladium have been shown by a number of studies in ILs both under conventional thermal and ultrasonic heating [113–116]. The Heck reactions could proceed smoothly in ILs, and the catalyst could be recycled without loss of its activity. For example, using in-situ EXAFS, palladium clusters have been found to be the main species present during the Heck reaction of aryl halides with alkylacrylate compounds in a range of $[PF_6]^-$, $[BF_4]^-$, and $[NTf_2]^-$ ILs using $Pd(OAc)_2$. Similarly, under ultrasonic activation, nanoparticles were observed in [bbim]Br and [bbim][BF_4] [114]. In this case, formation of the *trans*-Heck coupling products was found in yields between 73 and 87%; however, under similar conditions (30°C and ultrasound) no reaction was observed in dimethylformamide and *N*-methyl-2-pyrrolidinone (Scheme 7).

Heterogeneous catalysis. There have been many studies examining the role of dissolved palladium species in ILs for the Heck reaction. To facilitate the separation of catalyst and product, heterogeneous Heck reaction catalysts have also been reported. The solid catalysts, for example, Pd/C, allow the catalyst to be simply recovered by filtration and have been shown to be effective for a number of activated haloarenes in ILs [117–120]. Pd/C has been used to react iodo- and bromoarenes with and without microwave irradiation in [omim][BF_4] and [bmim][PF_6]. The reaction was carried out simply and quickly, and product was easily extracted by diethyl ether from catalyst after reaction. Especially, when the amount of Pd/C decreased from 5 to 1.5 mol %, the reaction still proceeded well, and high yields were obtained in the following four runs. However, little reaction was observed with chloroarenes unless microwave irradiation was used. Similarly, Pd(0) and Pd(II) supported on silica have been reported for iodoarene Heck reactions in [bmim][PF_6] [120]. The silica-supported Pd (II) catalysts were found to be highly active in the ILs compared with DMF. In addition, $Pd(II)/SiO_2$ shows higher activity than Pd/C and $Pd(NH_3)_4Cl_2$

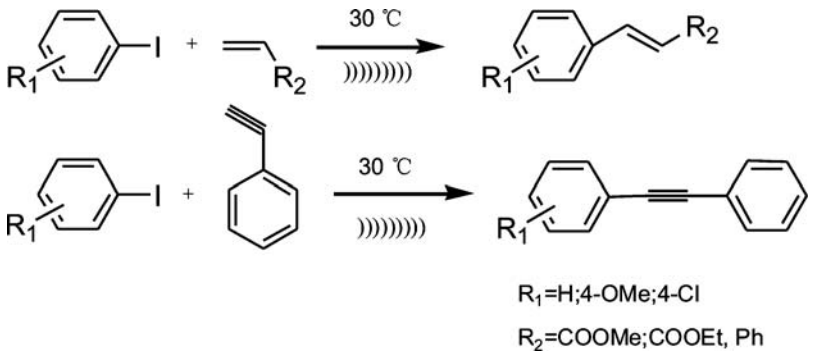

Scheme 7 Palladium nanoparticles in ILs for the Heck reaction

in [bmim][PF_6]. Significant leaching of Pd into the liquid phase was observed and found to be much higher in the ILs than in DMF. More recently, Forsyth et al. have shown clearly that palladium leaching from the Pd/C catalysts is high enough for the catalysis to be considered as homogeneously catalyzed rather than heterogeneously catalyzed [121]. Furthermore, much lower leaching is found in the absence of reagents, which indicates that it is the reaction that causes the dissolution and not the presence of the ILs or amine.

Recently, immobilization of $Pd(OAc)_2$ in silica gel pores with the aid of the [bmim][PF_6] has been found to be active for the Heck reaction in *n*dodecane at 150°C, giving an average of 95% and TON 68 000. The catalytic system could catalyze the Heck reaction of aryl halides with cyclohexyl acrylate in water without a phosphine ligand, with high yields and excellent recyclability for six reactions [122]. The basic support, Mg–Al-layered double hydroxides, has been reported to stabilize palladium nanoparticles in the Heck coupling of chloroarenes and olefins [123]. This system not only showed a higher activity over a range of other supported catalysts, including Pd/C, Pd/SiO_2, Pd/Al_2O_3, and resin-supported $[PdCl_4]^{2-}$, but also was found to be effective for Suzuki-, Sonogashira-, and Stille-type coupling reactions. PEG-supported 3-methylimidazolium chloride has also been shown to be an efficient recyclable medium for the Pd-catalyzed Heck reaction of aryl bromides and aryl chlorides [124]. The combination of PEG-supported 3-methylimidazolium chloride with $Pd(OAc)_2$ provides a ligandless catalytic system for such reactions.

Trosi–Tsuji Coupling Reaction

Biphasic Trost-Tsuji C-C coupling between ethyl cinnamyl carbonate and ethyl acetoacetate catalyzed by $PdCl_2$/[bmim]Cl in the presence of triphenylphosphine trisulfonate was described by de Belefon et al. (Scheme 8) [125]. Use of the IL increased the solubility of the reactants compared with the corresponding aqueous system resulting in increased reaction rates and also prevented conversion of the carbonate into cinnamyl alcohol [125]. Xiao et al. reported the mono-phasic reaction of 3-acetoxy-1,3-diphenylprop-1-ene with dimethyl malonate catalyzed by $Pd(OAc)_2$/[bmim][BF_4] in the presence of a phosphine ligand and base [126]. In this case, good yields were achieved and the catalyst could be recycled with no requirement to form the carbanion nucleophile separately [126].

Cycloaddition of Carbon Dioxide to Epoxide

Carbon dioxide (CO_2) is the most abundant greenhouse gas, and is also a renewable, safe, and cheap C1 resource. One of the most promising technologies in the

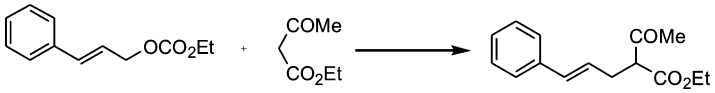

Scheme 8 Trost–Tsuji C–C coupling between ethyl cinnamyl carbonate and ethyl acetoacetate

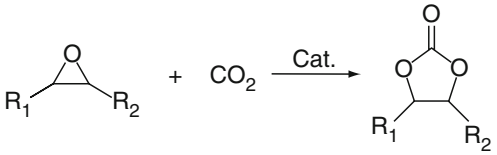

Scheme 9 Cycloaddition of CO_2 to epoxide in the presence of IL catalyst

utilization of CO_2 is the cycloaddition between epoxides and CO_2 to produce five-membered cyclic carbonates, as shown in Scheme 9 [67, 127, 128]. These are excellent aprotic polar solvents and intermediates extensively applied in the production of a variety of indispensable products such as pharmaceuticals, fine chemicals, and so on. In 2001, Peng et al. reported that cycloaddtion of CO_2 to propylene oxide (PO) could be carried out in 1,3-diakylimidazolium and N-alkylpyridinum-based ILs, and [bmim][BF_4] showing the best reactivity [129]. In comparison with aliphatic epoxides, aromatic compounds are less active in this reaction but may be performed in [N_{4444}]Br and [N_{4444}]I [130–133]. At atmospheric pressure, styrene oxide and glycidyl methacrylate oxirane, have been reacted with CO_2 in the $[N_{4444}]^+$ melts with the iodide anion showing higher activity than bromide due to its decreased nucleophilicity. Surprisingly, the activity of ionic liquid can be greatly enhanced by the addition of Lewis acidic compounds of metal halides or metal complexes. By reacting halide-based ILs, for example, [bmim]Cl and [bmim]Br, with Lewis acids such as zinc halides, the activity of the ILs and Lewis acid are improved for this reaction [134]. Recently, our group developed the $ZnCl_2$/phosphonium halide catalytic system [135]. This catalytic system achieved 96% yield, >98% selectivity, and $>4718\,h^{-1}$ TOF under mild reaction conditions without any cosolvents, and it could be reused five times with a little loss of catalytic activity. Formation of $[ZnX_2Y_2]^{2-}$ (X, Y are Cl or Br) was found to catalyze the cycloaddition of CO_2 to propylene oxide. A similar effect of metal halides has also been observed for styrene oxide with the activity determined by the ionization potential and ionic radius of the metal cations used [136]. In addition, chromium salen has been observed to catalyze the reaction of CO_2 with styrene oxide in [bmim][PF_6] [137].

On the other hand, although the combination of ILs with Lewis acid has resulted in many diverse and flexible "platforms" for establishment of a highly effective and easily separable catalytic system, its big problems are obvious, for example: (i) the activities of ILs are distinctly reduced in the absence of Lewis acid; (ii) anhydrous operation is necessary due to the water sensitivity of some Lewis acids; (iii) the higher cost needed compared to single-component catalyst systems. Therefore, developing water-stable, low-cost and efficient single-component catalysts for the synthesis of cyclic carbonate is still highly required. From the view of this point, it is important to avoid usage of binary component catalytic systems for convenient and economical operation of industrial processes. As continuing work, our group is developing the synthesis of cyclic carbonate in aqueous systems and has found that water could remarkably accelerate the synthesis rate of cyclic carbonate. A low-cost

and single Lewis base showed high activity without the presence of Lewis acid, which shows the potential for utilization in industrial applications.

Many of these studies have significant commercial applications, but fundamental studies of the relationship between the properties of ILs and the improved performance compared with conventional solvents are still rare. For example,

(1) the exact reasons why ILs show higher efficiency/specificity in the reactions than other traditional solvents;
(2) reducing the cost of ILs or developing efficient and economic ILs; and
(3) the fundamental research on the large scale applications of ILs in catalysis reactions.

4.2 ILs in Materials

ILs as solvents have received much attention in many areas of chemistry and industry due to their unique properties, such as extremely low vapor pressure, non-flammability, high stability, strong solvent power for organic and inorganic compounds, and wide liquid region [9, 27]. The importance of ILs in the field of material preparation has gradually been realized with published reports on the synthesis of nanostructured materials such as nanowires (Te, Pd, Bi_2S_3, $LaCO_3OH$) [84, 114, 138–142], nanorods (CoPt, cryptomelane, Bi_2S and Sb_2S) [138, 143–145], nanosheets (Au, ZnO, CuO) [145–147], nanoneedles (γ-MnO_2) [148], nanoclusters (Ir(0)) [84, 149, 150], and mesoporous TiO_2 films [151]. In addition, many inorganic structures have been fabricated via various IL-involved processes, for example, semiconductor compounds [152], coordination polymers [153], cluster compounds [154], and mesoporous materials [155]. Recently, preparation of inorganic solid-state materials in ILs has been increasing, and this new method is known as ionothermal synthesis, compared to the hydrothermal (solvothermal) method [156]. The main advantages of the method are that a large number of volatile organic compounds (VOCs) are avoided in the reaction system, and the synthesis is carried out at near atmospheric pressure. The recycling of ILs makes industrial production of porous materials more efficient under environmentally friendly conditions. Moreover, using ILs as reaction medium can potentially lead to novel frameworks. Some new topological structures have been prepared ionothermally, including aluminophosphates [156–162], metal oxalatophosphonates [163–165], and metal organic frameworks (MOFs) [153, 166–169].

4.2.1 Synthesis of Nanosized Particles in ILs

ILs as a kind of new reaction medium has many advantages for inorganic nanomaterials. Recently, novel nanostructures have been produced by selecting suitable ILs reaction systems. The advantages of ILs in inorganic nanostructure synthesis are as follows: (i) the low interface tensions of ILs result in high nucleation rates;

(ii) due to the high thermal stability of ILs, reactions can be conducted at temperatures well beyond 100°C in non-pressurized vessels; (iii) ILs facilitate inorganic synthesis from very polar starting materials under anhydrous or water-poor conditions. For example, semiconductor Bi_2S_3 flowers have been designed using an ILs, 1-butyl-3-methylimidazolium tetrafluoroborate ([bmim][BF_4]), as a reaction medium at low temperature and ambient atmosphere [170]. The scanning electron microscopy (SEM) of Bi_2S_3 flowers with a size of 3–5 μm showed that they were composed of nanowires with a diameter of 60–80 nm.

Catalytic iridium (Ir) nanoparticles were synthesized in ILs including 1-*n*-butyl-3-methyl tetrafluoroborate([bmim][BF_4]), hexafluorophosphate([bmim][PF_6]), and trifluoromethane sulphonate([bmim][CF_3SO_3]) [171]. Lead chromate ($PbCrO_4$) rods and dilead pentaoxochromate (Pb_2CrO_5) with bundle-like and rod-like morphologies have been successfully synthesized by a simple microwave-assisted ILs method [172]. The palladium nanowires with very high catalytic activity and stability for the Sonogashira coupling reaction were synthesized ionothermally by using a thiol-functionalized IL, 1-methyl-3-(2'-mercaptoacetoxyethyl) imidazolium chloride [173]. Large-sized single-crystal gold nanosheets have been successfully prepared by microwave heating of $HAuCl_4$ in ILs, [bmim][BF_4] without any additional template agent [145]. TiO_2 is one of the most studied nanocrystals (NCs) owing to its wide application, such as in pigments, photocatalysts, catalyst supports, solar-cell, gas sensors, and so on. High quality TiO_2 NC was synthesis in ILs via a microwave-assisted process [174].

4.2.2 Ionothermal Synthesis of Molecular Sieves

Morris et al. first reported the preparation of aluminophosphate zeolite analogs by using ILs and eutectic mixtures as both solvent and structure-directing agent (SDA) [156]. In comparison to hydrothermal or solvothermal methods, they termed this new method ionothermal synthesis, which could be carried out at near atmospheric pressure. Ionothermal synthesis removes the competition between template–framework and solvent–framework interactions that are present in hydrothermal preparations. Recently, many new structures using ionothermal synthesis have been reported, such as aluminophosphates, metal oxalatophosphonates, and organic–inorganic hybrid materials. Some structures of aluminophosphates SIZ-1, SIZ-3, SIZ-4, and SIZ-6, have also been ionothermally synthesized by using [emim]Br as both solvent and SDA. The synthesis of Co-AlPOs indicated that the ionothermal synthesis method was suitable for the preparation of transition metal-functionalized frameworks that may be useful for applications such as catalysis or gas adsorption [160]. Also, Wang et al. [175] and Xu et al. [176] studied the effects of amines and microwave heating on ionothermal synthesis of molecular sieves. In our previous research, transition metal (Co, Fe)-containing aluminophosphate molecular sieves with solidate (SOD) structure were synthesized ionothermally by using a series of imidazolium-based ILs as both solvent and structure-directing agents [177]. The recycling of ILs was studied based on the NMR and TGA, which

indicated that the ILs was not degraded at the reaction temperature and could be recycled. Moreover, there was no change in structure of the Co-substituted aluminophosphates prepared from the recycled ILs. The main advantages of this new method were that a large number of VOCs could be avoided and that the operation conditions became milder. Using ILs as both SDA and solvent can potentially lead to the formation of novel types of frameworks. Moreover, the recycling of IL made industrial production of molecular sieves more efficient and environmental.

4.2.3 Ionothermal Synthesis of Oxalatophosphates

There is interested in applying new synthetic methods to the exploratory synthetic and structural studies of new materials with open-framework structures. Recently, Lii et al. [164] reported the first use of an ILs of chlorine chloride/malonic acid in the synthesis of two new iron(III) oxalatophosphates, $Cs_2Fe(C_2O_4)_{0.5}(HPO_4)_2$ and $CsFe(C_2O_4)_{0.5}(H_2PO_4)(HPO_4)$. As they extended synthetic and structural studies to the class of metal oxalatophosphonates, a new iron(II) oxalatophosphonate, $Na_2Fe_3(C_2O_4)_3(CH_3PO_3H)_2$, and the Mn analog, $Na_2Mn_3(C_2O_4)_3(CH_3PO_3H)_2$, were synthesized ionothermally.These have a 3D framework structure built of corner-sharing octahedral trimers, in addition to methylphosphonate groups and two distinct oxalate units [165].

4.2.4 Ionothermal Synthesis of Metal–Organic Frameworks

Porous hybrid inorganic–organic solids have been extensively studied recently due to their interesting structures coupled with their promising applications in gas storage, separation, and catalysis. The first organic–inorganic hybrid material was synthesized ionothermally used [bmim][BF_4] as the solvent to synthesize Cu(bpp)[BF_4] [bpp=3-bis(4-pyridyl)propane] [153]. The first 3D organic–inorganic compound, $Cu_3(tpt)_4(BF_4)_3\cdot(tpt)_{2/3}\cdot 5H_2O$, with large channels ($\sim$5 Å in diameter) was synthesized with the same IL as the solvent and provider of the charge-compensating species, [BF_4] [166]. Recent work by Morris et al. reports chiral induction and anion control in the ionothermal synthesis of coordination polymers [168, 169].

In conclusion, ionothermal synthesis is a novel methodology for the synthesis of zeotype materials and inorganic–organic hybrid materials [178]. Theoretically, ionothermal methods could be used in any system for synthesis of inorganic materials due to the unique properties of ILs. The scope of the synthesis has been demonstrated in the review, including the synthesis of novel nanomaterials, AlPOs, GaPOs, oxalatophosphates, and MOFs. Therefore, it is expected that this new method will become an effective way for new and exciting structures to be sythesized, and will be realized in large-scale production in the future.

4.3 ILs in Electrochemistry

ILs are widely used in electrochemistry owing to their superior features compared to traditional solvents, such as excellent chemical and thermal stability, low melting points with negligible vapor pressure, high electrical conductivity and solvent transport properties, a wide range of operational liquid temperature, the ability to dissolve various organic, inorganic, and organometallic compounds, and a large electrochemical window of about 4.0 V.

4.3.1 Basic Electrochemical Properties

The conductivities of IL are mostly on the order of $0.1\,\mathrm{S\,m^{-1}}$ at ambient temperature. Some physical properties, such as viscosity, density, molecular weight, and ion size, can affect their conductivities. The conductivity usually increases with enhancing of temperature, and the existence of halogen (such as Cl^-, Br^-) can make the conductivity lower. Conductivity is often measured with a conductivity meter or alternating current impedance (AC impedance).

The electrochemical window of ILs is the difference between the oxidation potential and the deoxidization potential. It is usually measured by using cyclic voltammetry or linear sweep voltammetry in a three-electrode system. The existence of halogen and/or water can make the electrochemical window smaller. The material of the electrode also has great influence on the electrochemical windows of ILs. There is no detailed research on electrochemical reactions at the cathode and anode limits of each ILs. However, it is believed that at these limits, the cathodic reaction is reduction of imidazolium cations [55, 179, 180] and the anodic reaction is oxidation of anions [181, 182]. Further studies are necessary to characterize reactions at both the cathodic and anodic limits of these ILs.

4.3.2 Various Applications

Most of the research on ILs has focused on their applications as electrochemical solvents. The fundamental electrochemical properties and some applications of ILs have been reviewed in detail elsewhere [183–186]. As a short summary, ILs have been used as electrolytes in various applications, such as electrodeposition [187, 188], electropolishing [189–191], electrosynthesis [192–197], batteries [198–204], solar cells [205–213], fuel cells [213–218], capacitors [203,219–224], sensors [225–229], electrostatic control [230], and actuators [231–233].

In addition, there are other novel applications of ILs in electrochemistry. For example, ILs/polymer electrolyte composites [232–235] and polymer-in-ILs electrolytes [215, 216, 236] were synthesized, and their electrochemical properties were investigated. These novel electrolytes have potential applications in emerging electrochemical devices such as sensors, actuators, and lithium cells. Quite recently, the use of ILs as electrolytes in conjunction with carbon nanotube electrodes was inves-

tigated [237, 238]. Imidazolium-based ILs were even utilized as gelling media for fabrication of single-walled nanotubes, resulting in so-called carbon nanotube-based soft materials [239]. These new materials have reinforced mechanical strength and improved electrical conductivity, which allow them to have potential applications as components of electronic devices.

Electrodeposition and Electropolishing

Metals that can be obtained from aqueous media in most cases can also be deposited from ILs, often with superior quality because hydrogen evolution does not occur. Depending on the system, they can reach electrochemical windows of more than 4 V and thus they give access to a number of elements that cannot be electrodeposited from aqueous solutions, such as light and refractory metals, alloys, as well as elemental and compound semiconductors. Presumably, ILs will become important for electrochemical nanotechnology. ILs can be used in a wide temperature range, so temperatures can be elevated to accelerate such phenomena as nucleation, surface diffusion, and crystallization associated with the electrodeposition process. In addition, the process can be safely constructed because ILs are neither flammable nor volatile if kept below the thermal decomposition temperature of the organic cations.

The electropolishing of stainless steel was achieved in an ILs synthesized from ethylene glycol and choline chloride. The process is essentially the same as the sulfuric and phosphoric acid process currently operating but the process offers a number of advantages, including metal dissolving without prior passivation, no gassing at the anode surface, no substrate dealloying, and no changes in the polish quality as the ILs age. The future for IL-based technology in metal finishing is extremely bright, but more fundamental aspects of metal growth will have to be studied so that the subject becomes a practical reality instead of an academic curiosity.

Electrosynthesis

ILs have become increasingly popular solvents for a number of synthetic reactions, including Diels–Alder reactions and many catalytic organometallic reactions. Electrochemical synthesis and polymerization have been attempted in a variety of chloroaluminate ILs over the years. Use of these ILs requires a glove box or an otherwise inert atmosphere and results in high waste-removal costs. The ability of non-haloaluminate ILs to dissolve a wide range of compounds while remaining immiscible with water and stable to air enables their use as solvents in electrosynthetic investigations and facilitates product separation. Given their entirely ionic composition, the intrinsic conductivity of ILs eliminates the need for added supporting electrolyte, which can further simplify the experimental set-up. Furthermore, these ILs allow for recycling of the solvent—an asset that is incredibly valuable to the economically aware, "green" industrial community.

In terms of use as solvents for electrosynthesis, the recyclability and facile product separation possible with ILs certainly appeal. The handful of studies so far

performed have demonstrated promising results producing good to excellent product yields, comparable to those of conventional solvents.

Electrochemical Devices

At present, most electrochemical devices comprise an aqueous, gel, or polymer electrolyte whose conductivity and stability can determine the performance and lifetime of the device. The inherent properties of ILs, such as high conductivity, wide potential window, and air/moisture stability, make them promising alternatives as unreactive, stable electrolytes in the development of such devices. Their application as electroactive components in several devices has recently been explored, e.g., in batteries, solar cells, fuel cells, and capacitators. Some of the recent advances made in the application of ILs to electrochemical devices will be highlighted here.

Lithium batteries are used widely in portable electronic devices and electric vehicles. They show the highest energy density among the applicable chemical and electrochemical energy storage systems. It is necessary that solvents for the electrolytes in Li-batteries should be aprotic because of the requirements of wide electrochemical windows up to the cathodic limit of Li/Li^+ potential. As known, the aprotic organic solvents are usually volatile and flammable. Therefore, the use of ILs as electrolytes in Li-batteries is very promising. One report [198] showed that a lithium ion cell with an ILs electrolyte performed at a level of practical utility in terms of cell performance and cycle durability. Both the ILs [201] and proton-conducting gelatinous electrolytes templated by ILs [204] have been studied as possible solvents in lithium batteries.

The use of ILs in electrochemical capacitors also seems to be promising since they offer greater electrochemical stability compared to aqueous systems, thereby providing greater energy storage.

Electrochemical Sensors and Other Applications

Regarding their analytical utility, under controlled conditions ILs have proved to be viable solvents for the electrochemical detection of a number of molecules, particularly gaseous species. Electrochemical sensors with ILs as electrolyte solid-state amperometric O_2 gas sensors were successfully fabricated by using supported [bmim][PF_6] [217] or [emim][BF_4] [223] porous polyethylene membrane as a solid-state electrolyte. The presented O_2 gas sensor, which is capable of being operated at room temperature, shows a wide detection range and high stability, high sensitivity, and an excellent reproducibility.

An attempt has been made to use ILs as an ethanol sensor [221]. The detection limit was 0.13% (vol/vol) and its response time was 336 s, with a linear relationship between the response current and the concentration of ethanol over a relatively wide range.

The slow equilibration times and sensitivity of the current response to moisture contamination are clear drawbacks for some ILs. However, the latter is especially so

in the case of any sensor intended for operation under atmospheric conditions. The result of this, of course, is that an IL may make an ideal component for an alternative type of humidity sensor.

Conducting polymers have attracted considerable attention as new materials for the development of numerous electrochemical devices such as batteries, supercapacitors, sensors, electrochromic devices, electrochemical actuators, and light-emitting diodes. These polymers can either be prepared by chemical or electrochemical polymerization. Electrochemical synthesis offers some advantages, such as the generation of polymers in the doped state and easy control of the film thickness. Furthermore, electropolymerization is an easy and rapid method. Recently, attention has been directed at the potential benefits of using ILs as solvents for the electrochemical synthesis of conducting polymers. The polymer films grown in the ILs show higher conductivity and better mechanical behavior than those prepared in conventional solvents.

The wide electrochemical windows and high intrinsic conductivities displayed by ILs commend their use for electrochemistry and to date they have been successfully applied to study a number of fields, such as electrodeposition, electropolishing, electrosynthesis, electrochemical devices, and sensors. With even more stable ILs under constant development and existing ILs becoming progressively more available and inexpensive, an increasing amount of research involving these compounds is anticipated over the next few years. The potential of ILs in some electrochemistry field, such as electrodeposition, electropolishing, and electrochemical devices may become fully realized. In addition, it is expected that novel ILs with lower viscosity, higher conductivity, and wider electrochemical window will be developed to be suitable for research and practical use in the near future.

5 Evaluations and Toxicity of ILs

For today's chemists, designing benign industrial chemicals, products, and processes is both a vision and a mission. Room-temperature ILs are regarded as environmentally benign alternatives to volatile organic solvents. They are also considered a sustainable "green product". But, the potential toxicity of ILs has been neglected, and few toxicological data of ILs have been available until now [240]. However, the product designs for this promising group of compounds should be taken into account, not only the technological needs, but also the ecotoxicological hazards [241, 242]. Toxicity in ILs was first reported in 2003 [243]. The early work involved ILs composed of imidazolium [244, 245], pyridinium, and phosphonium [246]. These still play a major role, but the attention is slowly shifting toward new structural types, such as choline saccharinate and choline acesulfamate ILs [247, 248]. Up to now, a few conventional and some functional ILs have been studied for toxicity. For industrial process design, other influencing factors involving ILs biodegradability, bioaccumulation, life cycle, and release in the environment etc., should also be considered. But these studies are only just beginning,

so here a brief overview only on the toxicity of ILs will be presented with the aim of improving the knowledge base for the process design of ILs leading to a reduced (eco)toxicological hazard potential.

5.1 Influence of IL Structure on Toxicity

The general trend observed is that ILs are more toxic than many traditional solvents to aquatic organisms and that an increase in alkyl chain length of the substituted groups corresponds to an increase in both hydrophobicity and toxicity. However, a general lack of systematic information on the different molecular formations makes it difficult to predict actual specific structure–activity relationships [249–252].

The three structural elements of an IL that mainly impact on toxicity are the cation headgroup, the length of the cation side chain R_1, R_2 etc., and the kind of anion. There are also mixture effects. So far, Jastorff et al. have investigated a large number of ILs in screening assays (cytotoxicity assay with the IPC-81 cell line) to check the influence of the structural elements side chain [244, 246, 253], head group [253, 254], and anionic moiety [255] on cytotoxicity. Briefly summarizing their results, it is found that the side chain length is a dominating originator of toxicity. In general, the side chain effect was found consistently in all test systems used, from molecular up to organism level, and was independent of the investigated environmental compartment. In contrast, the analysis of structural heterogeneous moieties like commonly used anions leads to a diverse pattern for the observed toxicities in the different test systems, independent of trophic level or environmental compartment. Furthermore, anion effects were found but they were not as distinct as the demonstrated side chain length effects. The head group itself caused minor changes in toxicities, apart from quinolinium and dimethylaminopyridinium compounds [242].

5.1.1 Influence of IL Side Chain on Toxicity

Influence of IL Side Chain Length on Toxicity

In 2004, Ranke et al. published systematic investigations of the influence of an increasing chain length of R_1 or R_2 of the imidazolium cation moiety on the cytotoxicity in marine bacteria and two types of mammalian cell cultures [244]. They also checked this "side chain length effect" with a multitude of different combinations of cations and anions. It always became evident that the shorter the chain length(s) of side chain(s), the lower the cytotoxicity [246, 256].

The same conclusion can be drawn from Yun's examinations [241]. The susceptibility of algae to ILs was strongly dependent on the alkyl-chain length. According to their results, a longer alkyl-chain resulted in stronger inhibition of algal growth. In general, the toxicity could be summarized as decreasing in

the following order: [omim]Br>[hmim]Br>[bmim]Br>[pmim]Br. Among the ILs examined, [omim][Br] was found to be most toxic to *S capricornutum*, with EC_{50} values ranging from 26.3 to 54.9 μM after an incubating time of 96 h. Although [bmim]Br and [pmim]Br were relatively less toxic than [omim] and [hmim], their toxicity increased with increasing the incubation time from 48 to 96 h. This fact indicates that these kinds of ILs may become more toxic after being released and coming into contact with freshwater ecosystems.

According to Ranke, all test systems showed higher toxicity with increasing *n*-alkyl chain length because ILs with longer alkyl chains possess more lipophilic properties. These results are in accordance with toxicity studies using other chemicals. In addition, the structure of the investigated IL compounds show similarity to cationic surfactants, especially imidazolinium compounds. Cationic surfactants are known to increase membrane permeability and therefore cause narcotic effects with increasing chain length. The regression analysis data presented here suggests that toxicity tends to increase more when the chain length in R_1 position is extended, compared with elongation in the R_2 position, especially in the IPC-81 assay. This effect might be explained with weaker water bonding of the imidazolium compounds to the end of the longer R_2 residues. This would mean less energy is required for the insertion of an additional CH_2 group at the tip of the longer R_2 residue, and the hydrophobicity increase as well as the toxicity increase per CH_2 increment is smaller [244].

Influence of IL Side Chain Type on Toxicity

In 2007, Samort et al. studied a new class of ILs, ox ygenated chain-substituted ILs, 1-methoxyethyl-3-methylimidazolium salts (moemims), and compared the acute toxicity of [bmim][BF_4] and moemims in the crustacean *Daphnia magna* and the bacterium *Vibrio fischeri*. Two points emerge from the *D. magna* bioassay performed in the present study: First, the EC_{50}s for [moemim][BF_4] and [moemim][dca] are higher by two orders of magnitude than the EC_{50} for [bmim][BF_4]; second, the EC_{50}s for [moemim][BF_4] and [moemim][dca] are very similar. Results indicate that introduction of an oxygenated side chain in the imidazolium cation can greatly reduce the toxicity of ILs and that these ILs are less toxic than commonly used chlorinated solvents, such as tricloromethane, but are more toxic than non-chlorinated solvent, such as methanol and acetone [250].

It has not yet been possible to explain the dramatic difference in toxicity between bmim and moemim cations. It suggested that the higher hydrophobicity of the former may be the basis of the observed trend. Currently available information regarding the toxicity of alkyl imidazolium tetrafluoroborates to aquatic organisms shows that [bmim][BF_4] is less toxic than long alkyl chain imidazolium salts, indicating that toxicity increases with hydrophobicity. It is acutely toxic, however, to *D. magna* and *V. fischeri*, for example, at concentrations similar to those of common chlorinated organic solvents such as trichloromethane and tetrachloromethane.

It also is more toxic than other non-chlorinated organic solvents such as methanol, acetone, and acetonitrile [250].

5.1.2 Influence of IL Anion on Toxicity

Ranke et al. also studied the effect of the anions on the toxicity of ILs. Although it has been asserted that modifications of the anion lead to changes in the chemical and physical properties of ILs, the toxicity test systems showed no general systematic effect of the anion, and toxicity seems to be determined mainly by the cationic component. This could be explained by intercalation of the lipophilic part of the molecules into the membrane, whereas the ionic headgroup is at least partially solvatized in the aqueous solution [244].

In the majority of cases, the anion effect was not as drastic as the side chain effect (C_4 vs. C_8), but there are a few exceptions. For [bmim][NTf_2] within the reproduction inhibition assay with *Folsomia candida*, the anion effect was even significantly stronger than the side chain effect and the toxicity was comparable to the toxic reference substance. However, in most of the test systems, no clear increase in toxicity caused by the anion could be observed for the majority of the examined ILs [242]. However, for [hmim][PF_6] and [hemim] [PF_6], toxicity is similar to that of the anion, and compounds with $[PF_6]^-$ are slightly more toxic than compounds with other anions. This could be due to the higher toxicity of $[PF_6]^-$ compared to other anions [244]. For longer alkyl chain derivatives, toxicity of the anion can be neglected in comparison to the effects caused by the corresponding cation. The uptake of the cation does not seem to be influenced by the type of anion in the tested substance. For a larger set of anions, lipophilicity and chemical reactivity might be responsible for the observed cytotoxic effects.

5.1.3 Influence of the IL Cation Headgroup on Toxicity

Ranke has investigated the influence of seven headgroups on cytotoxicity by comparing the results obtained with ILs containing the same fixed side chain and halides as counterions [253]. Most of the ILs tested in their study had a relatively low cytotoxicity (high EC_{50} values). There were no clear differences in the EC_{50} values, indicating a generally low influence of the headgroup itself on cytotoxicity. Only for the butyl-substituted headgroups and for one further compound was a more general pattern in the EC_{50} values observed. By comparing the different headgroups with the butyl side chain, a clear headgroup effect on cytotoxicity was found for the 4-(dimethylamino)pyridinium cations. For this headgroup, no functionalized side chains were available. Thus, the test kit was supplemented by the ethyl and the hexyl side chains for a comparison with the corresponding imidazolium moieties. For all three side chains, the 4-(dimethylamino)pyridinium cation showed a remarkably lower EC_{50} value (by one to two orders of magnitude) than the corresponding imidazolium headgroup.

5.1.4 Mixture Effects

In general, one has to keep in mind that there is the possibility of mixture effects occurring within one ionic liquid. Study with the IPC-81 cells provided a first hint of combination effects [242]. It was found that the ILs containing [NTf_2] exhibited cytotoxicities higher than the intrinsic toxicities for the anionic and cationic species tested separately. The same results were achieved in the tests with *V. fischeri* for [bmim][NTf_2]. When tested separately, the toxicities for [bmim]Cl and Li[NTf_2] ranged over a moderate area, but when testing a mixture of [bmim]Cl and Li[NTf_2] (probably forming a new ionic liquid in the meantime, because upon mixing the two compounds a tarnished solution was observable and after 12 h stirring the solution became clear) the dose response curve is congruent with the curve achieved for the ionic liquid [bmim][NTf_2]. To exclude mixture effects caused by lithium or chloride, a mixture of [bmim][NTf_2] and LiCl was additionally tested. The dose–response curve obtained was congruent with that of [bmim][NTf_2], so lithium or chloride do not cause any toxic effects, as expected from testing NaCl and LiCl.

The same experiments were conducted for [omim][NTf_2]. In this case the influence of the cationic moiety was dominating. Here at least, no visible mixture effects could be demonstrated because all three dose response curves for [omim]Cl, [omim][NTf_2], and the mixture of [omim]Cl and Li[NTf_2] showed the same trend. The strong influence of the IM18 moiety masked possible mixture effects.

For [pmim][PF_6] up to [qmim][PF_6], toxicity is even lower than that of the anion itself. It is assumed that in this case the anion and cation of the IL are associated, i.e., they form an ion pair, reducing PF6 uptake and hence toxicity.

5.2 Metabolites of ILs

In 2003, Jastorff and coworkers studied the presumed metabolites of the [bmim] and [omim] IL cations [246]. Their biological data clearly indicated that the presumable transformation products (“metabolites”) of both IL entities are less toxic than their parent chemicals. Furthermore, a side chain length effect is found for both the alkyl imidazoles (methyl- and butyl- $>3000\,\mu M$, octyl- = $200\,\mu M$) and for some of the functionalized cations, e.g., those compounds carrying a terminal hydroxyl function at the butyl ($EC_{50} > 3000\,\mu M$) or octyl moiety ($EC_{50} = 250\,\mu M$). Metabolic transformation to the carboxyl function yielded no side chain length effect up to $3000\,\mu M$. The conclusion is that the introduction of polar functional groups into an alkyl chain yields a reduction in cytotoxicity.

5.3 Eco-Design of ILs

It is important to design eco-benign ILs. As an alternative concept, Ranke et al. proposed an application specific eco-design [246]. The first step is to describe

the necessary technicophore properties meeting the application and to propose the chemical structure according to the Toolbox and T-SAR of ILs; then the functional IL is synthesized. The IL is evaluated by screening tests. If it found to have a low EC_{50} value, the structure–activity relationships are again applied to propose and synthesize a new chemical structure with similar technicophore properties and lower toxicity. However, the risk potential is not only determined by the toxic character of the IL but by the three issues of (i) environmental relevance, (ii) the waste streams of production and regeneration, and (iii) the leakage during production, usage, and recycling. The second step is to take this application-specific risk potential into account in the risk assessment. Finally, if the IL passes an application test, it will be tested to see whether the compound can be recovered after usage, e.g., by regeneration, liquid–liquid extraction, or nanofiltration. Then the compound will be considered as a "green" product.

6 Conclusions and Prospects

Ionic liquids had made rapid development in many fields as green media, catalyst and material. Their major driving force of development is a strong desire to establish simple, efficient and green processes, because ILs offer new possibilities for reactions, technologies and products due to their unconventional properties. However, single reaction of IL is difficult to meet the needs of industrial applications. Corresponding changes in each aspect, such as reaction, equipment and technology, are indispensable to design new IL processes. While intrinsically understanding of ILs can be made only by solving the crucial problems in IL applications, so the comprehensive researches of ILs becomes significantly important for future development of IL.

There are hundreds of thousands of simple combination of ions to make ILs and a near-endless number of potential IL mixtures. How to design and filter the environmentally benign ILs and develop their synthetic technology is the first key step in the process design of ILs. Quantum calculation and molecular simulation are useful tools for predicting the physical properties of ILs; however, some properties, such as eco-effect and biodegradation, are little studied, which makes it difficult to design low toxicity ILs and the appropriate synthetic technology. At the same time, a challenging task is the atom-economic synthesis of functionally and environmentally benign ILs.

ILs are not same as conventional organic solvents. How to chose and design new types of reactor suitable for the properties of ILs and their attendant technology is the second key step in the process design of ILs. ILs can elevate efficiency, selectivity, and the distribution coefficient of equilibrium, but sometimes a higher viscosity can lead to longer times for reaction and separation. In fact, the result is sometimes lower efficiency and more difficulty in transporting mass. Therefore, it is necessary to research and develop new types of reactor and to intensify technologies that are suited to the specific properties of ILs.

Because of the low volatility of ILs, in theory it is easy for them to be separated from the product and reused. In some reactions, the outgrowths or polymers that are generally produced in the reaction process are very difficult to separate from products. Development of some non-conventional systems (e.g., physical–chemical supported IL systems, ILs/supercritical systems) should be reinforced, together with optimization and integration of recycling systems for ILs.

For process design, the risk assessment of ILs, especial for selected technical applications, should be enhanced. More (eco)toxicological data and data on the exposure pathways, (bio)transformation, and sorption processes as well as bioaccumulation studies are necessary. Also, research on suitable regeneration and recycling methods should take account the whole lifecycle of ILs. Up to now, little information on these aspects is available.

In conclusion, ILs are brand new compounds and although a lot of progress has been made, many great problems remain to be solved. We confidently expect that green and biocompatible ILs will contribute to a greener chemical industry. We believe ILs can provide new opportunity for a truly sustainable development.

Acknowledgements This work was supported financially by National Natural Science Foundation of China (no. 20776140), National Science Fund for Distinguished Young Scholars of China (no. 20625618) and National 863 Program of China (no. 2006AA06Z317 and no. 2006AA06Z371).

References

1. Han X, Armstrong DW (2007) Acc Chem Res 40:1079
2. Alkire RC, Braatz RD (2004) AIChE J 50:2000
3. El Seoud OA, Koschella A, Fidale LC, Dorn S, Heinze T (2007) Biomacromolecules 8:2629
4. Ranke J, Stolte S, Stormann R, Arning J, Jastorff B (2007) Chem Rev 107:2183
5. van Rantwijk F, Sheldon RA (2007) Chem Rev 107:2757
6. Fellay C (2007) Chimia 61:172
7. Weyershausen B, Hell K, Hesse U (2005) Green Chem 7:283
8. Chemical industry vision 2020 technology partnership. Ionic liquids. http://www.chemicalvision2020.org/ionic_liquids.html
9. Rogers RD, Seddon KR (2003) Science 302:792
10. Broch SC, Berthod A, Armstrong DW (2003) Anal Bioanal Chem 375:191
11. Zhang Q-G, Yang J-Z, Lu X-M, Gui LS, Huang M (2004) Fluid Phase Equilibria 226:207
12. Hanz KR, Riechel TL (1997) Inorg Chem 36:4024
13. Holbrey JD, Seddon KR (1999) J Chem Soc Dalton Trans 13:2133
14. Souza RFd, Rech V, Dupont J (2002) Adv Synth Catal 344:153
15. Tao G-H, He L, Sun N, Kou Y (2005) Chem Commun 28:3562
16. Holbrey JD, Reichert WM, Swatloski RP, Broker GA, Pitner WR, Seddon KR, Rogers RD (2002) Green Chem 4:407
17. Holbrey JD, Turner MB, Reichert WM, Rogers RD (2003) Green Chem 5:731
18. Tao G-H, He L, Liu W-S, Xu L, Xiong W, Wang T, Kou Y (2006) Green Chem 8:639
19. Allen CR, Richard PL, Ward AJ, van de Water LGA, Masters AF, Maschmeyer T (2006) Tetrahedron Lett 47:7367
20. Del Pópolo MG, Voth GA (2004) J Phys Chem B 108:1744
21. Wasserscheid P, Keim W (2000) Angew Chem 39:3772

22. Wang P, Zakeeruddin SM, Grätzel M, Kantlehner W, Mezger J, Stoyanov EV, Scherr O (2004) Appl Phys A: Mater Sci Process 79:73
23. Welton T (1999) Chem Rev 99:2071
24. Morrow TI, Maginn EJ (2002) J Phys Chem B 106:12807
25. Brennecke JF, Maginn EJ (2001) AIChE J 47:2384
26. Sheldon R (2001) Chem Commun 23:2399
27. Dupont J, de Souza RF, Suarez PAZ (2002) Chem Rev 102:3667
28. Smit B, Krishna R (2003) Chem Eng Sci 58:557
29. Rogers RD, Seddon KR (2003) Ionic liquids as green solvents: progress and prospects. American Chemical Society, Washington, DC
30. de Andrade J, Boes ES, Stassen H (2002) J Phys Chem B 106:13344
31. Liu Z, Huang S, Wang W (2004) J Phys Chem B 108:12978
32. Lopes JNC, Padua AAH (2004) J Phys Chem B 108:16893
33. Yu G, Zhang S, Yao X, Zhang J, Dong K, Dai W, Mori R (2006) Ind Eng Chem Res 45:2875
34. Yu G, Zhang S, Zhou G, Liu X, Chen X (2007) AIChE J 53:3210
35. Yu G, Zhang S (2007) Fluid Phase Equilib 255:86
36. Dong K, Zhang S, Wang D, Yao X (2006) J Phys Chem A 110:9775
37. Zhang S, Yuan X, Chen Y, Zhang X (2005) J Chem Eng Data 50:1582
38. Liu X, Zhang S, Zhou G, Wu G, Yuan X, Yao X (2006) J Phys Chem B 110:12062
39. Liu X, Zhou G, Zhang S, Wu G, Yu G (2007) J Phys Chem B 111:5658
40. Zhou G, Liu X, Zhang S, Yu G, He H (2007) J Phys Chem B 111:7078
41. Huddleston JG, Visser AE, Reichert WM, Willauer HD, Broker GA, Rogers RD (2001) Green Chem 3:156
42. Wilkes JS, Zaworotko MJ (1992) J Chem Soc Chem Commun 13:965
43. Gordon CM, Holbrey JD, Kennedy AR, Seddon KR (1998) J Mater Chem 8:2627
44. Ngo HL, LeCompte K, Hargens L, McEwen AB (2000) Thermochim Acta 357–358:97
45. Matsumoto H, Kageyama H, Miyazaki Y (2002) Chem Commun 16:1726
46. Zhou Z-B, Matsumoto H, Tatsumi K (2004) Chem Lett 33:680
47. Larsen AS, Holbrey JD, Tham FS, Reed CA (2000) J Am Chem Soc 122:7264
48. Branco LC, Rosa JN, Ramos JJM, Alfonso CAM (2002) Chem Eur J 8:3671
49. Omotowa BA, Shreeve JM (2004) Organometallics 23:783
50. Suarez PAZ, Einloft S, Dullius JEL, Souza Red, Dupont L (1998) J Chim Phys 95:1626
51. Crosthwaite JM, Muldoon MJ, Dixon JK, Anderson LL, Brennecke JE (2005) J Chem Thermodyn 37:559
52. Nishida T, Tashiro Y, Yamamoto M (2003) J Fluorine Chem 120:135
53. Law G, Watson PR (2001) Langmuir 17:6138
54. Dzyuba SV, Bartsch RA (2002) Chem Phys Chem 3:161
55. Perry RL, Jones KM, Scott WD, Liao Q, Hussey CL (1995) J Chem Eng Data 40:615
56. Bonhote P, Dias AP, Papageorgiou N, Kalyanasundaram K, Gratzel M (1996) Inorg Chem 35:1168
57. Gu Z, Brennecke JF (2002) J Chem Eng Data 47:339
58. Widegren JA, Laesecke A, Magee JW (2005) Chem Commun 12:1610
59. Seddon KR, Stark A, Torres M-J (2000) Pure Appl Chem 72:2275
60. Holbrey JD, Seddon KR (1999) Clean Prod Process 1:223
61. Parvulescu VI, Hardacre C (2007) Chem Rev 107:2615
62. Zhao D, Wu M, Kou Y, Min E (2002) Catal Today 74:157
63. Gibson DH (1996) Chem Rev 96:2063
64. Leitner W (1996) Coord Chem Rev 153:257
65. Darensbourg DJ, Holtcamp MW (1996) Coord Chem Rev 153:155
66. Yin X, Moss JR (1999) Coord Chem Rev 181:27
67. Shi M, Shen YM (2003) Curr Org Chem 7:737
68. White CM, Strazisar BR, Granite EJ, Hoffman JS, Pennline HW (2003) J Air Waste Manage Assoc 53:645
69. Pez GP, Carlin RT, Laciak DV, Sorensen JC (1988) US Patent 4761,164
70. Blanchard LA, Hancu D, Beckman EJ, Brennecke JF (1999) Nature 399:28

71. Anthony JL, Maginn EJ, Brennecke JF (2002) J Phys Chem B 106:7315
72. Blanchard LA, Gu Z, Brennecke JF (2001) J Phys Chem B 105:2437
73. Aki SNVK, Mellein BR, Saurer EM, Brenneke JF (2004) J Phys Chem B 108:20355
74. Cadena C, Anthony JL, Shah JK, Morrow TI, Brennecke JF, Maginn EJ (2004) J Am Chem Soc 126:5300
75. Shariati A, Peters CJ (2005) J Supercrit Fluids 34:171
76. Camper D, Scovazzo P, Koval C, Noble R (2004) Ind Eng Chem Res 43:3049
77. Kazarian SG, Briscoe BJ, Welton T (2000) Chem Commun 20:2047
78. Anthony JL, Anderson JL, Maginn EJ, Brennecke JF (2005) J Phys Chem B 109:6366
79. Zhang S, Chen Y, Ren RXF, Zhang Y, Zhang J, Zhang X (2005) J Chem Eng Data 50:230
80. Zhang J, Zhang S, Dong K, Zhang Y, Shen Y, Lu X (2006) Chem Eur J 12:4021
81. Yuan X, Zhang S, Chen Y, Lu X, Dai W, Mori R (2006) J Chem Eng Data 51:645
82. Dupont J, Suarez PAZ (2006) Phys Chem Chem Phys 8:244
83. Migowski P, Dupont J (2007) Chem Eur J 13:32
84. Dupont J, Fonseca GS, Umpierre AP, Fichtner PFP, Teixeira SR (2002) J Am Chem Soc 124:4228
85. Huang J, Jiang T, Han B, Gao H, Chang Y, Zhao G, Wu W (2003) Chem Commun 14:1654
86. Huang J, Jiang T, Gao H, Han B, Liu Z, Wu W, Chang Y, Zhao G (2004) Angew Chem Int Edn 43:1397
87. Zhao C, Wang H-Z, Yan N, Xiao CX, Mu XD, Dyson PJ, Kou Y (2007) J Catal 250:33
88. Riisager A, Wasserscheid P, Hal RV, Fehrmann R (2003) J Catal 219:452
89. Chauvin Y, Mussmann L, Olivier H (1996) Angew Chem Int Edn 34:2698
90. Zulfiqar F, Kitazume T (2000) Green Chem 2:296
91. Adams CJ, Earle MJ, Seddon KR (2000) Green Chem 2:21
92. Green L, Hemeon I, Singer RD (2000) Tetrahedron Lett 41:1343
93. Freemantle M (2000) Chem Eng News 15:20
94. Song CE, Oh CR, Roh EJ, Choo DJ (2000) Chem Commun 18:1743
95. Hardacre C, Katdare SP, Milroy D, Nancarrow P, Rooney DW, Thompson JM (2004) J Catal 227:44
96. Boon JA, Levisky JA, Pflug JL, Wilkes JS (1986) J Org Chem 51:480
97. Stark A, MacLean BL, Singer RD (1999) J Chem Soc Dalton Trans 1:63
98. Song CE, Roh EJ, Shim WH, Choi JH (2000) Chem Commun 17:1695
99. Rideout DC, Breslow R (1980) J Am Chem Soc 102:7816
100. Olivier H (1999) J Mol Catal A: Chem 146:285
101. Olivier H, Hirschauer A (1962) French patent application 96:1996
102. Abbott AP, Capper G, Davies DL, Rasheed RK, Tambyrajah V (2002) Green Chem 4:24
103. Meracz I, Oh T (2003) Tetrahedron Lett 44:6465
104. Doherty S, Goodrich P, Hardacre C, Luo HK, Rooney DW, Seddon KR, Styring P (2004) Green Chem 6:63
105. Mathews CJ, Smith PJ, Welton T (2003) J Mol Catal A: Chem 206:77
106. Mathews CJ, Smith PJ, Welton T (2004) J Mol Catal A: Chem 214:27
107. McLachlan F, Mathews CJ, Smith PJ, Welton T (2003) Organometallics 22:5350
108. Wang R, Twamley B, Shreeve JM (2006) J Org Chem 71:426
109. Jin CM, Twamley B, Shreeve JM (2005) Organometallics 24:3020
110. Xiao JC, Twamley B, Shreeve JM (2004) Org Lett 6:3845
111. Zou G, Wang Z, Zhu J, Tang J, He MY (2003) J Mol Catal A: Chem 206:193
112. Corma A, Garcia H, Leyva A (2004) Tetrahedron 60:8553
113. Hamill NA, Hardacre C, McMath SEJ (2002) Green Chem 4:139
114. Deshmukh RR, Rajagopal R, Srinivasan KV (2001) Chem Commun 17:1544
115. Cassol CC, Umpierre AP, Machado G, Wolke SI, Dupont J (2005) J Am Chem Soc 127:3298
116. Reetz MT, Westermann E (2000) Angew Chem Int Edn 39:165
117. Vallin KSA, Emilsson P, Larhed M, Hallberg A (2002) J Org Chem 67:6243
118. Xie X, Lu J, Chen B, Han J, She X, Pan X (2004) Tetrahedron Lett 45:809
119. Hagiwara H, Shimizu Y, Hoshi T, Suzuki T, Ando M, Ohkubo K, Yokoyama C (2001) Tetrahedron Lett 42:4349

120. Okubo K, Shirai M, Yokoyama C (2002) Tetrahedron Lett 43:7115
121. Forsyth SA, Gunaratne HQN, Hardacre C,McKeown A, Rooney DW, Seddon K (2005) J Mol Catal A: Chem 231:61
122. Hagiwara H, Sugawara Y, Hoshi T, Suzuki T (2005) Chem Commun, 23:2942
123. Wang L, Zhang Y, Xie C, Wang Y (2005) Synlett 12:1861
124. de Bellefon C, Pollet E, Grenouillet P (1999) J Mol Catal A: Chem 145:121
125. Chen W, Xu L, Chatterton C, Xiao J (1999) Chem Commun 13:1247
126. Zevenhoven R, Eloneva S, Teir S (2006) Catal Today 115:73
127. Jessop PG, Ikariya T, Noyori R (1999) Chem Rev 99:475
128. Zhang S, Chen Y, Li F et al (2006) Catal Today 115:61
129. Peng J, Deng Y (2001) New J Chem 25:639
130. Sun J, Fujita SI, Arai MJ (2005) Organomet Chem 690:3490
131. Bhanage BM, Fujita S-I, Ikushima Y, Arai M (2001) Appl Catal A: General 219:259
132. Kawanami H, Sasaki A, Matsui K, Ikushima Y (2003) Chem Commun 7:896
133. Calo V, Nacci A, Monopoli A, Fanizzi A (2002) Org Lett 4:2561
134. Kim HS, Kim JJ, Kim H, Jang HG (2003) J Catal 220:44
135. Sun J, Wang L, Zhang S, Li Z, Zhang X, Dai W, Mori R (2006) J Mol Catal A: Chem 256:295
136. Sun J, Fujita S-i, Zhao F, Arai M (2004) Green Chem 6:613
137. Alvaro M, Baleizao C, Das D, Carbonell E, Garcia H (2004) J Catal 228:254
138. Zhu YJ, Wang WW, Qi RJ, Hu XL (2004) Angew Chem Int Edn 43:1410
139. Endres F, Abedin SZE (2002) Chem Commun 8:892
140. Nakashima T, Kimizuka N (2003) J Am Chem Soc 125:6386
141. Zhou Y, Antonietti M (2003) J Am Chem Soc 125:14960
142. Li Z, Zhang J, Du J, Gao H, Gao Y, Mu T, Han B (2005) Mater Lett 59:963
143. Wang Y, Yang H (2005) J Am Chem Soc 127:5316
144. Jiang Y, Zhu YJ (2005) J Phys Chem B 109:4361
145. Li Z, Liu Z, Zhang J, Han B, Du J, Gao Y, Jiang T (2005) J Phys Chem B 109:14445
146. Cao J, Wang J, Fang B, Chang X, Zheng M, Wang H (2004) Chem Lett 33:1332
147. Wang W-W, Zhu Y-J, Cheng G-F, Huang YH (2006) Mater Lett 60:609
148. Yang LX, Zhu YJ, Wang WW, Tong H, Ruan ML (2006) J Phys Chem B 110:6609
149. Fonseca GS, Umpierre AP, Fichtner PFP, Teixeira SR, Dupont J (2003) Chem Eur J 9:3263
150. Fonseca GS, Scholten JD, Dupont J (2004) Synlett 9:1525
151. Miao S, Miao Z, Liu Z, Han B, Zhang H, Zhang J (2006) Microporous Mesoporous Mater 95:26
152. Biswas K, Rao CNR (2007) Chem Eur J 13:6123
153. Jin K, Huang X, Pang L, Li J, Appel A, Wherland S (2002) Chem Commun 23:2872
154. Sakamoto H, Watanabe Y, Saito T (2006) Inorg Chem 45:4578
155. Wang T, Kaper H, Antonietti M, Smarsly B (2007) Langmuir 23:1489
156. Cooper ER, Andrews CD, Wheatley PS, Webb PB, Wormald P, Morris RE (2004) Nature 430:1012
157. Parnham ER, Drylie EA, Wheatley PS, Slawin AMZ, Morris RE (2006) Angew Chem Int Edn 45:4962
158. Parnham ER, Wheatley PS, Morris RE (2006) Chem Commun 4:380
159. Parnham ER, Morris RE (2006) Chem Mater 18:4882
160. Parnham ER, Morris RE (2006) J Am Chem Soc 128:2204
161. Parnham ER, Morris RE (2006) J Mater Chem 16:3682
162. Cooper ER, Andrews CD, Wheatley PS, Webb PB, Wormald P, Morris RE (2005) Studies Surf Sci Catal 158:247
163. Tang M-F, Liu Y-H, Chang P-C, Liao YC, Kao HM, Lii KH (2007) Dalton Trans 40:4523
164. Sheu CY, Lee SF, Lii KH (2006) Inorg Chem 45:1891
165. Tsao CP, Sheu CY, Nguyen N, Lii KH (2006) Inorg Chem 45:6361
166. Dybtsev DN, Chun H, Kim K (2004) Chem Commun 14:1594
167. Liao J-H, Huang W-C (2006) Inorg Chem Commun 9:1227
168. Lin Z, Slawin AMZ, Morris RE (2007) J Am Chem Soc 129:4880
169. Lin Z, Wragg DS, Warren JE, Morris RE (2007) J Am Chem Soc 129:10334

170. Jiang J, Yu SH, Yao WT, Ge H, Zhang GZ (2005) Chem Mater 17:6094
171. Fonseca GS, Machado G, Teixeira SR, Fecher GH, Morais J, Alves MCM, Dupont J (2006) J Colloid Interf Sci 301:193
172. Wang WW, Zhu YJ (2005) Cryst Growth Des 5:505
173. Gao S, Zhang H, Wang X, Mai W, Peng C, Ge L (2005) Nanotechnology 16:1234
174. Ding K, Miao Z, Liu Z, Zhang Z, Han B, An G, Miao S, Xie Y (2007) J Am Chem Soc 129:6362
175. Wang L, Xu Y, Wei Y, Duan J, Chen A, Wang B, Ma H, Tian Z, Lin L (2006) J Am Chem Soc 128:7432
176. Xu Y-P, Tian Z-J, Wang S-J, Hu Y, Wang L, Wang BC, Ma YC, Hou L, Yu JY, Lin LW (2006) Angew Chem Int Edn 45:3965
177. Han L, Wang Y, Li C, Zhang S, Lu X, Cao M (2008) AIChE J 54:280
178. Parnham ER, Morris RE (2007) Acc Chem Res 40:1005
179. Fuller J, Carlin RT, Osteryoung RA (1997) J Electrochem Soc 144:3881
180. Nanjundiah C, McDevitt SF, Koch VR (1997) J Electrochem Soc 144:3392
181. Suarez PAZ, Selbach VM, Dullius JEL, Einloft S, Piatnicki CMS, Azambuja DS, de Souza RF, Dupont J (1997) Electrochim Acta 42:2533
182. Koch VR, Dominey LA, Nanjundiah C, Ondrechen MJ (1996) J Electrochem Soc 143:798
183. Trulove PC, Mantz RA (2003) Ionic liquids in synthesis. Wiley-VCH, New York
184. Buzzeo MC, Evans RG, Compton RG (2004) Chem Phys Chem 5:1106
185. Ito Y, Nohira T (2000) Electrochim Acta 45:2611
186. Ohno H (2005) Electrochemical aspects of ionic liquids. Wiley, Hoboken
187. Endres F (2002) Chem Phys Chem 3:144
188. Abbott AP, McKenzie KJ (2006) Phys Chem Chem Phys 8:4265
189. Abbott AP, Capper G, McKenzie KJ, Ryder KS (2006) Electrochim Acta 51:4420
190. Christopher S (2005) Engineer 293:36
191. Abbott AP, Capper G, Swain BG, Wheeler DA (2005) Trans Inst Metal Finish 83:51
192. Barhdadi R, Courtinard C, Nédélec JY, Troupel M (2003) Chem Commun 12:1434
193. Martiz B, Keyrouz R, Gmouh S, Vaultier M, Jouikov V (2004) Chem Commun 6:674
194. Doherty AP, Brooks CA (2004) Electrochim Acta 49:3821
195. Naudin E, Ho HA, Branchaud S, Breau L, Belanger D (2002) J Phys Chem B 106:10585
196. Koo YK, Kim BH, Park DH, Joo J (2004) Mol Crystals Liquid Crystals 425:55
197. Pringle JM, Efthimiadis J, Howlett PC, Efthimiadis J, MacFarlane DR, Chaplin AB, Hall SB, Officer L, Wallace G G, Forsyth M (2004) Polymer 45:1447
198. Webber A, Blomgren GE (2002) Advances in lithium-ion batteries. Springer, Berlin Heidelberg New York
199. Tobishima S-I (2002) Electrochemistry 70:198
200. Garcia B, Lavallee S, Perron G, Michot C, Armand M (2004) Electrochim Acta 49:4583
201. Rogers RD, Seddon KR, Volkov S (2003) Green industrial applications of ionic liquids. Kluwer, Dordrecht
202. Li Z, Liu H, Liu Y, He P, Li J (2004) J Phys Chem B 108:17512
203. Sato T, Maruo T, Marukane S, Takagi K (2004) J Power Sources 138:253
204. Lee JS, Bae JY, Lee H, Quan N D, Kim H S, Kim H (2004) J Ind Eng Chem 10:1086
205. Shibata Y, Kato T, Kado T, Shiratuchi R, Takashima W, Kaneto K, Hayase S (2003) Chem Commun 21:2730
206. Wang P, Zakeeruddin SM, Exnar I, Gratzel M (2002) Chem Commun 24:2972
207. Stathatos E, Lianos P, Zakeeruddin SM, Liska P, Gratzel M (2003) Chem Mater 15:1825
208. Mikoshiba S, Murai S, Sumino H, Kado T, Kosugi D, Hayase S (2005) Curr Appl Phys 5:152
209. Kang MG, Ryu KS, Chang SH, Park NG (2004) ETRI J 26:647
210. Wang P, Zakeeruddin SM, Comte P, Exnar I, Gratzel M (2003) J Am Chem Soc 125:1166
211. Wang P, Zakeeruddin SM, Moser JE, Gratzel M (2003) J Phys Chem B 107:13280
212. Kawano R, Matsui H, Matsuyama C Sato A, Susan MABH, Tanabe N, Watanabe M (2004) J Photochem Photobiol A: Chem 164:87
213. Xue B, Wang H, Hu Y, Li H, Wang Z, Meng Q, Huang X, Sato O, Chen L, Fujishima A (2004) Photochem Photobiol Sci 3:918

214. Angell CA, Xu W, Belieres J-P, Yoshizawa M (2004) International patent WO2004114445
215. Susan MABH, Noda A, Mitsushima S, Watanabe M (2003) Chem Commun 8:938
216. Susan MABH, Yoo M, Nakamoto H, Watanabe M (2003) Chem Lett 32:836
217. Hagiwara R, Nohira T, Matsumoto K, Tamba Y (2005) Electrochem Solid-State Lett 8:A231
218. de Souza RF, Padilha JC, Goncalves RS, Dupont J (2003) Electrochem Commun 5:728
219. Balducci A, Henderson WA, Mastragostino M, Passerini S, Simon P, Soavi F (2005) Electrochim Acta 50:2233
220. Sato T, Masuda G, Takagi K (2004) Electrochim Acta 49:3603
221. Ue M, Takeda M, Toriumi A, Kominato A, Hagiwara R, Ito Y (2003) J Electrochem Soc 150:A499
222. Ue M (2003) Mater Integration 16:40
223. Lewandowski AAS (2004) Polish J Chem 78:1371
224. Lewandowski A, Swiderska A (2003) Solid State Ionics 161:243
225. Buzzeo MC, Hardacre C, Compton RG (2004) Anal Chem 76:4583
226. Lee YG, Chou T-C (2004) Biosens Bioelectron 20:33
227. Wang R, Hoyano S, Ohsaka T (2004) Chem Lett 33:6
228. Wang R, Okajima T, Kitamura F, Obsaka T (2004) Electroanalysis 16:66
229. Brinz T, Simon U (2002) German patent DE 2002–10245337
230. Pernak J, Feder K (2005) Chem Eur J 11:4441
231. Ding J, Zhou D, Spinks G, Wallace G, Forsyth S, Forsyth M, MacFarlane D (2003) Chem Mater 15:2392
232. Zhou D, Spinks GM, Wallace GG, Tiyapiboonchaiya C, MacFarlane DR, Forsyth M, Sun J (2003) Electrochim Acta 48:2355
233. Vidal F, Plesse C, Teyssie D, Chevrot C (2004) Synth Metals 142:287
234. Zhao F, Wu X, Wang M, Liu Y, Gao L, Dong S (2004) Anal Chem 76:4960
235. Pappenfus TM, Henderson WA, Owens BB, Mann KR, Smyrl WH (2003) Polym Mater Sci Eng Prepr 88:302
236. Tiyapiboonchaiya C, MacFarlane DR, Sun J, Forsyth M (2002) Macromol Chem Phys 203:1906
237. Barisci JN, Wallace GG, MacFarlane DR, Baughman RH (2004) Electrochem Commun 6:22
238. Fukushima T, Kosaka A, Ishimura Y, Yamamoto T, Takigawa T, Ishii N, Aida T (2003) Science 300:2072
239. Fukushima T, Aida T (2004) Polym Prepr 45:306
240. Balczewski P, Bachowska B, Bialas T, Biczak R, Wieczorek WM, Balinska A (2007) J Agric Food Chem 55:1881
241. Cho CW, Pham TPT, Jeon YC, Vijayaraghavan K, Choe WS, Yun YS (2007) Chemosphere 69:1003
242. Matzke M, Stolte S, Thiele K, Juffernholz T, Arning J, Ranke J, Welz-Biermann U, Jastorff B (2007) Green Chem 9:1198
243. Jastorff B, Störmann R, Ranke JMölter K, Stock F, Oberheitmann B, Hoffmann W, Hoffmann J, Nüchter M, Ondruschka B, Filser J (2003) Green Chem 5:136
244. Ranke J, Molter K, Stock F, Bottin Weber U, Poczobutt J, Hoffmann J, Ondruschka B, Filser J, Jastorff B (2004) Ecotoxicol Environ Saf 58:396
245. Pernak J, Smiglak M, Griffin ST, Hough WL, Wilson TB, Pernak A, Matejuk JZ, Fojutowski A, Kita K, Rogers RD (2006) Green Chem 8:798
246. Jastorff B, Mölter K, Behrend P, Weber UB, Filser J, Heimers A, Ondruschka B, RankeJ, Schaefer M, Schröder H, Stark A, Stepnowski P, Stock F, Störmann R, Stolte S, Biermann UW, Ziegert S, Thöming J (2005) Green Chem 7:362
247. Frade RFM, Matias A, Branco LC, Afonso CAM, Duarte CMM (2007) Green Chem 9:873
248. Nockemann P, Thijs B, Driesen K, Janssen CR, VanHecke K, VanMeervelt L, Kossmann S, Kirchner B, Binnemans K (2007) J Phys Chem B 111:5254
249. Bernot RJ, Brueseke MA, Evans-White MAE, Lamberti GA (2005) Environ Toxicol Chem 24:87
250. Samorì C, Pasteris A, Galletti P, Tagliavini E (2007) Environ Toxicol Chem 26:2379

251. Garcia MT, Gathergood N, Scammells PJ (2005) Green Chem 7:9
252. Stock F, Hoffmann J, Ranke J, Störmann R, Ondruschka B, Jastorff B (2004) Green Chem 6:286
253. Stolte S, Arning J, Bottin-Weber U, Müller A, Pitner WR, Biermann UW, Jastorff B, Ranke J (2007) Green Chem 9:760
254. Ranke J, Muller A, Bottin-Weber U, Stock F, Stolte S, Arning J, Stormann R, Jastorff B (2007) Ecotoxicol Environ Safety 67:430
255. Stolte S, Arning J, Weber UB, Matzke M, Stock F, Thiele K, Uerdingen M, Biermann UW, Jastorff B, Ranke J (2006) Green Chem 8:621
256. Stepnowski P, Skladanowski AC, Ludwiczak A, Laczynska E (2004) Hum Exp Toxicol 23:513

Struct Bond
DOI:10.1007/430_2008_4

Thermodynamic Analysis for Synthesis of Advanced Materials

C. Liu, Y. Ji, Q. Shao, X. Feng, and X. Lu

Abstract In this paper, thermodynamic modeling for materials-oriented chemical engineering systems were investigated in order to solve critical scientific problems, such as the material structure, chemical properties, thermodynamic properties, and transfer behaviors on the interfaces or under confined circumstances. On the basis of the theory and approaches of chemical engineering, and the principles of chemical engineering thermodynamics and transfer processes, molecular simulations were combined with modern physical characterization methods to study thermodynamic modeling in materials-oriented chemical engineering processes.

Keywords: Advanced materials · Electrolyte · Interface ·Molecular simulation · Thermodynamics

Contents

C. Liu, Y. Ji, Q. Shao, X. Feng, and X. Lu(✉)
State Key Laboratory of Materials-Oriented Chemical Engineering, College of Chemistry and Chemical Engineering, Nanjing University of Technology, Nanjing 210009, China
e-mail: xhlu@njut.edu.cn

1 Introduction

With the development of science and technology, chemical engineering with the advantages of scaling-up has closer and closer relationships with the fields of energy, materials, biochemistry, etc. When the theories of chemical engineering are used for the preparation of new materials, a scaling-up of the process and a decrease in costs can be achieved. When advanced materials are used for the development of new chemical process, traditional chemical engineering processes will be more efficient and more environmentally friendly. The support of chemical engineering and material science to each other brings a new interdisciplinary field: materials-oriented chemical engineering.

However, the involved systems and the conformations of substances in this new field are more complex than those in traditional chemical engineering. The traditional theory of chemical engineering faces a big challenge due to the complex surface and porous structure of advanced materials, and to the rigorous preparation conditions such as hydrothermal environments or supercritical states.

Traditional chemical engineering theory usually deals with only the gas and liquid phases. However, many solids and solid–liquid interfaces come into being in the preparation of advanced materials, and rigorous conditions such as hydrothermal environments or supercritical states (high temperatures and high pressures) are required, which makes traditional chemical engineering theory useless. Therefore, predictive and extensive thermodynamic models are required. These can be obtained by considering the structures and chemical performances of solid materials and the

critical factors, such as the high temperatures and high pressures involved in the use of these materials. Advanced characterization methods are used to verify and modify the models.

Advanced materials for chemical application are mostly required to have performances with high catalytic activity and separation capability, so they usually have porous structures with high specific surface area. The behaviors of liquid on the surface or in nanopores are quite different from those in bulk phase and they are not well known. So, it is necessary to study the liquid properties, phase behaviors, and transport behaviors at the mesoscale, in microstructures, on solid–liquid interfaces, or in extreme conditions, which is also one of the world's hot issues.

With the development of information technology, computer simulation techniques have become an almost essential means for the study of complex macromolecular phenomena and phase behaviors at the molecular level. These techniques are becoming increasingly important. In the final analysis, the macroscopic properties of substances are the results of the molecular forces. Therefore, in order to investigate the behaviors of materials and liquids, the effects of molecules should be understood. The relationships between the material structures, chemical properties, and material performances should be investigated on the molecular level. The molecular simulations on the microstructures and interfaces concerned in the design, preparation, and application of advanced materials have been proved to provide a new method for the preparation and application of new materials for chemical use, such as for catalysis and separation by membranes. The simulations can give comprehensive predictive results from microscale to mesoscale with high efficiency for the design and synthesis of advanced materials, which cannot be obtained from recent experiments.

A schematic diagram for the general research outline is shown in Fig. 1.

In this paper, the following studies are involved:

1. At the mesoscale, the relationship between the microstructures of nanoporous materials and liquid behaviors was investigated. The microstructures and behaviors of several typical liquids such as H_2O, CH_4, CO_2, ethanol and their mixtures in model nanopores were systemically studied. The differences in liquid behaviors in confined circumstances and in bulk phase were examined.
2. Activity coefficient models for aqueous electrolyte solutions in hydrothermal reaction environments are presented by combining molecular simulation, quantum chemistry, and thermodynamic calculations.
3. On the basis of thermodynamic principles, a general method for the solid–liquid equilibrium (SLE) stage is proposed in this paper. The number of phases and their identities at solid–liquid equilibrium were determined automatically in advance, and the distribution of components at the solid–liquid equilibrium stage could be determined with decreased iterations, which could meet the requirements of chemical process simulation and chemical production.
4. Thermodynamic models for the preparation of a new functional material, potassium titanate whiskers, were studied, and relationships between material structure, performance, and manageable preparation parameters were proposed.

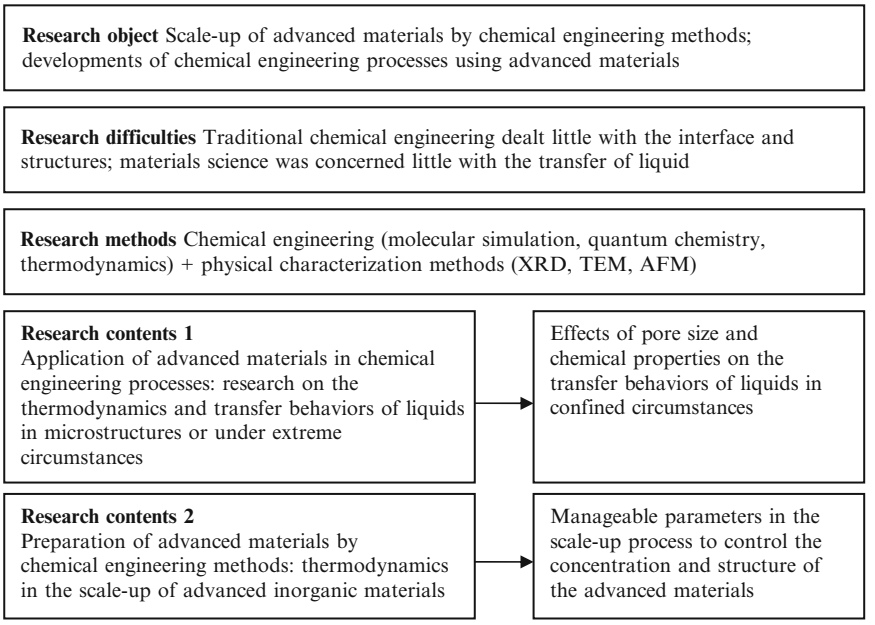

Fig. 1 Schematic of general research frame on molecular simulation and thermodynamic study in materials-oriented chemical engineering processes

Characterization experiments were carried out to verify the calculation results. The process scale-up and the application of this material were achieved.

A schematic diagram for the detailed research contents is shown in Fig. 2. The integrated use of a series of methods provides a good paradigm for thermodynamic investigations on the scale-up and applications of advanced materials for chemical application.

2 Molecular Simulation Study on Behavior of Fluids in Nanoconfinement

Nanoporous structure is considered to be one of the determinant factors for the excellent performance of advanced materials. The size of the pore is around several nanometers. The applications of the specific functions of the nanopores in the membrane separation and heterogeneous catalysis have attracted researchers in both scientific and industrial fields. Examples include the reverse osmosis process for desalination of sea water and hydrogen production by photocatalysis of porous TiO_2. Therefore, it is urgent to understand the properties of the fluid inside the nanopores. However, the classical transport theory is unable to solve the problems at this scale, especially those inside the pores with size of only 1–2 nm. The available

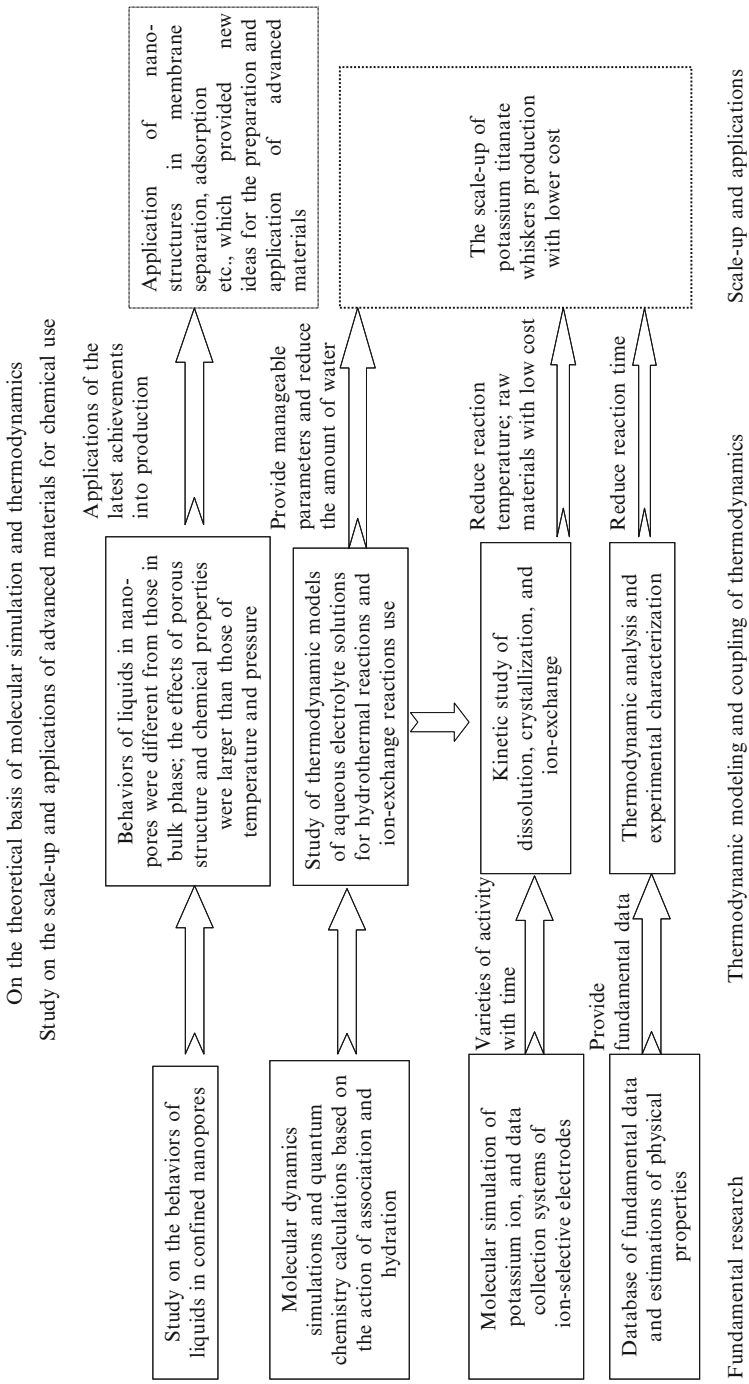

Fig. 2 Schematic of the detailed research contents

experiments also show that the fluid inside these pores does not follow known principles. Therefore, exploration of the behavior of fluid in nanoconfinement is critical for material-oriented chemical engineering.

However, real nanoporous material is very complicated, with inhomogeneous chemical and topological structure, making investigation a consuming task. It is necessary to build a relatively simple model from these assorted nanopores, and be able to represent the nanoconfinement. In 2001, Hummer et al. [1] simulated a single-walled armchair carbon nanotube (CNT) immersed in a water reservoir. They found that, despite the simplicity of the carbon nanotube, it can successfully mimic the water flow in the complex biological channel. The hydrophobic interior of CNTs is considered as a model for fundamental studies aimed at exploring the structural and phase behavior of water molecules within 1-D nanochannels [2, 3]. This has long been recognized as the key for both theory and practice, with various applications such as gas storage [4], nanoelectronics [5], molecular detection [6], drug delivery [7], and membrane separation [8].

Research on the fluid inside carbon nanotubes soon received attention from scientists in various fields. In this section, we mainly summarize our recent studies on the structure of water and ethanol in pristine and chemically modified CNT.

2.1 Effect of Diameter on Structure of Water Molecules in Carbon Nanotubes

CNTs can serve as prototypes for biological channels that can be investigated more easily by molecular dynamics (MD) simulations due to their simplicity, stability, and small size [9]. Therefore, the behavior of water confined in CNTs is attracting more and more attention from nanotube researchers. Some have only studied the properties of water inside CNTs and have never put any water molecules outside CNTs in their simulation systems [10, 11]. Marti and coworkers [12, 13] have completed a series of studies of static and dynamic properties of water within CNTs under ambient and supercritical conditions. Koga et al. [2, 14] also focused on new phase transitions of water inside CNTs. Several other researchers were particularly interested in water properties outside CNTs [15, 16]. Nevertheless, others paid special attention to water transportation through CNTs and hence the properties of water both inside and outside the CNTs. However, the properties of a nanotube strongly depend on its diameter and helicity. For instance, the electronic properties of an (n,m) nanotube vary in a periodic way between being metallic and being a semiconductor [17]. They follow a general rule: if (n,m) is a multiple of three, then the tube is metallic; if (n,m) is not a multiple of three, then the tube is semiconducting. On the other hand, the chemical activity of CNTs scales inversely with tube diameter [18].

Hence, we might expect great differences in the behavior of water molecules confined in CNTs of different diameter and helicity, and the aim of this study is to investigate this. Although there have been some scattered studies on this subject, to the best of our knowledge we have not seen any systematic study of their

influences to date. In this work, MD simulations for different SWCNTs with indices of (n,n) armchair ($n = 4,5,6,7,8,9,10$) and $(n,0)$ zigzag ($n = 6,8,10,12,14,16,18$) submerged in water are reported.

2.1.1 Cross-Section of Water Configuration Inside Various Tube Segments

The formation of ice-like water structures inside CNTs has been proposed in several simulation studies. However, the conditions of forming such ice-like structures are quite different. Koga et al. [2] found that n-gonal ring structures of water can be formed within CNTs under high pressures (50–500 MPa). Later, Noon et al. [19] pointed out that different numbers of water columns could appear inside various CNTs under ambient conditions. Although Mashl et al. [20] also observed a stacked column of cyclic hexamers inside a (9,9) CNT at ambient conditions, he did not find the formation of similar ordered structures within (7,7), (8,8), (9,9) and (10,10) tubes, which is inconsistent with the results by Noon et al. To further examine this diameter effect, cross-sections of water configurations inside various tube segments are shown in Fig. 3. No obvious multicolumnar water structures inside (n,n) tubes ($n = 7,8,9,10$) were found in our simulation results. So, the formation of ice-like water structures inside CNTs based on theoretical computations might be sensitive to potential models, key non-bond interaction parameters between oxygen and carbon, and tube length, etc. Apparently no water molecule could stay inside a (4,4) CNT, while a single-file water chain exists in a (5,5) tube. It seems that (5,5) CNT is the smallest armchair tube whose interior could be wetted by water, which contradicts the conclusion of Noon et al. [19] that a (5,5) tube was too small to accommodate any water molecules inside. However, Mashl et al. [20] observed a similar single-file water chain with all oxygen atoms concentrated in the center of a (5,5) tube. In fact, the possibility ofwater molecules entering a nanotube is mainly determined by σ_{CO} and tube diameter. In this work, a much higher oxygen density could be expected in the center of the (5,5) tube. On the whole, water molecules would like to adopt a single-file arrangement in narrow CNTs but become more disordered, as in bulk water, in wide CNTs. In general, there is no apparent qualitative difference of equilibrated configurations inside armchair and zigzag CNTs of almost the same diameter, based on the comparison of each row in Fig. 3. In other words, little helicity effect could be manifested by equilibrated configurations of water molecules confined inside CNTs. However, this rule is not obeyed in the comparison between (5,5) and (8,0) tubes. It is evident that no water molecule could enter a (8,0) tube, though its diameter is close to that of a (5,5) tube. This result is quite surprising and beyond our intuitive expectation. For the time being, such an exceptional phenomenon might be attributed to the helicity effect since there is no other big difference between them.

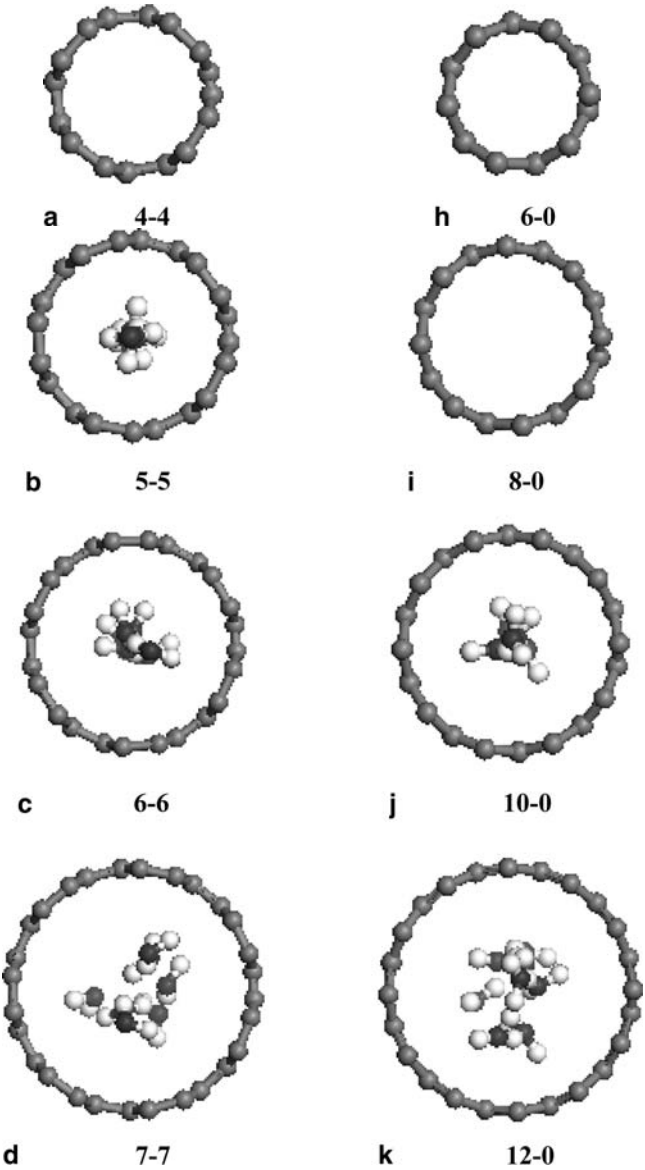

Fig. 3 Cross-sections of the water configurations inside various tube segments. *Left-hand column* (n,n) tubes; *right-hand column* $(n,0)$ tubes

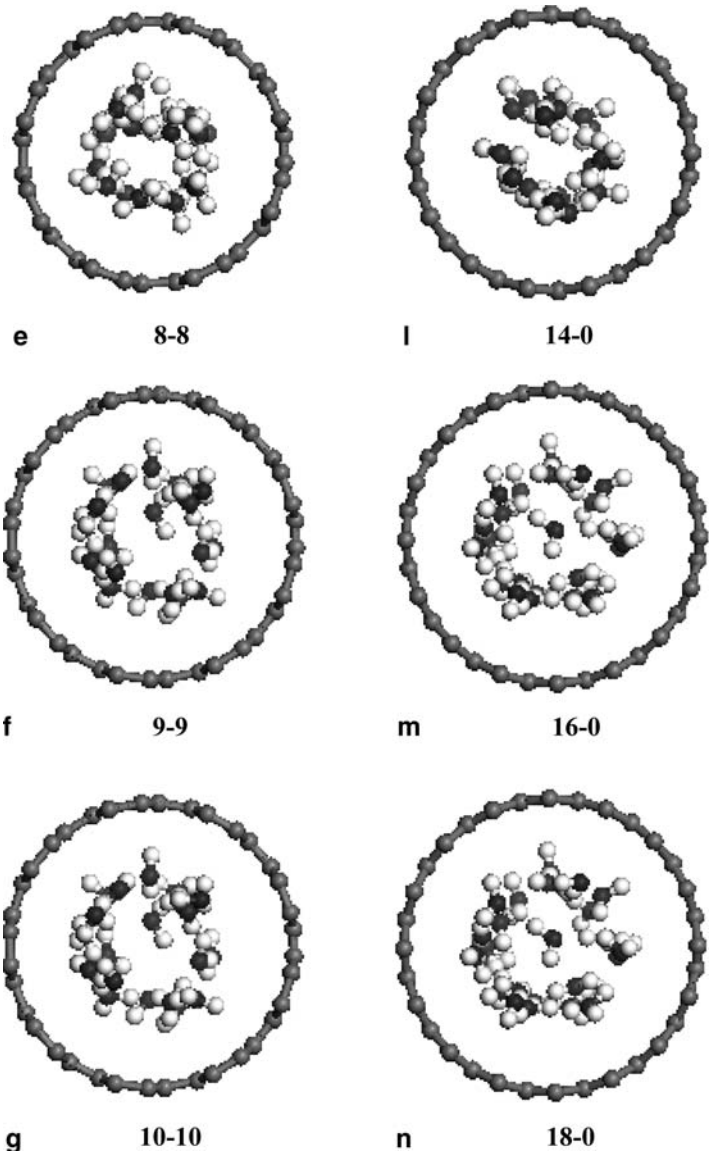

Fig. 3 (*Continued*)

2.1.2 Distribution of Number of Hydrogen Bonds

A geometrical definition of the hydrogen bond (HB) similar to that of Marti's work [21] is employed in this work to count the number of HBs formed in CNTs. That is to say, two water molecules are hydrogen-bonded if three conditions are fulfilled:

1. The distance R_{OO} between the oxygen atoms of both molecules has to be smaller than a cutoff distance R_{OO}^{C} : 0.375nm
2. The distance R_{OH} between the oxygen of the acceptor molecule and the hydrogen of the donor has to be lower than a cutoff distance R_{OH}^{C} : 0.246nm
3. The bond angle a between the O–O direction and the molecular O–H direction of the donor, where H is the hydrogen that forms the bond, has to be lower than a cutoff angle a^{c} : 37.3°

The percentages of water molecules involved in one to six HBs for both armchair and zigzag tubes are displayed in Table 1. Values for bulk water in the same simulation conditions are also shown. Although the average number of HBs per molecule, $<n_{\mathrm{HB}}>$, in this work is always lower than Marti's counterparts, several similar main features can still be observed. First, both $<n_{\mathrm{HB}}>$ and the position of the maxima of the HB distributions are lower than for their bulk counterparts. Second, $<n_{\mathrm{HB}}>$ within narrower CNTs such as (5,5), (10,0), and (6,6) are less than half of those corresponding to unconstrained water, whereas those inside wider CNTs such as (8,8) and (18,0) are quite similar in spite of great differences between their diameters. Such obvious variation in $<n_{\mathrm{HB}}>$ can only be attributed to confinement effects of nanoscale. The so-called nano-effect is mainly affected by tube diameter rather than tube helicity, which can be easily shown in Fig. 4. Such diameter dependence of $<n_{\mathrm{HB}}>$ may have a strong influence on diffusion rates of confined water. Normally, the diffusion rate of confined water should increase with tube diameter until it reaches the limit, namely the bulk value of water inside an infinitely large CNT, due to pure confinement effect. However, the destruction of complete HB networks would allow individual water molecules to move more freely, resulting in an increase of diffusion rate. So, the diffusion rate of confined water must be determined by the competition between confinement by CNTs and the extent of destruction of HB networks. We might expect that confinement will play a major role inside wider CNTs while the destruction of the HB network will make more contributions inside

Table 1 Percentages of water molecules (f_{n}) with $n(n = 1, 2, \ldots 6)$ H bonds within (n, m) CNTs

(n,m)	f_1	f_2	f_3	f_4	f_5	f_6	$< n_{\mathrm{HB}} >$
(5,5)	62.8	37.2	0.00	0.00	0.00	0.00	1.37
(6,6)	46.1	53.9	0.00	0.00	0.00	0.00	1.54
(7,7)	25.5	51.4	21.8	1.31	0.00	0.00	1.99
(8,8)	13.2	37.6	38.0	10.8	0.334	0.00246	2.47
(9,9)	11.9	35.6	39.0	13.0	0.558	0.0145	2.55
(10,10)	10.5	32.5	38.8	16.6	1.58	0.0415	2.66
(10,0)	49.7	50.3	0.00	0.00	0.00	0.00	1.50
(12,0)	26.1	52.2	20.8	0.919	0.00	0.00	1.96
(14,0)	11.8	35.7	39.9	12.3	0.319	0.00232	2.54
(16,0)	11.4	34.5	39.0	14.3	0.823	0.0182	2.59
(18,0)	10.8	32.6	37.7	17.1	1.71	0.0584	2.66
Bulk[a]	1.30	10.4	34.6	45.1	8.21	0.302	3.49

$<n_{\mathrm{HB}}>$ average number of H bonds per water molecule

[a]For reference, bulk TIP3P water was simulated for 100 ps (256 molecules, 300 K at a density of $1.0\,g\,\mathrm{cm}^{-3}$)

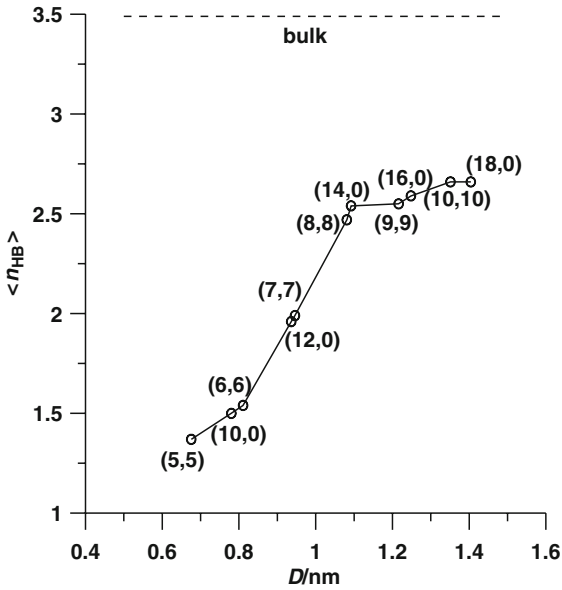

Fig. 4 $<n_{HB}>$ as a function of tube diameter D

narrower CNTs since $<n_{HB}>$ becomes nearly independent of tube diameter in wider tubes.

A general conclusion can be drawn from the comparisons of each pair of armchair and zigzag tubes that the static properties of water confined in CNTs are dominated by the tube diameter effect, rather than the helicity effect. In addition, the formation of ice-like water structures inside CNTs might be sensitive to the choice of potential models and corresponding parameters. On the whole, in narrower CNTs, water molecules would like to adopt a single-file arrangement but become more disordered, in a fashion similar to that of bulk water in wider CNTs. Furthermore, the distribution of water molecules at the CNT–water interface shows a characteristic layering and a continuous empty gap of 0.52 nm is always maintained. Narrow tubes do not allow complex HB structures and, in many cases, the adsorbed water molecules inside form single-file water chains. Obvious variation in the average number of HBs per molecule can only occur in narrower CNTs, which is expected to affect the diffusion rate of confined water significantly.

2.2 Effect of Chemical Modification on Behavior of Water Molecules in Carbon Nanotubes

CNTs are generally insoluble in common solvents [22, 23], which impedes the separation and manipulation of CNTs for specific applications. It is therefore a general

belief that chemical functionalization of CNTs is desirable to improve their solubility and processibility [18, 24], which can lead to a significant enhancement in the properties relevant to their practical applications [25]. As a result, the field of carbon nanotube functionalization is growing rapidly and has been the subject of recent research efforts [26,27]. Successful approaches so far reported for the chemical functionalization of CNTs can be achieved at the open ends, the inner and the outer sidewalls [28, 29].

The functionalizations also alter the structural and electronic properties of CNTs, which in turn deserve theoretical investigations before conducting purposeful experimental functionalizations of CNTs. As for the water–CNT system, Joseph et al. [20] used MD simulations to study the ionic flow in CNTs functionalized by –COOH groups at both ends. Their results showed that the selectivity between cations and anions could be obtained by symmetrical placement of the functional groups. Zheng and co-workers [30] anchored –COOH groups onto the inner wall of a CNT to alter the hydrophobic surface into a hydrophilic one, and carried out the dual-control-volume grand canonical molecular dynamics simulations to study the transport of water and methanol mixtures through the modified CNTs. Their results showed that transport of the mixture through hydrophilic tubes is faster than through hydrophobic nanotubes, although the diffusion of the mixture is slower inside hydrophilic than hydrophobic pores due to a hydrogen network. Halicioglu and Jaffe [31] carried out MD simulations to investigate the effect exerted by aqueous solutions on the equilibrium structure and configuration of functional groups attached to carbon nanotubes. Their simulation results indicated that polar functional groups are energetically more stable in extended configurations. Nonpolar functional groups, on the other hand, prefer to remain folded. Our previous MD simulations results [32] showed that because of helicity differences between (6,6) and (10,0) CNTs, the functionalization by hydrophilic –COOH groups at one end of the CNT results in different responses, which in turn have control over the flow direction of water molecules in these CNTs.

Despite this research, the nanoscale behavior of water molecules in such functionalized CNTs is not yet well understood. Taking the open end functionalized CNTs as an example, there exist several unsolved questions, including:

- Does it make any difference if the open ends of the CNTs are functionalized by hydrophobic methyl groups ($–CH_3$)?
- If the interesting results in previous work [32] are brought forth by the functionalization to just one end of the CNTs, then what happens if both ends of the CNTs are functionalized by –COOH groups?
- If, as pointed out in the literature [33], nanoscale confinement phenomena are dominated by tube diameter, then does a larger functionalized zigzag CNT have the ability to control the direction of water flow, as does the functionalized (10,0) CNT reported in previous work?

We performed a series of MD simulations on the water and functionalized CNT systems. The effects of different functional groups (hydrophilic –COOH or hydrophobic $–CH_3$), different functional styles (one end functionalized or both ends

modified), diameter, and helicity (armchair (6,6), (7,7) and zigzag (10,0), (12,0) CNTs) were investigated to study the structural characteristics of water molecules confined inside functionalized CNTs.

2.2.1 Length of Single-File Water Chain and the Hydrogen Bonds Inside CNTs

Hydrogen bonds play a crucial role in the behavior of water; their spatial patterns and fluctuations characterize the structure and dynamics of water molecules [34]. The hydrogen bond structure in this paper is given in terms of the average number of hydrogen bonds per water molecule ($<n_{HB}>$) and is determined by a geometrical criterion, similar to that of Marti et al. [21].

The ensemble properties were averaged over the last 200 ps for the total number of water molecules that once entered the CNT (n_T), the average length of single-file water chain($<n>$), and the average number of hydrogen bonds of water molecules inside the CNTs ($<n_{HB}>$). Detailed information from the MD runs is provided in Table 2. We can summarize two interesting results from Table 2. The first is that except for the (7,7) CNT, each of the three properties analyzed for the (6,6), (10,0), and (12,0) CNTs change in the order –COOH functionalized CNT > pristine CNT ≈ $–CH_3$ functionalized CNT. Although the $–CH_3$ functionalized (7,7) CNT is little different to the pristine (7,7) CNT as far as these properties are concerned, once the (7,7) CNT is modified by the –COOH groups at one end, the number of water molecules that are able to enter the interior observably decreases to a much smaller number. Secondly, we also found that the number of hydrogen bonds per entered water ($<n_{HB}>/<n>$) for –COOH functionalized CNTs is smaller than that for $–CH_3$ functionalized CNTs and for pristine CNTs. In our previous work [32], the as-functionalized (10,0) CNT only allows the water molecules to enter the interior from the unfunctionalized end because the –COOH groups at the other end block the way for water molecules. We attribute that phenomena to the helicity effects exerted by the zigzag (10,0) CNT. The simulation results here indicate that water molecules have difficulty in entering the –COOH group functionalized armchair (7,7) CNTs.

Table 2 Water molecules inside CNTs

(m,n)	(6,6)			(10,0)			(7,7)			(12,0)		
Functional style	P	2–C	CH_3	P	2–C	CH_3	P	C	CH_3	P	C	CH_3
n_T	17	32	19	15	26	15	31	13	32	29	48	27
$<n>$	9.8	10.6	8.9	8.7	10.2	8.9	12.2	5.1	12.3	12.5	20.4	12.6
$<n_{HB}>$	2.8	2.9	2.6	1.7	1.9	1.8	3.0	0.9	3.0	2.1	2.1	2.2
$<n_{HB}>/<n>$	0.16	0.09	0.14	0.11	0.07	0.12	0.10	0.06	0.09	0.07	0.04	0.08

$<n>$ Average length of single-file water chain, $<n_{HB}>$ average number of hydrogen bonds,n_T total number of water molecules that enter the CNT during the last 200 ps

P, *C*, 2–*C* and CH_3 stand for the pristine, functionalized by –COOH groups at one end, by –COOH groups at both ends and by $–CH_3$ groups at one end, respectively. The number of hydrogen bonds per entered water molecules in –COOH functionalized CNTs is less than that in pristine and $–CH_3$ functionalized CNTs

2.2.2 Positions of Water Molecules When First Entering the CNTs, and Fluctuations of the Functional Groups

In order to have a better understanding of how the functional groups affect the behavior of water molecules, all water molecules in the CNTs were tracked to find out how they had entered the CNTs. The fluctuations of the functional groups were analyzed to reveal the roles they play during that process. The positions of water molecules were recorded (as shown in Fig. 5) for the last 100 ps simulation time to show where they are and when they enter the CNTs for the first time. The *h*-axis (axial direction of CNTs) is along the *z*-axis, and if the CNT is functionalized at one end, that modified end is placed at the origin of the *h*-axis. The positions of the functional groups are defined by two angles, as shown in Fig. 6a. C_1 and C_2 are carbon atoms of CNT and C_3 and C_4 are the carbon atoms of –COOH or $–CH_3$ groups. The fluctuations of the angles $C_3C_1C_2$ and $C_4C_2C_1$ are plotted in Fig. 6b.

It is observed from Fig. 5 that in general water molecules can enter the CNTs, except for $–CH_3$ functionalized (7,7) CNTs, from both ends with almost equal probabilities. However, two CNTs, (7,7) functionalized by –COOH groups at one end and (10,0) functionalized by –COOH groups at both ends, display some abnormities. We can get direct and clear information from Table 2. Once the (7,7) CNT is functionalized by –COOH groups at one end, it only opens the unmodified end for water molecules, behaving exactly the same as the as-functionalized (10,0) CNT reported in [32]. Although the (10,0) CNT is symmetrically modified by –COOH groups at both ends, water molecules can only enter the interior from just one functionalized open end. The differences between the two functionalized ends can be clearly seen from the following analysis.

Figure 6 shows that the angles of –COOH groups at the functionalized end of (7,7) CNT seem to be fixed at about 20°, indicating that the –COOH groups at the modified end of the (7,7) CNT cover that end and block the way for water molecules. The exceptional fluctuations of the –COOH groups of (7,7) CNT also answer for all the abnormities in the properties analyzed above for that (7,7) CNT. As far as the modified (10,0) is concerned, the functional groups at the two ends behave differently. The values for two angles at one end (h = 2.5) are both around 30°, which indicates that the two functional groups cover that end and prevent water molecules from entering the interior. So, the water molecules can only enter that (10,0) CNT at the other modified end ($h = 0.0$), where the two angles are about 30° and 175°. Taking our previous work on the functionalized CNTs into consideration [32], it is obvious that the helicity and the diameter differences are responsible for the phenomenon observed for the –COOH functionalized CNTs. This deserves further study in order to fully understand the phenomenon, especially because good control over the flow direction of water molecules makes functionalized CNTs a proper candidate for a water molecular switch.

In addition, the other cases where the CNTs are modified by $–CH_3$ groups do not show any remarkable differences. It confirms the conclusion that the introduction of hydrophobic $–CH_3$ groups does not change the structural characteristics of water molecules confined in these CNTs.

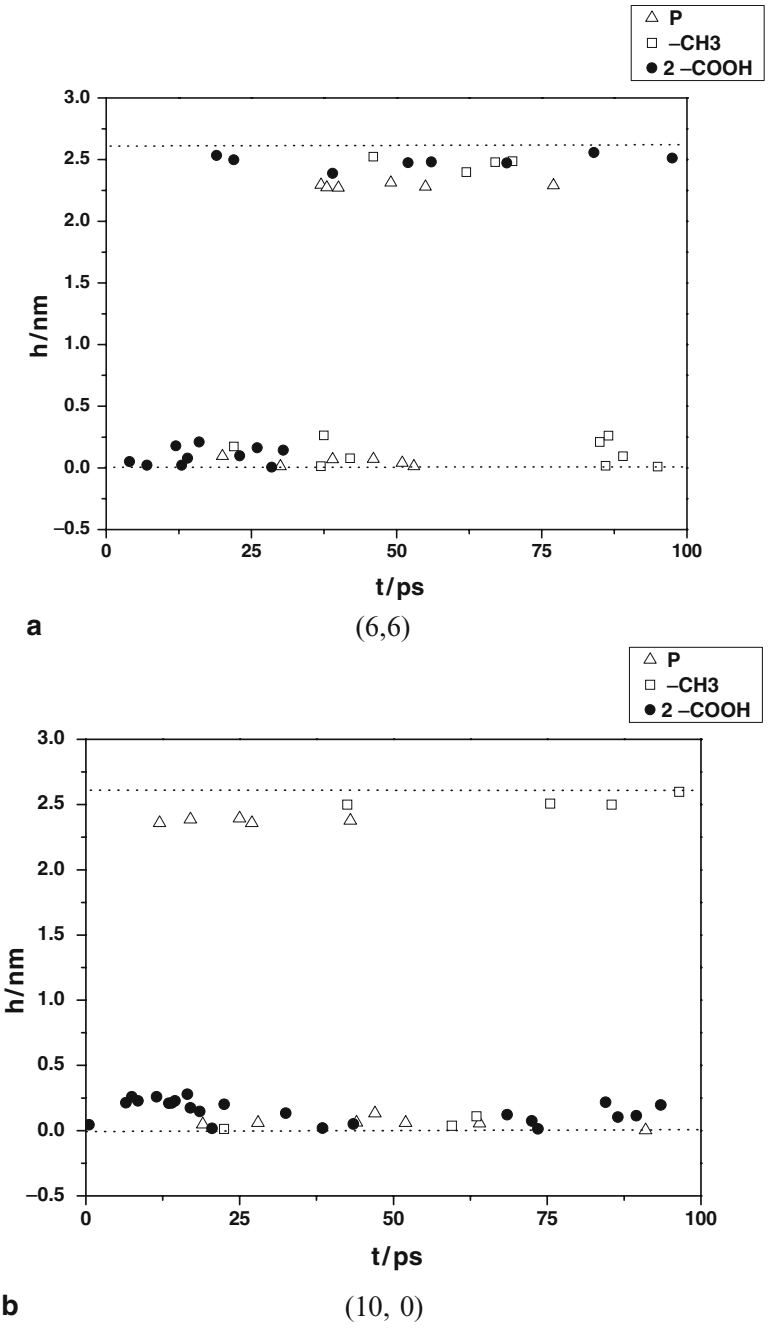

Fig. 5 Position of water molecules when entering different CNTs at 300 K: **a** (6,6), **b** (10,0), **c** (7,7), **d** (12,0). The *P*, $–CH_3$, –COOH and *2–COOH* stand for the pristine CNT, CNTs functionalized by $–CH_3$ groups at one end, –COOH groups at one end, and –COOH groups at both ends, respectively. The CNT is along the *h*-axis and the positions $h = 0.0$ and $h = 2.5$ correspond to the two ends of the CNTs. If the CNT is functionalized at one end, that end is placed at $h = 0.0$

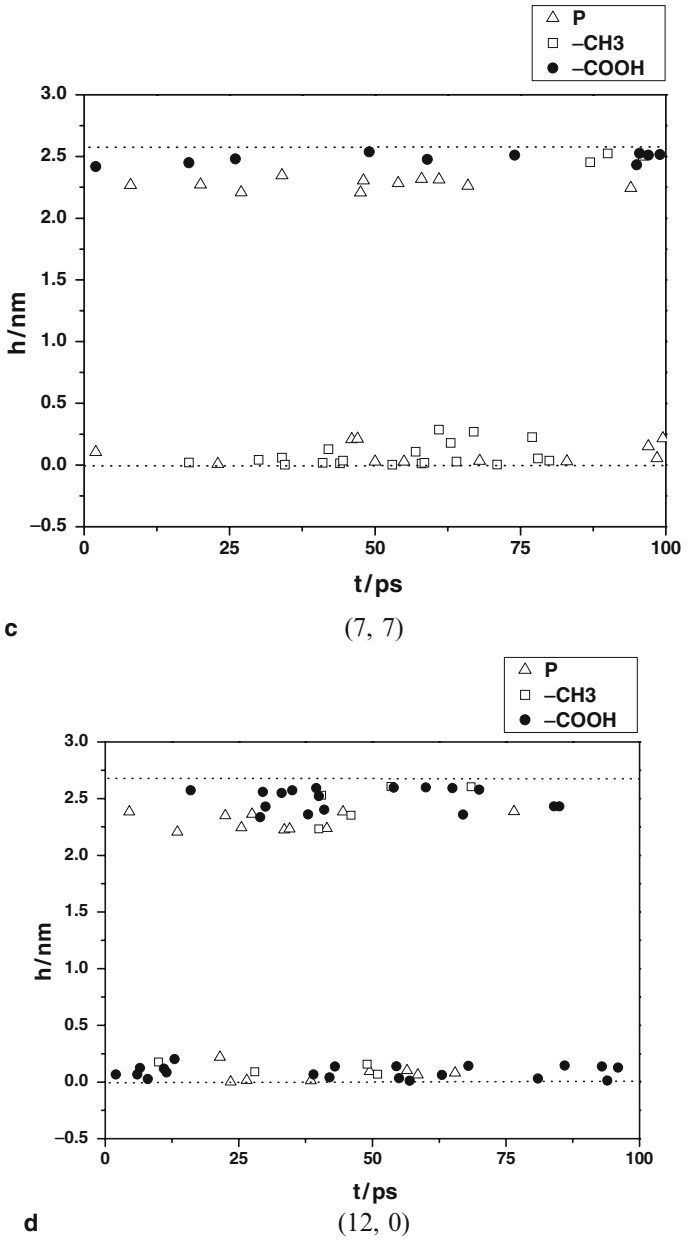

Fig. 5 (*Continued*)

Briefly, MD simulations have been performed to investigate the structural characteristics of water molecules confined in open end functionalized CNTs. The hydrophilic –COOH group and the hydrophobic $–CH_3$ group are chosen as the functional groups. Four carbon nanotubes, armchair type (6,6), (7,7) and zigzag

type (10,0), (12,0), representing different helicites and different diameters, are chosen and functionalized. Two styles of functionalizations have been tested. One is the symmetrical functionalization to one end of the CNT, and the other is where both ends are symmetrically modified.

The incurvature configurations of –COOH groups of (7,7) CNT block off all water molecules at that modified end, whereas the as-functionalized (12,0) CNT, with similar diameter to (7,7) CNT, enables the coexistence of the excurvature and incurvature configurations of –COOH, and therefore allows water molecules to enter from the modified end. As far as the (6,6) and (10,0) CNTs are concerned, they are functionalized by the –COOH groups at both ends. The excurvature configurations for all four –COOH groups of (6,6) CNT are responsible for the behavior

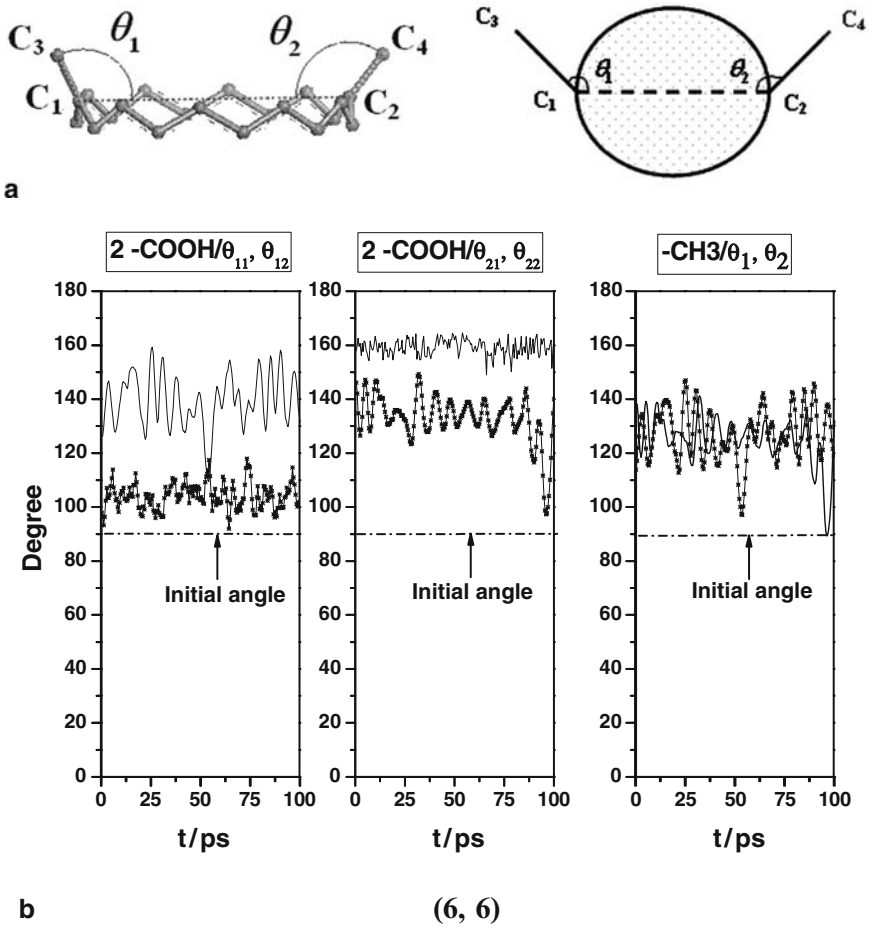

Fig. 6 Definition (**a**) and distribution (**b**) of angles θ_1 and θ_2 for four different CNTs. The angles reflect the position fluctuation of functional groups of CNTs at 300 K. The *label* above each picture, for example $-CH_3/\theta_1, \theta_2$, denotes the functional groups and the two angles at that end

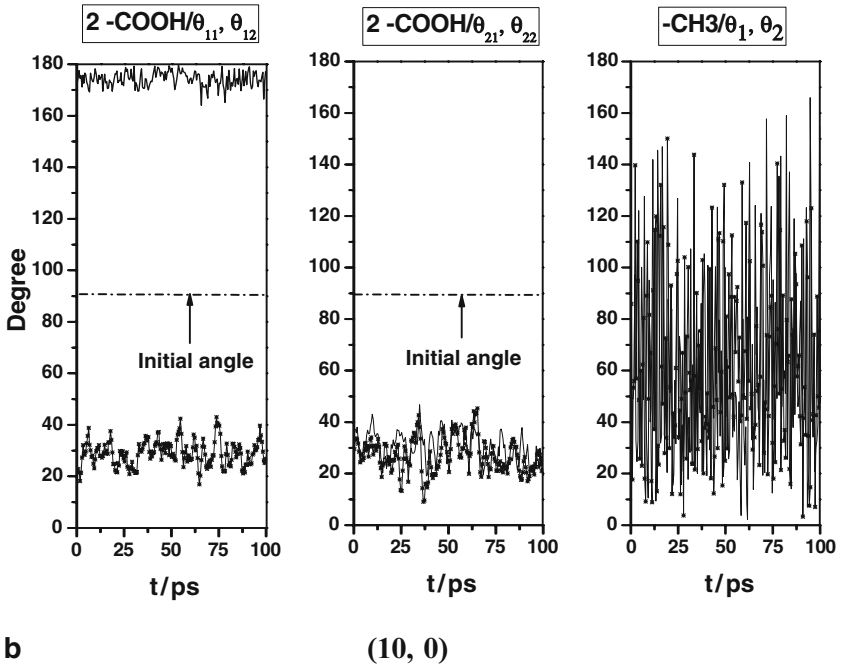

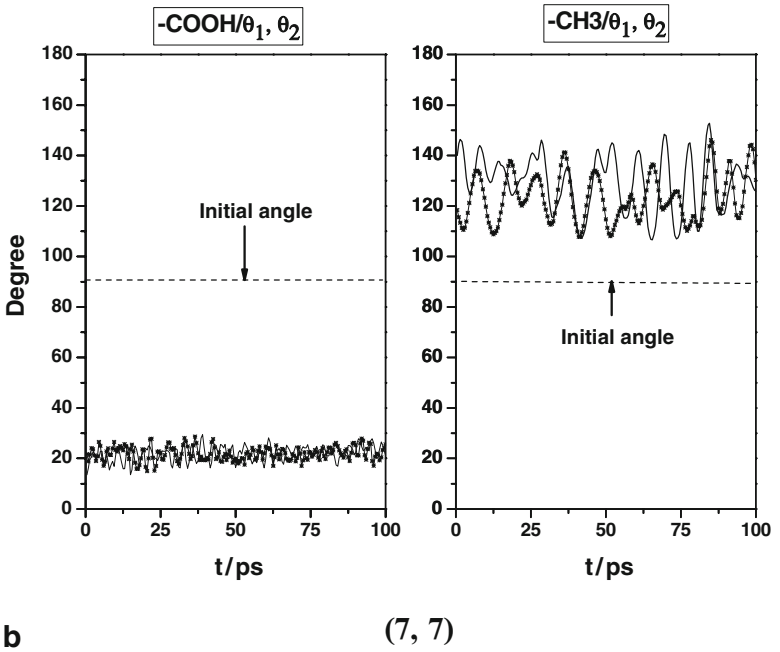

Fig. 6 (*Continued*)

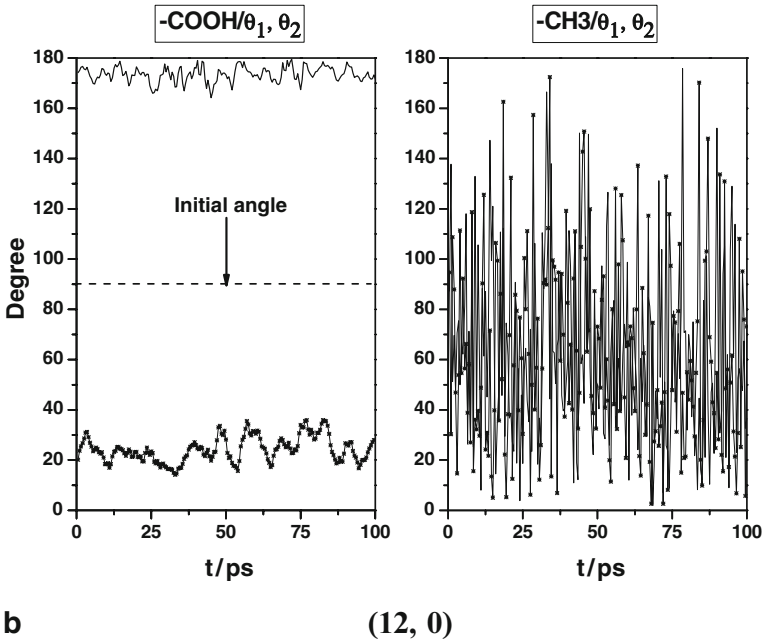

Fig. 6 (*Continued*)

differences of water molecules, compared with the water molecules confined in the as-functionalized (10,0) CNT. Of the four functional –COOH groups of (10,0) CNT, only one group takes the excurvature configuration, and the incurvature configurations of the two –COOH groups on the other end block off water molecules. Since there are no distinct differences between (6,6) and (10,0) CNTs, and between (7,7) and (12,0) CNTs, the phenomena observed is attributed to the helicity effects. The helicity of CNTs determines the fluctuations of the –COOH groups, which in turn brings forth the non-uniform distribution of CNT's electric field and alters the water conduction process. Similar conclusions are also summarized by Zimmerli et al. [35] in their simulation work on the curvature effects of CNTs on the conduction process of water molecules.

2.3 Structure of Ethanol Molecules in Carbon Nanotubes

As ethanol is an important fluid in both chemical and biological fields, the behavior of ethanol molecules in nanopores has a significant impact on many biological and chemical processes. Ethanol can modulate the function of the nicotinic receptor. Ethanol molecules are found to place themselves near the hydrophobic domain of the pore [36] and block the ion flux within the channel, causing many of the well-known effects of alcohol in humans, such as behavior disorder or anesthesia. The modulation function of alcohol on many other ion channels is also suggested

to be related to the behavior of ethanol molecules inside the channel pore [37, 38]. In addition, the behavior of ethanol within the nanopore is important for the production of fuel-grade ethanol [39], where the nanoporous material is applied broadly. However, little is known about the molecular-scale behavior of ethanol within the nanopore experimentally.

Alcohol molecules can form hydrogen bonds, as water molecules do. Moreover, the coexistence of non-polar and polar groups makes the interactions of wall–fluid and fluid–fluid more anisotropic. Jiang and coworkers [40] studied the flow of methanol molecules inside the hydrophobic and hydrophilic pores with non-equilibrium MD simulations. They found that the hydrophilic surface would inevitably change to a "hydrophobic" surface due to wetting by methanol, which has both hydrophobic methyl and hydrophilic hydroxyl groups. Morineau and coworkers studied methanol molecules confined in silica nanopores with neutron scattering analysis [41] and MD simulations [42]. Their results indicated that the hydrogen-bonding interactions of methanol with the surface would have significant influence on the local structure of methanol molecules since there is a non-polar group on the other side of a methanol molecule. The melting and freezing behavior of methanol inside carbon nanopores was also studied [43]. It was found that its melting point is very sensitive to the wall–fluid interaction.

As for ethanol, its steric structure is more complex than that of methanol because one ethanol molecule is made up of methyl, methylene, and hydroxyl groups, while one methanol molecule has only methyl and hydroxyl groups. Kaneko and coworkers [44, 45] studied the structure of methanol and ethanol confined in carbon nanopores with in situ X-ray diffraction. They found that, although both molecules could form ordered structures within the nanopore, only ethanol had a remarkable preferred orientation. Several molecular simulation studies have been carried out with confined ethanol molecules, including ethanol within lipid bilayers [46, 47], and ethanol/water mixtures in polymeric membranes [48] and zeolites [49], to gain more insight into the performance of ethanol in nanoporous materials.

However, the dependence of the structural properties of confined ethanol on pore diameter is not yet well elucidated. Theoretical studies have found that structural properties of confined molecules vary considerably with pore diameter, which in turn have significant impact on their transport [50] and phase transition [2]. As an anisotropic molecule, the hydrophobic part and hydrophilic part of ethanol molecule may behave differently in confinement, or alter their behaviors differently with the variation of confinement, which would induce some characteristic structure of confined ethanol molecules. Therefore, we performed MD simulations to investigate the structural properties of ethanol molecules inside a single-walled armchair CNT of 0.68–1.35 nm to investigate the size-dependence.

2.3.1 Number of Hydrogen Bonds of Ethanol Molecules in CNTs

The effect of confinement on the hydrogen bonding behavior of ethanol molecules was investigated in terms of the average number of hydrogen bonds $<n_{\mathrm{HB}}>$.

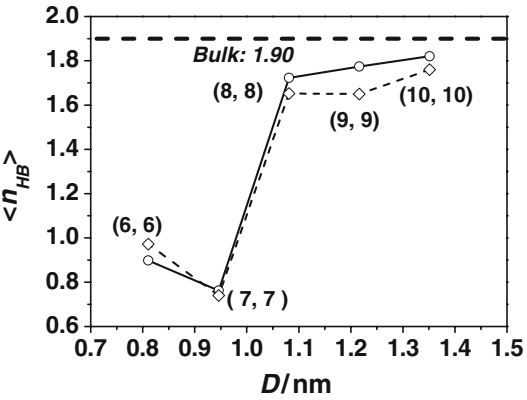

Fig. 7 Average number of hydrogen bonds $<n_{HB}>$ of confined ethanol molecules as a function of tube diameter D: ◯ united-atom model; ♢ all-atom model

A hydrogen bond is determined by a geometric criterion proposed by Luzar et al. [34]. Using this criterion, $<n_{HB}>$ of the bulk ethanol is 1.9 by the united-atom model and 1.87 by the all-atom model, a little larger than the simulation result (1.8) of Jorgensen et al. [51], who used both energy and geometric criteria. However, these differences should not affect the variation of $<n_{HB}>$ with the diameter D, which is the concern here.

Figure 7 shows $<n_{HB}>$ of ethanol molecules within various CNTs. We observed that corresponding results obtained from simulations with united-atom and all-atom models are quantitatively consistent. It was found that $<n_{HB}>$ of ethanol molecules within (8,8), (9,9), and (10,10) CNTs are quite similar, in spite of the increase in diameter. In their MD simulations, Gordillo et al. [21] and Wang et al. [33] found that water molecules confined in CNTs with diameters ranging from 1.0 to 1.5 nm would also have their $<n_{HB}>$ at around 2.4–2.6, nearly 1.0 less than the bulk counterpart. However, $<n_{HB}>$ of confined ethanol molecules within these CNTs was found to be bulk-like. The confinement effect of CNTs with diameters larger than 1.0 nm is small compared to the $<n_{HB}>$ of ethanol. This might be due to the different spatial requirement of hydrogen bond formation of the water and ethanol molecules. The hydrogen bonds of ethanol molecules do not have the complex tetrahedron structure that water molecules have. Consequently, the spatial requirement to form bulk-like hydrogen bonds is less than that of water molecules, which in turn makes the confinement effect of CNTs with diameters larger than 1.0 nm slight. However, the confinement of CNTs with diameters less than 1.0 nm has an obvious effect on $<n_{HB}>$ of ethanol, like that for water molecules [21, 33]. From Fig. 7, we find that $<n_{HB}>$ of ethanol molecules within the (6,6) and (7,7) CNTs is around 1.0, indicating that only 50% of the hydrogen bonds of ethanol molecules could be maintained within these two extremely narrow tubes.

2.3.2 Orientation Distributions of Ethanol Molecules in CNTs

The preferred dipole orientation of molecules could have a fundamental influence on the function of the pore [52]. As mentioned, ethanol is an intermediate polar molecule with both non-polar and polar groups. To better understand the orientation of ethanol molecules within CNTs, we define three angles: α, β, and θ between the non-polar part (CH_3–CH_2), polar part (O–H), and between the dipole moment of the ethanol molecule and the positive direction of the z axis (tube axial direction). Figure 8 defines these three angles.

Figure 9a,b show the distributions of cos α within various CNTs, gained with the all-atom and united-atom models, whereas those of cos β are shown in Fig. 9c,d. Values of 1 and -1 mean that the bond aligns along the axial direction, whereas zero indicates that the bond would align along the radial direction of the nanotube. In general, the results of united-atom and all-atom models agree with each other quantitatively.

We find that the orientation distributions of non-polar and polar parts behave differently with varying CNT diameter. As for the non-polar parts, the most concentrated distribution of cos α is found within the narrowest (6,6) CNT, with two peaks around -1 and 1, indicating that the CH_3–CH_2 bond prefers to align along the axial direction, as shown in Fig. 9a,b. With the increase in diameter, orientation of the CH_3–CH_2 bond in any direction becomes possible and the distribution becomes even. This monotonic tendency with diameter implies that the orientation of the non-polar parts of ethanol may be determined by the effect of the nanotube wall.

As for O–H bonds, interestingly, the distribution of cos β is found to be most concentrated within the (8,8) CNT instead of within the narrowest (6,6) CNT in which ethanol molecules could be confined, as shown in Fig. 9c,d. Within the (8,8) CNT, peaks are found around -1 (united-atom model) or 1 (all-atom model), indicating that O–H bonds prefer to align along the axial direction. The opposite preferred orientation predicted by the united-atom model and all-atom model may be because the

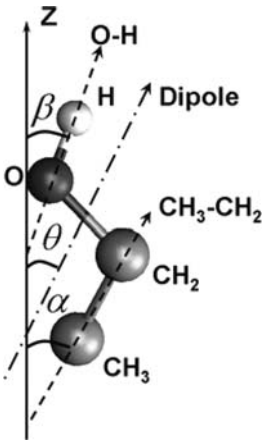

Fig. 8 Definitions of α, β, and θ. Hydrogen atoms of the methyl and methylene groups are not shown for clarity

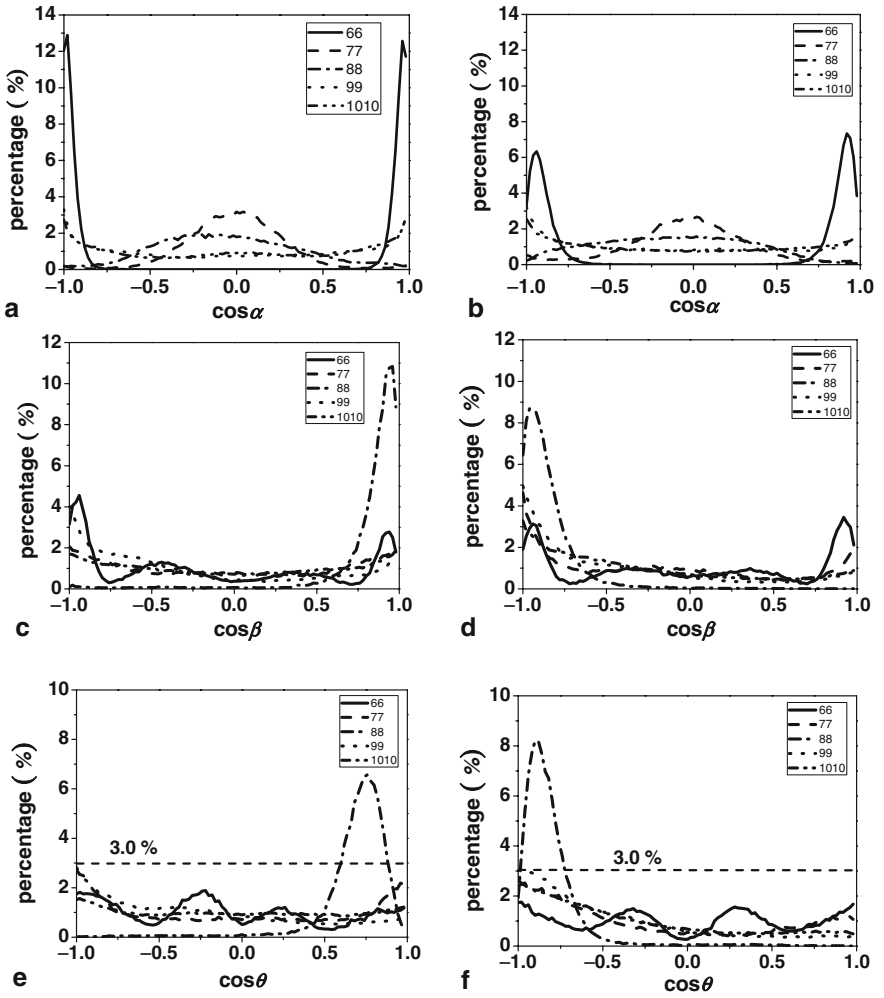

Fig. 9 Distributions of cos α, cos β, and cos θ within various CNTs. **a** cos α (all-atom model); **b** cos α (united-atom model); **c** cos β(all-atom model); **d** cos β (united-atom model); **e** cos θ (all-atom model) and **f** cos θ (united-atom model). The peak around -1 or 1 indicates that bonds prefer to align along the axial direction of the tube, whereas the peak around zero means that bonds prefer to align along the radial direction of the tube

CNT is uncapped at both terminals and the ethanol molecules could enter the pore of the CNT from either side equally. We might expect that with an extremely long MD run, both the peaks at -1 and 1 should appear and be similar for either model. Similar behavior has been reported for the dipole of water inside CNT. The dipole of water molecules inside the (6,6) CNT has been reported by Vaitheeswaran et al. [53] to have two preferred orientations, either pointing "up" or "down" along the tube axial using the grand canonical Monte Carlo (GCMC) simulation. In contrast, Wang

et al. [33] and Huang et al. [32] observed only one preferred orientation for water in the (6,6) CNT with MD simulations of less than 600 ps. In addition, the single peak indicates that the reorientation of O–H bonds may be extremely rare within the (8,8) CNT. Though peaks around -1 or 1 could be found within other tubes, their peak heights are much lower, meaning that the orientation of O–H bonds within other CNTs of this work is much more random than that within the (8,8) CNT. The wider distribution also implies that the reorientation of O–H bonds within other CNTs is easier than that in the (8,8) CNT.

Fluid–fluid interactions may play an important role in such non-monotonic behavior. In general, the confinement effect by CNT decreases with the increase of diameter. However, it is more complicated for the effect of fluid–fluid interactions. As discussed, for ethanol molecules, $<n_{\mathrm{HB}}>$ is bulk-like within (8,8), (9,9), and (10,10) CNTs. Then, the constraint on hydroxyl groups from fluid–fluid interactions within these three tubes are stronger than those within (6,6) and (7,7) CNTs where $<n_{\mathrm{HB}}>$ is only half of the bulk value. The two major constraint effects on the orientation of O–H bonds might have a different or even reverse tendency with the increase of diameter, which causes the synergistic effect to vary non-monotonically. Though the size of (8,8) CNT is moderate, the synergistic constraint effect within it might be the strongest, causing the most concentrated orientation. Mashl et al. [54] found similar phenomena for water molecules inside CNTs. Their MD simulation showed that water molecules inside a (9,9) CNT have more ordered structure than those inside other tubes. The fluid–fluid interactions are also found to be critical for this characteristic.

Consequently, the dipole orientation of ethanol molecules within CNTs is extremely sensitive to the diameter. Figure 9e,f show the distributions of $\cos\theta$ in various CNTs with simulation results using all-atom and united-atom models, respectively. As for the results of individual bonds, orientation distributions of dipole moments gained from different models quantitatively agree with each other. We observed that $\cos\theta$ has high preferred distribution with a peak around -1 or 1 within the (8,8) CNT, whereas those in other tubes distribute more evenly from -1 to 1. This means that the dipole orientation would be highly preferred within the (8,8) CNT, whose effective internal diameter is 0.731 nm. This confirms the conclusion of Kaneko et al. [44, 45], gained from X-ray measurement, that ethanol molecules should have high preferred orientation within a carbon nanopore of around 0.7 nm. Interestingly, the high preferred dipole orientation of ethanol is observed only within the (8,8) CNT (whose diameter is moderate among the tubes in this study), which is quite different from the observation from molecular simulations that the high preferred dipole orientation of water could be found within any CNT with diameter less than 0.811 nm [33]. A slight variation in tube diameter, either increase or decrease, could result in the dipole orientation of ethanol molecules altering from highly preferred to random. The opposite preferred dipole orientation of the all-atom model and the united-atom model should also be due to the O–H bonds, as discussed above.

2.4 Competition Adsorption of CO_2/Methane in CNT

Grand canonical Monte Carlo simulations were performed to investigate the adsorption behavior of an equimolar CO_2/CH_4 mixture in CNTs with diameters varying from 0.678 to 1.356 nm. Seven temperatures (283, 293, 303, 313, 323, 333, 343 K) and seven pressures (1, 5, 10, 15, 20, 25, 30 MPa) were chosen to investigate the effect of temperature and pressure on the adsorption behavior. Simulation results showed that CO_2 is preferentially adsorbed over CH_4 in CNTs. The adsorption amount of CO_2 is generally an increasing function of the diameter of the CNT, from 4 mol kg^{-1} in (6,6), (7,7), and (8,8) CNTs to 9 mol kg^{-1} in (9,9) and (10,10) CNTs. While on the other hand, the adsorption amounts of CH_4 remain at a relatively low value below 1 mol kg^{-1} in all CNTs investigated. Furthermore, in the investigated temperature and pressure ranges, the variations of temperature and pressure have little effect on the adsorption amounts in the (6,6), (7,7), and (8,8) CNTs, whose diameters are less than 1.1 nm. Whereas the adsorption amounts in (9,9) and (10,10) CNTs increase when the temperature decreases or the pressure increases. As far as the selectivity is concerned, the CNTs demonstrate themselves to be a better choice for the separation of CO_2 and CH_4 molecules. Despite changing the temperature, pressure, or CNT diameter, the selectivity is generally above 8. At 343 K and 1 MPa, the selectivity reaches 11.2 in (6,6) CNT. Additionally, the selectivity in narrow (6,6) and (7,7) CNTs fluctuates fiercely with pressure and temperature, but remains hardly affected in the CNTs with diameters greater than 1 nm. Last, but not least, the volume capacity, which could reflect the CO_2 storage capacity and the utility of the CNTs, is found to respond differently to temperature and pressure. The smaller (6,6), (7,7), and (8,8) CNTs are inert to such changes, whereas the volume capacity for larger (9,9) and (10,10) CNTs are in a decreasing function of temperature but an increasing function of pressure. The results in this work may not only strengthen our understanding of the molecular behavior under microscale confinement but also provide useful information on designing new materials for CO_2 storage/separation and CH_4 enhancing industry.

3 Thermodynamic Properties of Aqueous Electrolyte Solutions at High Temperature and High Pressure

Hydrothermal processes are a powerful method for preparing advance inorganic material such as nanoparticles and low-dimensional material. This method has the advantages of fast reaction velocity, high productivity, and near-zero pollution. The core of this method is to control the structure and functions of the products with considerable changes in the properties of water and electrolyte solutions with temperature, pressure, and concentration. Therefore, the key to fulfilling the controllable preparation of the advanced material is to understand the relationship between the properties of the electrolyte solutions and the real process parameters. However, it is very challenging for current thermodynamic experiments and models

to describe the whole process quantitatively because it usually happens at high temperatures and pressures.

We will first look at the hydration and association of ions with MD simulations. A new term "hydration factor" is proposed for quantitatively characterizing the strength of ionic hydration [55]. We also find two association forms of the alkali metal and haloid ions: the direct contact ion pair and the form separated by a layer of solvent [56]. The association of ions becomes stronger at supercritical conditions. This is the basis of the thermodynamic theory for electrolyte solutions at high concentration and supercritical conditions. Furthermore, we investigated the change in the competition of the hydration and association with temperature and pressure using quantum calculation, and developed a relationship between the hydration free energy and the pressure and temperature [57]. The results show that electrolyte solutions go through three stages with an increase of temperature: hydration control stage, hydration–association competition stage, and association control stage.

3.1 Hydration Factor

Because of electrostatic interactions between ions and water molecules, the water molecules around an ion will exhibit a certain orientation distribution. The overall coordination behavior of water molecules around an ion can be experimentally determined by X-ray and neutron diffraction, etc. [58, 59], while the orientation behavior of those water molecules is difficult to probe experimentally. However, it can be obtained easily by simulation. A new orientation distribution function is proposed for characterizing the orientation structure of water molecules around an ion. It is defined as the distribution probability of orientation angle between ion and water molecule. The orientation angle is illustrated in Fig. 10. The orientation distribution functions of five ions (Li^+, Na^+, K^+, F^-, and Cl^-) are shown in Fig. 11. For cations, the orientation of Li^+ is strongest, Na^+ takes a second place, and K^+ takes a third place. The cosine values of their orientation angle present a maximum at -1, which indicates that the water molecules around a cation approach the cation with the oxygen atom. For anions, the distribution of F^- is narrower than that of Cl^-. They all show peak values at cosine 0.58 (about half of the bond angle of HOH). This indicates that the water molecules around an anion approach the anion with the hydrogen atom.

Two snapshots of microscopic configurations of Li^+, F^-, and their surrounding water molecules obtained by computer molecular graphics are shown in Fig. 12. The central dark sphere represents an ion, while the surrounding dark spheres are oxygen atoms and the light spheres are hydrogen atoms. The illustration of microscopic configurations of solutions also clearly verifies the hydration structures. For Li^+, it is obvious that water molecules in the first coordination shell have strong hydration. In this work, the orientation behavior of water molecules in the second coordination shell is also analyzed. From Fig. 11, it could be found that the water molecules in the second coordination shell are distributed almost with equal probability. This means

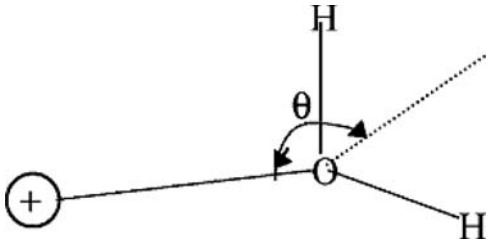

Fig. 10 Definition of orientation angle of a water molecule

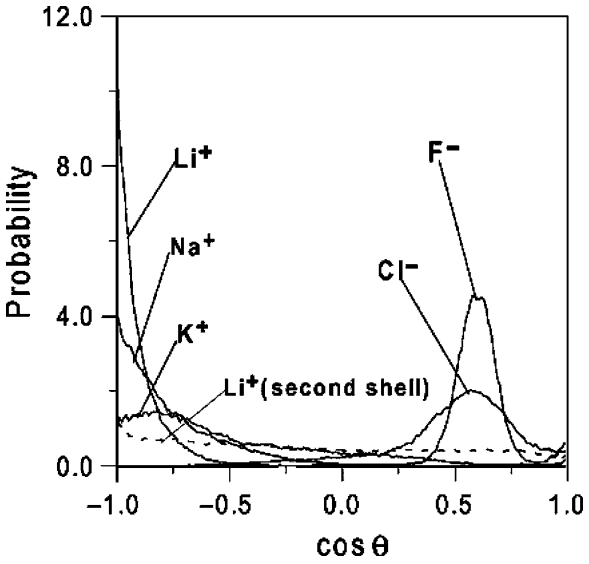

Fig. 11 Orientation distribution functions of five ions (Li^+, Na^+, K^+, F^-, and Cl^-)

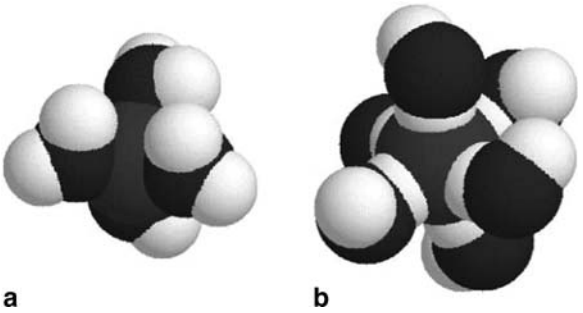

Fig. 12 Microscopic configurations of water molecules around Li^+ (**a**) and F^- (**b**)

that those water molecules are just coordinated around the ion, while no hydration occurs. This discovery clarifies the guess about the second hydration shell of Li^+. Historically, the hydration number of an ion is usually confused with the coordination number of the ion because of the difficulty in differentiating them quantitatively. Considering the orientation distribution of water molecules around an ion, we think that not all water molecules in the first coordination shell are hydrated, but only those in a certain orientation distribution range.

A new term, hydration factor, is proposed. The hydration factor of a cation is defined as the ratio of the number of water molecules whose value of orientation cosine is less than -0.71 to the total number of water molecules in the first coordination shell, which corresponds a 135° hydration angle. The criterion of the orientation cosine being less than -0.71 is based on the distribution probability of the orientation cosine of water molecules around Li^+ being larger than the probability of all the water molecules in the first coordination shell having an equal probability. The hydration factor of an anion is defined as the ratio of the number of water molecules whose value of orientation cosine is larger than 0.43 and smaller than 0.76 to the total number of water molecules in the first coordination shell, which corresponds a $40-65°$ hydration angle. The criterion of orientation cosine being larger than 0.43 and less than 0.76 is based on the distribution probability of the orientation cosine of water molecules around F^- being larger than the probability of all the water molecules in the first coordination shell having an equal probability. The hydration factors of the five ions are listed in Table 3. The hydration factor could represent the strength of ionic hydration. For both cations and anions, the hydration interaction becomes weaker with the increase of ionic radius. In this work, hydration number is defined as the product of coordination number and hydration factor. The values of the hydration number of the five ions are also listed in Table 3.

It is shown in Table 3 that with the increase in ionic radius, the hydration number decreases. For anions, their hydration number is not small. Since the water molecules around an anion approach the anion with the hydrogen atom, the repulsion interaction among the water molecules is relatively small and the radius of an anion is relatively large, so there may be more water molecules hydrated around the anion. When constructing a thermodynamic model for electrolyte solutions, we should account for the hydration of cation and anion simultaneously.

In summary, the hydration of five ions (Li^+, Na^+, K^+ F^-, and Cl^-) in infinite dilute aqueous solutions is investigated by MD simulations at 298 K. Clear microscopic configurations of ions in aqueous solutions are obtained. Cations are

Table 3 Coordination numbers, hydration factors, and hydration numbers of five ions

Ion	Effective radius (10^{-10} m)	Coordination number	Hydration factor	Hydration number
Li^+	0.59	4.4	0.95	4.16
Na^+	0.99	5.2	0.69	3.61
K^+	1.48	6.1	0.40	2.46
F^-	1.28	6.2	0.90	5.60
Cl^-	1.98	6.5	0.57	3.69

surrounded by water molecules with oxygen atoms approaching them, while anions are surrounded by water molecules with hydrogen atoms approaching them. A new hydration factor is proposed to quantitatively characterize the strength of ionic hydration. The order of hydration strength for cations is $Li^+ > Na^+ > K^+$, whereas, for anions $F^- > Cl^-$. For Li^+, although there is a second coordination shell, no second hydration shell exists. This is valuable information for further establishment of molecular thermodynamic models for electrolyte solutions. The Pauling radius of an ion is the most important factor that determines the strength of hydration. When constructing a corresponding molecular thermodynamic model for electrolyte solutions, parameters related to ionic radii should be preferred.

The electrostatic interaction between charged particle and water molecule is the essential reason for the hydration structure. For a cation and an anion with a same radius, the anion has stronger hydration ability. However, since the radius of a real anion is not small, its hydration ability appears somewhat weak.

3.2 Hydration Free Energy

In this section, quantum chemistry calculations have been carried out on $CaCl_2$ and $MgCl_2$ solution. The main purpose of this present work is to understand the hydration and association of $MgCl_2$ and $CaCl_2$ solutions at high temperature and pressure. Knowledge of the microstructure will provide theoretical support for the establishment of thermodynamic models. Correlation of the experimental data on $CaCl_2$ solutions is used to examine the model reliability.

To study the hydration and association in $MgCl_2$ and $CaCl_2$ solution at high temperature and pressure, quantum chemistry calculations have been carried out using GAUSSIAN 98 [60]. Before the calculations on hydration and association, the steady state structures of hydrated Mg^{2+} and Ca^{2+} must be determined.

Figure 13 shows the isobaric hydration free energy of Mg^{2+} and Ca^{2+} from 523.15 K to 673.15 K. The hydration free energy can be expressed by:

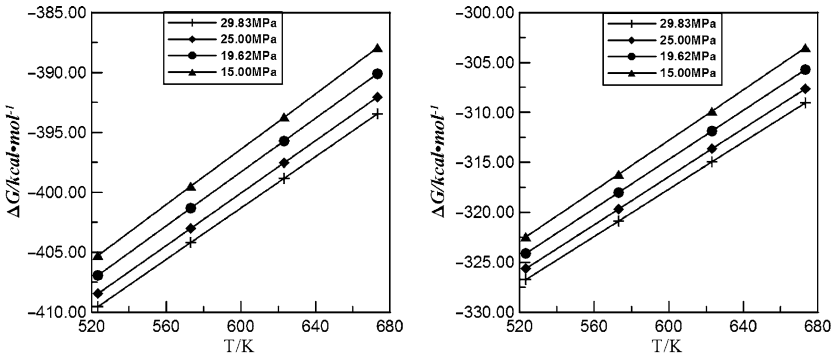

a Hydration free energy of Mg^{2+} **b** Hydration free energy of Ca^{2+}

Fig. 13 Isobaric hydration free energy of Mg^{2+} (**a**) and Ca^{2+} (**b**) at 523.15–673.15 K

Table 4 Regressed parameters for hydration free energy equation[a]

	a	*b*	*c*	*d*	*e*	*f*
Mg	−436.256	−0.081518	−3.28971	−6.03860	−2976.83	0.104774
Ca	−369.164	−0.076810	−3.25600	−6.01838	−1.15248	0.123681

[a]See Eq. 1 in the text. The reliability of regression is 0.99929 for Mg and 0.99962 for Ca. The proportion of variance accounted for is 0.99857 for Mg and 0.99924 for Ca

$$\Delta G_{\text{hydration}} = a + b \cdot P + c/P + d \ln P + e/T + f \cdot T, \tag{1}$$

where, $\Delta G_{\text{hydration}}$ is the hydration free energy, T is temperature, P is pressure, and *a, b, c, d, e,* and f are coefficients. A total of 25 sets of experimental data measured at 298.15 K and 1 bar (ambient conditions) to 673.15 K, 298.3 bar (29.83 MPa) were used for the regression. The regressed parameters are listed in Table 4.

3.3 Equilibrium Constants of Association Reaction

To study the association reaction further, the equilibrium constants have been calculated from the free energy. Figure 14 gives the isobaric equilibrium constants of Eq. 4. Two dashed lines, $K = 10$ and $K = 0.1$, divide Fig. 14 into three regions. In the top region, the equilibrium constant is bigger than 10, and the reaction could proceed almost completely. In this region, association is dominant and hydration could be neglected. In the bottom region, the equilibrium constant is less than 0.1, which means the reverse reaction could proceed completely. In this region, association has almost no influence on the solution. In the middle region, the reaction is at equilibrium. So, the microstructure of the solution is determined by the competition between hydration and association. As shown in Fig. 14, the equilibrium constants of Mg and Ca will stay in different regions, even under the same conditions. It is possible that both hydration and association have great influence on $MgCl_2$ solutions while hydration can be neglected in $CaCl_2$ solutions. In other words, the $MgCl_2$ solution will have hydration and association different from the $CaCl_2$ solution under some specific conditions, which agrees with our previous MD study [56].

3.4 Thermodynamic Model Based on the Microstructure from Quantum Chemistry Calculations

Pitzer and Li [61] have proposed an activity coefficients model for NaCl solution at high temperature and pressure. In this model, both hydration and association are considered. To apply this model to $MgCl_2$ and $CaCl_2$ solution, some modifications have been introduced. The experimental data of $CaCl_2$ solution at high temperature and pressure are used here for the verification.

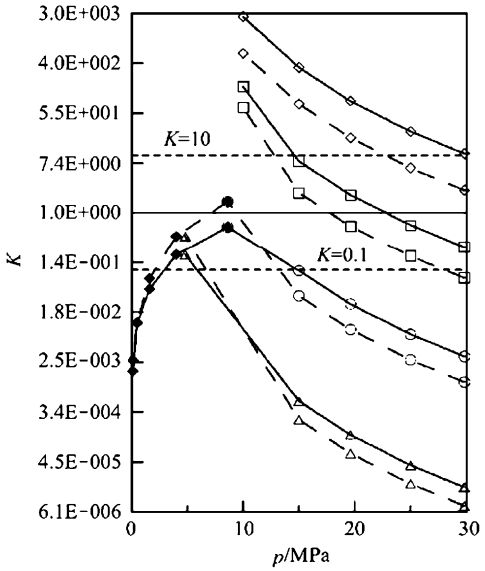

Fig. 14 Equilibrium constants of association reaction: *dashed lines* Mg, *solid lines* Ca; *diamonds* 673.15 K, *squares* 623.15 K, *circles* 573.15 K, *triangles* 523.15 K, *solid diamonds* saturated point of water 373.15–573.15 K

3.4.1 Association Parameters

In $MgCl_2$ and $CaCl_2$ solution, there are two association steps:

$$\begin{aligned} M^{2+} + Cl^- &\rightarrow MCl^+ \\ MCl^+ + Cl^- &\rightarrow MCl_2 \end{aligned} \tag{2}$$

where M = Mg, Ca. To calculate the real compositions of the solution, two equilibrium constants are needed for the two association steps. In this paper, the equilibrium constants of association are calculated using the Helgeson model [62]. When the equilibrium constants are relatively small, the association is neglected according to Fig. 14 and the model is simplified to a full-disassociation form.

3.4.2 Hydration Parameter

In Pitzer and Li's model, there is only one short-range-effect parameter w, which is regressed from experimental data. In this paper, this parameter is interpreted as a hydration parameter. This kind of physical meaning was first given to the hydration parameter by Lu [63]. In Lu's work, the hydration parameter is used to describe the interaction between ion and dipole of the water molecule in solution, and it is linear to $1/T$ when the temperature is less than 373.15 K.

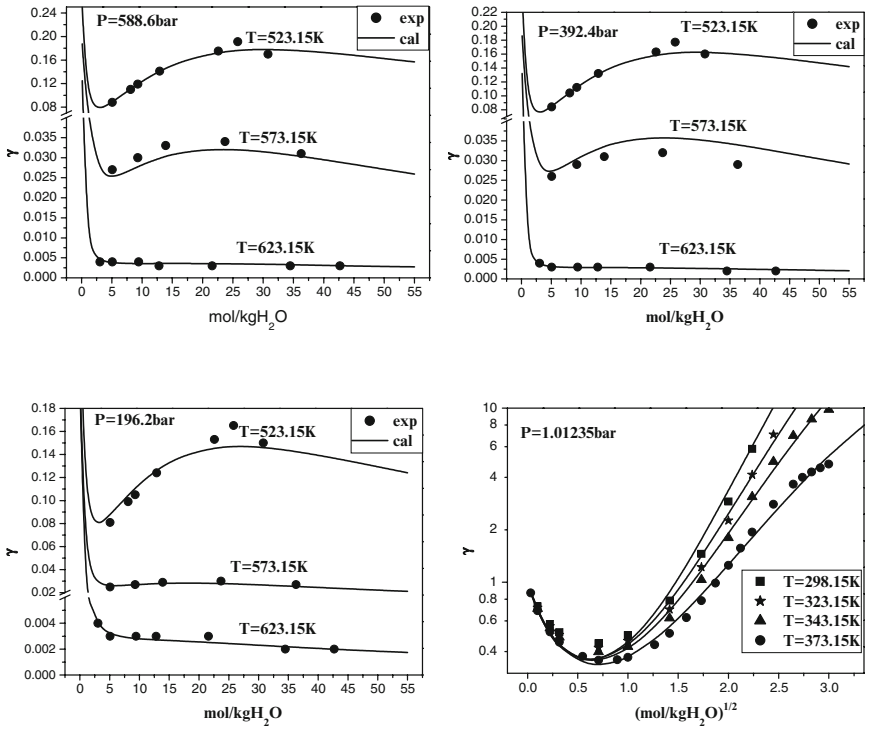

Fig. 15 Calculated activity coefficients and experimental data of $CaCl_2$ solution under different conditions

The hydration parameter w of $CaCl_2$ solution has been regressed. The experimental data are from Valyashko's work [64]. From regressed w, the activity coefficients of $CaCl_2$ solution have been calculated and compared with experimental data. The results are shown in Fig. 15.

It can be seen from Fig.15 that the behaviors of activity coefficients at different temperatures are quite different. Our model, however, is able to describe all kinds of concentration dependence of activity coefficients. And it can be used in a range from ambient condition, 298.15 K, 1 bar to supercritical conditions, 623.15 K, 588.6 bar.

Although Fig. 15 shows 13 sets of experimental data, the experimental data are still rare, and it is hard to obtain the hydration parameter by interpolation. Thus, it is necessary to establish an equation to predict the hydration parameter from temperature and pressure. According to the physical meaning, the temperature and pressure dependence of the hydration parameter must be identical to that of the hydration free energy. As mentioned above, the hydration free energy has a dependency relationship with temperature and pressure, described by Eq. 1. We believe this relationship is applicable to hydration parameter too:

$$w = a + b \cdot P + c/P + d \ln P + e/T + f \cdot T, \tag{3}$$

Table 5 Regressed parameters in hydration parameter equation[a] for $CaCl_2$ solution

a	*b*	*c*	*d*	*e*	*f*
29.70713	0.001295	−6.18841	−1.04814	−9132.27	−0.020032

[a]See Eq. 3 in the text. The reliability of regression is 0.99957, and the proportion of variance accounted for is 0.99814

where *w* is the hydration parameter. Then the 13 hydration parameters at different temperature and pressure are regressed by Eq. 3. The regressed coefficients in Eq. 3 are listed in Table 5. The regression results verify our guess that the hydration parameter does follow the law expressed by Eq. 3, from ambient conditions to supercritical conditions. This is evidence that the model is able to describe the activity coefficients of $CaCl_2$ solution from full hydration to full association using just one expression and one set of parameters.

In conclusion, the equilibrium constant of association is a direct criterion that can be used to describe the hydration and association of solutions simultaneously. It is found from equilibrium constants calculated from quantum chemistry calculations that, as temperature increases, a solution will undergo three states: hydration-dominating state, hydration–association competing state, and association-dominating state. It is necessary to determine in which state a solution is before establishing any thermodynamic model. The equilibrium constants give a clear definition of boundaries for these three states, and make it possible to establish a thermodynamic model. The calculation of hydration free energy also shows how ionic hydration depends on temperature and pressure. This relationship is also feasible for predicting the hydration parameter in thermodynamic models considering hydration effects. With these quantum chemistry calculations, the model from Pitzer and Li for NaCl solution is easily transplanted to $MgCl_2$ and $CaCl_2$ solutions, although there is less experimental data for $MgCl_2$ and $CaCl_2$ solutions than for NaCl solutions. In this work, the short-range-effect parameter is interpreted as a hydration parameter, which has a clear physical meaning for describing the interaction between ions and water molecules, therefore it has the same temperature and pressure dependence as that of the hydration free energy. A prediction function for the hydration parameter has been established and it is possible to obtain the hydration parameter from limited experimental data in a wide temperature range (298.15–673.15 K) and a wide pressure range (1–588.6 bar). This range is also the same for the whole model, since the hydration parameters are from the Helgson model, which could be used up to 1000 K and 5000 bar. We used the experimental data of $CaCl_2$ solution to examine the model reliability. The results show that this modified model can calculate the activity coefficients with a considerable accuracy from 298.15 K, 1 bar, to 673.15, 588.6 bar. This successful application to $CaCl_2$ solution shows that quantum chemistry calculation could provide a strong theoretical foundation for the establishment of thermodynamic models and is very useful for thermodynamic studies under hydrothermal and supercritical conditions.

3.5 Thermodynamics of Alkali Aqueous Solution in Hydrothermal Reaction Vessel

Hydrothermal reaction usually refers to any heterogeneous reaction in the presence of aqueous solvents under high pressure and temperature conditions. In recent years, the hydrothermal process has been widely applied, such as for synthesis of nanomaterials and removal of hazardous materials. Generally, the filling degree of solution in the hydrothermal vessel is an important factor in determining the reaction pressure and thermodynamic properties of solution. For a pure water system, the filling degree corresponding to different equilibrium pressures can be obtained from the pressure–temperature (*PT*) diagram for pure water. However, electrolyte solutions are usually involved in real hydrothermal reactions. For example, NaOH solution of high concentration is often used for hydrothermal synthesis of TiO_2 nanotubes [65]. Thus, the choice of filling degree of electrolyte solution is critical for the hydrothermal reaction performance and the vessel safety.

The hydrothermal reaction can be described as "any heterogenous chemical reaction in the presence of a solvent (whether aqueous or non-aqueous) above room temperature and at pressure greater than 1 atm in a closed system" [66]. That is to say, the total volume and mass of all phases (vapor and liquid, the volume of solid is omitted) is constant. Thus, we can combine the mass balance with phase equilibria to get the pressure and concentration of the liquid when the system reaches equilibrium at a given temperature. The filling degree model of pure water in hydrothermal conditions has been reported [61]. In this work, the filling degree model for aqueous alkali solutions was given by solving the material balance and phase equilibrium equations simultaneously. The general outline of the calculation process is shown in Fig. 16.

3.5.1 Pressure–Temperature Diagram

The filling of mineralizer solution is a very important factor for the pressure prevailing under working conditions in the vessel. However, the diagram we generally get is of pure water (Fig. 17) [67] . It seems to be the only criterion to determine the fill factor and the pressure in the reactor. However, for mineralizer solution, this can just be a reference. In any case, the vapor pressure of the mineralizer will be less than that of water since it contains dissolved electrolyte. This can be easily identified in Fig. 18a. We chose fillings of 10–90% for calculation. The pressure of pure water is much higher than that of NaOH solution. An enlargement of the region 50–250°C and 0–40 bar, can be seen in Fig. 18b It is clear that there are two types of lines for each concentration: a smooth curve and gradient beeline. The former is the equilibrium line of vapor and liquid, the latter indicates that all volume is occupied by liquid. With the degree of fill less than 90% (10–80%), the points of each concentration are dropped almost on one line of their own. Obviously, the pressure on the beeline increases much more rapidly with temperature than that on

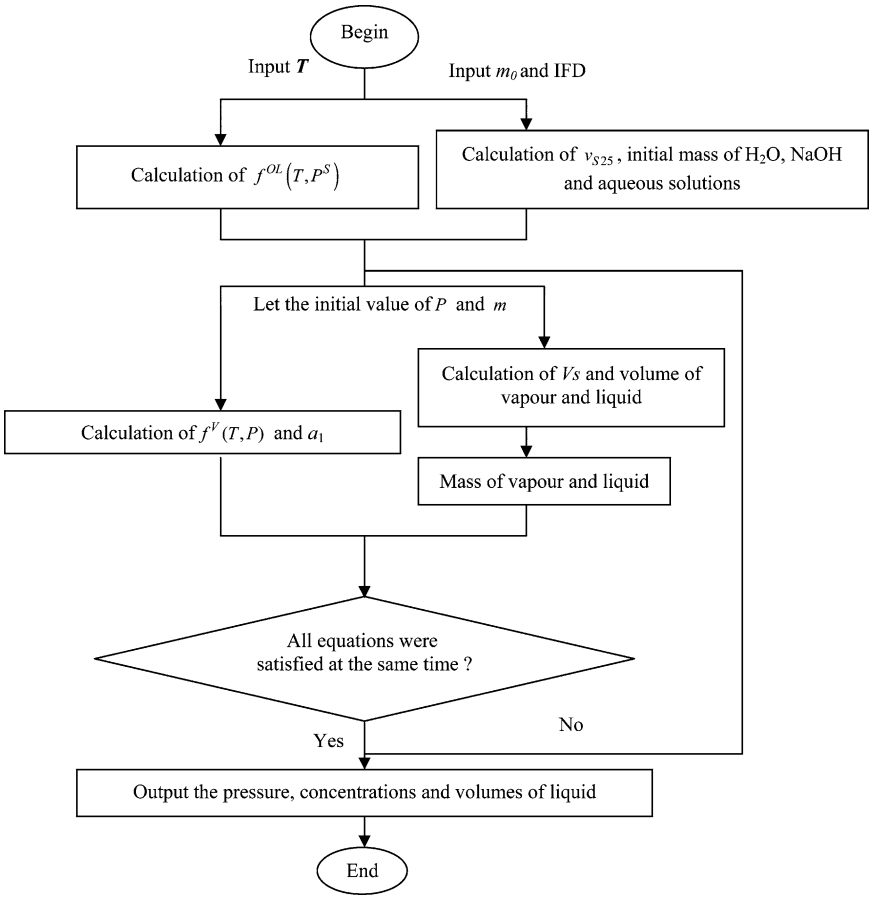

Fig. 16 General outline of calculation process

the co-existive curve. That is to say, if an autoclave is filled to 80% of its free volume (for an isothermal vessel), as the temperature is raised to 250°C the pressure will not go higher than 40 bar. But, when the initial filling is 90%, 1367 bar (our calculated data) can be reached.

3.5.2 Volume of Liquid

With the pressure at equilibrium, the volume of liquid can be calculated. Figure 19 shows the percent of vessel volume occupied by liquid and vapor for various initial % fills for H_2O, 5 M NaOH, and 10 M NaOH. It shows that there is obvious volume variation above 150°C. For pure water, with a fill degree of 90%, vapor disappears near 160°C. That is to say, the vessel is full of liquid above this temperature. Since the compressibility of liquid is very small (almost zero), the pressure

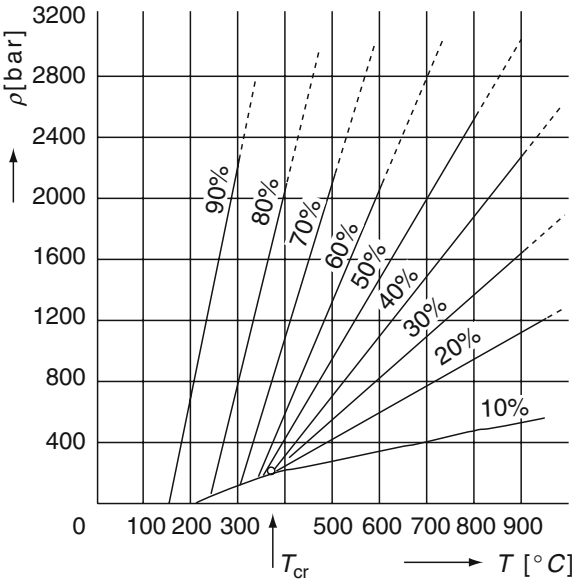

Fig. 17 Pressure–temperature diagram of pure water

increases rapidly with the temperature (Fig. 18). For hydrothermal reactions, this will be a great challenge to the endurance of the autoclave material. However, when it comes to the mineralizer solution, higher temperatures are needed. For 5 M NaOH solution, the point is about 180°C. For 10 M NaOH solution, 205°C may be needed.

3.5.3 Concentration of OH^-

The study on the mechanism of hydrothermal reactions shows that the concentrations of OH^- may not only affect the solubility of solute and the growth rate of the crystals, but also change the structures of the growth group in the solutions. The pH can determine the structure, morphology, size of crystal, and the temperature at which crystallization starts. For example, as shown in Fig. 20 [68], when the titanium oxide layers are immersed in a basic solution, the dangling bonds on the surface of the titanium oxide react with the hydroxide ions, making the sheet of titanium oxide curl. The curliness of the sheet of titanium oxide increases with the number of hydroxide ions. If the concentration of the base solution is low, flower-like titanium oxide powders are formed. As the concentration of hydroxide increases, titanium oxide nanotubes are obtained.

Generally, electrolytes are considered to be fully ionized in water. However, many strong electrolytes such as NaOH and KOH are not fully ionized in water.

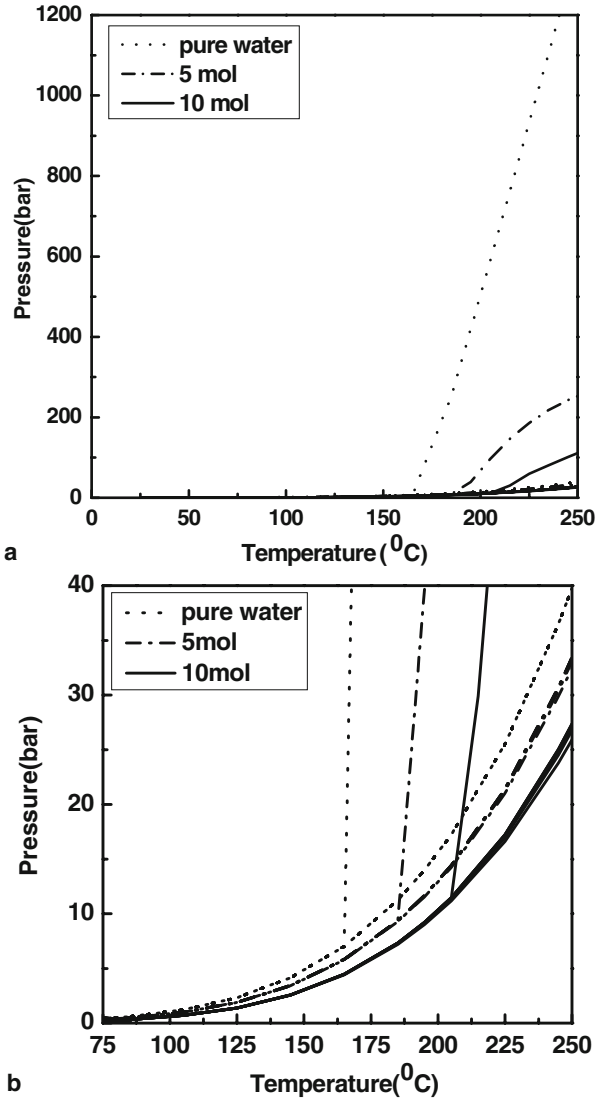

Fig. 18 Pressure–temperature diagram of NaOH solution at **a** 0–1200 bar, 0–250°C and **b** 0–40 bar, 75–250°C

The degree of association for ions is large, especially when the strong electrolytes are in hydrothermal reaction at high temperatures.

Figure 21 presents the relationship between the real concentration of hydroxyl ($[OH^-]$) and the solution temperature under the circumstances of different initial degrees of filling. The two solid curves in Fig. 21a represent the real $[OH^-]$

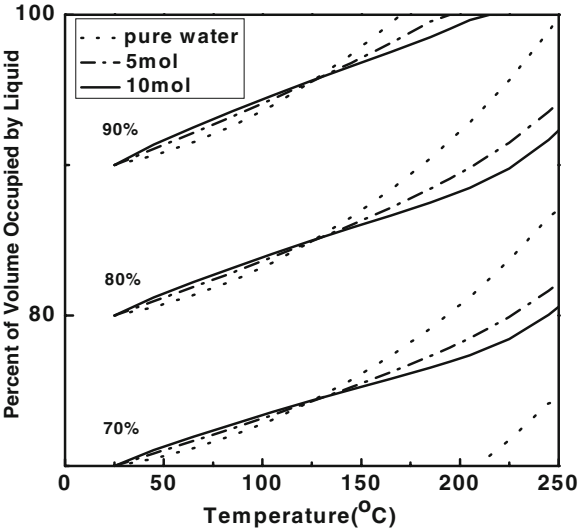

Fig. 19 Percent of autoclave volume occupied by liquid and gas for various initial % fills for NaOH solution

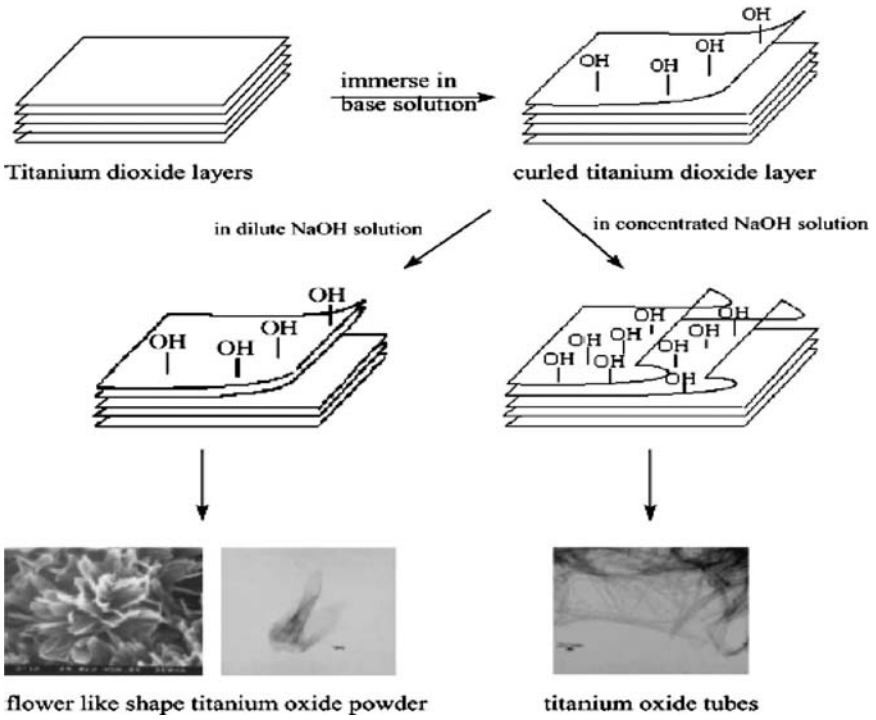

Fig. 20 Effect of NaOH concentration on reaction mechanism

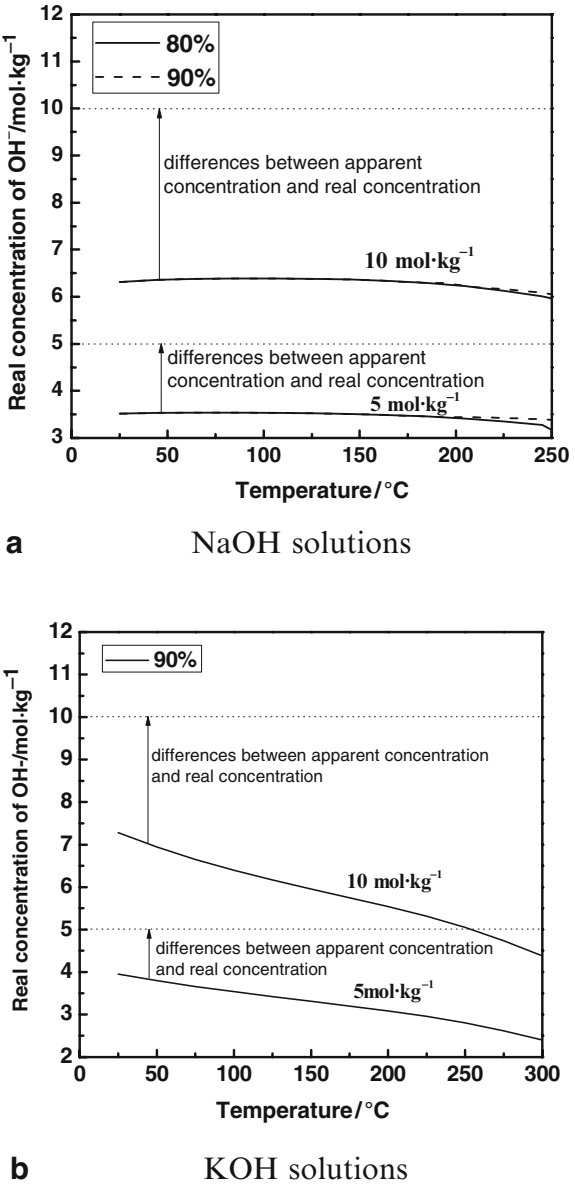

Fig. 21 Real concentration of OH^- at various temperatures in solution

of two different NaOH aqueous solutions with apparent concentrations of 5 and $10\,mol\,kg^{-1}$ at the same initial filling degree of 80%. When the solution is on the vapor–liquid phase equilibrium line, the $[OH^-]$ curve at the initial filling degree of 90% (dashed curves) overlaps that at 80%. As the temperature increases, the solution varies along the vapor–liquid phase equilibrium line and the $[OH^-]$ curve has

a deviation from that of 80%, which is shown as dashed at the end of the curve in Fig. 21a. Figure 21b shows the effects of temperature on the [OH^-] in KOH aqueous solution. It is obvious that the effect of temperature on the [OH^-] in KOH aqueous solutions is more remarkable than that in NaOH aqueous solutions.

Therefore, the differences between the real concentrations of ions and the apparent concentrations of ions under the circumstances of hydrothermal reactions are remarkable. The calculated real concentrations of ions in aqueous solutions by thermodynamic methods may provide a reliable theoretical guide for the accurate study of the reaction mechanism.

3.6 Conclusion

In this section, on the basis of MD simulations and quantum chemistry calculation on the hydration and association of ions in aqueous electrolyte solutions, an activity coefficient model for aqueous electrolyte solutions at temperatures of 273–673 K and pressures of 0.1–58.86 Mpa was built up. In addition, an activity coefficient model for alkali aqueous solutions in hydrothermal reaction media was set up based on the synergistic action of association and hydration. Using this model, the relationship of the pressure, liquid volume of the vessel, and real concentrations of ions in solutions with temperature, concentrations of solutions, and filling degree are obtained. According to the models, we can not only predict the composition and structure from synthesis conditions, but also analyze the kinetics of the related process. This will provide a theoretical basis for the preparation of advanced materials by solution chemistry and the hydrothermal method.

4 Thermodynamic Analysis of the Solid–Liquid Equilibrium in Aqueous Electrolyte Solution

4.1 Introduction

Processes involving solid phases are commonly used in fractional crystallization, reactive crystallization, and precipitation processes. They are all related to solid–liquid equilibrium (SLE) in the process design and optimization. In contrast to its wide application, the theory for these processes are not developed. In the crystallization process, the number and identity of the phases at equilibrium are too complicated to be predicted because of immiscibility of solid phases as well as compound formation in solid phases. Meanwhile, poor initial estimates often make computation expensive and difficult to converge. Furthermore, it is usually necessary to use phase diagrams to design the crystallization process. For systems with four ions and above, the number of the phases and the distribution of components in liquid may not be determined directly from only a phase diagram, and the method of using

phase diagrams becomes complicated. Determining the number and identity of the phases on the basis of phase diagrams is fragmentary information, and it is not feasible to calculate continuously in design, simulation, and optimization.

Recently, some work has been done in this field and it may be split into two parts: the graphical method (based on the phase diagram), and the enumerative method.

In the graphical method, process design, simulation, and optimization require SLE data in order to generate phase diagrams. The use of experimental data alone will be of limited scope. Recognizing this, in recent years many methods have been proposed for generating phase diagrams. One of these is the method proposed by Lu [69]. In this method the number and identity of the phases at equilibrium, as well as the initial values, were determined from the experimental data of SLE. The method is economical for computation but strongly depends on experimental data. Another method, the global minimum of Gibbs free energy [70], yields the true balanced state. However, the sheer complexity of minimizing the Gibbs energy function for an unknown number of phases makes the process fraught with numerical difficulties, and it is computationally expensive, particularly for complicated systems. Furthermore, this method is unsuitable for process simulation.

The enumerative method was also used to design the crystallization process [71–73] The number and identity of the phases and the distribution of components in liquid are determined simultaneously in these methods. Good initial estimates are needed in this method in order to reliably calculate the activity coefficients of components in liquid. Since there is still no general method for estimating the initial values, only some processes have been simulated by this method in the chemical industry.

In recent years, the advent of certain special chemicals (e.g., pharmaceuticals, high-performance polymers, etc.) has expanded interest in the process related to SLE. In this process, suitable reaction conditions are required in order to obtain lower cost product. Since the related system is more complicated, it is difficult to approach this goal by the experimental method. Conceptual design has been receiving a lot of attention in this field. Lencka and Riman [74, 75] and Lencka et al. [76] used precipitation diagrams to determine the effects of pH, temperature, and concentration on the crystallizing species. Simulation of these processes needs to predict whether or not a given feed will split into multiple phases, the number and identity of phases existing at equilibrium, and the distribution of components within these phases. Rafal et al. [71] proposed a method to simulate these processes. In this enumerative method all the cases or combinations should be tried and good initial values are needed in order to ensure convergence.

It is clear that the graphical method is rapid and simple but relies on phase diagrams; the enumerative method is relatively slow and complicated but more generalized. The difference between them is whether and how to determine the number and identity of the phases at equilibrium in advance. If the number and identity of the phases at equilibrium is determined in advance by a general rapid method, the calculation will be performed rapidly and generally. In this work a general method was proposed to predict SLE by identifying the number and identity of the phases at equilibrium automatically [77].

4.2 Thermodynamics of the Solid–Liquid Equilibrium Stage

The solid–liquid equilibrium stage (SLE stage), for a given feed, determines the number and identity of the phases at equilibrium and the distribution of components within these phases. This is shown schematically in Fig. 22. In actual cases, the feed may be more than one stream, however, the material balance and phase equilibria are independent of the number of streams and the phase-state of the feed. Therefore, one total feed stream is assumed in this chapter for convenient expression.

For the SLE stage there are two key problems. One is the determination of the number and identity of the phases at equilibrium, the other is the calculation of the distribution of components within these phases. This section discusses the latter.

When the number and identity of the phases at equilibrium are known, the distribution of components within these phases can be calculated by combining the mass balance with phase equilibria.

At a given temperature, pressure and feed (flow rate is F, $\mathrm{kg\,h^{-1}}$) containing N species with the composition of ω_i (mass fraction), the identities of solid phases at equilibrium are solid 1, solid 2, … solid J with the flow rate S_j, $\mathrm{kg\,h^{-1}}$. The flow rate of output liquid is L, with composition of x_i (mass fraction) at equilibrium. The number of phases is $J+1$. If the solid phases are of pure species, the mass balance can be written as:

$$F = \sum_{j=1}^{J} S_j + L \tag{4}$$

$$F \cdot w_i = \sum_{j=1}^{J} (\lambda_{ij} \cdot S_j) + L \cdot x_i (i = 1,2,\ldots,N), \tag{5}$$

where λ_{ij} is the stoichiometric coefficient between the components and the precipitated solid phases. For example, for the NaCl–KCl–H_2O system, the solid phases, which may be precipitated, are halite and sylvite. If the precipitated solid phase is halite, the stoichiometric coefficients λ_{ij} between the components and the precipitated solid phase are shown in Table 6.

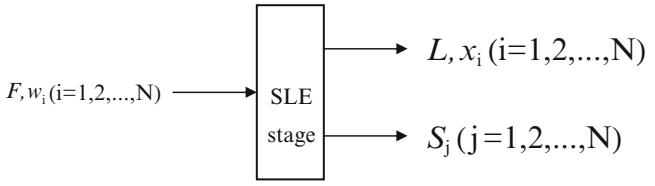

Fig. 22 Schematic for SLE stage

Table 6 Stoichiometric coefficients λ_{ij} between the components and the precipitated solid phases

	NaCl	KCl	H_2O
Halite	1	0	0

Let:

$$A_{spj} = \prod_{i=1}^{N} (x_i \cdot \gamma_i)^{\lambda_{ij}} (i = 1,2,\ldots,N), \tag{6}$$

where x_i is the distribution of component i in liquid phase. The activity coefficient of component i in liquid phase, γ_i, is generally a function of liquid composition and temperature and can be calculated by a suitable thermodynamic model.

At equilibrium, the chemical potential of the precipitated solid phase is equal to the sum of the chemical potential of the solid phase constituent parts, i.e., $\Delta G = 0$. The condition for phase equilibrium therefore is:

$$K_{\mathrm{spj}} = A_{\mathrm{spj}}, \tag{7}$$

$$K_{\mathrm{spj}} = \prod_{i=1}^{N} (x_i \cdot \gamma_i)^{\lambda_{ij}} \quad (j = 1,2,\ldots J), \tag{8}$$

where K_{sp} is the thermodynamic solubility product constant of a salt, it is only a function of temperature under normal conditions.

Equations 4, 5 and 8 involve $J + N + 1$ equations with $J + N + 1$ unknowns $(S_j, j = 1,2,\ldots J; x_i, i = 1,2, \ldots N; L)$. All variables can be solved directly, but the formation contains a large number of variables and the possibility of failure in convergence is very high. In order to avoid these numerical instabilities, an algorithm is proposed in the present work to ensure convergence. The algorithm is similar to the method developed by Prausnitz [78] for the calculation of flash vaporization. The calculation of mass balance was performed in the outer loop while the inner loop was used for the calculation of SLE. Rearranging Eqs. 4 and 5 yields:

$$w_i = \sum_{j=1}^{J} \left(\lambda_{i_j} \cdot \frac{S_j}{F} \right) + \left(1 - \sum_{j=1}^{J} \frac{S_j}{F} \right) \cdot x_i \quad (i = 1,2,\ldots,N). \tag{9}$$

Let:

$$\beta_j = \frac{S_j}{F} \quad (j = 1,2,\ldots J). \tag{10}$$

Equation 9 becomes:

$$w_i = \sum_{j=1}^{J} (\lambda_{ij} \cdot \beta_j) + (1 - \sum_{j=1}^{J} \beta_j) \cdot x_i (i = 1,2,\ldots,N), \tag{11}$$

$$x_i = \frac{w_i - \sum_{j=1}^{J} (\lambda_{ij} \cdot \beta_j)}{1 - \sum_{j=1}^{J} \beta_j} (i = 1,2,\ldots,N). \tag{12}$$

Combining Eq. 12 with 8, we finally have:

$$K_{\mathrm{spj}} = \prod_{i=1}^{N} \left(\frac{w_i - \sum_{j=1}^{J} (\lambda_{ij} \cdot \beta_j)}{1 - \sum_{j=1}^{J} \beta_j} \cdot \gamma_i \right)^{\lambda_{ij}} \quad (j = 1,2,\ldots J). \tag{13}$$

As a result of this arrangement, the initial system (Eqs. 4, 5 and 8 with $J + N + 1$ non-linear equations) is partitioned into two independent parts, namely a system of J non-linear equations and $N + 1$ linear expressions. The unknown variables of the system are $j(j = 1,2, \ldots J)$. The variables of x_i $(i = 1,2,\ldots N)$, S_j $(j = 1,2, \ldots J)$ and L can be calculated directly from Eqs. 12, 10 and 4 when $\beta_j(j = 1,2,\ldots J)$ are known. The corresponding Jacobian matrix in the former case is $(J + N + 1)^*(J + N + 1)$ dimensions, while in the latter case it is (J^*J). This already constitutes a considerable potential saving in computational effort. Also, the number of the variables is reduced to J from $J + N + 1$ and they lie between zero and one. This is economical in computational efforts and useful to ensure convergence.

It is important to observe that for aqueous electrolyte solutions the composition of species should satisfy the charge balance, therefore, the number of the equations is always larger than the variables. Writing the mass balance in aqueous systems is difficult and there is no general method to solve this problem. By arrangement of the equation performed in this work the number of the iteration variables is always equal to the number of the functions, and the possibility of generating equations relative to each ion is avoided.

If the process is an adiabatic process, the enthalpy balance for the system is:

$$Q + F \cdot h^F = L \cdot h^L + \sum_{j=1}^{J} (S_j \cdot h^{S_j}), \tag{14}$$

where Q is heat transferred with the environment. In adiabatic processes Q is equal to 0. Functions h^{F}, h^{L}, and h^{Sj} are the enthalpy of the feed, output liquid phase, and output solid phase, respectively. The detailed method is to calculate the distribution of components within each phase at a certain temperature, then calculate h^{L} and h^{Sj} $(j = 1,2, \ldots J)$. If they satisfy Eq. 14, stop. Otherwise, change the temperature and repeat the steps.

4.3 Determination of the Number and Identity of the Phases at Equilibrium

When the number and identity of the phases at equilibrium are known, the distribution of components within these phases can be determined by the SLE stage method proposed in Sect. 4.2. In this work a method is proposed to determine the number and identity of the phases at equilibrium and the principles of this method are discussed here.

4.3.1 Theoretical Background

In the graphical method, the number and identity of the phases at equilibrium are determined based on the location of feed in the phase diagrams. For example, a simple ternary system is NaCl–KCl–H_2O. The phase diagram for this system at a

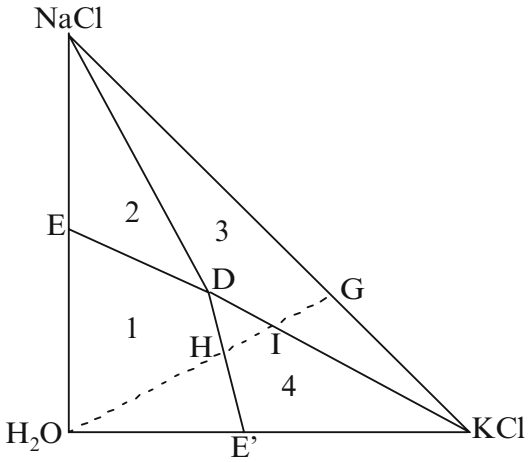

Fig. 23 Phase diagram for Na^+–K^+–Cl^-–H_2O system

certain temperature is shown in Fig. 23. Points on the line EDE′ represent saturated solutions. From E to D solutions are saturated with respect to halite. From D to E′ solutions are saturated with respect to sylvite. There are four regions in Fig. 23. The region of H_2O, E, D, E′, H_2O (region 1 in Fig. 23) represents unsaturated solutions. The region of E, NaCl, D, E (region 2 in Fig. 23) represents halite in equilibrium with saturated solutions. The region of E′, D, KCl, E′ (region 4 in Fig. 23) represents sylvite in equilibrium with saturated solutions. The region of D, NaCl, KCl, D (region 3 in Fig. 23) represents halite and sylvite in equilibrium with saturated solutions.

If the location of the feed is in region 1, the number of the solid phases at equilibrium is zero. If the location of the feed is in region 2, the number of the solid phases at equilibrium is one and the identity of the solid phase is halite. If the location of the feed is in region 4, the number of the solid phases at equilibrium is one and the identity of the solid phase is sylvite. If the location of the feed is in region 3, the number of the solid phases at equilibrium is two and the identities of the solid phases are halite and sylvite. This method of determining the number and identity of the phases at equilibrium is based on the regions. For a complicated system, the region is a polyhedron and it is difficult to represent by a geometric method. Therefore, this method is not feasible to be considered as a mathematical method.

On the other hand, if the proportion of species on a solvent-free basis for a given feed is known, the number and identity of the phases at equilibrium can be determined by the quantity of the solvent. In Fig. 23, points on the dotted line represent the different feeds in which the proportions of NaCl to KCl on a solvent-free basis are the same while the quantities of solvent are different. Based on the quantity of solvent there are three corresponding intervals. From H_2O to H (noted interval 1) represents unsaturated solutions and no solid phase is precipitated. From H to I (noted interval 2) represents sylvite in equilibrium with saturated solutions. From I to G (noted interval 3) represents halite and sylvite in equilibrium with saturated solutions.

If the quantity of the solvent in feed is located in interval 1, the number of the solid phases at equilibrium is zero. If the quantity of the solvent in feed is located in interval 2, the number of the solid phases at equilibrium is one and the identity of the solid phase is sylvite. If the quantity of the solvent in feed is located in interval 3, the number of the solid phases at equilibrium is two and the identities of the solid phases are halite and sylvite.

4.3.2 Method and Principle

It is clear that the number and identity of the phases at equilibrium can be determined if the proportion of species on solvent free basis in feed and the intervals are known. For a given feed the proportion of species on solvent-free basis is determined. Therefore, the determination of the number and identity of the phases at equilibrium is changed into the problem of determining the quantity of solvent.

Based on the phase diagram of Fig. 23, for a given feed, the quantity of the solvent at the point H is equal to that when the first solid phase is just saturated and no solid is formed. The quantity of the solvent at the point I is equal to that when the first solid phase is precipitated and the second solid phase is just saturated. If the quantities of solvent at the points H and I, the terminal vertex values of intervals, are determined, the intervals can be determined.

Therefore, a method was designed to determine the terminal vertex values of intervals. An initial and large trial value of solvent is first assumed, and the values of A_{sp} for solid phases that might precipitate are calculated to verify that in no case is the corresponding value of K_{sp} exceeded. Increments of solvent are now successively removed from the solution and the previous calculation repeated after each increment. New values of A_{sp} are calculated after each increment. Eventually, a point is reached when the ratio of A_{sp} to K_{sp} is unity for one solid phase while remaining less than unity for all the other solid phases. This point represents the situation where the first solid phase is just saturated and the value of the solvent at this point is one of the terminal vertex values of intervals.

If the increment of solvent is removed from solution continuously, the first solid phase is precipitated from liquid. Using SLE stage method, the quantity of this solid phase can be calculated. When the quantity of the solid phase is known, the distribution of components in liquid is able to be determined, and A_{sp} can also be calculated. Using the method proposed in this study, increments of solvent are successively removed from the solution, and after each increment new values of A_{sp} are calculated. Eventually, a point is reached when the ratio A_{sp} to K_{sp} is unity for two solid phases while remaining less than unity for all the other solid phases. This point represents the situation where the second solid phase is just saturated and the value of solvent at this point is another terminal vertex value of intervals.

The second step is repeated to determine the other terminal vertex value of intervals until the degree of freedom is zero. With the decrease of solvent in some systems, when the degree of freedom is zero the ratio of A_{sp} to K_{sp} is fixed for precipitated solid phases and the distribution of components in liquid is also fixed,

while the quantity of one solid phase is decreased. When the quantity of this solid phase approaches zero, this solid phase dissolves completely and the value of the solvent at this point is another terminal vertex value of intervals.

When the terminal vertex values of intervals are determined, the number and identity of the phases can be determined based on the location of the quantity of solvent in the feed.

It is important to realize that in the method proposed the first step is the same as the method proposed by Kusik et al. [79] However, the method proposed by Kusik et al. [79] cannot calculate the quantity of solid phases. While the distribution of components in liquid is related to the quantity of solid phases, and the value of A_{sp} is related to the distribution of components in liquid, the value of A_{sp} cannot be calculated when the solid phases are precipitated from the liquid phase. Therefore, the method of Kusik et al. [79] cannot be used when the solid phases are precipitated.

4.4 Application

To test the method proposed, examples of SLE with complicated phase behavior were examined. A satisfactory thermodynamic model for calculating the activity coefficients of components in liquid is essential for correct and consistent synthesis, simulation, and optimization of the desired process. The model proposed by Pitzer [80] was used to calculate the following examples. However, for the Na^+–K^+–Cl^-–$NO_3{}^-$–H_2O system the concentration of liquid components is so high that the model proposed by Pitzer cannot be applied. The model proposed by Lu and Maurer [81] was used to represent the activity coefficients of components.

4.4.1 Prediction of Crystallization Paths

At 298.15 K there are three possible precipitated solid phases for the Na^+–Cl^-–SO_4^{2-}–H_2O system: halite (1), thenardite (2), mirabilite (3), and two invariant points, (3 + 2) and (2 + 1). The phase diagram is shown in Fig. 24. For a given feed (point F in Fig. 24), when the solvent is evaporated from the point i, the change process is shown in Table 7.

For the given feed (F = 1 kg h^{-1}, NaCl 0.00758 kg, Na_2SO_4 0.02761 kg, H_2O 0.96482 kg) and using the method proposed, the crystallization paths were predicted and compared with literature data. The results are shown in Table 8. For this system, activity coefficients were calculated by the Pitzer equation [80], and the values of K_{sp} were taken from Pabalan and Pitzer [82].

As shown in Table 8, the saturated solution predicted is approximately similar to the literature data, the small difference comes from the thermodynamic model calculating activity coefficient. The crystallization paths are the same as the

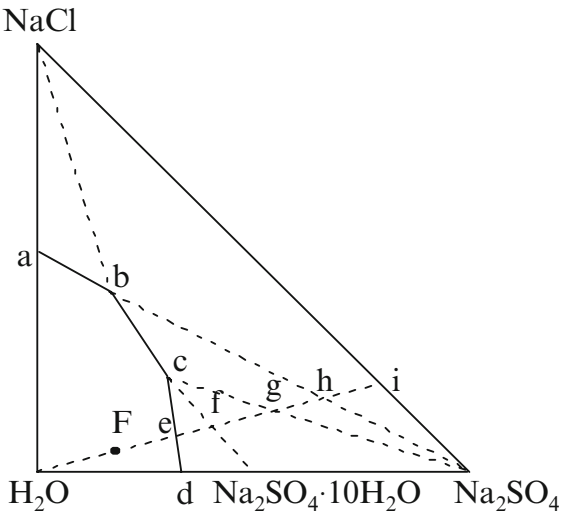

Fig. 24 Phase diagram of ternary system of Na^+–Cl^-–SO_4^{2-}–H_2O at 298.15 K

Table 7 Change process of evaporation for the Na^+–Cl^-–SO_4^{2-}–H_2O system

Quantity of solvent	Saturated solution	Significance
e	e	Solid 3 is not precipitated
e → f	e → g	Solid 3 is precipitated
f	c	Solid 3 is precipitated, solid 2 is not precipitated
f → g	c	Solid3 is dissolved, solid 2 is precipitated
g	c	Solid 3 is dissolved completely, solid 2 is precipitated
g → h	c → a	Solid 2 is precipitated
h	a	Solid 2 is precipitated, solid 1 is not precipitated
h → i	a	Solid 2 and solid 1 are precipitated

Letters correspond to points in the phase diagram shown in Fig. 24

Table 8 Comparison of the predicted results for saturated solution and the crystallization paths with literature data for the Na^+–Cl^-–SO_4^{2-}–H_2O system at 298.15 K

Point in Fig. 24	Solid type	Saturated solution (wt%)			
		Linke and Sediell [83]		This work	
		NaCl	Na_2SO_4	NaCl	Na_2SO_4
e	3	–	–	4.71	17.12
f	3+2	14.2	15.0	13.38	14.99
g	2	14.2	15.0	13.38	14.99
h	2+1	22.9	6.9	22.71	6.84

Letters correspond to points in the phase diagram shown in Fig. 24

literature data [83]. Therefore, the method proposed is capable of predicting crystallization paths.

The Na^+–K^+–Cl^-–NO_3^-–H_2O system is a quaternary conjugate salt system and its diagram is a Jänecke projection (Fig. 25), therefore, the contribution of each phase cannot be obtained directly. For this system there are four precip-

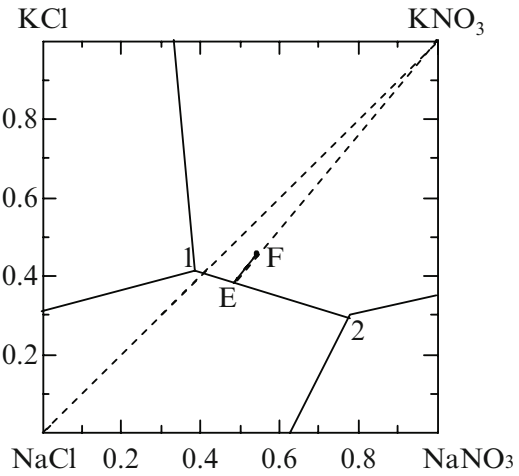

Fig. 25 Phase diagram for Na^+–K^+–Cl^-–NO_3^-–H_2O system

Table 9 Calculation results for the Na^+–K^+–Cl^-–NO_3^-–H_2O system at 293.15 K

Case	Salt concentration (M)				Crystallization paths
	NaCl	$NaNO_3$	KCl	KNO_3	
Case 1	1.0	0.0	0.0	1.0	Saltpeter → saltpeter + halite
Case 2	1.0	0.0	0.012	1.0	Saltpeter → saltpeter + halite → saltpeter + halite + sylvite
Case 3	1.0	0.013	0.0	1.0	Saltpeter → saltpeter + halite → saltpeter + halite + soda peter

itated solid phases, halite, sylvite, soda niter, and saltpeter, and two invariant points, one is saltpeter + halite + soda niter (point 1 in Fig. 25), the other is saltpeter + halite + sylvite (point 2 in Fig. 25). For the given feed (point F in Fig. 25), if the solvent is removed from solution, on the basis of the phase diagram the identity of the first solid phase is saltpeter and the ratio of ions moves along the line FE. At the point E, halite is just saturated. If the solvent is removed continuously, the ratio of the ions moving along E1 or E2 should be determined by experience or by combining the phase diagram with the quantity of solvent. In present study the crystallization paths were determined automatically (Table 9). For the given feed (point F in Fig. 25, F = 1 kg h^{-1}, KNO_3 0.198 kg, $NaNO_3$ 0.033 kg, NaCl 0.115 kg, H_2O 0.654 kg) the crystallization path is saltpeter → saltpeter + halite → saltpeter + halite + soda peter. For this system, activity coefficients were calculated by the model of Lu and Maurer [81], the values of K_{sp} were taken from literature [69].

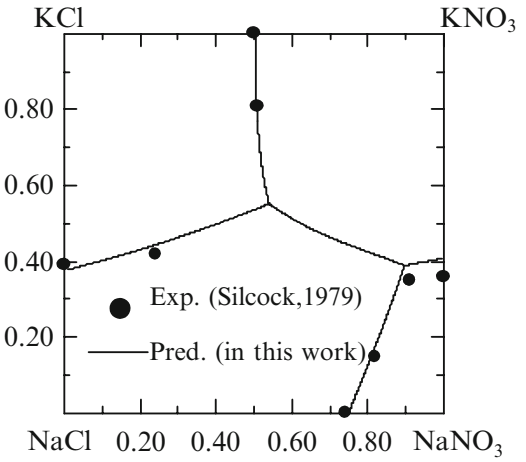

Fig. 26 Phase diagram for Na^+–K^+–Cl^-–NO_3^-–H_2O system at 298.15 K

4.4.2 Generation of Phase Diagrams

The merits and disadvantages of existing methods for generating phase diagrams have been discussed above. The method proposed in this work was also used to generate phase diagrams by calculating different mole proportions of feed. For the ternary system, the subsystem should be calculated first. Based on this, the different mole proportions of feed were derived by the linear relationship and each point was calculated until the first solid phase just appeared. For complicated systems it is difficult to generate phase diagrams. The general enumerative method is impractical because the possible solid phases and their combinations are numerous. The method proposed in this work was also used to generate phase diagrams by calculating different mole proportions of feed until the second solid phase was just saturated. The phase diagram for the Na^+–K^+–Cl^-–NO_3^-–H_2O system was calculated as an example and is shown in Fig. 26. Activity coefficients were calculated by the model of Lu and Maurer [81], the values of K_{sp} were taken from literature [69].

4.4.3 Calculation of the SLE Stage

SLE stage calculation determines the number and identity of the phases and calculates the distribution of components within these phases at equilibrium for a given feed. It is similar to that of flash vaporization at VLE. The calculation of flash vaporization at equilibrium is used in the simulation of related processes, but there is still no general method for related SLE processes because the determination of the number and identity of the phases at equilibrium is more complicated. The existing methods solved this problem by enumeration [71, 73] or phase diagrams. The complex calculation and long time of iteration make the enumerative method

impractical for a new and complicated system. The methods for determining the number and identity of the phases on the basis of phase diagrams are rapid and simple, however, they are not feasible for being plugged into the commercial software used in chemical engineering process simulation.

In this work, the method proposed not only determines the identity and number of the phases automatically but also establishes a general method for making good initial estimates and calculating iteration increments. Furthermore, the capability of the thermodynamic models in calculating the activity coefficients of components in liquid phase is also considered. All of these ensure rapid convergence. The production process of potash from sylvinite, a mixture of solid phases consisting of potassium chloride and sodium chloride (42.7% KCl, 56.6% NaCl), was simulated. The activity coefficients were calculated by the Pitzer equation [80] and the values of K_{sp} were taken from Pabalan and Pitzer [80A]. The simulation results were compared with the literature data of Cisternas and Rudd [84]. The comparison results are shown in Table 10. The simulation results are very close to the literature data. Furthermore, in the method proposed the requirements for calculation are only the values of K_{sp} of halite and sylvite which are independent of the experimental data of SLE. This is why the method proposed can be directly used for more complicated systems.

Another example is the Na^+–K^+–SO_4^{2-}–H_2O system. In this system there are three possible precipitated solid phases: thenardite (1), arcanite (2) and glasserite (3). For the given feed (Na_2SO_4 0.1826 kg, K_2SO_4 0.7990 kg, H_2O 0.0184 kg) the simulation results agree well with literature data and are shown in Table 11. Activity

Table 10 Comparison of simulation results with literature data for the Na^+–K^+–Cl^-–H_2O system at 373.15 K

Source	Crystallization path	Number of phases	Solid flow, S_j ($kg\ h^{-1}$)		Liquid flow, L(kgh^{-1})	Saturated solution (wt%)	
			Halite	Sylvite		NaCl	KCl
Cisternas and Rudd [84]	Halite → halite + sylvite	3	–	–	–	15.90	22.20
This work	Halite → halite + sylvite	3	0.5642	0.4245	0.01133	16.18	22.01

Table 11 Comparison of simulation results with literature data for the Na^+–K^+–SO_4^{2-}–H_2O system at 323.15 K

Source	Crystallization path	Number of phases	Solid flow, S_j ($kg\ h^{-1}$)			Liquid flow, L(kgh^{-1})	Saturated solution (wt%)	
			S_1	S_2	S_3	(kgh^{-1})	Na_2SO_4	K_2SO_4
Fitch [134]	2 → 2 + 3	3	–	–	–	–	6.00	14.00
This work	2 → 2 + 3	3	0.0	0.1296	0.8475	0.02290	5.96	13.69

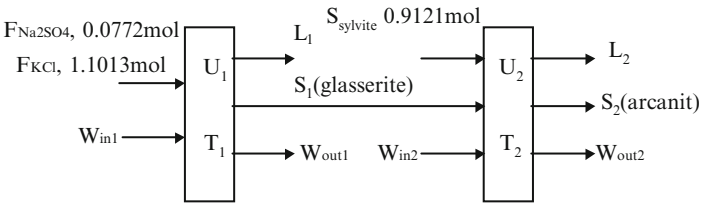

Fig. 27 Schematic of arcanite production process (case 1)

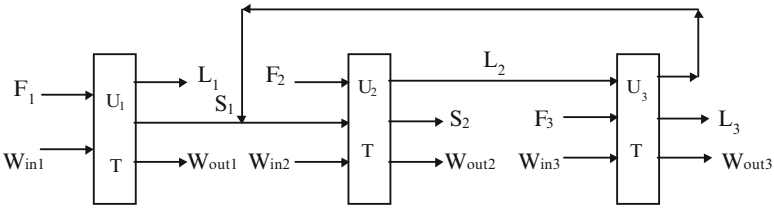

Fig. 28 Schematic of arcanite production process (case 2)

coefficients were calculated by the Pitzer equation [80], and the values of K_{sp} were taken from Greenberg and Møller [85].

4.4.4 Simulation of Fractional Crystallization Processes

Generally, simulation and optimization of arcanite production process are patented or depend on phase diagrams [86, 87]. In this system there are reactions, hydrates, and compound formation. Thomsen et al. [73] simulated this process using his own method. Good initial estimates were necessary because of the predictivity of the thermodynamic model. Generally, initial estimates are obtained from the real operation conditions to ensure convergence. For a new condition or system it is difficult to get good initial estimates and the calculation is rather complicated, and much experience is needed. However, in this work a reaction was considered in SLE stage to avoid negative stream variables, and it could be plugged into the commercial software such as Pro/II and Aspen.

In the present study, two cases (Figs. 27 and 28) of arcanite production were simulated and the results are displayed in Tables 12 and 13. Activity coefficients were calculated by the Pitzer equation [80], and the values of K_{sp} were taken from Greenberg and Møller [85].

4.5 Conclusions

Because of the important need for simulations of the crystallization process, a general method was proposed to calculate the SLE stage. The number and identity of

Table 12 Comparison of the simulation results with literature data for the Na^+–K^+–Cl^-–SO_4^{2-}–H_2O system at 298.15 K

Source	Amount of liquid product (g)		Amount of solid product (g)		Recovered fraction of K^+ (g)
	L_1	L_2	S_1	S_2	
Liu (unpublished results)	269	238.6	100	100	57
This work	276.17	238.4	97.28	96.1	54.8

Table 13 Simulation results for the Na^+–K^+–Cl^-–SO_4^{2-}–H_2O system at 298.15 K

Feed		Amount of feed (mol)	Solid product		Amount of solid product (g)
F_1	Sylvite	1.1013	S_1	Glasserite	165.32
	Thenardite	0.7472	S_2	Arcanite	150.04
F_2	Sylvite	1.0621	S_3	Glasserite	68.16
F_3	Thenardite	0.4275	Recovered fraction of K^+ 79.6%		

the phases at equilibrium were determined automatically by a general method based on the proportion of species in the feed, on a solvent-free basis, and on the intervals. The initial estimates, increments, and capability of the thermodynamic model were considered to ensure that the calculation was effective and rapid. Moreover, the range of iteration variables was limited to 0–1; this is more economical in the computational effort and can ensure convergence.

Meanwhile, the proposed method can be used to predict crystallization paths, and to generate phase diagrams of SLE. Several examples calculated by the method proposed in this work show that this method is suitable for the system with hydrate, multi-ion, and complex salts. Since the method proposed determined the number and identity of the solid phases in advance automatically and obtained the composition at equilibrium rapidly and steadily, it can be used as a mathematical module to plug into other software to design, simulate, and optimize related processes.

5 Mass Transfer Kinetic Analysis at the Solid–Liquid Interface Based on a Thermodynamic Method

In order to study the rapid process of transfer and reaction kinetics experimentally, an activity determination system was established on the basis of ion-selective electrodes (ISE), and a thermodynamic model was used to calculate the activity coefficients of liquid components in data processing to obtain the accurate concentration of ions.

5.1 Determination of Dissolution Kinetics of K_2SO_4 Crystal with an Ion-Selective Electrode

Dissolution of solid material from solutions has widespread and universal applications in oceanography, crystallography, metallurgy, ceramics, and desalination technology, as well as in a number of biological and environmental precipitation processes [88]. Concentration of solutions is often measured by sampling with a regular interval [89] or by the atomic absorption [88]; however, these methods cannot determine the concentration on-line. Furthermore, for a quick dissolution process, these two methods are unsuitable.

Ion-selective electrodes (ISEs) [90], conductimetric measurements [91], and calorimetric methods [92] have been used to determine the concentration on-line. For a high concentration or a complicated system, the deviation of the conductimetric measurement is very high. ISEs are currently being emphasized for obtaining basic and reliable experimental data in order to study dissolution processes [90].

When the concentration was measured with ISE, the response of the ISE is the activity. In the literature, the change of the activity coefficient was often neglected and, therefore, the determination range was narrow. In this work, a thermodynamic model calculating activity coefficients was combined with ISEs to determine the concentration for complicated systems over a wide range. Since the values of activity coefficients are related to concentration, the concentration cannot be calculated from the electromotive force function directly.

In this work, the concentration was iterated from the electromotive force function. If there were chemical reactions, the mathematical module of the chemical reaction proposed was used as the outer loop.

In practice, production of potassium sulfate plays an important role in the chemical industry. Many researchers have studied the kinetics of potassium sulfate [93, 94]. Previous work on the system performed in different types of equilibrium under different experimental conditions showed considerable variations in results [89]. Their emphasis has been on crystal growth. Furthermore, there is no systematic and special study for the dissolution process of potassium sulfate. Therefore, in this work, its dissolution experimental data will be determined with ISEs.

In order to determine the concentration of K_2SO_4 by this pair of ISEs, a dilute solution of KCl was used as the base solution. The concentrated stock mixed-electrolyte solution, KCl–K_2SO_4–H_2O, was prepared by dissolving the crystal K_2SO_4 into the dilute solution of KCl. Therefore, in the whole experimental procedure the molality of Cl was kept constant.

The K membrane ISE (model 401, China) and chloride solid-state ISE (model 301, China) were used to follow the ionic activity in solutions. Before determination, the K membrane ISE should be conditioned in a solution of KCl for 30 min (KCl concentration was about 0.01 mol kg^{-1}). The Cl solid-state ISE should be inserted in the same solution for 30 min.

The cell for the KCl–K_2SO_4–H_2O system was described as:

K membrane ISE | gKCl(m_1), K_2SO_4 (m_2), H_2O| gCl solid-state ISE

If the influence of SO_4^{2-} on this pair of ISEs was small enough to be neglected, the corresponding values of the cell EMF (E) could be expressed as:

$$E = E^0 + 2S\ln(m \cdot \gamma_{\pm}), \tag{15}$$

where the values of E^0 and S are the values regressed from the experimental data of the binary system. Symbols m and $\gamma_{\pm}$ represent the mean molality and activity coefficient of KCl in the KCl–K_2SO_4–H_2O system, respectively. The activity coefficients were calculated by the Pitzer equation [80] and the parameters were all taken from Greenberg and Møller [85].

The material balance for this system was:

$$m = \sqrt{(m_1 + 2m_2) \cdot m_1}, \tag{16}$$

$$m_1 = 0.05627. \tag{17}$$

In this work, the potential values of the cell were determined at 298.15 K in the KCl–K_2SO_4–H_2O system. The concentration of K_2SO_4, m_2, was iterated by combining the EMF equation with material balance. The determination results are listed in Table 14 (case 1).

For case 2, the activity coefficients in Table 14 were considered to be constant; in this example, at 0.679. As shown in Table 14, the deviation in this work (case 1 in Table 14) is small enough. In the literature, the activity coefficients were considered to be constant. When the change of the activity coefficients in the experimental

Table 14 Determination results for concentration of K_2SO_4 in the KCl–K_2SO_4–H_2O system at 298.15 K

E_i	$\gamma_{\pm}$	$m_{2,\exp}$	Case 1		Case 2[a]	
			$m_{2,cal}$	$\lvert\Delta m_2\rvert$[b]	$m_{2,cal}$	$\lvert\Delta m_2\rvert$
(mV)		(mol kg^{-1})	(mol kg^{-1})	(mol kg^{-1})	(mol kg^{-1})	(mol kg^{-1})
83.6	0.796	0.003	0.003	0	0.072	0.069
84.4	0.790	0.005	0.005	0	0.074	0.069
91.3	0.751	0.020	0.019	0.001	0.084	0.064
99.1	0.709	0.045	0.044	0.001	0.098	0.053
106.6	0.670	0.080	0.080	0	0.113	0.033
113.1	0.637	0.125	0.125	0	0.128	0.003
119.0	0.609	0.180	0.182	0.002	0.143	0.037
123.8	0.584	0.245	0.247	0.002	0.157	0.088
128.1	0.563	0.320	0.321	0.001	0.171	0.149
E^0(mV)			240.01	219.90		
AV[c]			474.74	1.05		

m_{kcl} = 0.0563 mol kg$^{-1}_{-}$, S = 51.94 mV

$E_i$cell EMF, E^0 regressed EMF, $m_{2,exp}$ molar concentration of K_2SO_4determined experimentally, $m_{2,cal}$ calculated molar concentration of K_2SO_4, γ activity coefficient of KCl

[a] In case 2, γ was considered constant, and equal to 0.679

[b] Deviation $^{\Delta}m_2 = m_{2,exp} - m_{2,cal}$

[c] $AV = \frac{1}{9} \cdot \sum_{i=1}^{9} \frac{\Delta m_2}{m_{2,\exp}} \times 100\%$, which is the standard deviation for the determination results

concentration is small, the experimental error may be less. Otherwise, it is difficult to obtain reliable results. In this example when the activity coefficient was considered to be constant (the mean value of 0.679 was chosen as the constant), the deviation is very high (case 2 in Table 14). Therefore, the application of a suitable thermodynamic model for the calculating activity coefficient is very important for determining the concentration over a wide range with ISE. Since the accuracy is high, another conclusion is obtained that the influence of SO_4^{2-} on the K membrane ISE can be neglected.

Since the determination accuracy is high enough, this pair of ISEs was used to determine the concentration of K_2SO_4 in the dissolving process.

The experimental data were determined at 288.15, 298.15 and 308.15 K and the values of the speed of agitator were 500, 600, and 700 rpm. The potential values of the cell were recorded per second automatically with a computer and the concentration was iterated by Eq. 15, in which the activity coefficients were calculated by the Pitzer equation [80] and the parameters were taken from Greenberg and Møller [85].

The determination results are shown in Fig. 29, and the comparison results with experimental data are listed in Table 15. The maximum deviation from the experimental data is less than 2%, implying that the determination results are accurate.

With the determined experimental data and the modified statistical rate theory, the thickness of the diffusion layer was estimated. The effects of temperature and stirring speed on the thickness of diffusion layer are also shown in Fig. 30. It is clear that when the stirring speed was increased, the thickness of the diffusion layer decreased, and when the stirring speed was constant and the temperature was increased, the thickness of diffusion layer again decreased. Furthermore, the effect of temperature on the thickness of diffusion layer is more than that of stirring speed.

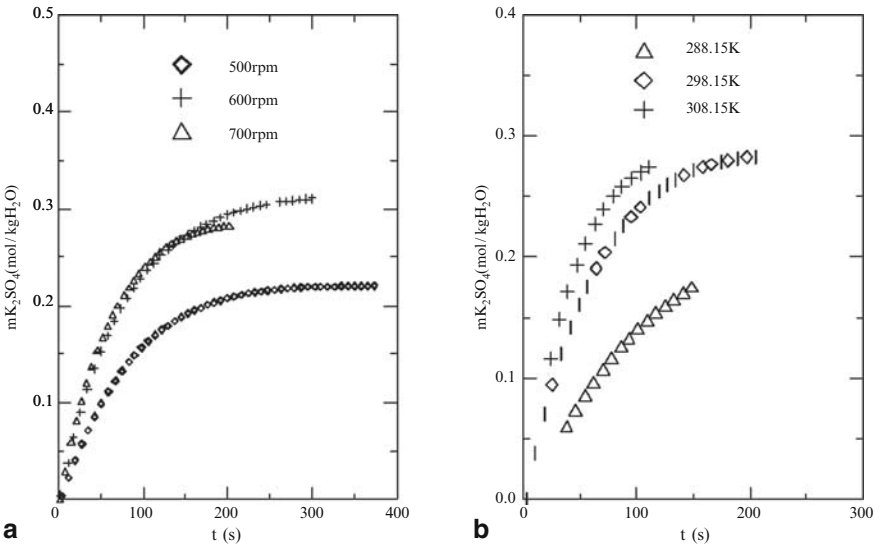

Fig. 29 Detection concentration of K_2SO_4 in the KCl–K_2SO_4–H_2O system when crystal K_2SO_4 is dissolved: **a** at 298.15 K and different agitator speeds; **b** at 700 rpm and different temperatures

Table 15 Concentration of K_2SO_4 determined with ISEs

Case	Temperature (K)	Speed of agitator (rpm)	$m_{2,\exp}$ (mol kg^{-1})	$m_{2,cal}$ (mol kg^{-1})	$\lvert\Delta m_2\rvert / m^a_{2,\exp}$ (%)
Case 1	298.15	500	0.2255	0.2217	1.680
Case 2	298.15	600	0.3017	0.3077	1.990
Case 3	298.15	700	0.2835	0.2842	0.247
Case 4	288.15	700	0.2561	0.2551	0.390
Case 5	298.15	700	0.2835	0.2842	0.247
Case 6	308.15	700	0.2839	0.2832	0.261

m_{kcl} = 0.04479 mol kg^{-1}
[a]Deviation $\Delta m_2 = m_{2,\exp} - m_{2,\mathrm{cal}}$

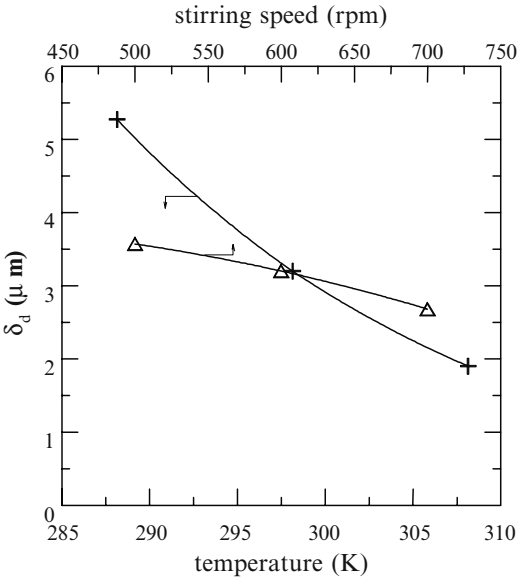

Fig. 30 Effects of temperature and stirring speed on the thickness of diffusion layer: + effect of temperature, Δ effect of stirring speed

The dissolution of potassium sulfate crystals in aqueous ethanol solution was also determined experimentally with ISE (Fig. 31). In order to obtain a reliable concentration in the bulk, the model of Lu et al. [95], with consideration of the effect of ethanol, was used to calculate the activity coefficients of liquid components. The modified statistical rate theory was used to investigate the process of dissolution kinetics of K_2SO_4 crystals, and parameters were regressed from the determined experimental data. Resistances of the process of surface reaction and the process of diffusion in liquid were analyzed (Fig. 32 and Table 16).

From the result listed in Table 16, it is clear that in pure aqueous solution, the diffusion resistance is more 80% of total resistance. Therefore, the dissolution is diffusion-controlled. However, in mixed solvent solution, the diffusion resistance is

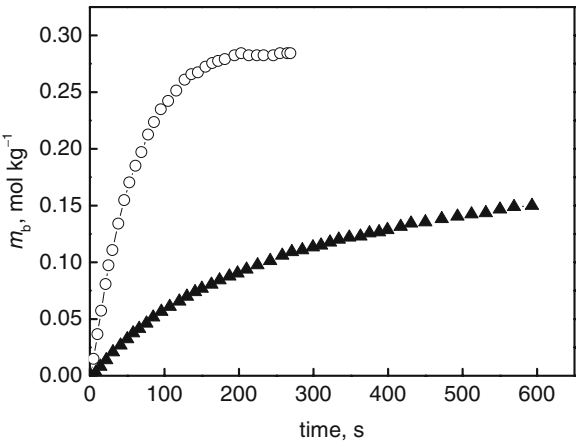

Fig. 31 Concentration–time curve for the dissolution process of K_2SO_4 at different ethanol contents

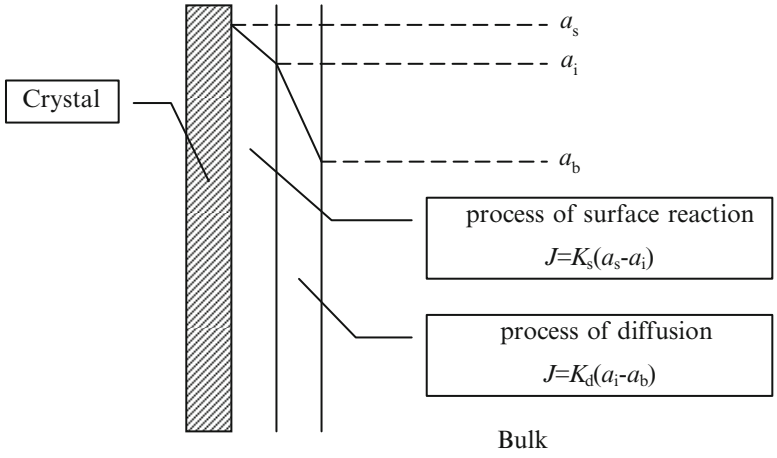

Fig. 32 Definition of the resistance of the process of surface reaction and diffusion

Table 16 Resistance in dissolution processes at different ethanol content at 298.15 K and 700 rpm

EtOH	Surface resistance $\frac{1}{K_s}$	Diffusion resistance $\frac{1}{K_d}$	$\frac{\frac{1}{K_d}}{\frac{1}{K_s}+\frac{1}{K_d}}$
(mol%)	(sm^{-1})	(sm^{-1})	(%)
0	402 ± 56	1,916	81–85
5.85	3533 ± 143	221	5.7–6.1

only about 6% of total resistance. This means that the total resistance mostly comes from the surface reaction resistance. The dissolution is surface reaction controlled. Therefore, we can conclude that the decrease in the rate of surface reaction causes the slowness of the dissolution process in the mixed solvent solution.

The reason why the speed of surface reaction is slowed in aqueous ethanol solutions is probably the weakness of hydrogen bonding between water molecules. The addition of ethanol reduces the polarity of solvent, so the hydrogen bonding among the water molecules is weakened. This causes reactive forces between water molecules so that surface molecules of solid are reduced. Thus, it is more difficult for K_2SO_4 to dissolute into aqueous ethanol solutions than into aqueous solutions [95].

5.2 Thermodynamic Analysis of Crystal Growth Kinetics of Potassium Sulfate

Crystallization is an important solid–liquid separation method and has been used to separate and purify a variety of substances, including inorganic salt and proteins [96, 97]. Because crystallization temperature has a notable effect on the solubility of solute, product yield, and crystallization rate, it is one of the key parameters for both the design of a crystallizer and the crystallization process [97].

Generally, the crystal growth rate increases with increasing temperature. However, the temperature dependence of the crystal growth rate of K_2SO_4 is abnormal in the low temperature range; i.e., the growth rate decreases with the increase of the temperature from 273.15 to 293.15 K. This abnormal phenomenon is probably due to the deposition of fine crystals on the seed crystal surface, which may enhance the crystal growth rate [98]. Theoretical explanation is still needed to understand it clearly.

On the other hand, the solution is too complicated for the large scale production of K_2SO_4. For example, if K_2SO_4 is produced from sodium sulfate and potassium chloride, the solution contains Na^+, K^+, Cl^-, and $SO_4{}^{2-}$ during the crystallization process [99]. This complicated solution causes the complexity of the temperature effect on the growth rate of K_2SO_4 and the difficulty in the theoretical study of crystallization.

Most of the available studies are based on empirical equations to correlate experimental data, where the driving force for crystallization is simplified to be the concentration difference between the crystal and the bulk solution. However, as Myerson et al. have pointed out, the fundamental driving force for crystallization is the difference in the chemical potential of crystal at the solid–liquid interface [100, 101], so a thermodynamic model is needed to calculate the thermodynamic properties of the activity coefficients and chemical potentials. A rigorous theoretical study on crystallization should be carried out based on this point.

In our previous work, the thermodynamic properties of aqueous electrolyte solutions were studied. In this work, the temperature dependence of the crystal growth rate of K_2SO_4 is investigated from a rigorous theoretical model.

5.2.1 Theory

Generally, the crystal growth rate is expressed as:

$$G = k \cdot \sigma^g, \tag{18}$$

where G is an empirical parameter regressed from experimental data, σ is the driving force, g is the growth order, and k is the crystal growth rate coefficient related with temperature and the hydrodynamic state in solution:

$$k = k_0 \cdot \mathrm{e}^{-E/(RT)}. \tag{19}$$

The driving force σ is described by the chemistry potential difference at the solid–liquid interface $\Delta\mu/RT$, as suggested by Myerson [101], instead of by the concentration difference:

$$\sigma = \frac{\Delta\mu}{RT} = \ln\left(\frac{a}{a^*}\right) = \ln\left(\frac{m_\pm^\nu \cdot \gamma_\pm^\nu}{K_{\mathrm{sp}}}\right), \tag{20}$$

where $\gamma_\pm$ is the mean ionic activity coefficient of an electrolyte in supersaturated solution, $m_\pm$ is the mean ionic molality, ν is the stoichiometric coefficient, and $a^*(K_{\mathrm{sp}})$ is the solubility product.

Substitute Eqs. 19 and 20, and Eq. 18 becomes:

$$G = k_0 \cdot \mathrm{e}^{-E/(RT)} \left(\ln\left(\frac{m_\pm^\nu \cdot \gamma_\pm^\nu}{K_{\mathrm{sp}}}\right)\right)^g. \tag{21}$$

For K_2SO_4 crystal, according to the Burton–Cabrera–Frank (BCF) surface diffusion theory [101, 102], the index g is equal to 2 at low supersaturations. Equation 21 becomes:

$$G = k_0 \cdot \mathrm{e}^{-E/(RT)} \left(\ln\left(\frac{m_\pm^\nu \cdot \gamma_\pm^\nu}{K_{\mathrm{sp}}}\right)\right)^2. \tag{22}$$

5.2.2 Results and Discussion

The solubility product of K_2SO_4 in aqueous solution is calculated by:

$$\begin{aligned} K_{\mathrm{sp}} &= m_{\mathrm{K}}'^2 \cdot m'_{\mathrm{SO_4}} \cdot \gamma_\pm'^3 \\ m'_{\mathrm{K}} &= 2m^* \\ m'_{\mathrm{SO_4}} &= m^*, \end{aligned} \tag{23}$$

where m^* is the solubility of K_2SO_4 in aqueous solution and is notably affected by temperature. In the temperature range 273.15–333.15 K, the solubility data of K_2SO_4 are taken from the literature [103] and regressed using a polynomial of six orders by the least-squares method. The fit results are listed in Table 17, and the corresponding correlation coefficient is $R^2 = 0.999988$.

Table 17 Coefficients[a] used for the solubility of K_2SO_4

a	*b*	*c*	*d*	*e*	*f*	*g*
7.65438	0.0893443	0.0130133	−0.00083532	2.63598×10^5	-3.9454×10^7	2.23079×10^9

[a]Coefficients used in Eq. 24 in the text for the solubility of K_2SO_4 (m^*)

Table 18 Parameters[a] used for the solubility product of K_2SO_4

Salt	T(K)	U_1	U_2	U_3	U_4
K_2SO_4	273–373	−4.18629	79646.1	443.046	0.622767

[a]Parameters used in Eq. 25 in the text for the solubility product of K_2SO_4

Table 19 Correlated activation energy (E) & Pre-exponential factor (k_0) from experimental results by Garside et al. [106]

E (kJ mol^{-1})	k_0 (kg (m^{2}s)$^{-1}$)	R^2
48.981	2.903×10^7	0.9903

$$m^* = \left(a + b \cdot x + c \cdot x^2 + d \cdot x^3 + e \cdot x^4 + f \cdot x^5 + g \cdot x^6\right) \cdot 10/174.25, (x = T - 273.15). \tag{24}$$

At a certain temperature, the solubility product (K_{sp}) of K_2SO_4 can be calculated from Eq. 23 and by using the Lu–Maurer model to calculate the corresponding mean ionic activity coefficient [104, 105]. The temperature dependence of K_{sp} is expressed as in Eq. 25 with the corresponding coefficients listed in Table 18:

$$\ln K_{sp} = U_1 + U_2\left(\frac{1}{T} - \frac{1}{298.15}\right) + U_3 \ln\left(\frac{T}{298.15}\right) + U_4 (T - 298.15), \tag{25}$$

where U_1, U_2, U_3, and U_4 are the model parameters.

Parameters E and k_0 are regressed from the experimental results reported by Garside et al. [106], and the results are listed in Table 19.

Equation 22 can be used to analyze the effect of temperature on the crystal growth rate of K_2SO_4 in aqueous solutions.

Figure 33 shows the temperature effect on the crystal growth rate at different supersaturations ($\Delta m = m_{K2SO4} - m^*$) in K_2SO_4aqueous solution, calculated using Eq. 22. The activity coefficient of K_2SO_4 in the solution is calculated with the Lu–Maurer model. It is clear that the crystal growth rate increases with increasing supersaturation in solution at the same temperature. At a certain supersaturation, the crystal growth rate decreases first and then increases with increasing temperature, and the minimum growth rate is found at around 303.15 K, which is in accordance with the data reported by Taguchi et al. [98]. This phenomenon can be explained theoretically according to Eq. 22.

The crystal growth rate G can be written as $G = G_T G_m$, where $G = k_0\, e^{-E/(RT)}$ and $G = (\ln((m_k^2 m_{so4} \gamma_\pm^3)/K_{sp}))^2$. The term G_T represents the Arrhenius relationship

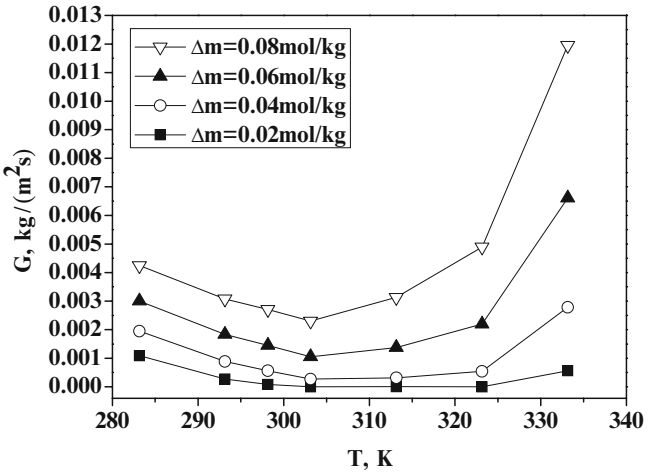

Fig. 33 Effect of temperature on crystal growth rate (G) in aqueous K_2SO_4 solution at different supersaturations. The activity coefficient is calculated using the Lu–Maurer model ($E = 48.981\,\mathrm{kJ\,mol^{-1}}$, $k_0 = 2.903 \times 10^7\,\mathrm{kg(m^2\,s)^{-1}}$)

of the crystal growth rate coefficient, which increases with increasing temperature, as shown in Fig. 34. The term G_m represents the driving force in crystallization by the chemical potential difference of K_2SO_4 at the solid–liquid interface. The value $(m_k^2 m_{so4} \gamma_\pm^3)/K_{\mathrm{sp}}$ in the expression for G_m is always more than 1 under the conditions of interest. With increasing temperature, the solubility of K_2SO_4 in the aqueous solution and the solubility product K_{sp} increase, which results in the decrease of $(m_k^2 m_{so4} \gamma_\pm^3)/K_{\mathrm{sp}}$ and its approach to 1. When the temperature is lower than 303.15 K, the effect of temperature on G_m is more than that on G_T, and the crystal growth rate of K_2SO_4 decreases with increasing temperature. However, when the temperature is higher than 303.15 K, with increasing temperature, the change of G_m is very small while G_T still increases, which causes the crystal growth rate of K_2SO_4 to increase.

If the activity coefficient of K_2SO_4 is not considered, i.e., $\gamma_\pm$ in the supersaturated solution is assumed to be the same as $\gamma_\pm^*$ in the saturated solution, the crystal growth rates at different temperatures and supersaturations are also calculated, and are shown in Fig. 35. At a certain supersaturation, the crystal growth rate increases when the temperature increases from 283.15 to 333.15 K. The tendency of crystal growth rate to decrease with increasing temperature does not exist.

This result can be explained from the curve $G_m\prime$ in Fig. 33. Here:

$$G_{m'} = \left(\ln\left(\frac{m_K^2 \cdot m_{\mathrm{SO_4}}}{4m^{*3}}\right)\right)^2 = \left(\ln\left(\frac{4\,(m^* + \Delta m)^3}{4m^{*3}}\right)\right)^2, \tag{26}$$

which is the contribution due to the concentration difference on crystal growth rate without accounting for the difference of activity coefficients of K_2SO_4 in supersaturated and saturated solutions. In the expression for G_m and $G_m\prime$, the terms K_{sp}, $\gamma_\pm$,

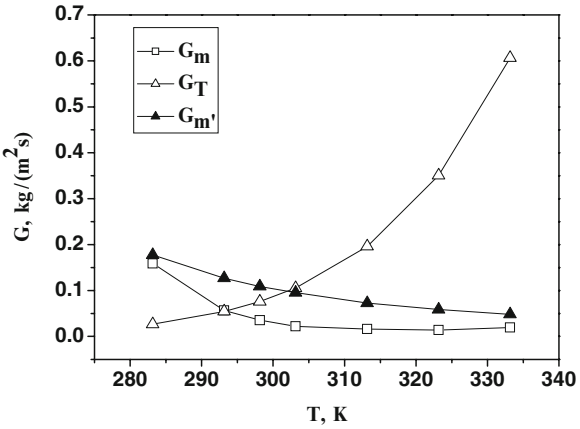

Fig. 34 Effects of the terms G_T, G_m, and $G_{m\prime}$ on crystal growth rate in supersaturated solution ($\Delta m = 0.08\,\mathrm{mol\,kg^{-1}}$, $E = 48.981\,\mathrm{kJ\,mol^{-1}}$, $k_0 = 2.903 \times 10^7\,\mathrm{kg\,(m^2\,s)^{-1}}$)

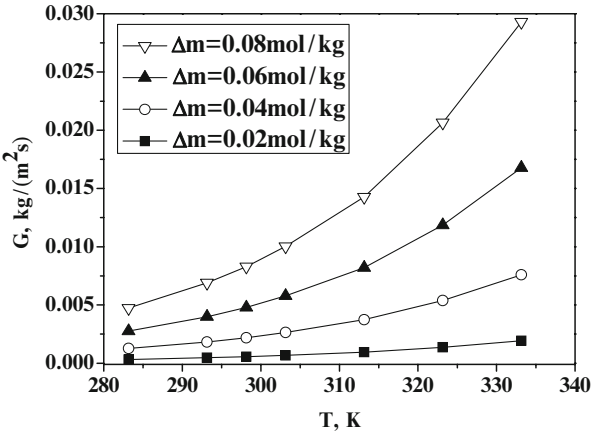

Fig. 35 Effect of temperature on the crystal growth rate in aqueous K_2SO_4 solution where the activity coefficient is neglected ($E = 48.981\,\mathrm{kJ\,mol^{-1}}$, $k_0 = 2.903 \times 10^7\,\mathrm{kg\,(m^2\,s)^{-1}}$)

and m^* are all sensitive to temperature. Thus, G_m and $G_{m\prime}$ will change with temperature. The notable difference between G_m and $G_{m\prime}$ in Fig. 34 results in the wrong result in the low-temperature range (283.15–303.15 K). This implies the importance of considering the activity coefficient in studying the crystal growth process of K_2SO_4, especially at low temperature [107].

5.3 Conclusion

In order to study the rapid process of transfer and reaction kinetics experimentally, an activity determination system was established on the basis of ion-selective electrodes, and a thermodynamic model was used to calculate the activity coefficients

of liquid components to obtain the accurate concentration of ions. The determination in the proposed system is very rapid, and the determination results are precise and reliable, with maximum deviation of less than 2%. The established method can also be used in other processes such as dissolution, crystallization, precipitation, ion-exchange reaction, adsorption, and diffusion for other systems. Meanwhile, the crystal growth rate equation of K_2SO_4 is developed on the basis of the difference of chemical potentials of K_2SO_4 at the solid–liquid interface instead of the concentration difference. The Lu–Maurer model is used to predict the activity coefficient of K_2SO_4. The new kinetic model can predict the crystal growth rate at low temperature and is in accordance with the experimental results.

6 Thermodynamics and Kinetics Analysis for Preparation of Potassium Titanate Fibers

6.1 Introduction

Potassium titanate fibers of the chemical formula $K_2O{\cdot}nTiO_2$ (n = 2, 4, 6, 8) are a class of one-dimensional inorganic materials whose diameters range from 1 to 10 μm and whose lengths can be up to several hundred microns (see Fig. 36). Fibers of potassium titanate with n = 6 and 8, i.e., $K_2Ti_6O_{13}$ and $K_2Ti_8O_{17}$, have been used as reinforcement materials for plastics and metals and as frictional materials for brakes due to their stable tunnel structure and chemical stability [108]. Fibers of potassium titanate with n = 2 and 4, i.e., $K_2Ti_2O_5$ and $K_2Ti_4O_9$, possess a layered structure and have been used as inorganic ion-exchangers or photocatalysts [109–113] (see Fig. 37).

The synthesis of potassium titanate fibers includes two steps: calcination and ion-exchange.

$$\text{Calcination step}: K_2CO_3 + nTiO_2 \xrightarrow{\text{calcination}} K_2Ti_2O_5(\text{or } K_2Ti_4O_9) + CO_2. \quad (27)$$

$$\text{Ionexchangestep}: K_2Ti_4O_9 + H^+ \begin{cases} \xrightarrow{\text{pH=9.2}} K_2Ti_6O_{13} + K^+ + H_2O \\ \xrightarrow{\text{pH=6}} K_2Ti_8O_{17} + K^+ + H_2O \\ \xrightarrow{\text{pH=2}} TiO_2 + K^+ + H_2O \end{cases} . \quad (28)$$

At present, there are still some problems with the commercial use of potassium titanate fibers in large scale production.

1. The cost of calcination is too high: Potassium titanate fibers with layered structure ($K_2Ti_2O_5$, $K_2Ti_4O_9$) are usually prepared from starting materials of anatase/rutile and potassium carbonate by the calcination method. Usually, a relatively high temperature is required for the formation of fibers, and particles but no fiber products are synthesized below 1000°C.

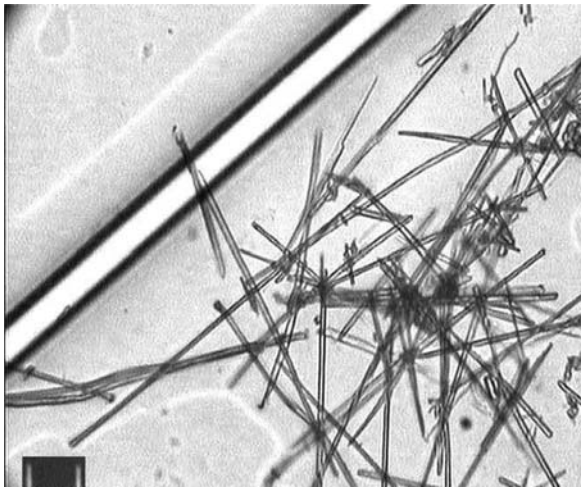

Fig. 36 Comparison between appearance of PTW and glass fibers

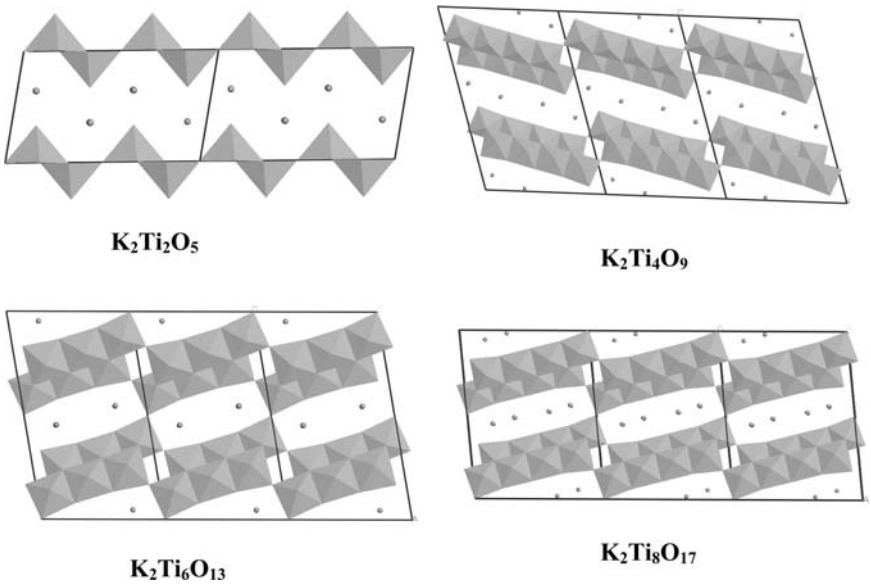

Fig. 37 Idealized crystal structure of potassium titanate

2. Control of the ion-exchange step is difficult: For the ion-exchange process, many factors (e.g., pH, the amount of water, the concentration of ions in the aqueous phase, reaction time) affect the composition of the hydrate intermediates (Table 20). Therefore, it is difficult to produce pure titanate derivatives because the content of potassium ions of the hydrate intermediates cannot be accurately controlled in the ion-exchange process.

Table 20 Ion-exchange conditions for $K_2Ti_6O_{13}$ being hydrate, taken from different literature sources

Case	Ion-exchange conditions					Ref.
	pH	Ratio[a]	Solution	Temperature	Time	
Case 1[b]	7→11	100–150	Water	RT	12 h	[127]
Case 2[c]	7→11	100–150	Water	50°C+RT	1 h + 3–4 h	[127]
Case 3	–	100	Water	RT	24 h	[128]
Case 4	–	200	Water	RT	3 h	[129]
Case 5	6→11.1	10	Water	RT	12 days	[130]
Case 6	9.3	7.4	HCl (2N)	60°C	3–5 h	[131]
Case 7	9.5	5	HCl (5N)	60°C	5 h	[132]
Case 8[d]	2.3→2.7	952	H_2SO_4(0.005N)	RT	24 h	[133]

[a]Ratio = water:initial solid (weight)
[b]Yield: 80%$K_2Ti_6O_{13}$ + 20%$K_2Ti_4O_9$
[c]Yield: 87% $K_2Ti_6O_{13}$ + 13% $K_2Ti_4O_9$
[d]Yield: 50% $K_2Ti_6O_{13}$ + 50%TiO_2

6.2 Thermodynamic Analysis of the Calcination Step

In this work, thermodynamic calculations are used to study the influence of titania reactants on the lowest generation temperature of $K_2Ti_2O_5$ by calcination [114]. The Gibbs function is usually used to estimate the direction of a spontaneous change of a chemical reaction, and gives possible reaction conditions, such as temperature and pressure, after these reaction conditions are quantitatively correlated to the thermodynamic calculation for determining the Gibbs energy of the reaction of the formation of the intended product [115].

For generalized chemical reactions, the change in Gibbs energy at constant pressure with the change of temperature is expressed by:

$$\Delta G^0_{f,T} = \Delta H^0_{f,298} - T\Delta S^0_{f,298} + \int_{298}^{T} \Delta C_p \, \mathrm{d}T - T\int_{298}^{T} \Delta C_p \, \mathrm{d}T/T. \tag{29}$$

Where $\Delta G^0_{f,T}$, $\Delta H^0_{f,T}$, and $\Delta S^0_{f,T}$ are changes of Gibbs energy, enthalpy, and entropy, respectively. C_p is heat capacity. If the Gibbs energy change at constant pressure and a certain temperature is ≤ 0, the reaction will have a tendency to roll from left to right.

Reaction equations for preparing $K_2Ti_2O_5$ from $TiO_2 \cdot nH_2O$ and anatase are expressed by Eqs. 30 and 31, respectively.

$$K_2CO_3 + 2TiO_2(\text{anatase}) \rightarrow K_2Ti_2O_5 + CO_2, \tag{30}$$

$$K_2CO_3 + 2TiO_2 \cdot nH_2O \rightarrow K_2Ti_2O_5 + CO_2 + 2nH_2O. \tag{31}$$

In the thermodynamic calculations for $\Delta G^0_{f,T}$ of Eqs. 30 and 31 with the change in temperature, we first obtain $\Delta G^0_{f,298}$, $\Delta H^0_{f,298}$, or $\Delta S^0_{f,298}$, and the relation between C_p and temperature for all solid compounds. Then we use the software packages

of Supcrt92, edited by Professor Helgeson, to calculate the thermodynamic properties of compounds at arbitrary temperature and pressure. For ordinary compounds of CO_2, H_2O, K_2CO_3, and anatase, their thermodynamic data are obtained from handbooks and Supcrt92. For $TiO_2 \cdot nH_2O$, its thermodynamic properties are obtained from the primary literature [75, 76]. However, it is difficult to obtain all the thermodynamic properties of some compounds. For example, we can obtain only $H^0_{f,298}$ of $K_2Ti_2O_5$ from the primary literature [116]. Thus, the other thermodynamic properties of $K_2Ti_2O_5$ are obtained by the regression of thermodynamic data of several thousands of solid compounds from handbooks listing the thermodynamic properties of compounds. The simplified equation for estimating $\Delta G^0_{f,298}$ and $\Delta H^0_{f,298}$ of $K_2Ti_2O_5$ is given by:

$$\Delta G^0_{f,298} = \left(\Delta H^0_{f,298} + 12822.8\right)/1.10501\,\mathrm{J\,kmol^{-1}}. \tag{32}$$

Combined with the following precise equation, we obtain $\Delta G^0_{f,298}$ and $\Delta S^0_{f,298}$ for $K_2Ti_2O_5$:

$$\Delta G^0_{f,298} = \Delta H^0_{f,298} - 298\Delta S^0_{f,298}. \tag{33}$$

The relationship between C_p and temperature for both $TiO_2 \cdot nH_2O$ and $K_2Ti_2O_5$ are estimated by the Cirss–Coble method [117].

The free energy for reactions of anatase and $TiO_2 \cdot nH_2O$ with K_2CO_3 to generate $K_2Ti_2O_5$ at $25 - 1200°C$ is estimated as shown in Fig. 38. It can be found that the

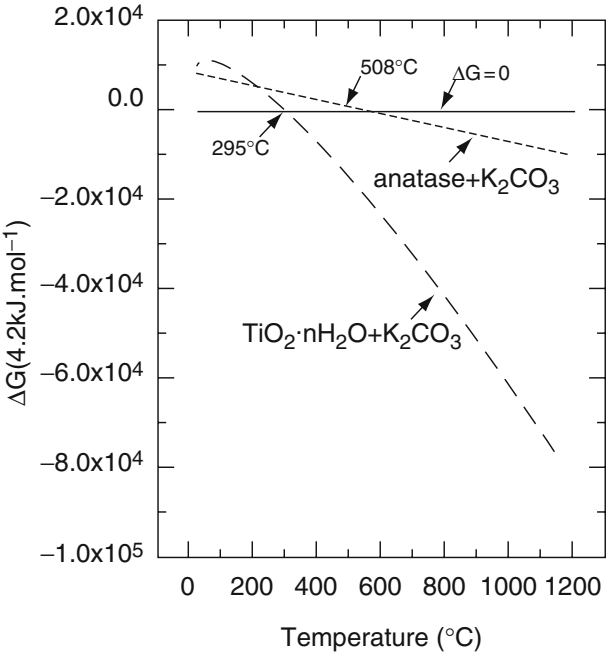

Fig. 38 Changes in Gibbs free energy (ΔG) for reactions of anatase and $TiO_2 \cdot nH_2O$ with K_2CO_3 to form $K_2Ti_2O_5$, calculated by Supcrt92

Gibbs free energy changes are lower than zero at $T > 508°C$ for reaction 30 and at $T > 295°C$ for reaction 31, indicating that estimated starting generation temperatures for preparing $K_2Ti_2O_5$ from anatase and $TiO_2 \cdot nH_2O$ are 508 and 295°C, respectively. These estimated temperatures are far lower than the reported temperature of 1000°C [118–120].

Because of the lack of comprehensive thermodynamic properties for all compounds, we attempted to obtain precise data from handbooks, primary literature, or by some estimated methods in the primary literature and the regression method with deviation of <5%. Thermodynamic calculation results confirmed that amorphous $TiO_2 \cdot nH_2O$ can decrease the lowest generation temperature of $K_2Ti_2O_5$ because of its high reaction activity compared to that of anatase. This agrees with similar thermodynamic calculations for hydrothermal syntheses of some perovskites [75, 76].

Thermogravimetric analysis and differential thermal analysis (TGA-DTA) traces of the anatase–K_2CO_3 mixture and the $TiO_2 \cdot nH_2O$–K_2CO_3 mixture, both with a TiO_2/K_2O molar value of 2.05, are shown in Fig. 39a,b, respectively, illustrating that the reaction process occurred in calcinations. The TGA trace for the anatase–K_2CO_3 mixture exhibits two obvious weight-loss steps (see Fig. 39a). A first weight loss step is attributed to the rapid decrease of free water. A second weight-loss step is observed at higher temperatures of 500–860°C, corresponding to a very broad exothermic peak centered at 550°C. With respect to the second weight loss, its starting temperature of 500°C agrees with the 508°C from thermodynamic calculations.

In Fig. 39b, a continuous weight-loss line with various slopes is observed at 100–840°C on the TGA trace. The starting weight loss at $T < 200°C$ is attributed to the rapid decrease of the free water. The following weight loss at $200 - 500°C$ is relatively slow and steady. The weight loss at $500 - 660°C$ is less than the theoretical weight loss attributed to the decomposition of K_2CO_3 of the powder mixture. We believe that the weight loss at $200 - 500°C$ is attributed to both the dehydration of $TiO_2 \cdot nH_2O$ and the slow decomposition of K_2CO_3, which result in the slow reaction between titanium and potassium oxides to form potassium dititanate hydrate.

The mixing mode of K_2CO_3 with anatase and hydrous titanium dioxide ($TiO_2 \cdot nH_2O$) was studied using thermoanalytical methods, XRD, and TEM characterization. XRD results (Fig. 40) revealed a rather poor inter-contact in the anatase–K_2CO_3 system since there were no peaks attributed to potassic salts. In contrast, the counterpart of the $TiO_2 \cdot nH_2O$–K_2CO_3 system demonstrated well-defined peaks ascribed to $KHCO_3$ and $K_2CO_3 \cdot 1.5H_2O$, at 25 and 300°C, respectively. TEM characterization (Fig. 41) showed that TiO_2 crystallites in the latter tended to disperse in a favorable way and the crystallite sizes were conspicuously smaller. These results suggested that the potassic salts could enter into the framework of $TiO_2 \cdot nH_2O$ and restricted further crystallite growth. Furthermore, the thermogravimetric analyses demonstrated the preferable nanoscale mixing status resulting from the reaction of K_2CO_3 with hydroxyl in the framework of $TiO_2 \cdot nH_2O$ [121].

The formation mechanism of $K_2Ti_2O_5$ fibers prepared with amorphous titania and K_2CO_3 at low temperatures was also investigated and is shown in Fig. 42. The growth and aggregation of the $K_2Ti_2O_5$ nucleus are prevented due to the existence of K_2CO_3 in $TiO_2 \cdot nH_2O$–K_2CO_3 samples, and $K_2Ti_2O_5$ nanofibers can be obtained

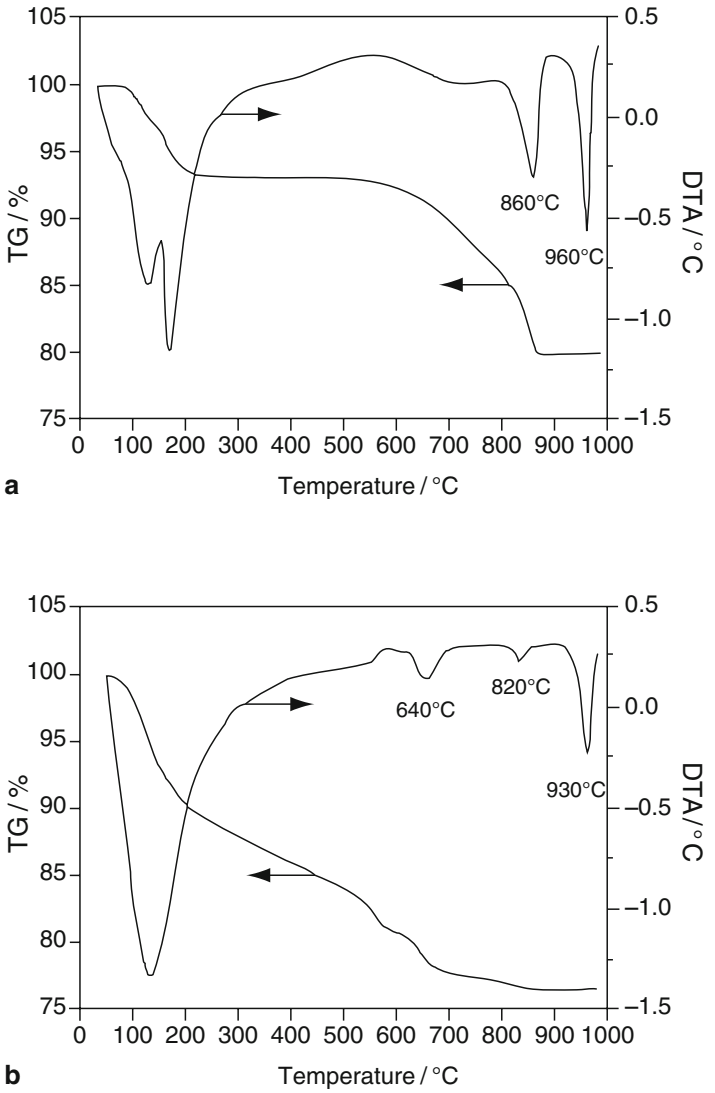

Fig. 39 TGA–DTA curves for mixtures under N_2 atmosphere: **a** anatase and K_2CO_3; **b** TiO_2fflnH_2O and K_2CO_3

at 820°C. The reaction between potassium carbonate and amorphous titania below 640°C is ascribed to the solid-state reaction process, and the reaction process around 820°C is ascribed to the $K_2Ti_2O_5$ fiber growth process due to the appearance of the K_2O melt. The separation between the reaction and the crystallization process is critical for control of the morphologies and microstructures of $K_2Ti_2O_5$ fibers at low temperatures [122].

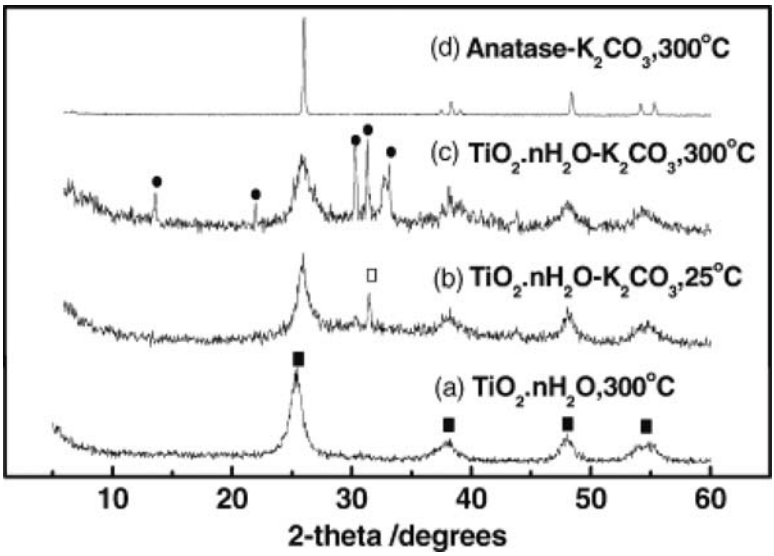

Fig. 40 XRD spectrum of the calcined samples: *a* $TiO_2 \cdot nH_2O$, 300°C; *b* $TiO_2 \cdot nH_2O$–K_2CO_3, 25°C; *c* $TiO_2 \cdot nH_2O$–K_2CO_3, 300°C; *d* anatase-K_2CO_3, 300°C. ■ Anatase, □ $KHCO_3$, • $K_2CO_3 \cdot 1.5H_2O$

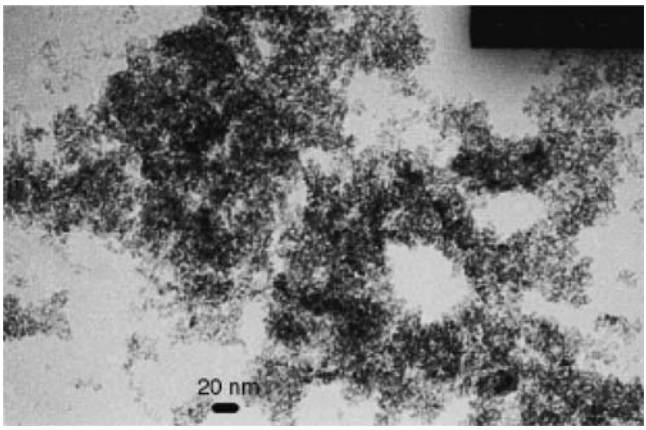

Fig. 41 TEM of the mixture of $TiO_2 \cdot nH_2O$ and K_2CO_3 that was prepared at 300°C for 2 h after the removal of the soluble potassium composites with 1 M HCl solution

Therefore, there are many advantages of using hydrous titanium dioxide as precursor in the practical production on a large scale. On one hand, the reaction temperature is decreased sharply. Thus the cost for raw materials and equipment is reduced. On the other hand, the compositions, structures, and morphologies of potassium titanate fibers are easy to control due to the separation of reaction process and crystal growth process.

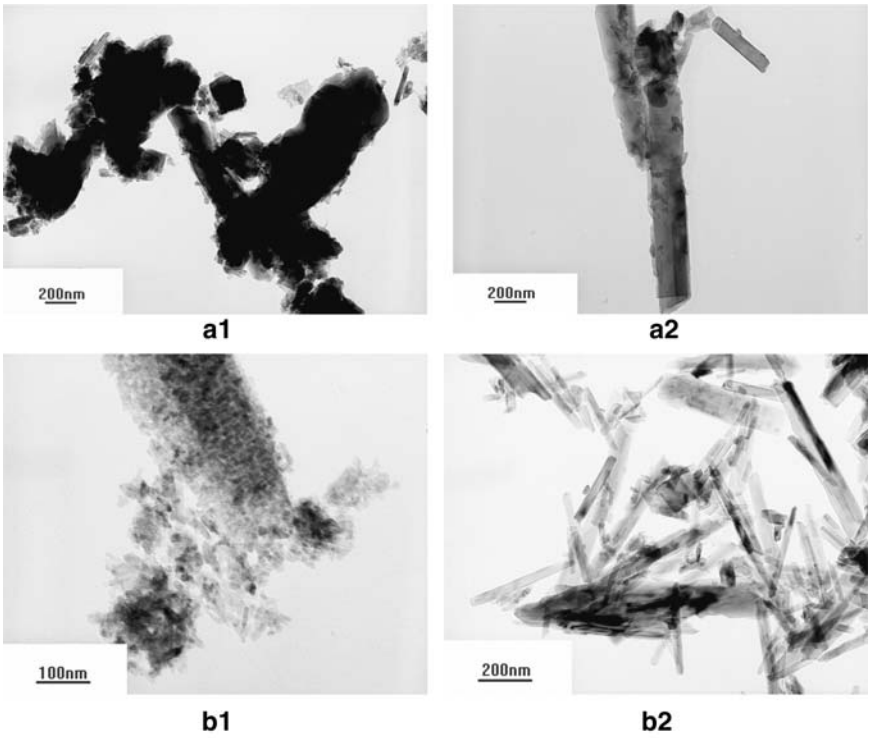

Fig. 42 TEM image of calcinated samples: **a1** anatase-K_2CO_3 heated at 640°C for 8 h; **a2** anatase-K_2CO_3 heated at 820°C for 8 h; **b1** TiO_2fflnH_2O–K_2CO_3 heated at 640°C for 8 h; **b2** TiO_2fflnH_2O–K_2CO_3 heated at 820°C for 8 h

6.3 Thermodynamic Analysis of the Ion-Exchange Step

The synthesis of $K_2Ti_6O_{13}$, $K_2Ti_8O_{17}$, and TiO_2 fiber from $K_2Ti_4O_9$ fiber is split into two steps. Firstly, $K_2Ti_4O_9$ fiber is put into water or acid solution to perform ion-exchange. In the complete process, five ion-exchange intermediates appear [123, 124], so the whole ion-exchange process is written as follows:

$$\begin{aligned}
&K_2Ti_4O_9 \cdot 2.2H_2O + 0.6H^+ \overset{K_1}{\longleftrightarrow} K_{1.4}H_{0.6}Ti_4O_9 \cdot 1.2H_2O + 0.6K^+ + H_2O \\
&K_2Ti_4O_9 \cdot 2.2H_2O + H^+ \overset{K_2}{\longleftrightarrow} KHTi_4O_9 \cdot 0.5H_2O + K^+ + 1.7H_2O \\
&K_2Ti_4O_9 \cdot 2.2H_2O + 1.5H^+ \overset{K_3}{\longleftrightarrow} K_{0.5}H_{1.5}Ti_4O_9 \cdot 0.6H_2O + 1.5K^+ + 1.6H_2O \\
&K_2Ti_4O_9 \cdot 2.2H_2O + 2.0H^+ \overset{K_4}{\longleftrightarrow} H_2Ti_4O_9 \cdot 1.2H_2O + 2.0K^+ + H_2O
\end{aligned} \tag{34}$$

Where $K_2Ti_4O_9 \cdot 2.2H_2O$ is the solid phase when $K_2Ti_4O_9$ fiber exists in aqueous solutions. Secondly, the intermediates are heated at suitable temperatures to form the final products.

The value of the equilibrium constant for each reaction is calculated from the experimental data of the potassium ion titration curve of layered protonic tetratitanate of Sasaki et al. [123]. When the corresponding equilibrium constants are determined and the equilibrium composition in the liquid phase is known, the mole fraction of each solid phase (x_i) can be calculated by combining the equation for K (Eq. 35) with a mass balance (Eq. 36):

$$K = \frac{x_{\mathrm{K_{2-b}\cdot H_b\cdot 4TiO_2\cdot cH_2O}} (m\gamma)^b_{\mathrm{K^+}}}{x_{\mathrm{K_2Ti_4O_9\cdot 2.2H_2O}} (m\gamma)^b_{\mathrm{H^+}}}, \tag{35}$$

where K is the corresponding equilibrium constant, b and c are stoichiometric coefficients; x is the mole fraction of a solid component, and m and γ are molarities and activity coefficients of H^+ or K^+ in the liquid phase, respectively. In the calculation, activity coefficients of liquid components are calculated by the Pitzer equation [80] and the parameters are taken from Greenberg and Møller [85].

$$x_{\mathrm{K_2Ti_4O_9\cdot 2.2H_2O}} + \sum_{i=1}^{N} x_i = 1. \tag{36}$$

where N is the number of solid phases except $K_2Ti_4O_9.2.2H_2O$ at equilibrium.

From the mole fraction of ion-exchange solid products it is easy to calculate the mole ratio of Ti/K in the solid phase (R), which is shown as follows:

$$R = \frac{4}{2\left(1 - \sum_{i=1}^{N} x_i\right) + \left(\sum_{i=1}^{N} (2-b)x_i\right)}. \tag{37}$$

From Fig. 43, it is obvious that the pH value has more influence on R than the concentration of K^+ and it becomes quite clear with increasing concentrations of K^+. In practice, the composition of the intermediates is controlled by adjusting the equilibrium concentration of pH and K^+ until the mole ratio of Ti/K in the solid phase (R) is the same as that of the target product. When R is 3, the $K_2Ti_6O_{13}$ yield region around the line labeled 3 is broad because the synthesis of $K_2Ti_6O_{13}$ is weakly affected by m_K and pH. These results coincide with the literature, which report a wide range of synthetic conditions for $K_2Ti_6O_{13}$. As expected, when R is 4, the $K_2Ti_8O_{17}$ yield region is smaller and it becomes more difficult to control the synthetic conditions of $K_2Ti_8O_{17}$ than those of $K_2Ti_6O_{13}$. In the case of $H_2Ti_4O_9.1.2H_2O$ (or TiO_2) when $R > 20$, the ion-exchange solid products with a higher R are generated at lower values of pH and m_K. Lower m_K can be obtained by treating with fresh HCl for more times if the pH is controlled at 2–2.5.

According to the above thermodynamics analysis, the predicted ion-exchange conditions, hydrated intermediates, temperature for heat treatment, and the final products are listed in Table 21. The XRD pattern of the final products (Fig. 44) definitely exhibited only single-phase products and good crystallinity.

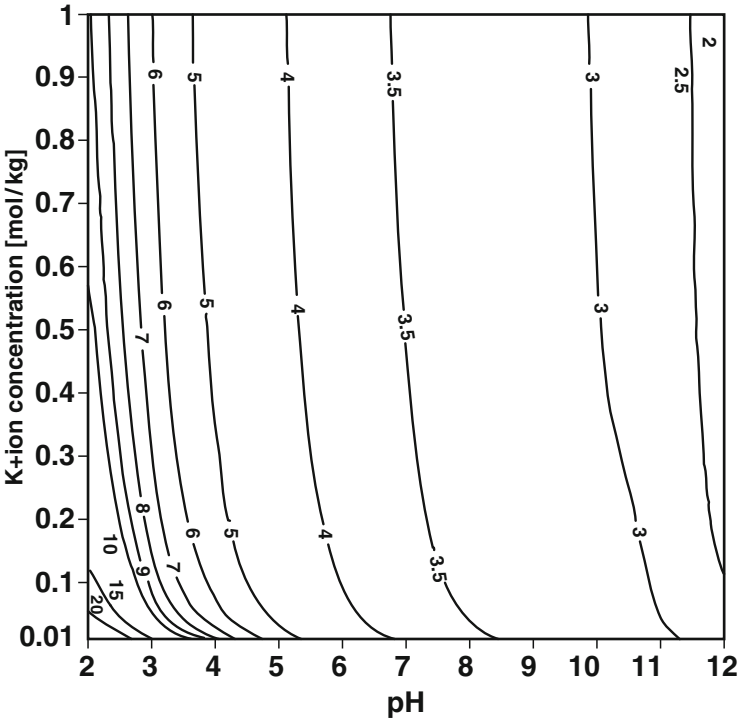

Fig. 43 Contour map of ion-exchange conditions predicted by the thermodynamic model, showing that the Ti/K molar ratio in the solid phase (*R*, values are given within each *contour line*) is a function of pH and the equilibrium concentration of K^+

Table 21 Synthesis of the hydrous intermediates and the final products, according to thermodynamics analysis

R^a	Ion-exchange conditions		Hydrated intermediates	T^c	Final product
	pH	$m_K{}^b(mol\ kg^{-1})$		(°C)	
3	9	0.06	$K_{1.33}H_0.67\ Ti_4O_9.H_2O$	850	$K_2Ti_6O_{13}$
4	6.5	0.14	$KHTi_4O_9.0.5H_2O$	500	$K_2Ti_8O_{17}$
>20	2	<0.01	$H_2Ti_4O_9.1.2H_2O$	800	TiO_2(anatase)

[a]Molar ratio of Ti/K in the solid phase
[b]Concentration of K^+
[c]Temperature for heat treatment

With the thermodynamics and kinetics models for the ion-exchange process, we attempted to optimize the operation conditions for ion-exchange processes in industrial production [125,126]. It was reported that a large amount of water ($100\,mL\,g^{-1}$) and a long reaction time (a week) are often needed in the ion-exchange process, which results in the high cost of preparation and serious environmental problems. In this work, we found that pH is the critical parameter in the ion-exchange process, and that the process can be intensified. By choosing the proper pH value, the

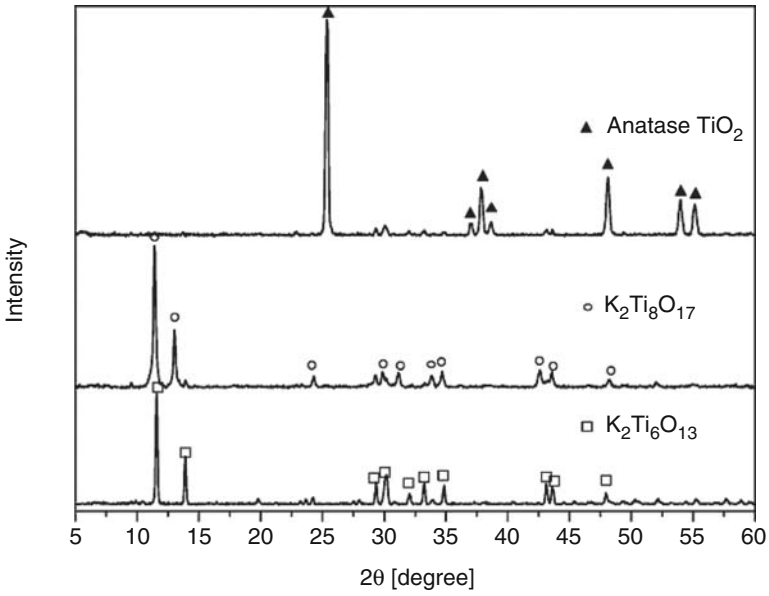

Fig. 44 XRD patterns of the target products $K_2Ti_6O_{13}$, $K_2Ti_8O_{17}$, and TiO_2 (anatase) fibers

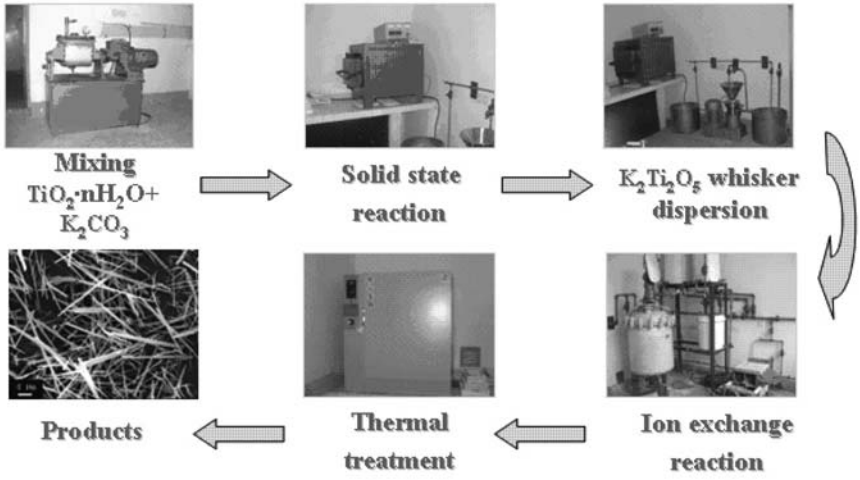

Fig. 45 Process chart for preparing potassium titanate fibers with production capacity of 20 tons per year

initial water amount, and the ion-exchange times, the total amount of water in the ion-exchange process can be reduced to 10–20 mL g^{-1}. Meanwhile, the reaction time can be shortened to 4 h. We have established a pilot plant to prepare potassium titanate fibers with producing capacity of 20 tons per year (Fig. 45).

6.4 Conclusion

In this work, we have established a method to control the composition and microstructure of advanced materials based on thermodynamic and kinetic analysis. The aim is to simplify the operation conditions and lower the production cost. We believe that this method is a guide for the synthesis of other advanced materials using chemical engineering processes.

7 Summary

In this paper, thermodynamic modeling for materials-oriented chemical engineering systems were investigated in order to solve critical scientific problems such as the material structure, chemical properties, thermodynamic properties, and transfer behaviors on the interfaces or under the confined circumstances. On the basis of the theory and approaches of chemical engineering, and the principles of chemical engineering thermodynamics,and transfer processes, molecular simulation were combined with modern physical characterization methods to study thermodynamic modeling for materials-oriented chemical engineering processes.

Acknowledgment

This work was supported by the Program for Changjiang Scholars and Innovative Research Team in University (no. IRT0732), the National Natural Science Foundation of China (NSFC) and the Research Grants Council (RGC) of Hong Kong Joint Research Scheme (JRS) (no. 20731160614), the Joint Research Fund of NSFC for Young Scholars Abroad (no. 20428606), the NSFC (nos. 20236010, 20676062, 20736002, 20706029, and 20706028), National High Technology Research and Development Program of China (no. 2006AA03Z455), and the Key Science Foundation of Jiangsu Province, China (BK2007051).

References

1. Hummer G, Rasaiah JC, Noworyta JP (2001) Nature 414:188
2. Koga K, Gao GT, Tanaka H, Zeng XC (2001) Nature 412:802
3. Thallapally PK, Lloyd GO, Atwood JL, Barbour LJ (2005) Angew Chem Int Ed 44:3848
4. Liu C, Fan YY, Liu M, Cong HT, Cheng HM, Dresselhaus MS (1999) Science 286:1127
5. Sazonova V, Yaish Y, Ustunel H, Roundy D, Arias TA, Mceuen PL (2004) Nature 431:284
6. Snow ES, Perkins FK, Houser EJ, Badescu SC, Reinecke TL (2005) Science 307:1942
7. Portney NG, Ozkan M (2006) Anal Bioanal Chem 384:620
8. Hinds BJ, Chopra N, Rantell T, Andrews R, Gavalas V, Bachas LG (2004) Science 303:5654

9. Zhu FQ, Schulten K (2003) Biophys J 85:236
10. Rivera JL, McCabe C, Cummings PT (2002) Nano Lett 2:1427
11. Marti J, Gordillo MC (2002) Chem Phys Lett 354:227
12. Marti J, Guardia E, Gordillo MC (2002) Chem Phys Lett 365:536
13. Gordillo MC, Marti J (2001) Chem Phys Lett 341:250
14. Koga K, Gao GT, Tanaka H, Zeng XC (2002) Physica A 314:462
15. Walther JH, Jaffe R, Halicioglu T, Koumoutsakos P (2001) J Phys Chem B 105:9980
16. Gordillo MC, Marti J (2003) Phys Rev B 67:205425
17. Charlier JC (2002) Acc Chem Res 35:1063
18. Niyogi S, Hamon MA, Hu H, Zhao B, Bhowmik P, Sen R, Itkis ME, Haddon RC (2002) Acc Chem Res 35:1105
19. Noon WH, Ausman KD, Smalley RE, Ma JP (2002) Chem Phys Lett 355:445
20. Joseph S, Mashl RJ, Jakobsson E, Aluru NR (2003) Nano Lett 3:1399
21. Gordillo MC, Marti J (2000) Chem Phys Lett 329:341
22. Ruoff RS, Tse DS, Malhotra R, Lorents DC (1993) J Phys Chem 97:3379
23. Scrivens WA, Tour JM (1993) J Chem Soc Chem Commun 18:1207
24. Yao Z, Braidy N, Botton GA, Adronov A (2003) J Am Chem Soc 125:16015
25. Kong J, Franklin NR, Zhou CW, Chapline MG, Peng S, Cho KJ, Dai HJ (2000) Science 287:5453
26. Pantarotto D, Partidos CD, Graff R, Hoebeke J, Briand JP, Prato M, Bianco A (2003) J Am Chem Soc 125:6160
27. Tasis D, Tagmatachis N, Bianco A, Prato M (2006) Chem Rev 106:1105
28. Hirsh A (2002) Angew Chem Int Ed 41:1853
29. Sun YP, Fu K, Lin Y, Huang W (2002) Acc Chem Res 35:1096
30. Zheng J, Lennon EM, Tsao HK, Sheng YJ, Jiang SY (2005) J Chem Phys 122:214702
31. Halicioglu T, Jaffe RL (2002) Nano Lett 2:573
32. Huang LL, Shao Q, Lu LH, Lu XH, Zhang LZ, Wang J, Jiang SY (2006) Phys Chem Chem Phys 8:3836
33. Wang J, Zhu Y, Zhou J, Lu XH (2004) Phys Chem Chem Phys 6:829
34. Luzar A, Chandler D (1996) Nature 379:55
35. Zimmerli U, Gonnet PG, Walther JH, Koumoutsakos P (2005) Nano Lett 5:1017
36. Zhou QL, Zhou Q, Forman SA (2000) Biochemistry 39:14920
37. Mihic SJ, Ye Q, Wick MJ, Koltchine VV, Krasowski MD, Finn SE, Mascia MP, Valenzuela CF, Hanson KK, Greenblatt EP, Harris RA, Harrison NL (1997) Nature 389:385
38. Ren H, Honse Y, Peoples RW (2003) J Biol Chem 278:48815
39. Vane LM (2005) J Chem Technol Biotechnol 80:603
40. Zhang QX, Zheng J, Shevade A, Zhang LZ, Gehrke SH, Heffelfinger GS, Jiang SY (2002) J Chem Phys 117:808
41. Denis M, Regis G, Yongde X, Christiane A-S (2004) J Chem Phys 121:1466
42. Guegan R, Morineau D, Alba-Simionesco C (2005) Chem Phys 317:236
43. Sliwinska-Bartkowiak M, Dudziak G, Sikorski R, Gras R, Gubbins KE, Radhakrishnan R (2001) Phys Chem Chem Phys 3:1179
44. Ohkubo T, Iiyama T, Kaneko K (1999) Chem Phys Lett 312:191
45. Kaneko K (2000) Carbon 38:287
46. Feller SE, Brown CA, Nizza DT, Gawrisch K (2002) Biophys J 82:1396
47. Patra M, Salonen E, Terama E, Vattulainen I, Faller R, Lee BW, Holopainen J, Karttunen M (2006) Biophys J 90:1121
48. Hofmann D, Fritz L, Paul D (1998) J Membr Sci 144:145
49. Takaba H, Koyama A, Nakao S (2000) J Phys Chem B 104:6353
50. Striolo A (2006) Nano Lett 6:633
51. Jorgensen WL (1986) J Phys Chem 90:1276
52. Compoint M, Boiteux C, Huetz P, Ramseyer C, Girardet C (2005) Phys Chem Chem Phys 7:4138
53. Vaitheeswaran S, Rasaiah JC, Hummer G (2004) J Chem Phys 121:7955
54. Mashl RJ, Joseph S, Aluru NR, Jakobsson E (2003) Nano Lett 3:589

55. Zhou J, Lu XH, Wang YR, Shi J (2002) Fluid Phase Equilibria 194–197:257
56. Zhu Y, Lu XH, Ding H, Wang YR (2003) Mol Simul 29:767
57. Ding H, Zhu Y, Wang J, Lu XH, Ma J (2004) Acta Chim Sin 62:1287
58. Burgess J (1978) Metal ions in solution. Ellis Horwood, Chichester
59. Marcus Y (1985) Ion solvation. Wiley, Chichester
60. Frisch MJ, Trucks GW, Schlegel HB (1998) Gaussian 98. Gaussian, Pittsburgh
61. Pitzer KS, Li YG (1984) Proc Natl Acad Sci USA 81:1268
62. Oelkers EH, Helgeson HC (1991) Geochim Cosmochim Acta 55:1235
63. Lu XH, Wang YR, Shi J (1988) Fluid Phase Equilibria 43:137
64. Valyashko VM, Urusova MA, Ketsko VA (1987) Zhurnal Neorganicheskoi Khimii 32:2811
65. Armstrong AR, Armstrong G, Canales J, Bruce PG (2004) Ang Chem Int Ed 43:2286
66. Byrappa K, Yoshimura M (2001) Handbook of hydrothermal technology: a technology for crystal growth and materials processing. William Andrew, New York
67. Rabenau H, Rau H (1969) Philips Techn Rev 30:89
68. Chen YF, Lee CY, Yeng MY, Chiu HT (2003) Mater Chem Phys 81:39
69. Lu XH, Zhang LZ, Wang YR, Shi J (1996) Fluid Phase Equilibria 116:201
70. Harvie CE, Weare JH (1980) Geochim Cosmochim Acta 44:981
71. Rafal M, Berthold JW, Scrivner NC, Grise SL (1994) Models for electrolyte solutions. Marcel Dekker, New York
72. Berry DA, Ng KM (1997) AIChE J 43:1737
73. Thomsen K, Rasmussen P, Gani R (1998) Chem Eng Sci 53:1551
74. Lencka MM, Riman RE (1993) Chem Mater 5:61
75. Lencka MM, Riman RE (1993) J Am Ceram Soc 76:2649
76. Lencka MM, Anderko A, Riman RE (1995) J Am Ceram Soc 78:2609
77. Ji XY, Feng X, Lu XH, Zhang LH, Wang YR, Shi J, Liu YD (2002) Ind Eng Chem Res 41:2040
78. Prausnitz JM, Anderson TF, Grens EA (1980) Computer calculations for multicomponent vapor–liquid and liquid–liquid equilibria. Prentice-Hall, New Jersey
79. Kusik CL, Meissner HP, Field EL (1979) AIChE J 25:759
80. Pitzer KS (ed) (1991) Activity coefficients in electrolyte solution. CRC, Boston
81. Lu XH, Maurer G (1993) AIChE J 39:1527
82. Pabalan RT, Pitzer KS (1991) Mineral solubilities in electrolyte solutions. In: Pitzer KS (ed) Activity coefficients in electrolyte solution. CRC, Boston, p 435
83. Linke WF, Seidell A (1965) Solubilities of inorganic and metal-organic compounds. American Chemical Society, Washington DC
84. Cisternas LA, Rudd DF (1993) Ind Eng Chem Res 32:1993
85. Greenberg JP, Moller N (1989) Geochim Cosmochim Acta 53:2503
86. Yan LM (1998) J Chem Ind Eng Technol (Chinese) 19:28
87. Sun Q (1999) Sea Lake & Chem Ind (Chinese) 28:24
88. Salem MR, Mangood AH, Hamdona SK (1994) J Mater Sci 29:6463
89. Palwe BG, Tavare NS (1984) Chem Eng Sci 39:903
90. Kralj D, Brecevic L, Kontrec J (1997) J Cryst Growth 177:248
91. Bovinton CH, Jones AL (1970) Trans Faraday Soc 66:2088
92. Kallay N, Tomasic V, Zalac S, Brecevic L (1997) J Colloid Interf Sci 188:68
93. Garside J, Mullin JW (1968) Trans Inst Chem Eng 46:T11
94. Mydlarz J, Jones AG (1989) Chem Eng Sci 44:1391
95. Liu C, Feng X, Ji XY, Chen DL, Wei T, Lu XH (2004) Chinese J Chem Eng 12:128
96. Bergfors TM (1999) Protein crystallization. International University Line, La Jooa
97. Mullin JW (1997) Crystallization. Butterworth-Heinnemann, Woburn
98. Taguchi Y, Yoshida M, Kobayashi H (2002) J Chem Eng Jpn 35:1038
99. Feng X, Liu C, Ji X-Y, Chen D-l, Lu X-h (2000) Gaoxiao Huaxue Gongcheng Xuebao 14:583
100. Kim S, Myerson AS (1996) Ind Eng Chem Res 35:1078
101. Mohan R, Myerson AS (2002) Chem Eng Sci 57:4277
102. Burton WK, Cabrera N, Frank FC (1951) Philos Trans R Soc London, Ser A 243:299

103. Soehnel O, Novotny P (1985) Densities of aqueous solutions of inorganic substances. Elsevier, New York
104. Lu X, Zhang L, Wang Y, Shi J, Maurer G (1996) Ind Eng Chem Res 35:1777
105. Ji XY, Zhang LZ, Lu XH, Wang YR, Shi J (1997) J Chem Ind Eng (Chinese) 48:532
106. Garside J, Mullin JW, Das SN (1974) Ind Eng Chem Fundam 13:299
107. Cheng FQ, Bai Y, Liu C, Lu XH, Dong CA (2006) Ind Eng Chem Res 45:6266
108. Feng X, Diao XS, Shi YJ, Wang HY, Sun SH, Lu XH (2006) WEAR 261:1208
109. Bao N, Feng X, Yang Z, Shen L, Lu X (2004) Environ Sci Technol 38:2729
110. He M, Lu XH, Feng X, Yu L, Yang ZH (2004) Chem Comm, p 2202
111. He M, Yu L, Lu XH, Feng X (2007) J Am Ceram Soc 90:319
112. Feng X, Lu J, Lu X, Bao N, Chen D (1999) Fuhe Cailiao Xuebao 16:1
113. Lu JZ, Lu XH (2001) Appl Polym Sci 82:368
114. Bao N, Feng X, Lu X, Shen L, Yanagisawa K (2004) AIChE J 50:1568
115. Smith JM, Van Ness HC (1975) Introduction to chemical engineering thermodynamics, 3rd edn. McGraw-Hill, Kogakusha, Japan
116. Khakonov AI (1974) J Phys Chem (USSR) 48:1552
117. Criss CM, Cobble JW (1964) J Am Ceram Soc 86:5385
118. Andersson S, Woadsley AD (1960) Nature 187:499
119. Andersson S, Woadsley AD (1961) Acta Chem Scand 15:663
120. Fujiki Y, Ohsaka T (1982) Yogyo Kyokaishi 90:19
121. Yu L, He M, Liu C, Lu XH, Feng X (2005) Mater Chem Phys 93:342
122. Liu C, He M, Lu XH, Zhang QT, Xu ZZ (2005) Crystal Growth Design 5:1399
123. Sasaki T, Watanabe M, Komatsu Y, Fujiki Y (1985) Inorg Chem 24:2265
124. He M, Feng X, Lu XH, Ji XY, Liu C, Bao NZ, Xie JW (2004) J Mater Sci 39:3745
125. He M, Feng X, Lu XH, Ji XY, Liu C, Bao NZ, Xie JW (2003) J Chem Eng Jpn 36:1259
126. Bao NZ, Lu XH, Ji XY, Feng X, Xie JW (2002) Fluid Phase Equilibria 193:229
127. Xie K, Pan Y, Wang XH, Li Y (1997) Inorg Chem Ind (Chinese) 1:16
128. Tajima M, Noda K, Morita Y, Matsutani Y (1988) Japan patent 63064998
129. Kobayashi I, Fukami J, Ootsubo K (1993) Japan patent 05009462
130. Shimizu T, Yanagida H, Hori M, Hashimoto K, Nishikawa Y (1979) Yogyo Kyokaishi 87:565
131. Harada H, Kudoh Y, Inoue Y, Shima H (1995) J Ceram Soc Jpn 103:155
132. Harada H, Inoue Y (1992) US patent 5084422
133. Ohta N, Fujiki Y (1980) Yogyo Kyokaishi 88:1
134. Fitch B (1970) Ind Eng Chem Res 62:6

Index